Design of environmentally friendly calcium sulfate-based building materials : towards an improved indoor air quality

Citation for published version (APA):
Yu, Q. (2012). *Design of environmentally friendly calcium sulfate-based building materials : towards an improved indoor air quality*. [Phd Thesis 1 (Research TU/e / Graduation TU/e), Built Environment]. Technische Universiteit Eindhoven. https://doi.org/10.6100/IR732956

DOI:
10.6100/IR732956

Document status and date:
Published: 01/01/2012

Document Version:
Publisher's PDF, also known as Version of Record (includes final page, issue and volume numbers)

Please check the document version of this publication:

• A submitted manuscript is the version of the article upon submission and before peer-review. There can be important differences between the submitted version and the official published version of record. People interested in the research are advised to contact the author for the final version of the publication, or visit the DOI to the publisher's website.
• The final author version and the galley proof are versions of the publication after peer review.
• The final published version features the final layout of the paper including the volume, issue and page numbers.

Link to publication

General rights
Copyright and moral rights for the publications made accessible in the public portal are retained by the authors and/or other copyright owners and it is a condition of accessing publications that users recognise and abide by the legal requirements associated with these rights.

- Users may download and print one copy of any publication from the public portal for the purpose of private study or research.
- You may not further distribute the material or use it for any profit-making activity or commercial gain
- You may freely distribute the URL identifying the publication in the public portal.

If the publication is distributed under the terms of Article 25fa of the Dutch Copyright Act, indicated by the "Taverne" license above, please follow below link for the End User Agreement:

www.tue.nl/taverne

Take down policy
If you believe that this document breaches copyright please contact us at:

openaccess@tue.nl

providing details and we will investigate your claim.

Download date: 22. Aug. 2022

Design of environmentally friendly calcium sulfate-based building materials

Towards an improved indoor air quality

De promotiecommissie is als volgt samengesteld:

Voorzitter:

prof.ir. J. Westra	Technische Universiteit Eindhoven

Promotor:

prof.dr.ir. H.J.H. Brouwers	Technische Universiteit Eindhoven

Leden (in alfabetische volgorde):

prof.dr.ir. N. De Belie	Universiteit Ghent
Dr.-Ing H.-B. Fischer	Bauhaus-Universität Weimar
prof.dr.ir. E.J.M. Hensen	Technische Universiteit Eindhoven
Prof. Dr. H.-U. Hummel	Friedrich-Alexander-Universität Erlangen-Nürnberg
prof.dr.ir. J.J.N. Lichtenberg	Technische Universiteit Eindhoven
prof.dr.ir. Dr. -Ing. e.h.J.C.Walraven	Technische Universiteit Delft

CIP-DATA LIBRARY TECHNISCHE UNIVERSITEIT EINDHOVEN

Design of environmentally friendly calcium sulfate-based building materials - towards an improved indoor air quality / by Qingliang Yu.

ISBN 978-90-6814-647-9

Bouwstenen 164

NUR 955

Ph.D. Thesis, Eindhoven University of Technology, the Netherlands

Cover design: Mr. H.J.M. Lammers, Grafische Studio Bouwkunde, Eindhoven University of Technology, the Netherlands.

Cover photograph supplied by the author (Building and Environment).

Printed by: Universiteitsdrukkerij, Eindhoven University of Technology, the Netherlands.

Design of environmentally friendly calcium sulfate-based building materials

---- Towards an improved indoor air quality

PROEFSCHRIFT

ter verkrijging van de graad van doctor aan de
Technische Universiteit Eindhoven, op gezag van de
rector magnificus, prof.dr.ir. C.J. van Duijn, voor een
commissie aangewezen door het College voor
Promoties in het openbaar te verdedigen
op donderdag 3 mei 2012 om 16.00 uur

door

Qingliang Yu

geboren te Henan, China

Dit proefschrift is goedgekeurd door de promotor:

prof.dr.ir. H.J.H. Brouwers

Dedicated to my brother ***Tao Yu***
(October 21, 1973 – March 22, 2002)

Preface

"Wow! It has already been almost four years since I started my PhD study!" This was my first impression when I just started thinking about the preface for this thesis. I still clearly remember the day, January 12, 2008, when I arrived in the Netherlands for my PhD study. When looking back, there were difficulties, frustrations, unhappiness, but in overall I can say, I have never enjoyed my life so much. I received so much help and support during this long period from so many people, who truly deserve my sincere thanks.

First, I would like to express my gratitude to my supervisor and promoter prof.dr.ir. Jos Brouwers. Jos, thank you really very much, not only for providing me this valuable chance to do my PhD research under your supervision, but also for all your guidance, suggestions, comments, patience and trust in the last four years. I learned a lot from you, and I really enjoyed all the time working with you.

I also appreciate the financial support of the European Commission (6th FP Integrated Project "The Integrated Safe and Smart Built Project" (I-SSB), Proposal No. 026661-2) and of the sponsor group who funded this research. Special thanks are given to: Prof. Dr. H.U. Hummel and Mrs. K. Engelhardt (Knauf Gips KG, Germany) for all the calcium sulfate-related materials supply and their advices during this study; Mr. H. Vos (Lias Benelux BV, the Netherlands) for the lightweight aggregates supply; Dr. Ch. Hampel (Sika Technology AG, Switzerland) for the superplasticizer supply; and Dr. S. P. Blöß and Mr. J. Bender (Kronos International, Germany) for the photocatalyst supply. My gratitude is also given to: Dr. A.M. Lopez Buendia and Mrs. C. Suesta Falco (Aidico, Spain) for performing the fire tests; Prof. C.U. Grosse and Mr. F. Lehmann (University of Stuttgart, Germany) for executing the ultrasonic measurements; Prof. Dr. Dr. H. Pöllmann (Martin-Luther-Universität Halle-Wittenberg, Germany) for the XRF measurements; prof.dr.ir. J.W.M. Noordermeer and Mr. J. Lopulissa (University of Twente, the Netherlands) for allowing me to use their DSC & TGA analyzer; Ing. P.J.L. Lipman (Technische Universiteit Eindhoven (TU/e)) for allowing me to use the BET analyzer; and Mr. M.P.F.H.L. van Maris (TU/e) for allowing me to use the SEM.

Furthermore, I would like to express my appreciation to prof.dr.ir. N. De Belie (Universiteit Ghent, Belgium), Dr.-Ing H.-B. Fischer (Bauhaus-Universität Weimar, Germany), prof.dr.ir. E.J.M. Hensen (Technische Universiteit Eindhoven, the Netherlands), Prof. Dr. H.-U. Hummel (Knauf Gips KG & Friedrich-Alexander-Universität Erlangen-Nürnberg, Germany), prof.dr.ir. J.J.N. Lichtenberg (Technische Universiteit Eindhoven, the Netherlands), and prof.dr.ir. J.C. Walraven (Technische Universiteit Delft, the Netherlands) for their comments on this thesis and for agreeing to be members of my PhD defense committee.

In addition, I would like to thank Prof. Zhean Lu, Dr. Wei Chen, and Prof. Dr. Zhonghe Shui at Wuhan University of Technology (China) for their advice, support and encouragement during the last years.

I started my PhD research in University of Twente before I moved to Eindhoven University of Technology in September 2009. I would like to address my appreciation to some former colleagues for their help and support: Ariën de Korte, Jimmy Avendano Castillo, Tatsiana Haponava, Bram Entrop, Maarten Rutten, Erwin Hofman, and Yolanda Bosch. Ariën, I need to express my special gratitude to you. You know how difficult it was, especially during the first months of my PhD research. But you were just so kind to help and encourage me for everything! I spent too much of your time, sorry!

My thanks are also given to the following colleagues: Martin Hunger, Götz Hüsken, Mili Ballari, Przemek Spiesz, Miruna Florea, Alberto Lazaro Garcia, George Quercia Bianchi, Azee Taher, Štěpán Lorenčik, Rui Yu and Pei Tang. It is my true fortune to work with you in such a lovely group. Mili, we worked together almost three years until December 2010, when you moved back to Argentina. You helped me so much but you never complained about anything. I really appreciate it! I wish you all the best in Argentina. Przemek, you know how difficult it is to spell your name, not even mentioning its pronunciation. But I managed to do both quickly and you know the reason. We sit face to face for already such a long time, that I even sometimes think, ok, I need to take a day off. Thanks, really for everything. Here, special thanks are also given to Przemek Spiesz, Miruna Florea, Dr. A.J.J. van der Zanden, George Quercia Bianchi, Ariën de Korte, Alberto Lazaro Garcia and Štěpán Lorenčik for reading and correcting my thesis. In addition, my thanks are also given to Hector Cubillos Sanabria for his contribution to the CFD modeling work in this thesis. My appreciations are also expressed to our lovely secretaries: Renée van Geene and Yeliz Varol. My thanks are also given to all the colleagues in the laboratories of both unit BPS and unit structural design. I need to express my special gratitude to Peter Cappon. Peter, thank you very much for spending so much time to help me, even so many times until very late in the evening, but you never complained. I really appreciate it.

I would like to express my thanks to all my Chinese friends here in the Netherlands as well. The list would be too long to mention everybody here, but to all of you, thanks a lot!

Finally, I need to express my appreciations to my family. Mum and Dad, thank you very much for always supporting me. My thanks are also given to my sister Aimei and my brother-in-law Wenju for taking care of our parents when I was not in China. Finally, but definitely most importantly, I need to express my appreciations and sorry to my wife. Juanjuan, you sacrificed your career to take care of our family. I owe you so much that I could never compensate! We received our son Daniel from God in December 2008. Everyday no matter how tired I am, when I see Daniel, I am immediately refreshed. Daniel, I am really very proud of being your dad!

Qingliang Yu

Eindhoven, December 2011

Contents

Chapter 1

Introduction

1.1 General

$CaSO_4$·H_2O systems

Building materials, a term referring to materials used in construction and building, can be classified based on their type into categories such as metal (e.g. steel, aluminum), mineral (e.g. natural stone, concrete, gypsum, glass), or organic (e.g. plastic, bitumen). Table 1.1 lists the global production of the most used man-made building materials in 2008. These enormous amounts indicate the great consumption of energy for the production and for the transport of raw materials and of their products.

Table 1.1: Annual global production of materials in 2008 (Brouwers, 2010).

Material	Amount (ton)	Material	Amount (ton)
Timber	4000×10^6	Quicklime	130×10^6
Plastics and rubber	250×10^6	Glass	120×10^6
Steel	1400×10^6	Cement	2500×10^6
Gypsum	250×10^6	Concrete	15000×10^6

Among all the above listed materials, concrete is by far the most used man-made building material because it is cheap, easily cast to any shape according to requirements, mechanically strong and durable. Concrete normally has five main constituents: cement, aggregates, water, additives and admixtures, among which cement plays the crucial role of the binding agent. However, cement is a highly energy-intensive material and great amounts of CO_2 are emitted during its production process. Nevertheless, it is very difficult to reduce this negative impact since about 90% of the energy needed for concrete production is spent in the cement production (Hüsken, 2010).

Hence, the question arises whether it is possible to use other materials instead of cement as binders, and the answer is positive, for instance the $CaSO_4·H_2O$ (calcium sulfate) system. Most calcium sulphate systems are characterized by three solid phases, depending on the stoichiometric amount of the crystallized water: calcium sulphate dihydrate (also called gypsum, $CaSO_4·2H_2O$), calcium sulphate hemihydrate ($CaSO_4·0.5H_2O$, including the α- and β-types) and calcium sulphate anhydrite ($CaSO_4$) (Wirsching, 2005). Gypsum plaster (calcium sulphate hemihydrate in β-type) was already used in Egyptian pyramids at least 4000 years ago (Ryan, 1962), and is still extensively applied in buildings along with other cementitious materials such as cement and lime.

Calcium sulphate systems, compared to cement, are much more environmentally friendly. They are very suitable to be used as building materials also because of the following characteristics they possess. Calcium sulphate hemihydrate is a hydraulic material, which undergoes chemical reactions quickly when in contact with water, generating calcium sulphate dihydrate. Thus calcium sulphate hemihydrate can be used as a binding agent. Calcium sulphate dihydrate, on the other hand, readily loses its chemically combined water at elevated temperatures and this process absorbs a great amount of heat, so that calcium sulphate dihydrate can be used as a perfect fire/thermal insulation material.

Indoor air quality

In modern urban areas, the majority of people spend approximately 80% of their time indoors, exposing themselves to the indoor environment more than to the outdoors (Lebowitz and Walkinshaw, 1992), indicating the importance of the indoor air quality (IAQ). Indoor air quality is a term referring to the air quality within and around buildings and structures, especially as it is related to the health and comfort of building occupants, which can be affected by temperature, humidity, microorganisms, particulate matters, air pollutants etc. (Finnegan et al., 1984; Cooley et al., 1998; Wargocki et al., 2000; Harrison et al., 1992).

Thermal comfort is influenced by heat conduction, convection, radiation and evaporative heat loss, which is linked to temperature and humidity under indoor air conditions. Enormous efforts have been made to address a better indoor thermal comfort, for instance by designing much tighter and compact buildings. However, this could cause problems of Sick Building Syndrome (SBS) (will be analyzed intensively later in this Thesis). Indoor air pollutants, strongly linked to the health of residents, are related to various factors such as indoor building materials, furniture, human behavior such as smoking and cooking, and air pollutants from outside such as traffic emissions close to the building, etc. Conventional methods of reducing indoor air pollutants include controlling pollutant sources, increasing air exchange and using air purification systems, which, however, have many disadvantages.

1.2 Research objective and strategy

Research objective

Modern building materials are usually applied in a combination of different types, in order to produce new materials with improved properties over the individual materials themselves, and they can be termed “composite building materials”. Currently, materials design has shifted from prescription based to performance based, in order to add extra values or functionality to the new development (Brouwers, 2010). This will be applied as the design methodology in the present study. Therefore, the main research objective of this project is formulated as follows:

The development of novel calcium sulfate-based environmentally friendly indoor building materials, which contribute to an improved indoor air quality efficiently and sustainably.

Research strategy

In the present study, indoor air quality is investigated in its macro-level definition, i.e. related to both health and comfort, while health is linked to indoor air pollutants and comfort is linked to thermal comfort. In this thesis, the term "environmentally friendly" is used not only because of new advanced properties the new product possesses, i.e. the improved indoor thermal comfort and indoor air pollutants removal function, but also because the main raw material used here is a sustainable by-product of an industrial process. A calcium sulphate hemihydrate produced from the flue gas desulfurization (FGD) gypsum is used as the raw material, taking sustainability into account, since FGD gypsum is a by-product of the process of desulfurization of combustion gases of fossil fuels (coal, lignite, oil) in power stations (Wirsching, 2005).

This research is performed based on a combination of theoretical and experimental investigation. Furthermore, modeling work is carried out as well for a deeper understanding of the investigated materials. Figure 1.1 gives a schematic description of the relations between the designed products towards the research objective.

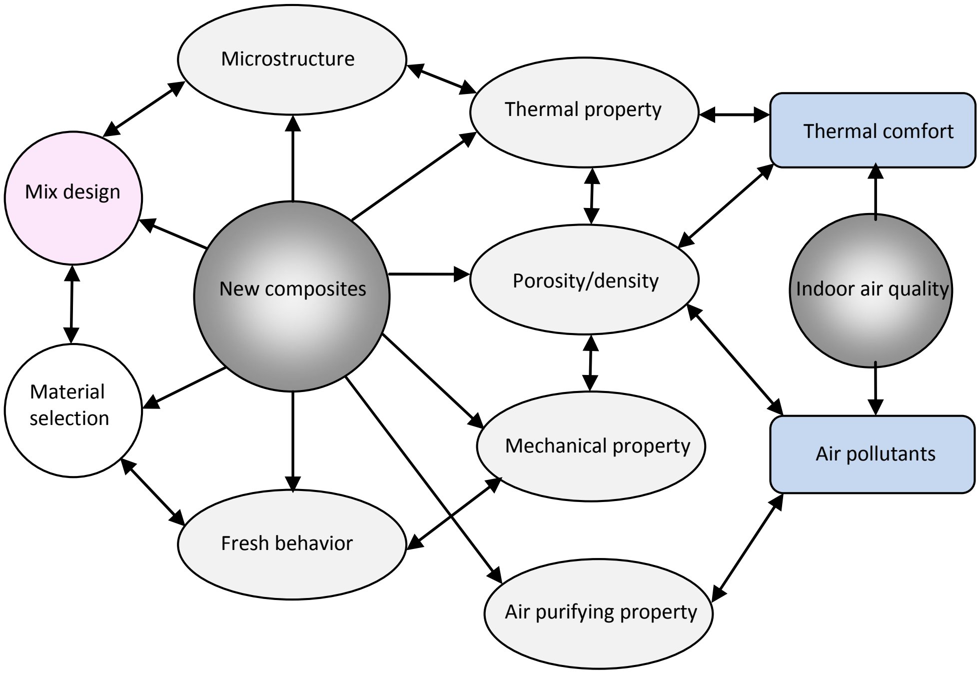

Figure 1.1: Schematic description of the new composite development.

In this new product development, the thermal properties and the indoor air purification properties will be especially addressed, since they are directly linked to the thermal comfort and air pollutants that significantly affect indoor air quality. Nevertheless, other properties such as fresh state behavior, mechanical properties, and physical properties such as density/porosity are also essential in designing this new composite. Fresh state behavior such as the flowability is influenced by the used water content, which in turn affects the density as well as the mechanical properties of the composite in its hardened state, while density is strongly related to thermal properties such as thermal conductivity. Therefore, these properties are investigated as well.

1.3 Research targets

Following the research objective and research strategy discussed above, the research targets of this study are described here. These targets are defined and investigated based on the desired performance that the designed product should have.

Mechanical properties analysis

Strength is commonly considered as one of the most important mechanical properties of building materials such as concrete or gypsum, although other parameters for instance hardness or elastic modulus are also important. This is understandable because the strength is a fairly good index of the mechanical properties and also because routine strength tests are relatively simple to perform (Popovics, 1998). In this research, strength is investigated as the main indicator of the mechanical properties.

Thermal behavior analysis

Thermal behavior investigation is one of the most important research topics here. In order to have a deep understanding of the thermal behavior of the designed composite, firstly the thermo physical properties of the products such as the thermal conductivity and specific heat capacity are studied. At high temperatures (for instance during a fire) the microstructure of the material experiences a noncontinuous change with an increase of temperature, which leads to the thermal degradation of the material. Abrams (1971) reported a reduction of the compressive strength of concrete of up to 90% when the temperature reaches 850 °C. Cramer et al. (2003) reported a 94% flexural strength loss of gypsum plasterboard at the temperature of 400 °C. Therefore, the thermal degradation is also investigated in the present study. The fire resistance, a main characteristic of the studied material, is also investigated by performing the real fire test on the developed composite following the standard ISO 834-1 (1999).

Microstructure analysis

Mechanical and thermal properties of a material are strongly linked to its microstructure. Good particle-matrix bond ensures that the matrix is developed efficiently (Newman, 1993). Hence, the microstructure of the studied materials is investigated intensively here. The scanning electron microscope (SEM) is employed experimentally, while modeling work is carried out theoretically in order to achieve this purpose.

Air purifying property analysis

One of the characteristics of the developed product is its indoor air pollutants purification property, which is achieved by applying the heterogeneous photocatalytic oxidation (PCO) technology. The performance of this property is assessed by using an experimental set-up on laboratory-scale following the standard ISO 22197-1 (2007) as a reference.

Furthermore, kinetic modeling is performed to understand the working principle of the photocatalytic oxidation and a computational fluid dynamics (CFD) model of the used reactor is built, employing the commercial software Fluent®, in order to validate its effectiveness.

1.4 Outline of this thesis

This research aims at the development of novel calcium sulfate-based building materials with the function of indoor air quality improvement. Thus, it obviously leads to investigating a variety of complex fields and topics. The research is performed based on multidisciplinary approaches, while they are all relevant, to obtain a new product that contributes to a better life for human beings.

The research framework of this thesis is presented in Figure 1.2. The contents of the chapters are explained in the following paragraphs.

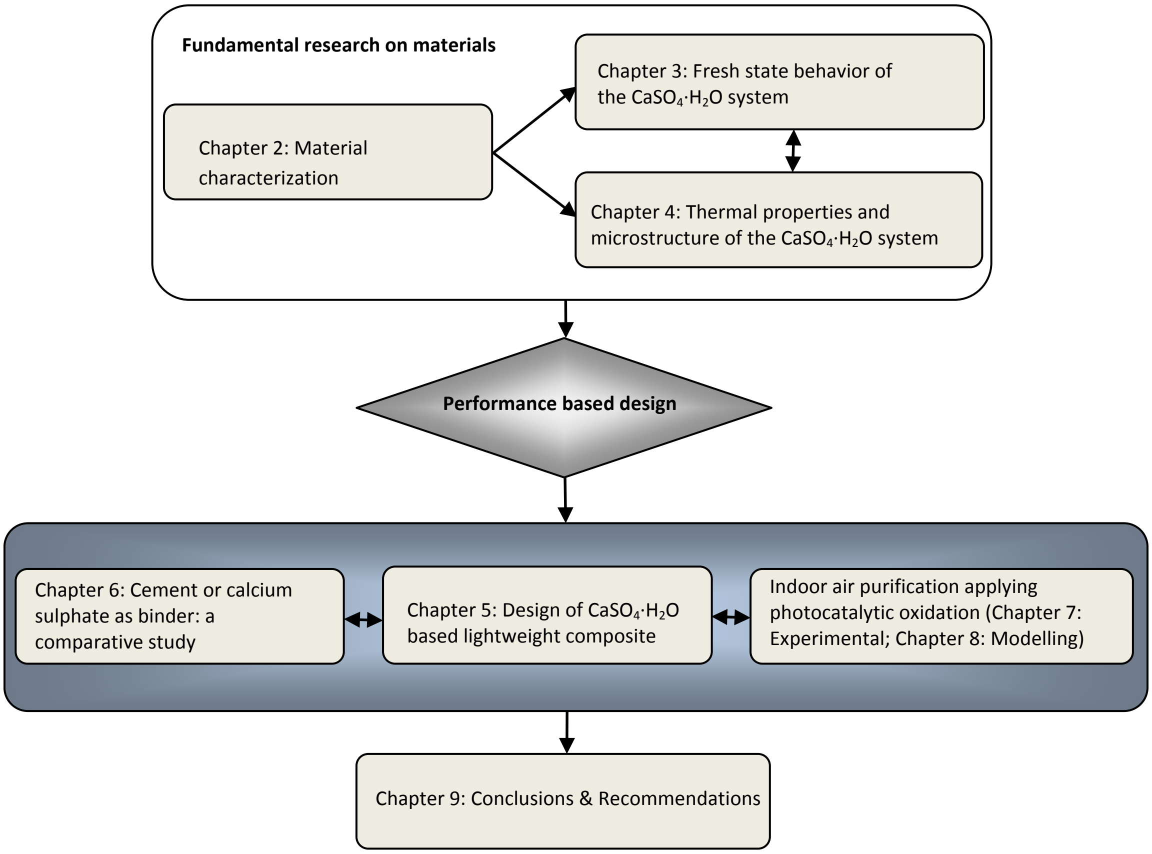

Figure 1.2: Outline of the thesis.

In Chapter 2, the materials used in the present study are characterized according to their physical and chemical properties, including for instance the density, particle size distribution (PSD), specific surface area (SSA), microstructure, water content and water absorption, and chemical composition. The particle size distribution serves as a basis of the mix design concept applied in the present study. Hence, the PSDs of all the used materials are analyzed in detail. Water absorption is essential when applying lightweight aggregates since the possible large water absorption of lightweight aggregates (LWA) affects the workability of the designed composite; hence, it is also specifically addressed here.

In Chapter 3, the fresh state behavior of the $CaSO_4 \cdot H_2O$ system is investigated, including the water demand determination, hydration process, and microstructure development. The water demand is determined by using a mini-spread flow test employing a Hägermann cone. The hydration process is studied by using an ultrasonic wave method. The effect of the water dosage on the hydration process is analyzed in terms of the setting time and the heat release.

In Chapter 4, the thermal properties and the microstructure of the $CaSO_4 \cdot H_2O$ system are addressed. The water release of $CaSO_4 \cdot 2H_2O$ (calcium sulfate dihydrate) upon heating is studied from both macro- and micro-level. The thermal properties of the $CaSO_4 \cdot H_2O$ system are studied by both experiments and modeling. The microstructure of the $CaSO_4 \cdot H_2O$ system is studied in terms of modeling and experiments using scanning electron microscope (SEM). Furthermore, the change of the microstructure of $CaSO_4 \cdot 2H_2O$ is also studied by investigating its strength change at elevated temperatures.

In Chapter 5, a novel $CaSO_4 \cdot H_2O$-based lightweight composite is designed and developed based on the properties of the used materials analyzed in the previous chapters. The applied mix design methodology is presented and the influential factors are discussed. The developed composite is investigated from both fresh and hardened states, including the flowability, density and porosity, strength, thermal properties, and fire behavior.

In Chapter 6, a comparative study is performed by investigating also cement as binder to produce lightweight composites. The mix is developed using the same design methodology as presented in Chapter 5. The properties of the developed cement-based composites are also analyzed from the point of view of their porosity, strength and thermal properties. Based on this, a comparative discussion is presented on why/how calcium sulfate or cement is used as binder and some interesting conclusions are drawn.

In Chapter 7, the heterogeneous photocatalytic oxidation (PCO) technology is applied as indoor air pollutants abatement method. The air purification function of the developed product is assessed by using a laboratory-scale test set-up, and the influential factors which affect the air purification performance are systematically studied.

In Chapter 8, the modeling of the photocatalytic oxidation reaction is presented. A kinetic model to describe the PCO process is proposed and validated by the current experimental data. The employed reactor is modeled using the computational fluid dynamics (CFD) software Fluent. The built CFD model is validated by the present experimental results. The study indicates that there is ample room for the PCO research using CFD as a powerful tool.

In Chapter 9, comprehensive conclusions of the present work are drawn and some recommendations for future research are presented.

Chapter 2

Material characterization

2.1 Introduction

A variety of materials is applied in this research, as will be discussed in this chapter. These materials consist of powders and aggregates; powders are here considered as granular materials with particle size smaller than 125 μm. These materials have different physico-chemical characteristics, which affect the final properties of the composed materials in various ways. Physical properties include density, particle size, microstructure, etc. The understanding of the basic physical properties of a material is essential in order to investigate the performance of products made of it. The chemical composition determines the reaction behavior as well as the physical properties of the generated product. Thus, it is of vital interest to grasp all the related properties of the used materials, which are therefore addressed in this chapter.

Powders can usually be divided into two categories, i.e. reactive and nonreactive. Reactive materials undergo chemical reactions when put in contact with water, for instance the reaction of calcium sulfate hemihydrate ($CaSO_4{\cdot}0.5H_2O$) or cement with water, also termed hydration. Nonreactive fine materials, e.g. limestone powder, do not react when in contact with water, and can therefore be used as inert fillers to fill the voids between the coarser aggregates. Hence, the density, particle size distribution, specific surface area, and chemical composition of the powders are important factors that need to be known in order to better control the properties of the developed materials, containing these fine powders.

Aggregates, which can be natural, artificial or recycled materials, constitute a large part of calcium sulfate- or cement-based composites. According to their particle sizes, aggregates can be classified into fine aggregates with the maximum particle size smaller than 4 mm and coarse aggregates with the maximum particle size larger than 4 mm. Lightweight aggregates (LWA) are used in order to reduce the density of the developed composite. Again, the density, particle size distribution and chemical composition of these materials should be fully understood. Normally, LWA absorb a certain amount of free water when being in contact with water and this affects the performance of the developed materials, which is also addressed here.

In the following sections, the powders and aggregates will be investigated concerning the abovementioned properties. The specific surface area of powders is studied by two methods, particle size distribution (PSD)-based and N_2 adsorption-based (applying BET theory), and the relation between the results obtained from these two methods is discussed. Scanning electron microscopy (SEM) is employed to study the microstructure of the used powders and LWA in order to understand their surface morphology and internal porosity. Additionally, a new test set-up is developed and used here to determine the water absorption of the lightweight aggregates with a particle size smaller than 4 mm.

2.2 Powder analysis

Introduction

In the present study, several powders of different types are used, including reactive materials, such as calcium sulfate hemihydrate (α- and β-type) and cement, and nonreactive materials such as limestone powder, micro-sand, and photocatalyst TiO_2 powder such as VPC10 (provided by TitanPE Technology, China) (Nitrogen doped TiO_2), and KRONOClean 7000 (shortened as K-7000, provided by Kronos International, Germany) (Carbon doped TiO_2). In this section, the used powders will be systematically analyzed from their densities, granular properties such as particle size distribution and specific surface area, microstructure and chemical composition.

Specific density

The specific density, also referred to as the absolute density, of a material is defined as its mass divided by its true volume, i.e. pores inside of the material are excluded, reading

$$\rho_{spe} = \frac{m}{V_{true}} \tag{2.2.1}$$

where ρ_{spe} is the specific density (g cm^{-3}), m is the mass (g), and V_{true} is the true volume of the material (cm^3).

Table 2.1: Specific densities of powders measured by AccuPyc 1340 II gas Pycnometer.

Materials	Type	Specific density (g cm^{-3})			
		Sample 1	Sample 2	Sample 3	Average
β-hemihydrate	$CaSO_4·0.5H_20$	2.5940	2.5954	2.5920	2.5940
α-hemihydrate	$CaSO_4·0.5H_20$	2.7436	2.7450	2.7454	2.7447
Cement I 52.5N	Cement	3.1764	3.1754	3.1747	3.1755
Limestone powder	Limestone	2.7278	2.7257	2.7244	2.7260
VPC 10	Modified TiO_2	2.9792	2.9637	2.9603	2.9677
K-7000	Modified TiO_2	3.4749	3.4616	3.3893	3.4419

Normally the true volume of the materials can be measured according to EN 1097-7 (1999) employing a liquid pycnometer, using water for nonreactive materials and ethanol for reactive materials. However, surface tension of the powders and entrapped gases affect the filling of very small pores. Hence, here the true volume is measured using a gas pycnometer method employing an AccuPyc 1340 II Pycnometer, which is more accurate and the measurement is easier and faster compared to the liquid pycnometer, also less human errors can be incorporated into the gas pycnometer measurement. The AccuPyc works by measuring the amount of displaced gas (helium). The very small helium molecules rapidly fill the tiniest pores of the sample and only the true solid phase of the sample displaces the gas. The pressures are measured upon filling the gas into the sample chamber and then discharging it into a second empty chamber, to compute the solid phase volume of the sample.

The samples are always first dried in an oven (at the temperature of 105 °C) until a constant mass is reached in order to remove the free moisture, prior to the specific density measurements. Three measurements are usually performed in order to obtain a representative value. The test results of some selected materials are listed in Table 2.1.

Quercia et al. (2012b) compared the specific density measurement from both gas and liquid pycnometer for some micro- and nano-SiO_2, and reported a measurement difference between 2.0% - 4.5%. This is in line with the present measurement; also here a comparative study is carried out and a difference of 2.2% to β-hemihydrate and 1.4% to limestone is found by performing the liquid pycnometer density measurement following EN 1097-7. In addition, both the present results and the values from Quercia et al. (2012b) show that the true volume of a material measured by a gas pycnometer is smaller, which can be explained by the fact that the molecule of the gas (helium) is smaller than the molecule of water or alcohol, hence finer pores can be filled.

Particle size distribution

The detailed information about the particle size distribution (PSD) of the investigated materials is essential since this is the foundation of the mix design methodology applied in the present study. Here, a laser light scattering (LLS) technique is employed to determine the PSDs of materials, and a Malvern Mastersizer 2000$^{®}$ PSD analyzer is used for the measurement.

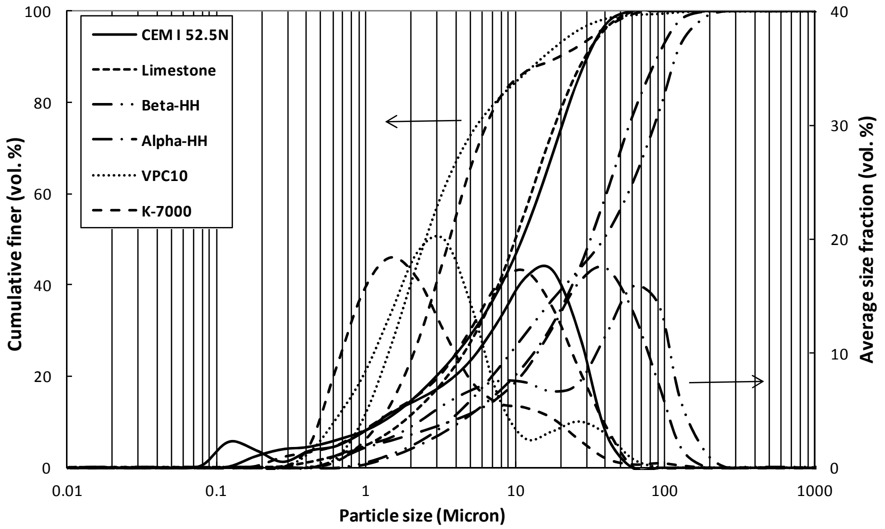

Figure 2.1: Particle size distribution of the used powders.

There are two measurement principles: the powder is either dispersed in air (so called dry mode) or in a transport liquid (wet mode). Under dry conditions, electrostatic forces are generated because of the collisions of particles or induced by particles friction, which results in agglomerations. Hence, usually the wet mode is used, and the Hydro S unit is applied as the wet dispersing unit. The PSDs of all materials are measured in liquid dispersion using the Mie scattering model as the measuring principle following the ISO standard 13320-1 (2009). Depending on the fact whether the measured material is reactive with water or not, water or propan-2-ol is used as the dispersion liquid.

The results of the investigated materials are shown in Figure 2.1. It can be seen that the PSD of the limestone powder almost overlaps with that of CEM I 52.5N, which means that the limestone powder can be used perfectly as a filler to replace the cement without causing any significant change of the PSD of the designed mixes. Although produced with a different process, α-hemihydrate has a PSD quite similar to β-hemihydrate. Both VPC 10 and K-7000 have much finer particles than the other powders, as shown in Figure 2.1, which is beneficial for their photocatalytic oxidation behavior because of the crystal facet-dependent feature of PCO, which will be analyzed in the pertaining chapters.

Specific surface area

The specific surface area (SSA) is the surface area of a material divided by its mass. The water accessible outer surface of materials is essential in the mix design of calcium sulfate- or cement-based composites because water needs to be in contact with powders in order to gain the workability, and the air/water accessible surface is of interest for the PCO efficiency, since air pollutants need to be adsorbed onto the surface of the photocatalyst before the PCO reaction. In the present study, two methods are used to determine the SSA of the investigated materials, i.e. based on the PSD measurement applying LLS technique and the N_2 adsorption measurement applying BET theory.

The SSA can be calculated from the measured PSDs. If all the particles are assumed to be ideal spheres, then the surface area of each single spherical particle is:

$$a_{sph} = \pi \cdot d^2 = \frac{6 \cdot V_{sph}}{d} \qquad (2.2.2)$$

where a_{sph} is the surface area of the sphere (m^2), d is the diameter (m) and V_{sph} is the volume (m^3).

Table 2.2: Specific surface areas of some powders.

Materials	SSA_{PSD} ($m^2\ g^{-1}$)	SSA_{BET} ($m^2\ g^{-1}$)
α-hemihydrate	0.31	0.30
β-hemihydrate	0.37	7.50
CEM I 52.5N	0.89	0.91
Limestone powder	0.74	0.89
VPC10	1.12	34.01
K-7000	0.80	251.23

Therefore, the specific surface area of a material is computed from the total surface area of all size fractions divided by its mass (total mass of all size fractions), reading

$$SSA_{PSD} = \frac{\sum_i a_{sph,i}}{\sum_i m_i} = \frac{6 \cdot \sum_i \frac{V_{sph,i}}{d_i}}{\rho \sum_i V_{sph,i}} \tag{2.2.3}$$

where SSA_{PSD} is the SSA calculated from the measured PSD ($m^2\ g^{-1}$), i is the fraction size of the material, m is the mass (g) and ρ is the specific density ($g\ cm^{-3}$). It should be pointed out that this equation is derived based on that the numbers of particles in each size fraction are the same. The calculated SSA_{PSD} values of the selected materials are listed in Table 2.2. It should be noted that particles of most materials are not spherical, which should be taken into consideration prior to application of the calculated results.

Furthermore, another widely accepted method to determine the surface area is the gas sorption method based on the BET theory (Brunauer et al., 1938). The BET surface area is calculated from the amount of N_2 gas adsorbed based on the N_2 molecular cross sectional area of 0.162 nm^2.

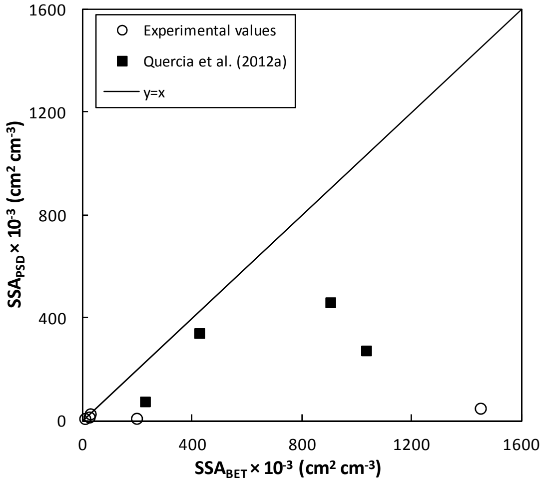

Figure 2.2: Comparison between SSA_{PSD} and SSA_{BET} of the investigated materials.

In the present study, the BET surface areas of the investigated materials are measured using a Micromeritics Tristar 3000 BET analyzer. The experiments are performed following the procedure described in Yu (2010). The first step is the sample preparation, where the mass of the sample is measured and the moisture in the sample is removed by degassing. The second step is the sample analysis, where the surface area of the degassed sample is measured through the physical adsorption of N_2. Finally, the results are reported, including the physical properties such as specific surface area and size of micro pores. The measured BET values of the materials are also listed in Table 2.2.

The SSA_{BET} values of the selected materials are plotted against the SSA_{PSD} in Figure 2.2. Here, the specific surface areas determined from both PSD method and BET method are expressed as the total area per total volume ($cm^2\ cm^{-3}$), which is calculated by multiplying the relevant density values (with the unit of $g\ cm^{-3}$) with the relevant SSA (with the unit of $m^2\ g^{-1}$). The cited values from Quercia et al. (2012a) in Figure 2.2 were measured using the same analyzers (Micromeritics Tristar 3000 and Malvern Mastersizer 2000) and calculated using the same methods. It can be seen that the values do not show a linear relation between the SSA_{PSD} and SSA_{BET}, an opinion held by some other researchers. This also indicates that the SSA_{PSD} and SSA_{BET} of materials of different types are not suitable to be compared or linked due to the possible significant differences between their porosities, pore sizes and surface morphologies.

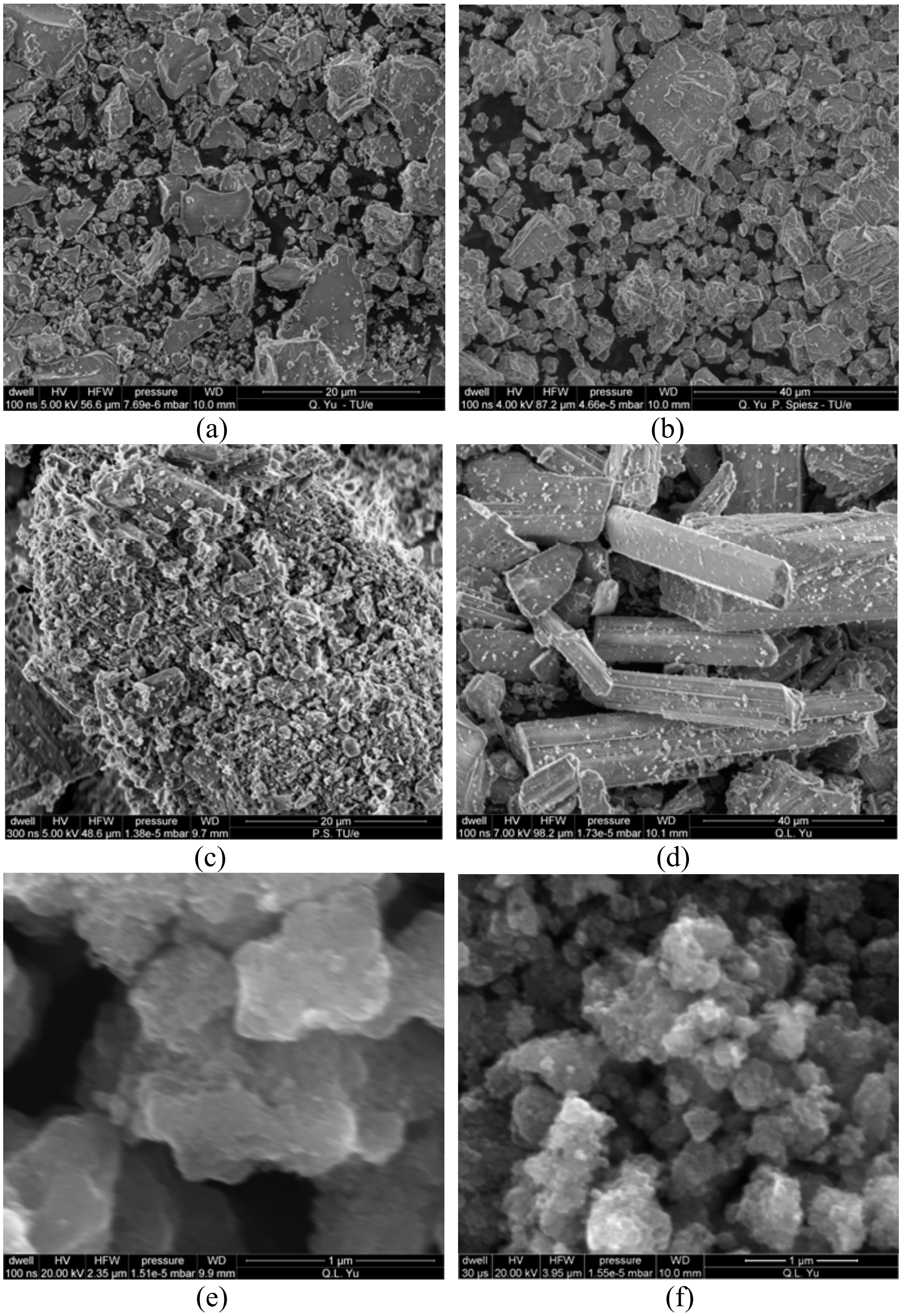

(a) (b)

(c) (d)

(e) (f)

Figure 2.3: SEM pictures of some materials (a: CEM I 52.5N; b: Limestone powder; c: β-hemihydrate; d: α-hemihydrate; e: K-7000; f: VPC10).

In addition, there is a possible agglomeration during the PSD measurement of very fine materials such as the photocatalyst. Furthermore, various errors can be caused for instance by the operators, the used dispersion agent, dispersion method, stirring speed, etc. It is hence concluded here that the specific surface area calculated from the measured PSD should be seriously assessed before any application.

Microstructure

Microstructure is the morphology and texture of a material in micro level, which strongly influences the physical properties. The reason lies in the fact that the geometry of the particles and the surface roughness of a material affect the bonding behavior, absorption capacity, etc. In the present study, the microstructure of the investigated materials is determined by employing scanning electron microscopy (SEM) (Quanta 650 FEG, FEI), and the results are shown in Figure 2.3.

It can be clearly seen from Figure 2.3a-f that the analyzed particles are not spherical, which indicates that the SSA calculated from the measured PSD should be corrected based on the particle shape. However, on the other hand, the irregular particle shape of the materials contributes to a better bonding and interlocking between materials in the matrix, which in turn leads to a better strength development of the calcium sulfate- and/or cement-based composites.

It is shown that α-hemihydrate has very regularly shaped particles, especially compared to these of β-hemihydrate, as seen in Figures 2.3c and 2.3d, which is in line with Wirsching (2005) who also reported that α-hemihydrate consists of compact, well formed and large primary particles while β-hemihydrate forms flaky, rugged secondary particles made up of extremely small particles. This explains the clear difference of the water demand and the flowability of the two hemihydrates, as will be discussed later. This also confirms that the SSA of β-hemihydrate should be much larger than that of α-hemihydrate, as can be seen in Table 2.2 for the BET measurement.

Figures 2.3e and 2.3f show that both K-7000 and VPC10 consist of particles in the nano-meter size range. This indicates that the PSD measurement of materials in nano range employing Matersizer 2000 is questionable due to the possible agglomeration, which leads to a significant error in the calculated specific surface area based on PSD values.

Chemical composition

The chemical composition of cement and hemihydrate affects their hydration behavior, while the chemical composition of photocatalyst affects its photocatalytic oxidation (PCO) efficiency. The chemical compositions of the powders are analyzed here by using X-ray Fluorescence (XRF) (Pöllmann, 2009), and the results are shown in Table 2.3.

Taking β-hemihydrate as an example, the theoretical molar proportion of Ca and S atoms is 1:1, but the measured value is 1:1.28, which indicates that there might be measurement errors during the XRF test. Therefore, here it is also analyzed by the energy-dispersive X-ray spectroscopy (EDX), and the results are listed in Table 2.4. It is shown that there are only very small quantities of impurities in the sample (Si, Mg, and Al in total less than 3% by mass), which are also confirmed by the XRF result (Table 2.3). The measured proportion of Ca and S is in line with the value (i.e. 1:1 in molar proportion in $CaSO_4$), which indicates that there is no Ca-based impurity in the material. The computed mass content of $CaSO_4 \cdot 0.5H_2O$ is 96.94%, but this value may have a very slight error because hydrogen could not be detected during the EDX analysis.

Table 2.3: Chemical composition of the powders measured by XRF (*Hunger, 2012).

substance (%)	β-hemihydrate	α-hemihydrate	CEM I 52.5N*	VPC10	K-7000
LOI	8.84	6.54	1.56	21.38	11.79
Na_2O	0.00	0.00	0.35	0.39	0.31
MgO	0.69	0.29	1.99	0.00	0.00
Al_2O_3	0.54	0.23	4.80	0.00	0.00
SiO_2	1.28	0.54	19.64	0.83	0.06
P_2O_5	0.00	0.00	0.59	0.76	0.06
SO_3	57.05	60.11	2.87	0.25	1.65
Cl	0.00	0.00	0.06	6.29	0.05
K_2O	0.17	0.10	0.56	0.01	0.01
CaO	31.19	32.04	63.34	0.02	0.24
TiO_2	0.03	0.04	0.34	69.81	85.64
Fe_2O_3	0.16	0.09	3.28	0.04	0.04
Others	0.05	0.02	0.62	0.22	0.15

Table 2.4: Chemical composition of β-hemihydrate measured by EDX.

Element	wt.%	at.%	K-Ratio
O	48.86	67.84	0.0714
Mg	0.87	0.80	0.0030
Al	0.80	0.66	0.0037
Si	1.32	1.05	0.0082
S	21.46	14.87	0.1758
Ca	26.68	14.79	0.2285
Total	100.00	100.00	

2.3 Aggregates analysis

Normal weight aggregates

Aggregates with normal weight used in the present study are fine aggregates (sands) with the particle size smaller than 4 mm, including three different particle size fractions, but all are natural sands. These aggregates are characterized according to the following properties: (1) particle size distribution (PSD); (2) specific density; (3) moisture content.

- Particle size distribution

The PSDs of the used sands are analyzed by sieve analysis according to EN 933-1 (1997). The samples are passing through a stack of sieves which are arranged in the order of decreasing sieve openings from top to bottom. The amount of material retained on each sieve can be then weighed and calculated to the proportion of the total mass. The results are shown in Figure 2.4.

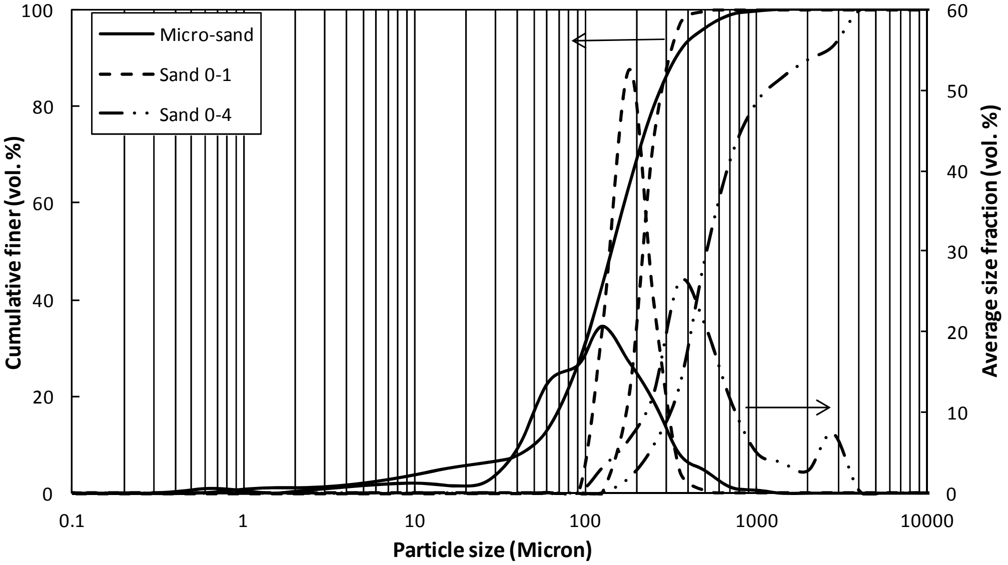

Figure 2.4: Particle size distribution of used sands.

Here, it should be pointed out that the PSD of micro-sand is obtained from a combination of measurements from both sieve analysis and laser diffraction analysis using Mastersizer 2000, as the micro-sand contains a significant amount of very fine particles, which are not suitable to be analyzed by sieve analysis, as shown in Figure 2.4.

- Density

The specific densities of the three used sands are measured using the same methodology presented in the previous section, i.e. with the gas Pycnometer (AccuPyc II 1340, Micromeritics). The samples first are dried in an oven (with a temperature of 105 °C) until the mass is constant in order to remove the free water prior to the density measurement. The results are shown in Table 2.5.

Table 2.5: Specific densities of the sands measured by AccuPyc 1340 II gas Pycnometer.

Materials	Specific density (g cm^{-3})			
	Sample 1	Sample 2	Sample 3	Average
Micro-sand	2.7212	2.7219	2.7228	2.7220
Sand 0-1 mm	2.6533	2.6531	2.6531	2.6532
Sand 0-4 mm	2.6635	2.6636	2.6631	2.6534

- Moisture content

The moisture content of aggregates affects the workability of the designed mixture, if not taken into account and corrected. Therefore, it should be determined in order to modify the total water dosage in the mixing process. The water content can be directly calculated from the mass difference between the aggregates in their initial condition (moist) and dry condition, which is achieved by drying the sample in an oven until the mass is constant.

The moisture contents of these three sands are quite different. When just delivered, the micro-sand has a moisture content of 6.0%, since it is filtered from water in the production process, while the other sands are very dry. The free water is gradually evacuated from the micro-sand because of the relatively dry storing environment. Hence, the moisture content of the micro-sand during this period is corrected accordingly each time when used.

Lightweight aggregates

There are two types of lightweight aggregates (LWA) from the point of view of their origin, namely natural aggregates and synthetic aggregates, while natural LWA can be of volcanic origin, organic root, etc., and synthetic aggregates are usually produced by a thermal treatment process in order to make them expansive (Chandra and Berntsson, 2003). The synthetic aggregates can be generally divided into three groups of natural materials such as perlite, vermiculite and clay, industrial products such as glass, and industrial by-products such as fly ash. The LWA used here are synthetic aggregates made of recycled glass, in five different size fractions of 0.1-0.3 mm, 0.25-0.5 mm, 0.5-1.0 mm, 1.0-2.0 mm, and 2.0-4.0 mm.

The LWA have quite unique features compared to normal weight aggregates, such as low density and large water absorption. The low density is resulting from the great amount of open and closed pores in the particles created in the production process. The open pores as well as the internal pores interconnected with the surface pores of the LWA lead to a much larger water absorption compared to normal weight aggregates, which has a negative effect in both cement and calcium sulfate based composites. The LWA used here are produced from recycled glass, so there is a potential that they can react with the alkalis originating from the cement, which is also negative for cement based composites.

The LWA therefore are analyzed for the following properties: (1) particle size distribution (PSD); (2) density; (3) water content and water absorption; (4) chemical composition and (5) microstructure.

- Particle size distribution

The PSDs of the LWA are measured by sieving analysis, and the obtained results are in line with the data from the provider. The results are shown in Figure 2.5. It can be seen that, although the LWA have a quite narrow particle size distribution in each fraction type, there are sufficient overlaps between each fraction, which provides the possibility of creating a continuous grading of the solids in the mixture.

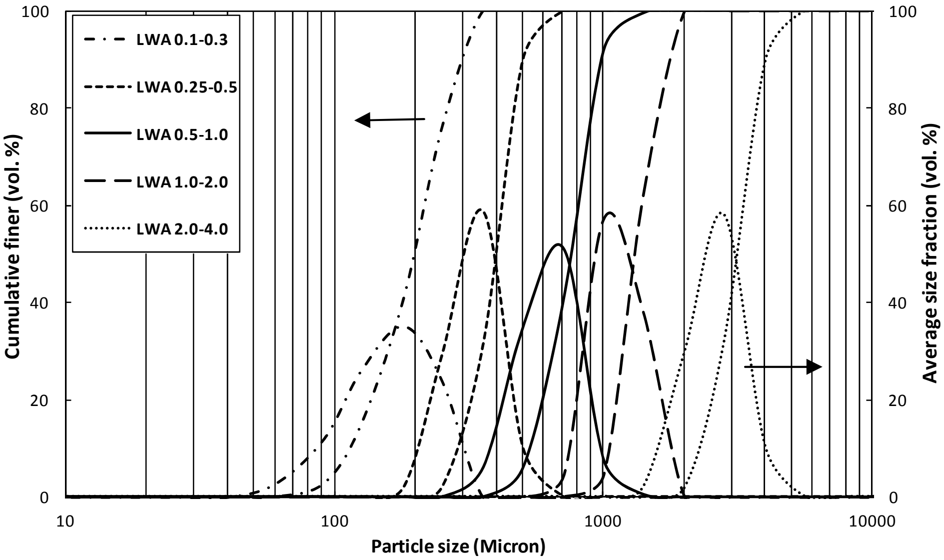

Figure 2.5: Particle size distribution of the LWA.

- Density

The bulk densities and specific density of the LWA particles, obtained from the producer, are measured according to the standard EN 1097-3 and DIN V 18004 respectively. The results are listed in Table 2.6.

Table 2.6: Bulk density and specific density of the LWA particles.

Materials Size range (mm)	Bulk density (kg m^{-3})	Specific density (kg m^{-3})	Error
LWA 0.1-0.3	450	800	±15%
LWA 0.25-0.5	300	540	±15%
LWA 0.5-1.0	350	450	±15%
LWA 1.0-2.0	220	350	±15%
LWA 2.0-4.0	190	310	±15%

The specific density of the material used in LWA is measured by gas Pycnometer (AccuPyc II 1340, Micromeritics) following the same procedure presented in the previous sections. The LWA are firstly ground to powder by a ball milling method, and then subjected to the density measurements, resulting 2.458 g cm^{-3} in average.

- Chemical composition

The chemical composition of the LWA is taken from the data sheet from the producer, and is listed in Table 2.7. The EDX tests are also performed to analyze the chemical composition, and the results are listed in Table 2.7 as well.

Table 2.7: Chemical composition of the LWA.

Substance	Producer (%)	EDX (%)
Chloride	< 0.01	-
Acid soluble sulfate	< 0.1	-
Total sulfur	< 0.1	-
SiO_2	71 ± 2	81.3
Al_2O_3	2 ± 0.3	5.3
Na_2O	3 ± 1	11.6
Fe_2O_3	0.5 ± 0.2	0
CaO	8 ± 2	6.0
MgO	2 ± 1	3.4
K_2O	1 ± 0.2	0.9

It should be pointed out here that the oxide content is calculated from the measured element content by EDX. It can be noticed that the amounts of the substances measured by EDX are similar as given by the producer except for the amount of SiO_2 and Na_2O, which are larger than the provided values. The LWA have a high content of SiO_2 (up to 80 wt.%), and two other main components: Na_2O and CaO of about 15.0 wt.% in total.

- Microstructure

The surface morphology influences the bonding behavior between the LWA and the matrix, which is an important factor for the strength development of the produced gypsum/cement based composites. The pores of the LWA are significantly contributing to the thermal insulation of the composites, which, however, also depends on the internal connection of the LWA. Hence, the microstructure and the pores of the LWA are investigated here employing scanning electron microscope (SEM). The results are shown in Figure 2.6.

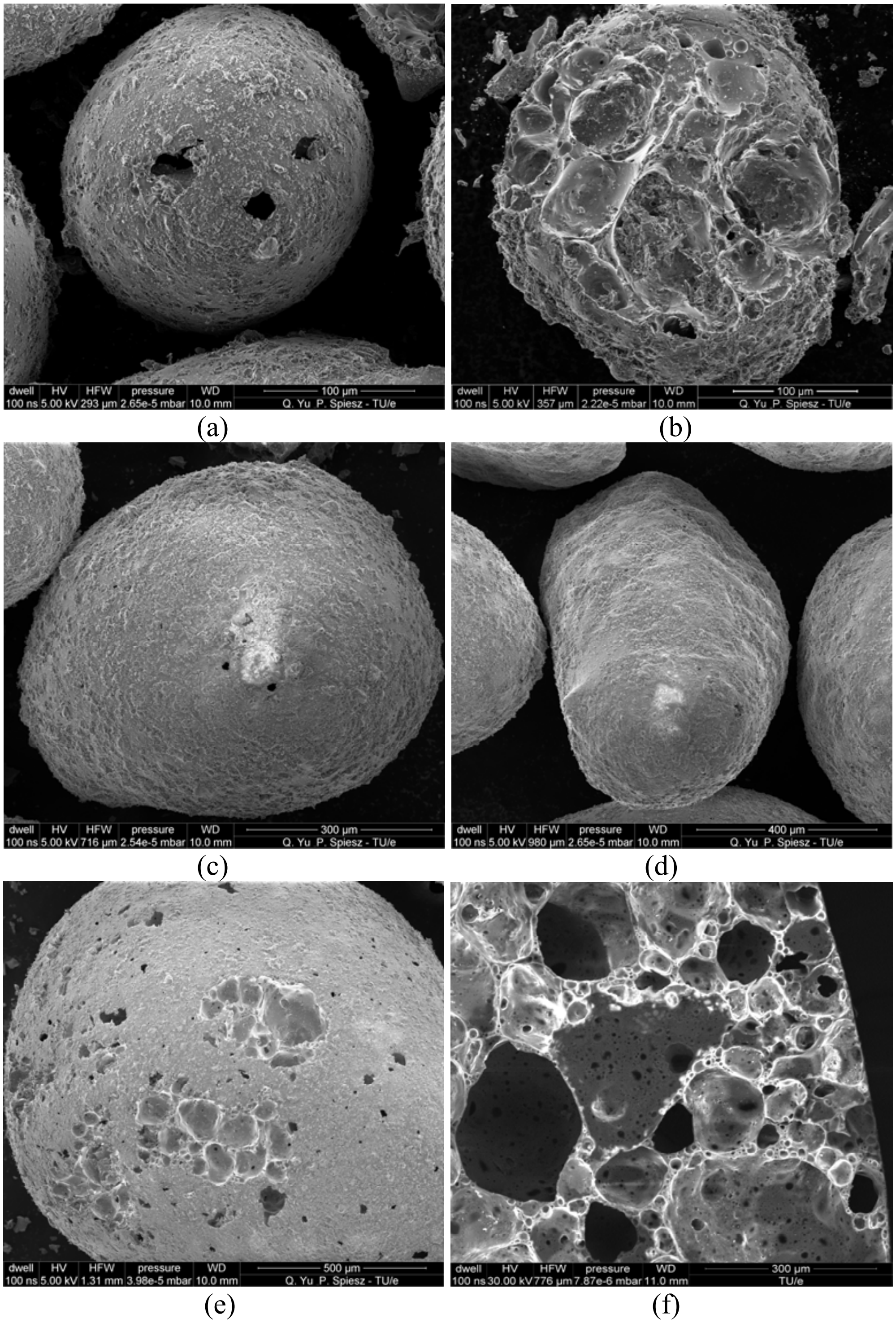

Figure 2.6: SEM pictures of LWA (a: LWA 0.1-0.3 outer surface; b: LWA 0.1-0.3 internal pore structure; c: LWA 0.25-0.5 outer surface; d: LWA 0.5-1.0 outer surface; e: LWA 1.0-2.0 outer surface & internal pore structure; f: LWA 2.0-4.0 internal pore structure).

It can be seen from Figure 2.6 (a) (c) (d) and (e) that the outer surface texture is rather rough, which is beneficial for a better bonding between the LWA and the gypsum/cement paste. However, from these pictures it is also obvious that the outer surfaces are not completely closed, which leads to a possible water absorption. The SEM pictures listed in Figure 2.6 (b) and (f) show that there are various pores inside of the LWA. Although these internal pores are quite closed, they are interconnected to some extent.

- Water content and water absorption

The initial water (moisture) content of the LWA is determined by first drying the materials in the oven at 105 °C until constant mass is reached, and then measuring the mass difference. The LWA have very low initial moisture content in all size fractions (about 0.1% in average). Thus, the LWA can be considered as completely dry. The detailed measurement data are presented in Appendix A.

Table 2.8: Water absorption of LWA (EuroLightCon, 2000; Chandra and Berntsson, 2003).

Samples	Raw material	Particle size (mm)	Water absorption (wt. %)			Method
			30 min	1 hour	24 hour	
Pumice	Pumice	4-8	-	-	19.3	EN 13055
Pumice	Pumice	4-16	-	-	9.9	EN 13055
Scoria	Pumice	0-64	-	-	6.3	EN 13055
Liapor1	Expanded clay	4-8	-	-	12.1	EN 13055
Lytag UK	Fly ash	4-12	-	-	8.6	EN 13055
Vasim5	Fly ash	4-8	-	-	21.8	EN 13055
Vasim8	Fly ash	4-8	-	-	10.8	EN 13055
Vasim9	Fly ash	4-8	-	-	11.9	EN 13055
Solite US	Expanded shale	4-16	-	-	8.4	EN 13055
Vasim1	Fly ash	4-8	31	-	33	-
Vasim2	Fly ash	8-16	30	-	32	-
Lytag NL	Fly ash	0.5-4	-	-	-	-
Lytag NL	Fly ash	4-8	15	-	18	-
Lytag NL	Fly ash	6-12	15	-	18	-
Leca290	Expanded clay	4-10	-	9	12	-
Leca700	Expanded clay	4-12	-	10.1	13.8	-
Leca800	Expanded clay	4-8	-	7	11	-
Leca800	Expanded clay	8-12	-	9.4	12.9	-
Liapor3	Expanded clay	4-8	-	12.5	16.1	-
Liapor4	Expanded clay	4-8	-	10.8	15.6	-
Liapor5	Expanded clay	4-8	-	8.0	17.2	-

Liapor9.5	Expanded clay	4-8	-	6.5	11.0	-
S-c	Steam cured fly ash	-	-	27.0	-	-
A-c	Air cured fly ash	-	-	23.9	-	-
L1	Expanded clay	-	-	9.3	-	-
S-f	Sintered fly ash	-	-	14.1	-	-
L2	Expanded clay	-	-	11.7	-	-
Ulopor	Expanded clay	0-4	-	-	6.2*	-
Liapor6	Expanded clay	0-4	-	-	4.8*	-
Leca100	Expanded clay	0-2	-	-	4.7*	-
Embra	Expanded clay	0-4	-	-	4.6*	-
Liaver	Expanded glass	0.25-4	-	-	4.4*	-

(*the duration for water absorption values are not given).

The water absorption of LWA affects the workability of the developed calcium sulfate/cement based composites, since the LWA absorb a certain amount of free water from the mixture before setting. The water absorption ability of LWA depends on various factors such as the surface structure, raw material type, production method etc. A summary of the water absorption of various types of LWA is listed in Table 2.8.

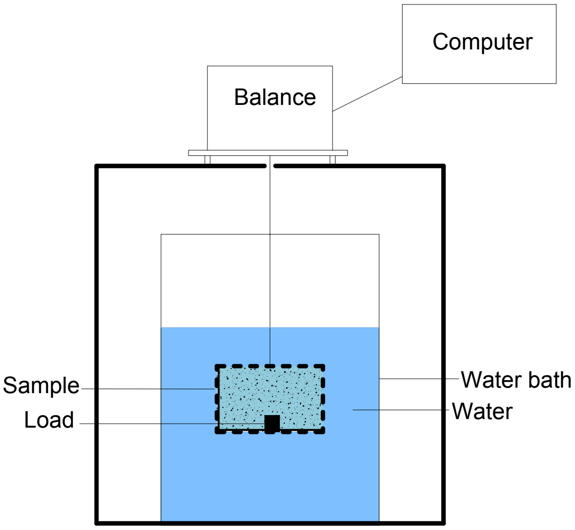

Figure 2.7: Water absorption measurement using hydrostatic weighing.

It can be clearly seen from Table 2.8 that there is a great variation in the reported water absorption values even for the same type of the LWA. There is no unified test duration, as shown in Table 2.8. Some values reported are based on 30 minutes water absorption, while some others are based on 1 hour water absorption and some values are reported without even giving the measurement time. Following the standard EN 1097-6 (2000), the water absorption ability of LWA should be calculated based on the 24-hour water absorption. This standard, however, is only applied to lightweight particles in the size range between 4 mm and 31.5 mm, while in the present study the maximum particle size is only 4 mm. Furthermore, according to EN 1097-6 (2000), the surfaces of soaked lightweight aggregates are dried by gently rolling the aggregates in a cloth for not more than 15 s, which in fact can cause considerable errors especially in the case of aggregates with very small particle sizes.

To the author's knowledge, no study has been performed to systematically investigate the water absorption of LWA with particle sizes smaller than 4 mm. For instance, Liu et al. (2010) reported the water absorption of LWA with the particle size fraction of 0-4 mm, which however are estimated values only. Therefore, the water absorption of the used LWA with the size of 0-4 mm (in different fractions as introduced above) is investigated, using a novel test set-up developed in the present study. It is based on a hydrostatic weighing approach, built for the water absorption measurement here, as shown in Figure 2.7.

Table 2.9: Water absorption of the lightweight aggregates.

LWA type	Particle size (mm)	1h water absorption (wt. %)	24 h water absorption (wt. %)
LWA 0.1-0.3	0.1-0.3	1.06	2.81
LWA 0.25-0.5	0.25-0.5	0.88	3.90
LWA 0.5-1.0	0.5-1.0	1.59	8.50
LWA 1.0-2.0	1.0-2.0	1.71	7.63
LWA 2.0-4.0	2.0-4.0	0.55	7.80

The set-up is composed of a basket, a bath, a balance and a computer. The basket is made of meshed fabric with openings smaller than 0.1 mm. These openings ensure the water in the bath can move freely into the basket while the entire samples remain inside. The basket is preloaded in order to ensure that it will stay immersed in water after loading with LWA samples. The balance has an accuracy of 0.0001 g. The mass of the air dried samples is measured before transferring into the basket. Then the basket is hung on the balance that is connected to the computer for data logging, which is continuously done by a program edited in LabVIEW®. Subsequently, the basket is completely immersed in water and the air escapes, so all the particles are surrounded by water. From this time the mass is continuously recorded by a computer until the end of the test (here the measurement duration is 24 hours).

The results are shown in Figure 2.8 and Table 2.9. It is shown that the water absorption of the LWA with the particle size smaller than 2 mm increases very fast within the first hour, and then increases slowly but almost linearly until the end of the measurement. The 24 hours water absorption values of the LWA are not directly related to their particle sizes, which can be seen from Table 2.7, for instance the LWA 0.5-1.0 with the particle size of 0.5-1.0 mm has the largest water absorption. Overall, it is clear that the 24 hours water absorption of the investigated LWA is less than 10% by mass, and the first hour water absorption is rather low (less than 2.0%) for all size fractions. This indicates that the water absorption ability of the used LWA do not have a significant influence on the flowability of the present developed composites, especially in the case of calcium sulfate-based composites, since their setting occurs very rapidly.

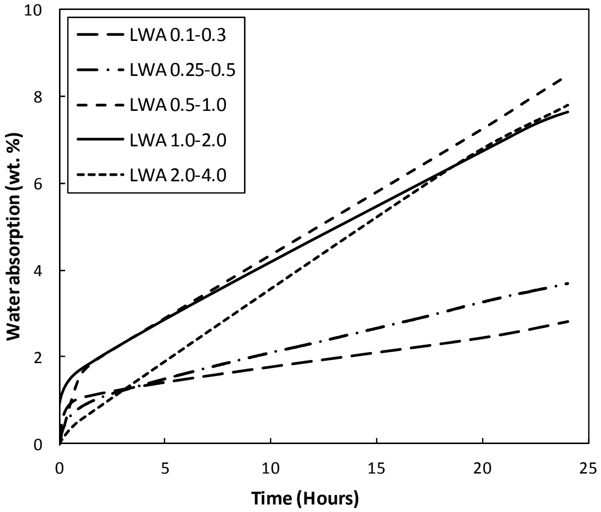

Figure 2.8: Water absorption of LWA versus time.

2.4 Conclusions

This chapter addresses the characterization of the granular materials used in the present research. The materials are analyzed for their physical properties such as density, particle size distribution, specific surface area, microstructure, and chemical composition. The following conclusions are reached:

- The densities are measured using a gas pycnometer method; this method is accurate, easy to be operated and fewer errors are introduced compared to the liquid pycnometer method; normally the values measured by the gas pycnometer method are slightly larger than the ones measured by liquid pycnometer method, but the difference is smaller than 5.0%.
- The calculated specific surface area from the PSD measurement is based on the assumption that all the particles are spherical, which is confirmed to be not realistic by the performed SEM results; therefore the values should be corrected taking into account the shape of the particles.
- The determined BET surface area is not suitable to be linked with the PSD calculated specific surface area of the investigated materials due to the significant difference between their surface morphology, production process etc.
- The outer surfaces of the used LWA are rather rough which would help to build a good bonding between the LWA and the paste; the outer surfaces are rather closed but there are still some openings, which have a negative effect on the water absorption and an increased heat transfer rate.
- A novel water absorption measurement methodology to determine the water absorption ability of LWA with the particle size smaller than 4 mm is proposed and a new water absorption apparatus is designed and developed to determine their water absorption ability.

- The water absorption of the used LWA is measured using this developed set-up; the LWA has a fast water absorption within the first hour, followed by a linear but slower water absorption until the end of the measurement (24 hours).

Chapter 3

Fresh state behavior of the $CaSO_4 \cdot H_2O$ system

3.1 Introduction

The calcium sulfate hemihydrate ($CaSO_4 \cdot 0.5H_2O$) is going to be used as binder for the development of a new composite, and also, as will be discussed in the following chapters, the modified Andreasen and Andersen model will be used as a base for the mix design, whereas it is only focusing on the packing of the solid ingredients. However, as indicated in literature (Schiller, 1963; Hunger, 2010), the water amount added to the mix apparently affects very much the workability as well as the fresh state behavior such as setting and the properties in the hardened state such as the strength of the cementitious materials based product. Therefore, in this chapter the fresh behavior of $CaSO_4 \cdot H_2O$ systems is addressed, including the water demand and the hydration behavior of calcium sulfate hemihydrate.

The hydration of hemihydrate, including the hydration kinetics and setting, has been studied intensively (Ridge and Surkevicius, 1961; Ridge, 1964; Schiller, 1962; Schiller 1974), but the emphasis is mostly focused on α-hemihydrate. However, products generated from α-hemihydrate are too brittle to be used as building materials (Wirsching, 2005). Therefore, in the present study β-hemihydrate is used as raw material. Nevertheless, topics such as the hydration of β-hemihydrate induced properties are still insufficiently understood. Based on a comparison of available test methods, the water demand of β-hemihydrate, as well as the flowability of the hydrating system is investigated using the spread-flow test. The deformation coefficient and a water layer, needed to ensure the fluidity of the slurry, are derived and analyzed. The particle shape factor of the investigated β-hemihydrate is derived based on the experimental results. The hydration of β-hemihydrate is investigated by applying an ultrasonic wave method. The hydration mechanism of the β-hemihydrate is analyzed and the factors influencing setting are studied. The relation between the hydration process and the heat release is investigated.

3.2 Determination of water demand

3.2.1 Introduction

Workability is widely used to describe the properties of building materials such as concrete or gypsum in fresh state and it is related to properties such as fluidity, mobility, and compactability. The term workability is defined as "the property of freshly mixed concrete or mortar that determines the ease, with which it can be mixed, placed, consolidated, and finished to a homogenous condition" (Koehler and Fowler, 2003). To ensure the mixture is fluid, a thin layer of adsorbed water molecules around the particles and an extra amount of water to fill the intergranular voids of the system is necessary (Brouwers and Radix, 2005; Hunger and Brouwers, 2009). Hence, the determination of water demand of fine powders is of vital importance.

With the void fraction filled, the proportion of the total specific surface area of the powders and the remaining water determines the workability (Hunger, 2010). Also, it is widely recognized that the workability is strongly related to the properties of cement or calcium sulfate-based composite in hardened state. Thus, the rheology of the β-hemihydrate-produced slurry is addressed.

3.2.2 Test methods and discussion

A number of test devices and methods with varying degrees of complexity are available to measure the rheology of cement as well as calcium sulfate-based paste, including flow cone test, turning tube viscometer, Wuerpel device, mini-slump flow test, Vicat needle test, and ViscoCorder test (Koehler and Fowler, 2003). EN 13279-2 (2004) introduces as well several methods for the water content determination of gypsum binder. Here, starting from EN 13279-2 (2004), some test methods specifically suitable for water determination of gypsum binder are discussed, and a comparative analysis is carried out. The detailed test methods description is presented in Appendix B.

The three methods introduced in Appendix B can be used to study the workability from different angles. The sprinkling method considers the saturation point of powders in water, the knife cut method links the flowability and setting of the slurry, the Vicat needle method investigates the hardening behavior during the setting, while the spread flow test studies the flow behavior of the mix. In the present study, these methods are compared experimentally, and the results are listed in Table 3.1.

Table 3.1: Comparison of the different methods for workability measurement.

Water/hemihydrate	Mini-slump flow test (mm)	Knife method (sec)	Vicat needle method (sec)	Sprinkling method
0.61	182	185	300	Saturation point
0.65	240	210	345	--
0.80	360	300	420	--
1.00	490	480	550	--

Although comparable results are obtained from both sprinkling method and the mini-slump flow method (the results of the mini-slump flow method will be analyzed in detail in next section), the sprinkling method is quite difficult to be executed. A fluent sprinkling skill and a precise control of the testing time are very important. Considerable differences can be found among different operators. Besides, this method can only be used to determine the water demand, i.e. by measuring the saturation content of the powder in a fixed amount of water. The effect of the excess water content on the workability is not possible to be investigated by means of this method.

The Vicat needle test and the knife method are very suitable test methods for determining the initial setting time. The knife method is based on the fact that the initial setting begins as the paste stops flowing. Therefore it can be used to compare the flowability of the slurry with different initial water contents by measuring the initial setting time. Also, the similar increase rate of both of the spread flow values and the initial setting time from the knife method as the water content increases confirms that the knife method is more suitable compared to the Vicat needle method to study the flow ability. However, it is very difficult to translate the setting time results measured from both Vicat needle and knife cut methods to the flowability directly, although they give a good indication of the behavior of the slurry with different initial water contents.

Hence, in this study the slump-flow test is applied to determine the water demand as well as the effect of water content on the workability of a β-hemihydrate binder. In the next section, the test procedure is firstly introduced, and then the experiments as well as the results are analyzed.

3.2.3 Spread flow test and analysis

The spread flow tests are performed using EN 13279-2 (2004) as a reference. A Hägermann cone is employed for the slump flow test. Besides the Hägermann cone, several other cones with different shapes and volumes are also widely used in determining the water demand, such as the Abrams cone, Marsh cone, Paste cone, Graf cone etc. Hunger (2010) studied the influence of the volume and geometry of different cones on the water demand and reported that with reasonable reliability, water demand derived from various cone shapes and volumes can be compared with each other. Figure 3.1 shows the used Hägermann cone as well as a test specimen (Hunger, 2010).

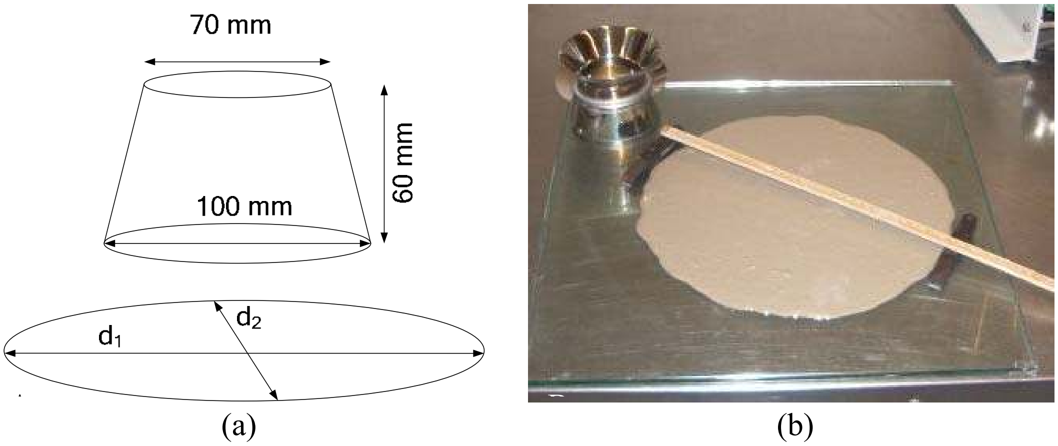

(a) (b)

Figure 3.1: Scheme of a spread flow test. a: size of the Hägermann-cone, b: Example of an executed spread flow test (taken from Hunger (2010)).

The first step is the preparation of the test sample. A sample preparation procedure is composed and strictly followed during all the tests, since water plays a very sensitive role on the workability of gypsum plaster, which will be discussed later as well. The applied test procedure is described as follows:

- Measure the used water and β-hemihydrate to ± 0.1 g;
- Add the measured water into a clean and dampened mixing bowl;
- Add the β-hemihydrate evenly into the mixing bowl within 15 s, while start counting time from the beginning of the contact between water and powder;
- Allow the powder soaking in the water for 15 s;
- Start mixing the slurry for 60 s by hand using a mixing paddle (here a spoon is used) with a speed about (140 ± 5) rpm;

- Fill the paste into the Hägermann cone immediately, and remove the excessive material with a spatula;
- Lift the Hägermann cone vertically and allow a free spread flow of the paste onto a dampened, clean and flat glass surface;
- Measure two perpendicular diameters of the resulting pat.

Each test should be performed at least twice to obtain a reliable result. Ten mixes with different initial water contents (expressed by the mass ratio of water to β-hemihydrate: w_0/h_0) are measured in the present study in order to obtain a statistically reliable trend line for the regression analysis.

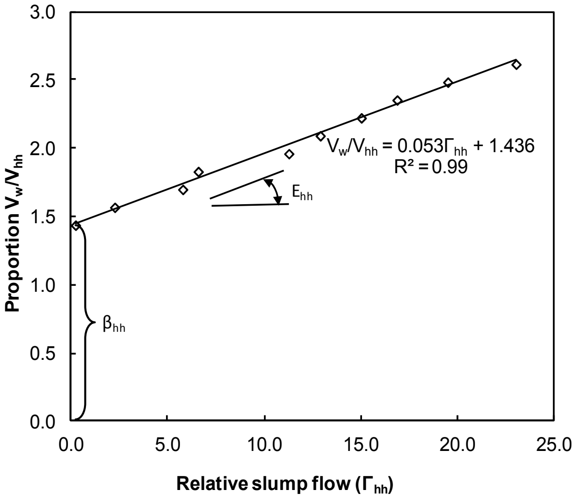

Figure 3.2: Results of the spread flow test, plot of relative slump flow versus water/hemihydrate volume ratio.

A concept of relative slump is used to analyze the water demand and workability in the present study. The relative slump is calculated from:

$$\Gamma_{hh} = (d/d_0)^2 - 1 \tag{3.2.1}$$

where Γ_{hh} represents the deformability of one mixture, which is originally introduced by Okamura and Ozawa (1995); d is the average value of the two perpendicular diameters measured from the spread of the homogeneously prepared sample and d_0 is the base diameter of the employed Hägermann cone (here 100 mm).

All the computed Γ_{hh} based on Equation (3.2.1) are then plotted versus the respective water/hemihydrate volume ratio (V_w/V_{hh}), as shown in Figure. 3.2, whereas the relation between V_w/V_{hh} and w_0/h_0 is:

$$\frac{V_w}{V_{hh}} = \frac{w_0/\rho_w}{h_0/\rho_{hh}} = \frac{w_0 \cdot \nu_w}{h_0 \cdot \nu_{hh}} \tag{3.2.2}$$

where V is the volume (cm^3), w_0/h_0 is the initial water/hemihydrate ratio by mass, ρ is the density ($g\ cm^{-3}$), υ is the specific volume ($cm^3\ g^{-1}$), subscripts w and hh are water and β-hemihydrate, respectively.

A linear trend line is fitted through the plotted values:

$$\frac{V_w}{V_{hh}} = E_{hh}\Gamma_{hh} + \beta_{hh} \tag{3.2.3}$$

where E_{hh} is the deformation coefficient and β_{hh} is the water demand of the β-hemihydrate, respectively.

From Equation (3.2.3), the water demand (β_{hh}) of the used β-hemihydrate, which represents when the slump flow of a mix equals zero, is derived. This indicates the minimum water content to ensure a fluid paste. In the present study, a β_{hh} value of 1.436 is obtained, which is in line with Yu et al. (2009), where the water demand is determined using a different technique. This also confirms that the mini-slump flow test is suitable for the determination of the water demand of the hemihydrate. A water demand of 0.31 (w_0/h_0 by mass, corresponding to 0.85 by volume) of α-hemihydrate is found here. It can be seen that the clear difference between the water demands of α- and β-hemihydrate is caused by the significant difference between their specific surface areas (see Chapter 2).

The deformation coefficient (E_{hh}) is also defined in Equation (3.2.3), i.e. the slope of this function. This value indicates the sensitivity of a material on the water demand for a specified workability, which means that material with a lower deformation coefficient shows a larger change in deformability to a certain change in water amount (Hunger, 2010). A deformation coefficient of 0.062 for cement (CEM Ш/B 42.5 N LH/HS) is reported by Brouwers and Radix (2005) that is larger than that of β-hemihydrate (0.053). This indicates that water has a larger influence on the workability of the β-hemihydrate paste, which is probably due to the smaller specific surface area of the β-hemihydrate (9877 cm^2 cm^{-3}) than that of the above mentioned cement (15300 cm^2 cm^{-3}).

As discussed above, a thin layer of adsorbed water molecules around the particles is necessary to ensure the fluidity of the hydrating system. Brouwers and Radix (2005) reported that the thickness of this layer (δ) is related to the deformation coefficient and the surface area of the used material, which is later confirmed by Hunger (2010):

$$E_{hh} = \delta_{Blaine} \cdot a_{Blaine} \cdot \rho_{hh} = \delta \cdot \xi \cdot a_{sphere} \cdot \rho_{hh} \tag{3.2.4}$$

where δ is the thickness of the water layer (cm), δ_{Blaine} is the thickness of the water layer expressed using Blaine measurement, a_{Blaine} is the surface area measured using Blaine method (cm^2 g^{-1}), ξ is the shape factor and a_{sphere} is the specific surface area computed using the PSD and assuming spheres (cm^2 g^{-1}) (see Chapter 2).

Here, using a a_{Blaine} value of 3025 cm^2 g^{-1} (Engelhardt, 2009) and a ρ_{hh} value of 2.62 g cm^{-3}, a δ_{Blaine} value of 66.8 nm is obtained, while Brouwers and Radix (2005) reported a δ_{Blaine} value of 44.6 nm for CEM Ш/B 42.5 N LH/HS.

The specific surface area of the investigated β-hemihydrate computed from the measured particle size distribution, as introduced in Chapter 2, is 1.26 times larger compared to the Blaine surface area value provided by Engelhardt (2009). This is in line with Robens et al. (2002), who reported that the computed specific surface area based on the measurement with a laser granulometry technique is 1.3 times larger than the Blaine surface area for different types of cement.

A linear relation is reported (Hunger and Brouwers, 2009) between the specific surface area from Blaine method and computed specific surface area from PSD method modified by the particle shape factor, given by

$$\xi \cdot a_{sphere} = 1.7 \cdot a_{Blaine} \tag{3.2.5}$$

Substituting the surface areas yields $\xi = 1.36$.

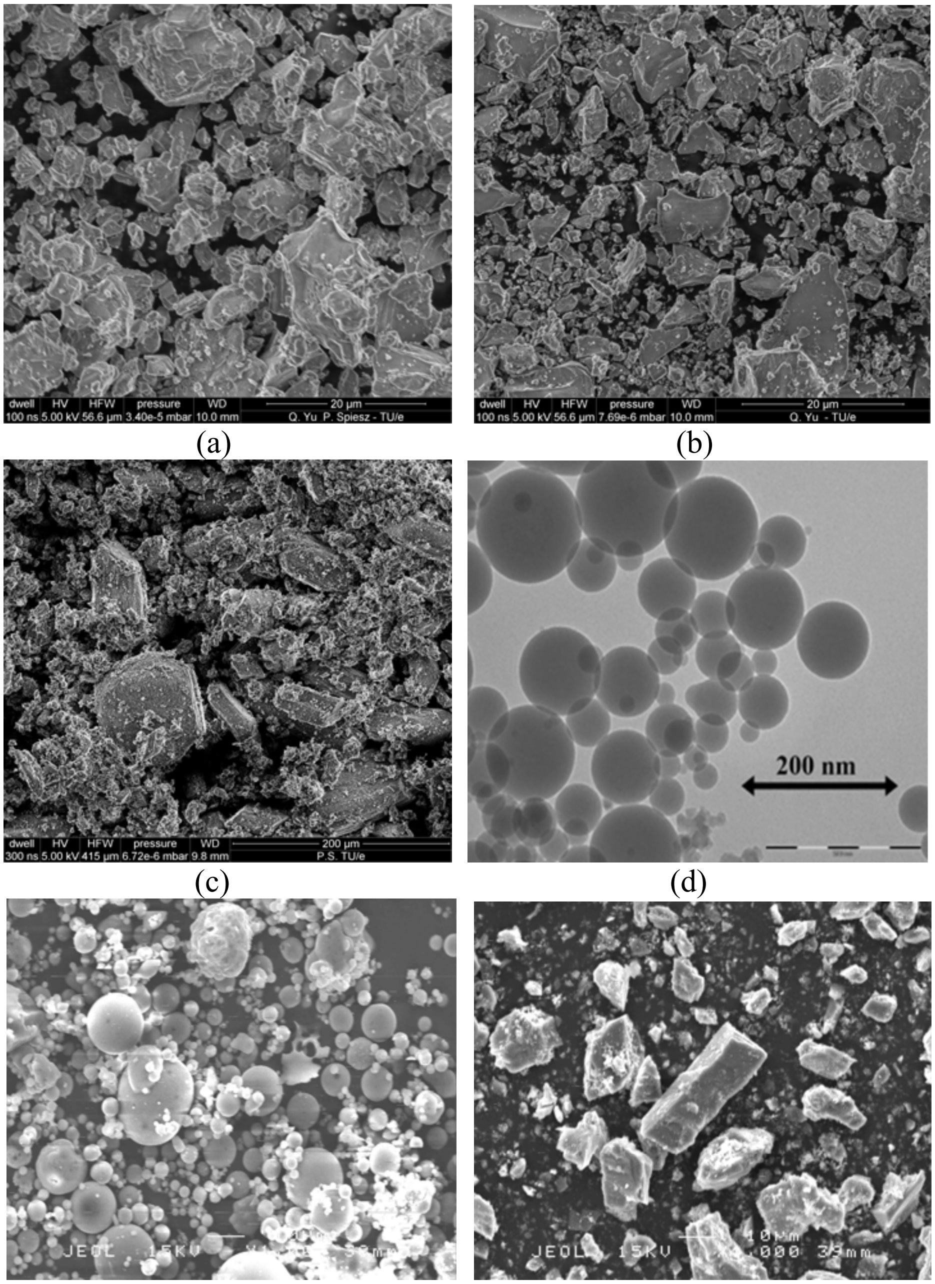

(a) (b)

(c) (d)

(e) (f)

Figure 3.3: SEM/STEM pictures of different particles (a: Limestone powder; b: CEM I 52.5 N; c: β-hemihydrate; d: Micro-silica; e: fly ash; f: marble powder) (e and f taken from Hunger (2010); d taken from Quercia et al. (2012a)).

Hunger (2010) reported various shape factor values for different granular materials. The derived shape factor (1.36) of the β-hemihydrate here is different from the values for materials such as limestone powder and micro-silica. This can be seen from the SEM pictures of these materials, as shown in Figure 3.3, which clearly shows that the discussed materials have different particle shapes.

Substituting the derived shape factor of the β-hemihydrate into Equation (3.2.4), the water layer thickness (δ) is computed, yielding 39.3 nm. This is in line with Marquardt (2002) who reported a δ value of 45 nm with a different test, which is discussed in (Hunger and Brouwers, 2009). For material with a spherical particle shape (as shown in Figure 3.3), Hunger and Brouwers (2009) and Quercia et al. (2012a) separately reported the same water layer thickness of 25 nm for fly ash and silica, respectively. It can be seen that even after the shape correction, i.e. multiplying the calculated shape factor, the current derived water layer thickness of the β-hemihydrate is still a little bit larger. Hunger and Brouwers (2009) reported a deformation coefficient value of about 0.035 for fly ash with a specific surface area of 13419 cm^2 cm^{-3}, while Quercia et al. (2012a) reported a deformation coefficient value of 0.8947 for nano-silica with a specific surface area of 460000 cm^2 cm^{-3}. In the present study, the deformation coefficient of the β-hemihydrate is 0.053 but with a specific surface area of only 9877 cm^2 cm^{-3}. It can be seen that the particles with a more spherical particle shape are more sensitive to the water content, as indicated by the abovementioned deformation coefficients. This explains why smaller water layer thicknesses are needed for materials with spherical particles than that of materials with irregular particle shapes.

3.3 Hydration of $CaSO_4·0.5H_2O$

3.3.1 Introduction

The term hydration can be understood as the adsorption and/or combination of water with dry compounds and the formation of some other solid materials. This process is called hydration and the solid products are called hydration products (Taylor, 1985). The hydration is thus a chemical process including phase transformation, substances redistribution, energy change and physical consequences (Chen, 2006). The hydration study of calcium sulfate can be traced back even to 1768 when Lavoisier first discussed setting as a crystallization process and proposed a mechanism including the dissolution of hemihydrate which precedes the crystal growth of dihydrate.

Hemihydrate, as well as dihydrate, is a relatively simple material, however, although great effort has been devoted to the study of its hydration behavior. The kinetics as well as the hydration process are still incompletely understood and the reported results vary considerably (Schiller, 1962; Ridge, 1964; Lancia et al., 1999; Gmouh et al., 2004). Hence in this section, the hydration of the investigated β-hemihydrate is addressed. Some available hydration measurement methods as well as their application are firstly discussed, then the hydration of the used β-hemihydrate is measured applying an ultrasonic wave method, and subsequently an analysis of the test results is presented.

3.3.2 Hydration of $CaSO_4·0.5H_2O$

Hydration reaction

Equations (3.3.1) and (3.3.2) show the hydration of hemihydrate, which takes place quickly after mixing it with water via a through-solution route, firstly the hemihydrate dissolves (Equation (3.3.1)) and then the generated dihydrate precipitates from the solution (Equation (3.3.2)). Equation (3.3.3) shows the integral hydration reaction as a combination of the foregoing two steps.

$$CaSO_4 \cdot 0.5H_2O \rightarrow Ca^{2+} + SO_4{}^{2-} + 0.5H_2O \tag{3.3.1}$$

$$Ca^{2+} + SO_4{}^{2-} + 2H_2O \rightarrow CaSO_4 \cdot 2H_2O \tag{3.3.2}$$

$$CaSO_4 \cdot 0.5H_2O + 1.5H_2O \rightarrow CaSO_4 \cdot 2H_2O \tag{3.3.3}$$

During the first step (shown in Equation (3.3.1)), the hemihydrate ($CaSO_4 \cdot 0.5H_2O$) breaks into ions of Ca^{2+} and SO_4^{2-} in the solution and saturation point is quickly reached. The dissolution rate is influenced by many factors such as the particles size and the temperature. Because dihydrate is less soluble in water than hemihydrate, i.e. at room temperature, the solubility of β-hemihydrate is 8.72 g L^{-1} (6.01×10^{-2} mol L^{-1}) whereas the solubility of dihydrate is 2.62 g L^{-1} (1.52×10^{-2} mol L^{-1}) (Amathieu and Boistelle, 1988), the needle like material quickly precipitates from the solution as shown by Equation (3.3.2). The total hydration is an exothermic process, which can be used to determine the hydration progress with methods such as calorimetry. The hydration process has been intensively studied by Ridge and Surkevigius (1961), Ridge (1964), Schiller (1962) and Fujii and Kondo (1986), and different mechanisms were proposed.

Amathieu and Boistelle (1988) studied the crystallization of dihydrate from dense suspension of hemihydrate in water. The fast dissolution of hemihydrate after it is put in contact with water results in not only free Ca^{2+} and SO_4^{2-} ions but also in soluble complexes like $CaSO_4$, $CaOH^+$ and HSO_4^-. The ionic product at 25 °C reads:

$$\gamma = \alpha(Ca^{2+})\alpha(SO_4{}^{2-})/10^{-4.62} \tag{3.3.4}$$

where γ is the super saturation, and α is the activity of the free ions. Nucleation and growth occur when $\gamma > 1$.

Lewry and Williamson (1994a) studied the hydration of α- and β- hemihydrate with the same water/hemihydrate ratio of 0.60. The degree of hydration is measured by stopping the reaction at various stages, which is achieved by washing the specimen with excess ethanol, and determining the phases present using XRD and thermal analysis. The temperature increase and electrical resistance of the hydrating system are monitored by a calorimeter and an electrical resistance analyzer, respectively. The results show that the temperature and electrical resistance change are not synchronized. They concluded that the hemihydrate hydration experiences a two stage reaction, i.e. dissolution of hemihydrate and nucleation and growth of the dihydrate.

Lancia et al. (1999) studied the nucleation of dihydrate. Homogeneous nucleation of dihydrate is studied using an optical diagnostic technique within a super saturation degree of 1-4 at 25-90 °C. Signals of scattered and transmitted light coming from a He-Ne laser source are analyzed to determine the induction time. The effect of temperature on the super saturation increase is investigated.

Solberg and Hansen (2001) studied the dissolution of $CaSO_4 \cdot 0.5H_2O$ and precipitation of $CaSO_4 \cdot 2H_2O$ during the hydration of hemihydrate. X-ray diffraction is employed and the influence of the water/hemihydrate ratio is studied as well. Results show that the reaction is almost independent from the water amount (water/hemihydrate ratios vary from 0.50 to 1.50). There is a slight tendency for a more rapid reaction at low w_0/h_0 ratio, but the effect is very small. Calorimetry results show that the growth rate of dihydrate is equal to the dissolution rate of the hemihydrate.

Gmouh et al. (2004) studied the setting process of gypsum, which is associated to the temperature change during the whole process. The first stage can be described as the induction period, in which the nucleus of dihydrate starts developing immediately after the hemihydrate is poured into water. The growth of the gypsum crystals is accompanied by a clear heat release in the second stage. The beginning of the setting is roughly associated to the instant steep rise of the temperature. The gypsum crystals stop growing as the temperature reaches a plateau, which can be considered as the end of the setting.

Discussion

It can be concluded that so far numerous studies have been carried out on calcium sulfate hydration. Different methodologies and test equipments are used. Hydration kinetics is addressed and several models are proposed; the hydration process is experimentally studied extensively; the effect of the hemihydrate type is investigated, and the effect of experimental conditions such as water amount and temperature is studied.

The calorimetry method is widely used in cementitious materials hydration study since the calorimeter can be used to measure the heat release and temperature change continuously. It is possible to measure the dissolution of hemihydrate. However, due to the low reaction heat during the precipitation of dihydrate, it is impossible to test the formation of dihydrate during the hydration. The knife cut closure and Vicat needle methods are used widely and recommended by standard EN 13279-2 (2004), because they are fast and easy to perform. But these two methods only provide information about the formation of dihydrate as they monitor the physical setting of the slurry. Thermal analysis such as DSC or TGA can give information on both the dissolution of hemihydrate and the formation of dihydrate, but it can only be performed on samples in which the hydration has stopped. However, different from cement hydration, the calcium sulfate hydration process is quite fast and rather sensitive (this will be discussed and analyzed intensively in the next section). Obviously, to stop the hydration of hemihydrate by washing the hydrating paste with excess alcohol will easily cause considerable errors. X-ray diffraction can be used to test both the dissolution of hemihydrate and the formation of dihydrate during hydration. It is, however, very difficult to quantitatively study the gypsum hydration using the X-ray diffraction method.

Based on the analysis above, a different type of test method is applied here to determine the hydration of hemihydrate, which is the ultrasonic wave method. The test method, theoretical background, procedure and results are discussed in the next section.

3.3.3 Hydration analysis

Introduction

The ultrasonic wave technology is widely used to detect the microstructure defects, variation and fracture of solids since the ultrasonic wave propagation velocity changes in different media. Phani et al. (1986) studied the strength and elastic modulus of gypsum using the ultrasonic wave technology. The ultrasonic wave method has also been extensively applied to study the hydration and setting of concrete (Reinhardt and Grosse, 2004; De Belie et al., 2005; Grosse et al., 2006; Robeyst et al., 2008).

The ultrasonic wave velocity varies in different media. Harker and Temple (1988) proposed a model to describe the ultrasonic sound propagation in colloids, and pointed out that the ultrasonic wave velocity is related to many factors such as the bulk modulus of the solid and liquid and their volume proportion in the colloid, and the particle size and shape of the solid. During the setting, the hydrating system begins to acquire mechanical strength and therefore can be considered as a solid. Hence, the ultrasonic wave velocity is related to the Young's modulus and Poisson's ratio, and the density of the system.

During the hydration of the β-hemihydrate, the microstructure of the hydrating system experiences a continuous microstructural change due to firstly the dissolution of the hemihydrate, which can be considered as slurry, and then to the generation and the precipitation of the dihydrate due to the lower solubility as indicated from Equation (3.3.4), when the system starts to acquire mechanical strength and can be eventually treated as a homogeneous elastic solid material (Lewry and Williamson, 1994a). Therefore, the ultrasonic wave technology could be suitable to be employed for calcium sulfate hydration measurement.

Ultrasonic wave velocity measurement

The hemihydrate hydration experiments applying the ultrasonic wave method were performed at the University of Stuttgart (Germany), using the FreshCon system as shown in Figure 3.4 (Lehmann and Grosse, 2008). A pulse is generated at one surface of the specimen and the onset of the pulse is picked at the other side. The pulse can be generated mechanically and recorded at both sides by a receiver, or it can be imposed by an ultrasound transmitter.

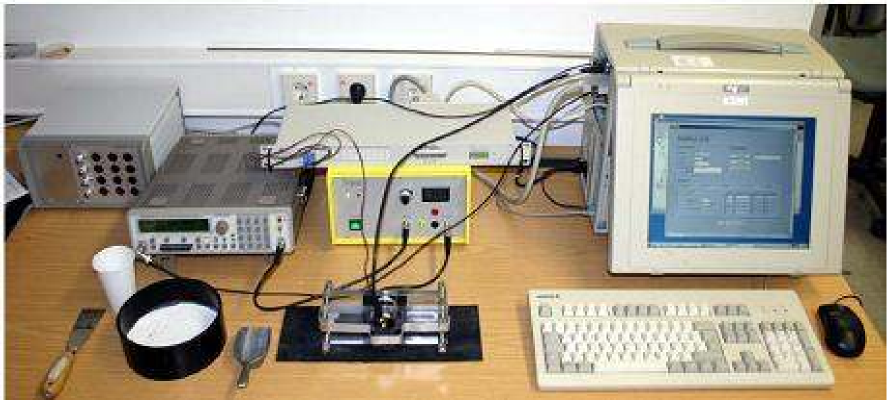

Figure 3.4: The FreshCon system for ultrasonic wave velocity measurement (Lehmann and Grosse, 2008).

The sample holder, with a volume of 45 cm^3, shown in Figure 3.4, has the following characteristics: (1) the compressive pulse is directly transmitted through the specimen, and no transmission through the wall of the holder, and (2) the transducers are coupled reliably (Reinhardt and Grosse, 2004).

The frequency generator is connected to the amplifier which generates a signal for the transmitter. In the present study, a sensor with a frequency of 2.25 MHz is used (Lehmann and Grosse, 2008). The transmitted analogue signal is digitized in an AD converter which is then transferred to a computer. The used software, named FreshCon, is used to analyze the data online during the tests. Furthermore, the temperature evolution during the hydration reaction is also recorded, which can be used to determine the hydration heat. The temperature in the sample holder and the surrounding ambient environment is continuously monitored and recorded. More detailed information is presented in Reinhardt and Grosse (2004).

The hydration tests of β-hemihydrate were performed under ambient conditions. Various initial water contents of 0.65, 0.80 and 1.25 are used to investigate the influence of the water on the hydration process of the hemihydrate. The mixing procedure is following the same procedure as introduced in Section 3.2.3. In each test, a total amount of 98.0 g including the β-hemihydrate and water is used. During the measurement, the sample was sealed with a plastic film to avoid water evaporation and shrinkage of the specimen. The received signals, their frequency spectra, wave velocities as well as energy are monitored online during the whole measurement period.

Results analysis

- Ultrasonic velocity results

The measured ultrasonic velocity during the hydration of β-hemihydrate with different w_0/h_0 is shown in Figure 3.5 (Yu and Brouwers, 2011a). The velocity curve of the ultrasonic wave has the following characteristics: the first part is a dormant period, which is distinguished by a constant low velocity value, which is then followed by the second part, in which the velocity increases rapidly until it finally reaches a plateau.

The constant velocity value in the first period indicates that the microstructure of the hydrating system remains stable or this period can be considered as the induction time of the β-hemihydrate in water. This confirms the results of Ridge and Surkevigius (1961) and Lewry and Williamson (1994) who reported that there is no production of dihydrate during the induction period of the hemihydrate. Solberg and Hansen (2001) also reported that no dihydrate is produced after mixing hemihydrate with water until a certain period measured using X-ray diffraction method. Fujii and Kondo (1986) reported that the amount of free Ca^{2+} remains constant during the first minutes after mixing hemihydrate with water, which means that during this period the equilibrium is reached very quickly. It is therefore shown that, during this period, a part of β-hemihydrate is dissolved in the solution and dihydrate is generated around the particles of the hemihydrate but not precipitated in the rest of the slurry.

The ultrasonic wave velocity changes quickly after the induction time due to the change of the void fraction of the hydrating system and the physical properties of the materials in the system (Harker and Temple, 1988; Robeyst et al., 2008), which indicates the generation and precipitation of gypsum. This can also be explained by Equation (3.3.4), in which nucleation and growth of the gypsum crystals take place when $\gamma > 1$. Although the measured ultrasonic velocity values increase quickly in the precipitation period, the increase rate gradually slows down later until finally a plateau is reached. This can also be explained by Equation (3.3.4): the reduction of the amount of free ions in the solution due to the precipitation of the gypsum leads to the decrease of the hydration speed. The plateau of the ultrasonic wave velocity indicates the end of the hydration.

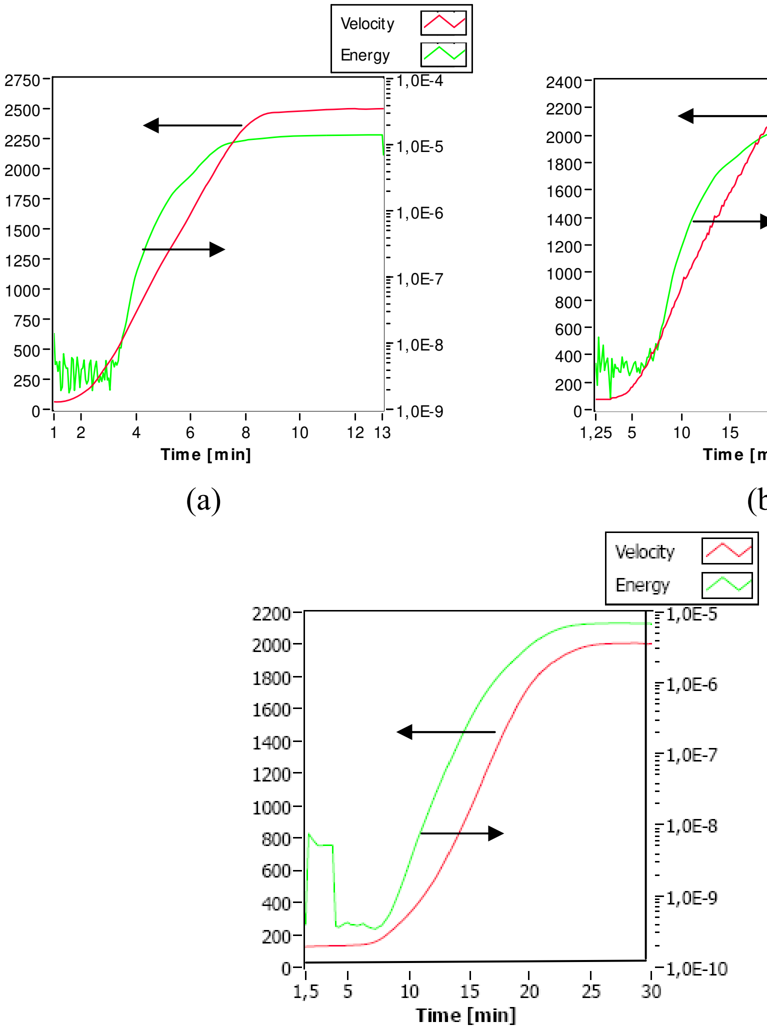

(a)

(b)

(c)

Figure 3.5: Ultrasonic velocity during β-hemihydrate hydration measured by the FreshCon system (a: $w_0/h_0 = 0.65$; b: $w_0/h_0 = 0.80$; c: $w_0/h_0 = 1.25$) (Lehmann and Grosse, 2008).

Schiller (1974) reported a standard hemihydrate hydration curve, which is a plot of the hydration degree as a function of time. Although the curve can be influenced by many factors, such as the initial water content, the hemihydrate dissolution rate, the number of the hemihydrate particles, the dihydrate growth rate, the number of the effective dihydrate nuclei, the solubility of both hemihydrate and dihydrate, and the shape factor of both hemihydrate and dihydrate, still it can be seen that the measured ultrasonic wave velocity curve has a high similarity with it. These factors overall indicate that the ultrasonic wave method is suitable for the measurement of the hemihydrate hydration.

The measured initial setting time of about 4.5 minutes in the case of w_0/h_0 of 0.65 is in line with Yu et al. (2009), in which the setting is measured with a different method (the knife method according to EN 13279-2, 2004). The setting time measured using this method in this study is much shorter compared to the value from the electrical resistance method (Lewry and Williamson, 1994a). Besides the difference between the measuring methods, this probably also can be explained by the difference between the microstructure of the used materials. This is also confirmed by Schiller (1974) who studied the setting of four different types of hemihydrate and reported a quite varied initial as well as final setting time with the same initial water content.

- Heat evolution analysis

The results of the measured temperature change during the hydration of β-hemihydrate are shown in Figure 3.6. It can be clearly seen that the temperature change is strongly related with the ultrasonic velocity change, i.e. first the temperature remains constant, and then it increases until a maximum value and then finally decreases.

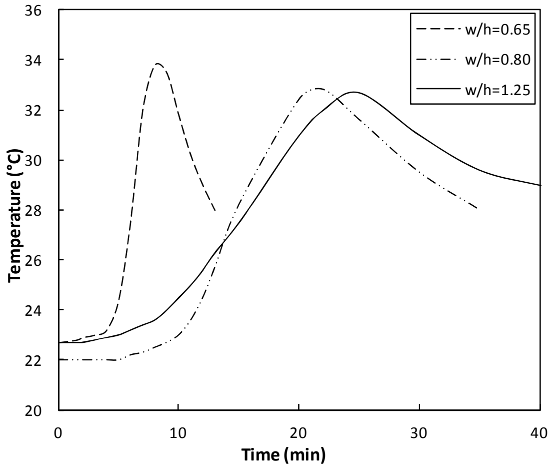

Figure 3.6: Temperature increases during the hydration of $CaSO_4 \cdot 0.5H_2O$ at different w_0/h_0.

During the first period, i.e. the so-called induction time, the temperature remains stable in all the experiments regardless of the water/hemihydrate ratios. This confirms the results of Lewry and Williamson (1994a) who measured the temperature change during both α- and β-hemihydrate hydration using calorimetry. Robeyst et al. (2008) reported a very similar trend in the case of cement hydration measured by calorimetry too. Solberg and Hansen (2001) reported that the process of the hemihydrate dissolution is an exothermic reaction, in which the enthalpy change associated with the dissolution of hemihydrate is very large (-18.0 kJ mol^{-1}). It is hence again indicated here that during the induction period, the amount of β-hemihydrate that has dissolved in the solution is very small and a very small amount of dihydrate is generated around the particles of the hemihydrate but not precipitated from the slurry, which is in line with the measured ultrasonic velocity values.

The temperature then increases steadily until it finally reaches a maximum value, as shown in Figure 3.6. The periods, as demonstrated by Figures 3.5 and 3.6 for three cases with different initial water contents, are strongly related as well with the ultrasonic velocity variation. It is shown that for different initial water contents, the temperature reaches its maximum value at different times, which correspond to the time when the ultrasonic velocity reaches the maximum value. Hence, it can be seen that the heat release is synchronized with the microstructural change of the hydrating system (which is represented by the change of the ultrasonic velocity), whereas the microstructure change is the result of the consumption of the hemihydrate and the generation and precipitation of the dihydrate. This is confirmed by Lewry and Williamson (1994a) who reported a 100% of the dihydrate formation, and Schiller (1974) who reported a full hydration (full consumption of hemihydrate) when the temperature reached the maximum value. This shows that the monitoring of the temperature change can be suitably used to determine the hydration degree.

- Effect of initial water content

The hydrating systems with different w_0/h_0 show different workabilities (see Section 3.2). This finding indicates that the distance between the molecules in the hydrating system is different under different water content conditions. The distance between the molecules becomes larger when the water amount is higher, which in turn should result in a longer reaction time. This is confirmed by the measured results with the ultrasonic wave velocity method, as shown in Figure 3.5. The results show that the induction time becomes longer with an increase of the water amount. The induction time is about 1.5 minutes with the w_0/h_0 of 0.65 while around 7 minutes when the w_0/h_0 increases to 1.25. The longer induction time with the higher w_0/h_0, as shown in Figure 3.6, can also be explained by Equation (3.3.4) as the generated gypsum needs longer time to become saturated. The relation between the water amount and induction time found in this study is shown in Figure 3.7.

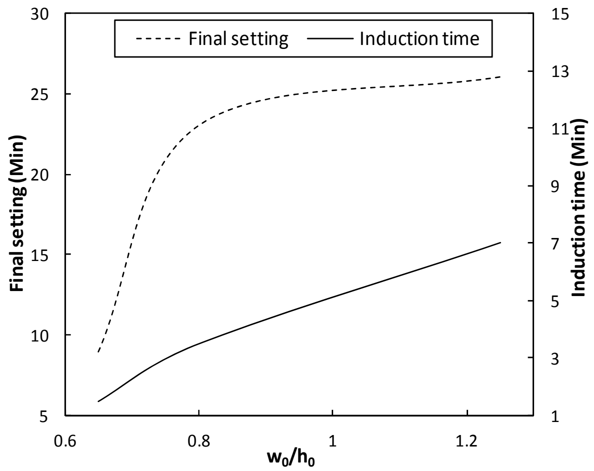

Figure 3.7: Analysis of the hydration process, induction time and final setting time versus w_0/h_0.

The influence of the water amount on the period of precipitation is reflected from the period duration and the velocity variation. With the w_0/h_0 of 0.65, the duration of this period is about 7 minutes only and the final velocity reaches to about 2500 m s^{-1}, while with the w_0/h_0 of 1.25, the duration of this period is about 18 minutes and the final velocity reaches about 2000 m s^{-1}. The duration of the precipitation period indicates evidently that the water amount influences greatly the hydration process of the hemihydrate. The result of the final setting time of the hydration is shown in Figure 3.7. These results indicate that the water content at a lower w_0/h_0 has a dominant influence on the final setting of the hydrating system. This finding confirms the results of Schiller (1974) who reported a similar relation between the water ratio and the setting time. However, this finding is in contrast to Solberg and Hansen (2001) who reported that hydration of the β-hemihydrate is almost independent of the water amount within the w_0/h_0 range of 0.5 to 1.5.

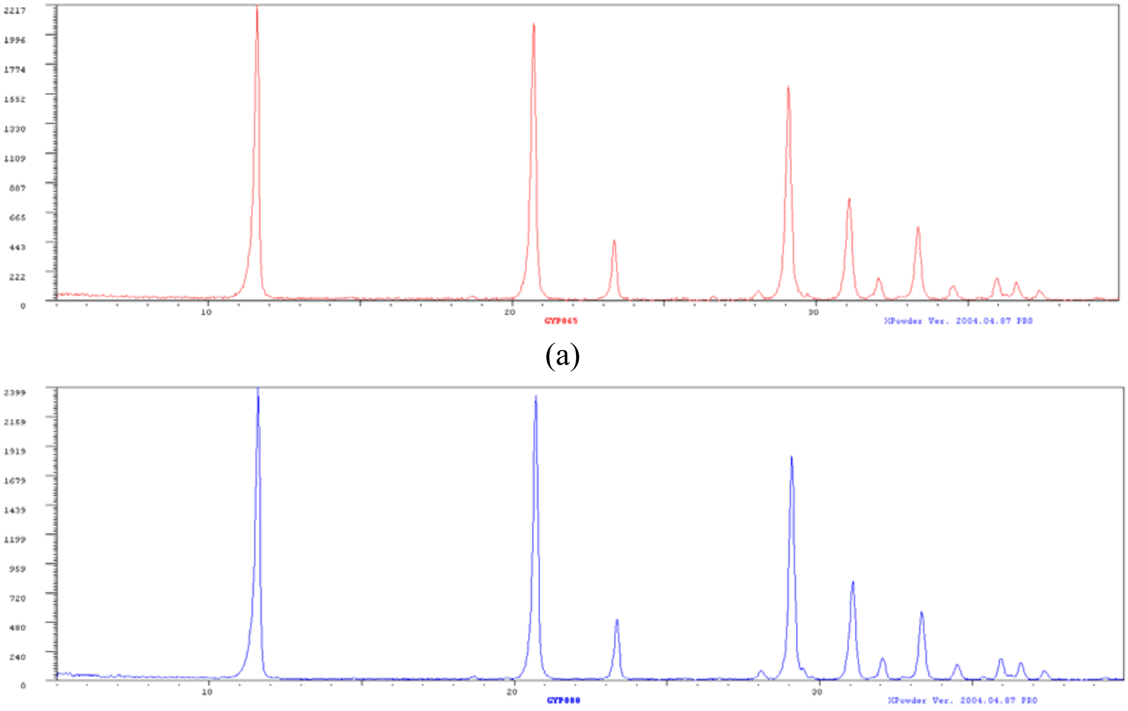

(a)

(b)

Figure 3.8: XRD patterns of gypsum produced with (a: $w_0/h_0 = 0.65$; b: $w_0/h_0 = 0.80$).

Figures 3.8a and 3.8b show the XRD pattern of the gypsum with w_0/h_0 of 0.65 and 0.80, respectively. The results show clearly that the hydrated system only includes $CaSO_4 \cdot 2H_2O$, which indicates that the β-hemihydrate is fully hydrated and the water content does not influence the final chemical composition of the hydrated system. The difference between the final velocities indicates that the final hydrated system has different microstructures due to the different initial water amount, which will be discussed in next chapter. This also can be explained by the void fraction of the system, which will be discussed in next chapter as well.

3.4 Conclusions

In this chapter the fresh state behavior of the $CaSO_4 \cdot H_2O$ system is investigated. The following conclusions can be drawn:

- The water demand of the used β-hemihydrate is studied applying the mini-spread flow test, which is chosen based on an analysis of several available test methods.
- The deformation coefficient of the β-hemihydrate is experimentally derived.

- A water layer to cover the particles for the onset of the fluidity of the system is computed and discussed.
- The particle shape factor of the β-hemihydrate is derived and the effect of the particle shape on the deformation coefficient is discussed.
- The hydration of the β-hemihydrate is studied using the ultrasonic sound velocity method.
- The characteristics of the hydration process of the β-hemihydrate are analyzed.
- The heat evolution during the hydration of the β-hemihydrate is investigated by studying the temperature of the hydrating system and a relation between the temperature change and microstructure change is found.
- The effect of the initial water content on the hydration behavior is analyzed.

Chapter 4

Thermal properties and microstructure of the $CaSO_4 \cdot H_2O$ system

4.1 Introduction

Calcium sulfate dihydrate ($CaSO_4 \cdot 2H_2O$, or gypsum) readily loses its chemically bound water at elevated temperatures, through a process usually called dehydration. This reaction strongly affects the thermal properties as well as the microstructure of the system. The dehydration mechanism of gypsum has been extensively investigated (Groves, 1958; Kunte, 1965; Paulik et al., 1992; Deutsch et al., 1994; Hudson-Lamb et al., 1996). Groves (1958) reported that first $CaSO_4 \cdot 0.5H_2O$ and later $CaSO_4$ are formed during gypsum dehydration, which is also confirmed by Kunte (1965) and Paulik et al. (1992). The effect of experimental conditions such as temperature, pressure and particle size is investigated as well. The dehydration is endothermic, i.e. a certain amount of energy is needed to release the chemically bound water (Andersson and Jansson, 1987; Mehaffey et al., 1994; Thomas, 2002), which also explains why gypsum has a good fire resistance.

Thermal properties such as the specific heat and thermal conductivity of gypsum are also extensively studied (Andersson and Jansson, 1987; Mehaffey et al., 1994; Sultan, 1996; Thomas, 2002; Ang and Wang, 2004; Manzello et al., 2007; Ghazi Wakili et al., 2007; Ghazi Wakili and Hugi, 2008). However, the reported thermal properties of gypsum (plasterboard) vary considerably due to many reasons such as the physical properties of the applied raw material, the composition of the investigated gypsum (plasterboard) and the production procedure of the gypsum plasterboard etc. Thermal properties of a material are strongly linked to its microstructure. In addition, the thermal properties of gypsum influence its dehydration behavior.

The present work aims at a better understanding of the $CaSO_4 \cdot H_2O$ systems from the point of view of their thermal properties and microstructure. The thermal behavior of the $CaSO_4 \cdot H_2O$ systems is investigated by means of thermogravimetric analysis (TGA), differential scanning calorimetry (DSC) and thermal conductivity measurements employing a commercial heat transfer analyzer. The dehydration mechanism of gypsum is investigated and discussed in the present study. The microstructure of the $CaSO_4 \cdot H_2O$ systems is investigated by both modeling and experiments. The relation between the void fraction of the $CaSO_4 \cdot H_2O$ systems and their thermal conductivities is analyzed. Furthermore, the effect of the microstructure change of the $CaSO_4 \cdot H_2O$ systems is studied by investigating the change of the strength at elevated temperatures.

4.2 Thermal properties

4.2.1 Thermal behavior at elevated temperature

Here, the calcium sulfate dihydrate ($CaSO_4 \cdot 2H_2O$) is produced from the $CaSO_4 \cdot 0.5H_2O$ (calcium sulfate hemihydrate of β-type) using a similar method as for real gypsum board production (Barthelmes, 2008; Yu et al., 2009). An accelerator (a fine gypsum powder) is used to adjust a final setting time of 5-7 minutes in order to simulate a real gypsum plasterboard production process (Barthelmes, 2008). The studied specimen includes powder, prism, and board according to the different objectives with the powder sampled from the prepared prisms or boards.

Dehydration of $CaSO_4{\cdot}2H_2O$

When heated, dihydrate undergoes two steps of endothermic decomposition reactions (Groves, 1958; Kunte, 1965; Paulik et al., 1992). When the first dehydration reaction occurs, $CaSO_4{\cdot}2H_2O$ is converted to $CaSO_4{\cdot}0.5H_2O$, which reads as follows:

$$CaSO_4 \cdot 2H_2O + heat \rightarrow CaSO_4 \cdot 0.5H_2O + 1.5H_2O \tag{4.2.1}$$

The second dehydration reaction occurs when $CaSO_4{\cdot}0.5H_2O$ is converted to $CaSO_4$, which reads as follows:

$$CaSO_4 \cdot 0.5H_2O + heat \rightarrow CaSO_4 + 0.5H_2O \tag{4.2.2}$$

However, it is indicated that the thermal properties related to the dehydration reaction such as the dehydration temperature and the required energy are still not certain (Groves, 1958; Kunte, 1965; Paulik et al., 1992; Deutsch et al., 1994; Hudson-Lamb et al., 1996). This can be caused by the physical properties such as the composition and microstructure of the investigated gypsum. Therefore, in the present study the dehydration reaction is studied. The dehydration of the gypsum board is investigated applying both a discrete and a continuous heating rate. The dehydration reaction is studied from a micro level by employing a simultaneous TGA-DSC test equipment (STA 449 F1 Jupiter®). The investigated gypsum powder is sampled from the prepared gypsum boards. A ventilated oven is also used to study the dehydration reaction in a macro-level. The gypsum board is used for the macro level dehydration study. Prior to the tests, all the samples are dried in the oven at 40 °C to a constant mass in order to remove the free moisture.

Dehydration process analysis

The dehydration of the gypsum board in microscale (the mass of the samples is in the range of 40-50 mg) is measured by employing TGA-DSC and the final heating temperature is set at a quite high temperature of 1000 °C, considering the possible decomposition of the impurities in the used raw material. Two different heating rates of 20 °C min^{-1} and 5 °C min^{-1} are applied to study the effect of heating rate on the dehydration process. The mass loss during the dehydration of gypsum is shown in Figure 4.1. TGA results show that under both heating rates, the sample starts losing weight at about 80 °C, but the mass becomes constant at different temperatures of 270 °C (20 °C min^{-1}) and 180 °C (5 °C min^{-1}), respectively, which indicates a completion of the dehydration reaction. It is demonstrated that the heating rate does not affect the dehydration commencing temperature, but it influences its ending temperature, which indicates the energy needed for the dehydration is related not only to the temperature but also to the heating duration.

Mehaffey et al. (1994) reported that all chemically bound water is released between 100 °C and 160 °C and Ghazi Wakili et al. (2008) reported a temperature range of about 150 °C to 300 °C using the same heating rate of 20 °C min^{-1}. As can be seen, here the values are considerably different from each other. This probably can be explained by the microstructure of the investigated gypsum, which indicates its effect on the thermal behavior of gypsum board. The derivative curve of the mass loss in Figure 4.1 shows that two steps of the reaction occur, which is in line with literature (Groves, 1958; Kunte, 1965; Paulik et al., 1992; Deutsch et al., 1994; Hudson-Lamb et al., 1996). However, it is also clear that these two steps are not distinguishable, especially in the case of the higher heating rate test (i.e. 20 °C min^{-1}).

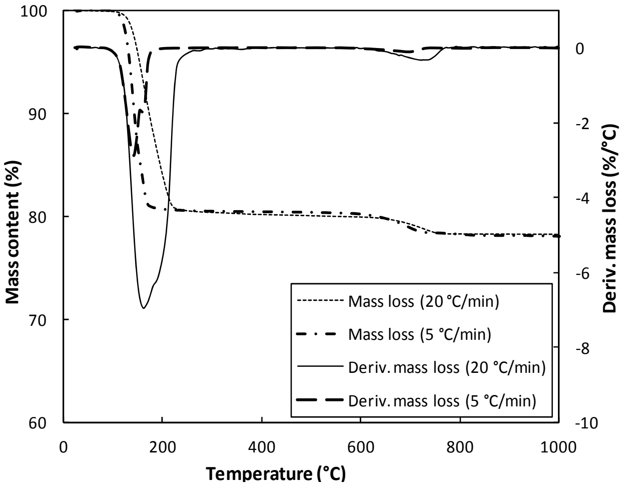

Figure 4.1: TGA results of the samples from gypsum boards (heating rates: 20 and 5 °C min^{-1}).

There is another clear mass loss observed at about 620 °C until about 800 °C, as shown in Figure 4.1. According to the chemical analysis results listed in Table 2.4 (Chapter 2), the molar amounts of Ca, S, and O are in accordance with the theoretical calculation (see Chapter 2), which indicates that there is no impurity of $CaCO_3$ in the used material. From the decomposition temperature of about 600 °C and the chemical element analysis as listed in Table 2.4, it can be concluded that the impurity is $MgCO_3$ and the decomposition reaction reads:

$$MgCO_3 \rightarrow MgO + CO_2 \tag{4.2.3}$$

This finding is different from Ghazi Wakili et al. (2007) who considered the second mass loss as the decomposition of the $CaCO_3$, only based on the fact that $CaCO_3$ decomposes in this temperature range. Mehaffey et al. (1994) also reported a mass loss at around 650 °C but they did not analyze the possible reason.

The mass loss of the samples at macroscale during the heating using a ventilated oven is shown in Figure 4.2a. Here, the samples are heated in a discrete order, i.e. firstly the temperature is fixed at one value and the samples are heated until a constant mass (here the constant mass means the mass remains the same with a measurement interval of 24h), then the temperature is raised to another value and the samples are heated again until a constant mass, and so on. The tests are performed twice with the same experimental conditions. The excellent agreement between the results from the two batches indicates the reliability of the results.

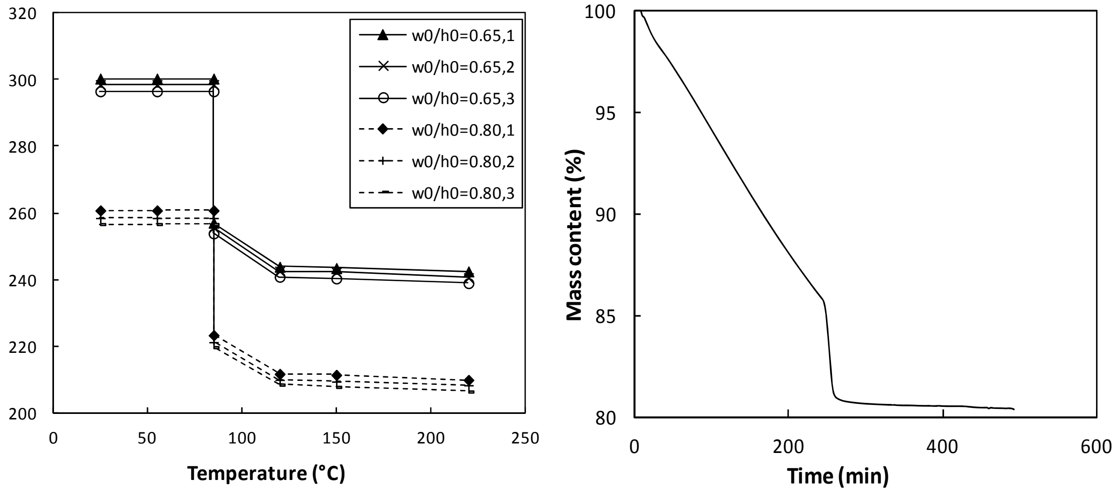

(a) (b)

Figure 4.2: Mass loss of the gypsum boards measured with discrete heating order (a: heated with a ventilated oven (6 specimen); b: heated with TGA analyzer).

Results show no mass loss occurs at 55 °C, and then the dehydration reaction takes place between 80 °C and 120 °C. The very small mass loss between 120 and 220 °C (less than 1%) indicates the completion of the water release. The average mass loss is in good agreement with the mass loss measured with the TGA by both continuous and discrete heating methods. The mass loss of gypsum board measured by the TGA in discrete order is shown in Figure 4.2b. The heating order (the sample first is heated to 80 °C at 20 °C min^{-1}, and then the temperature is kept at 80 °C for 4 h; next, the temperature is increased to 120 °C at 20 °C min^{-1} and kept for 3 h; and then the temperature is increased to 150 °C and kept for 1h; and finally, the temperature is increased to 300 °C) is the same as the test performed in macrolevel, as shown in Figure 4.2b. It can be seen that these two results are in line with each other, which indicates that the isothermal time is sufficient for the total water release within that period. These findings indicate that, given sufficient heating time, the gypsum board produced from β-hemihydrate can accomplish the first step of dehydration (i.e. a release of 1.5 molecules of crystal water, Equation (4.2.1)) at 80 °C and a total dehydration (i.e. a release of the remaining crystal water, Equation (4.2.2)) at 120 °C. To the author's knowledge, this has never been reported before.

4.2.2 Thermo physical properties

Thermal properties of the $CaSO_4{\cdot}H_2O$ systems

To study the thermal behavior such as the heat transfer of a material during fire, obviously the understanding of its thermo physical properties is of vital importance. However, available literature (Andersson and Jansson, 1987; Mehaffey et al., 1994;

Sultan, 1996; Thomas, 2002; Ang and Wang, 2004; Manzello et al., 2007; Ghazi Wakili et al., 2007; Ghazi Wakili and Hugi, 2008) demonstrates a wide variation among the thermal properties such as enthalpy, thermal conductivity, and specific heat capacity. Hence, experiments are performed in the present study to study the thermo physical properties of the gypsum boards.

Specific heat capacity is the measure of the heat energy required to increase the temperature of a unit quantity of a substance by a certain temperature interval, while the thermal conductivity is the property of a material that indicates its ability to conduct heat. The specific heat capacity of calcium sulfate dihydrate is investigated on the format of board because to date most of the effort is only put on the powder (Mehaffey et al., 1994; Andersson and Jansson, 1987; Thomas, 2002; Sultan, 1996; Ang and Wang, 2004; Manzello et al., 2007; Ghazi Wakili et al., 2007; Ghazi Wakili and Hugi, 2008). A commercial heat transfer analyzer (ISOMET 2104, Applied Precision) is used to measure the volumetric heat capacity of the prepared gypsum board. It applies a dynamic measurement method to determine simultaneously the volumetric heat capacity (J $m^{-3}K^{-1}$) and the thermal conductivity (W $(m\ K)^{-1}$) of a material with a measurement time of about 8-16 minutes. The measurement is based on the analysis of the temperature response of the tested sample to heat flow impulses, while the heat flow is excited by electrical heating of a resistor heater inserted into the probe which is in direct contact with the test sample. The equipment has a wide measurement range of 0.04-6.0 W $(m\ K)^{-1}$ depending on the selected probes, and it is possible to measure solid materials from soft foams to hard rocks, liquids, suspensions, etc. This heat transfer analyzer could not be operated above 40 °C, so the following procedure is used to measure the volumetric heat capacity of the gypsum board at a high temperature. Firstly, the samples, here the gypsum boards, are heated to the desired temperature for dehydration reaction (here, a sufficient time is used to ensure a full dehydration reaction), then the samples are cooled down to room temperature, and finally, the volumetric heat capacity is measured.

The dehydration reaction is an endothermic reaction, i.e. a certain amount of heat is needed. The difference between the values reported in literature (Andersson and Jansson, 1987; Mehaffey et al., 1994; Sultan, 1996; Thomas, 2002; Ang and Wang, 2004; Manzello et al., 2007; Ghazi Wakili et al., 2007; Ghazi Wakili and Hugi, 2008) indicates the effect of the composition and the microstructure of the investigated gypsum. Ghazi Wakili et al. (2007) also investigated the influence of the heating rate of the employed DSC and they reported that only at a low heating rate (5 °C min^{-1}) the peaks of the two dehydration steps (Equations. (4.2.1) and (4.2.2)) are clearly distinguishable. In the present study the energy needed for the dehydration reaction of the used gypsum is measured employing DSC (STA 449 F1 Jupiter®), and the influence of the heating rate is also studied by using two different heating rates of 5 °C min^{-1} and 20 °C min^{-1}, respectively.

The thermal conductivity of a material is related to its density and composition, which was for instance investigated by De Korte and Brouwers (2010). However, it is shown that most of the available literature only studied one or two types of commercially available gypsum plasterboards without providing detailed composition information (Mehaffey et al., 1994; Andersson and Jansson, 1987; Thomas, 2002; Sultan, 1996; Ang and Wang, 2004; Manzello et al., 2007; Ghazi Wakili et al., 2007; Ghazi Wakili and Hugi, 2008). The effect of water content on thermal conductivity of gypsum board, represented by different densities, has not been reported before. The thermal conductivity of the gypsum board is analyzed here employing the heat transfer analyzer (ISOMET 2104). The water content and the effect of dehydration are investigated as well.

Thermo physical property analysis

Figure 4.3 shows the heat flow results of the gypsum powder measured with DSC. The energy needed for the dehydration reaction is calculated by the DSC system, yielding 500 kJ kg^{-1} under the heating rate of 20 °C min^{-1} and 515 kJ kg^{-1} under the heating rate of 5 °C min^{-1}, respectively. These values are in line with Mehaffey et al. (1994) and Ghazi Wakili et al. (2007), who reported a value of 500 kJ kg^{-1} and 450 kJ kg^{-1}, respectively. However, this is questionable, since the investigated gypsum in the present study has a quite different purity (~96.9%, calculated from the results presented in Table 2.4 (Chapter 2)) (69.5% and 81% in Mehaffey et al. (1994) and Ghazi Wakili et al. (2007), respectively), whereas according to Mehaffey et al. (1994) the energy is only calculated based on the composition. This finding indicates that the energy needed for the dehydration is related not only to the composition, i.e. purity of the gypsum, but also strongly to the microstructure.

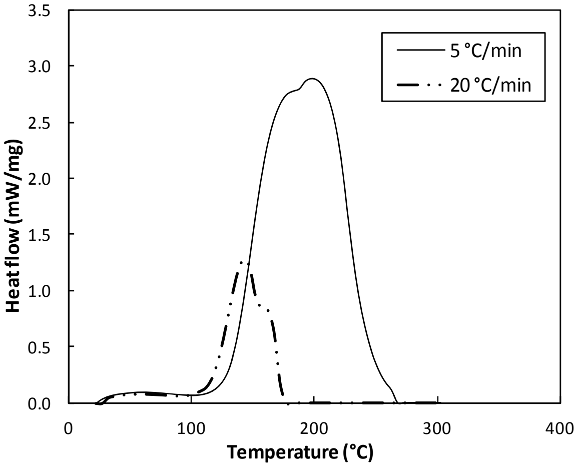

Figure 4.3: Measured DSC result of the calcium sulfate dihydrate powder.

The present study also investigates the influence of the heating rate on the dehydration reaction, as shown in Figure 4.3. The energies needed for the dehydration reaction with different heating rates are in line with each other. This means that the heat needed for the dehydration is independent from the employed heating rate. However, it is different from Ghazi Wakili et al. (2007) who reported that two clearly distinguishable peaks are found when applying a lower heating rate of 5 °C min^{-1}, with the first peak at about 145 °C and the second peak at about 200 °C. In the present study, there is only one clear peak under both heating rates, as shown in Figure 4.3. The difference is that the peak values are different under different heating rates, which is in line with those of Mehaffey et al. (1994).

The measured volumetric heat capacity of the gypsum board prepared with different water contents is listed in Table 4.1. It is clear that the calculated specific heats based on mass of different samples are in line with each other, which also confirms the validity of the volumetric specific capacity measurement. The calculated specific heat of gypsum here (1355 J (kg K)$^{-1}$ in average) is higher than that of Mehaffey et al. (1994), who reported a value of 950 J (kg K)$^{-1}$ under room temperature. This might be caused by the difference of the composition and the microstructure between the two applied materials.

Table 4.1: Measured thermo physical properties of gypsum boards (density, volumetric heat capacity and thermal conductivity).

Mix (w_0/h_0)	Density (g cm^{-3})		Volumetric heat capacity (J (m^3 K)$^{-1}$)		Thermal conductivity (W (m K)$^{-1}$)	
Conditions	**Room temperature**	**After dehydration**	**Room temperature**	**After dehydration**	**Room temperature**	**After dehydration**
0.65	1.112	0.895	1.54×10^6	0.72×10^6	0.359	0.159
0.70	1.084	0.872	1.50×10^6	0.68×10^6	0.346	0.138
0.85	0.956	0.768	1.20×10^6	0.59×10^6	0.276	0.111
1.00	0.845	0.678	0.96×10^6	0.54×10^6	0.238	0.106

The volumetric specific heat capacity of the gypsum boards decreases after the dehydration reaction, as shown in Table 4.1. The specific heat capacity based on the mass of the dehydrated system is calculated, yielding 787 J (kg K)$^{-1}$ in average. The lower value of the heat capacity of the dehydrated system compared to the gypsum board also indicates a reduction of the bonding between the anhydrite crystals, which will be confirmed also by the microstructure analysis in the next section.

Modeling of the thermal conductivity

The measured thermal conductivities of the investigated gypsum board prepared with different water contents are listed in Table 4.1. It can be seen that the thermal conductivity is strongly related to the density or to the porosity of the gypsum board. The thermal conductivity increases with an increase of the density. Zehner and Schlunder (1970) proposed an expression to describe the relation between the thermal conductivity and the porosity with the consideration of the particle shape as:

$$\lambda_e = \lambda_{fluid}(1-\sqrt{1-\varphi_v}) + \lambda_{fluid}\sqrt{1-\varphi_v}\cdot A \tag{4.2.4}$$

where

$$\begin{aligned} A &= \frac{2}{N}\left(\frac{B}{N^2}\frac{k-1}{k}\ln\left(\frac{k}{B}\right) - \frac{B+1}{2} - \frac{B-1}{N}\right), N = 1-\frac{B}{k}; \\ B &= C\left(\frac{1-\varphi_v}{\varphi_v}\right)^{10/9}, k = \frac{\lambda_{solid}}{\lambda_{fluid}} \end{aligned} \tag{4.2.5}$$

where λ_e is the effective thermal conductivity (W (m K)$^{-1}$), λ_{solid} and λ_{fluid} are the thermal conductivities of solid and fluid (here the fluid can be either water or air), φ is the volume fraction, parameter C is the shape factor (Zehner and Schlunder, 1970), and subscripts v, *solid* and *fluid* are void, solid and fluid, respectively.

Table 4.2: Physical properties and computed initial w_0/h_0 of gypsum boards from Refs. (Mehaffey et al. (1994); Sultan, 1996; Ghazi Wakili et al., 2007; Ghazi Wakili and Hugi, 2008) (Density and thermal conductivity before and after dehydration).

Density ($g\ cm^{-3}$)		**Initial w_0/h_0**	**Thermal conductivity ($W\ (m\ K)^{-1}$)**		**References**
Room temperature	**After dehydration**		**Room temperature**	**After dehydration**	
0.810	0.673	1.08	0.280	0.140	Ghazi Wakili, et al., 2007
0.732	0.600	1.24	0.250	0.113	Mehaffey et al., 1994
0.698	0.576	1.32	0.250	0.120	Sultan, 1996
0.835	0.726	1.04	0.300	0.140	Ghazi Wakili and Hugi, 2008
0.740	0.622	1.22	0.230	0.100	Ghazi Wakili and Hugi, 2008
0.870	0.692	0.98	0.320	0.090	Ghazi Wakili and Hugi, 2008

In this model, the system is considered as a combination of two phases, but normally, gypsum boards absorb a little amount of free water from the ambient conditions during the storage/exposure. Somerton et al. (1974) proposed an expression for a porous medium filled by a mixture of two fluids (i.e. air and free moisture) as follows:

$$\lambda_e = \lambda_{e,air} + \sqrt{s} \cdot (\lambda_{e,w} - \lambda_{e,air}) \tag{4.2.6}$$

where $\lambda_{e,air}$ and $\lambda_{e,w}$ are the thermal conductivities of a material when the fluid is air or water, respectively, s is the water saturation in a material in volume proportion. Here $\lambda_{e,air}$ and $\lambda_{e,w}$ are computed from Equations (4.2.4) and (4.2.5), using the thermal conductivity of air and water, respectively.

Table 4.3: Thermo physical properties of nonporous dihydrate and nonporous anhydrite.

Material	**Conditions**	**Thermal conductivity ($W\ (m\ K)^{-1}$)**	**Particle shape factor (C)**	
			Computed	**Reference***
Anhydrite	Pure	0.90	1.30	1.40
Dihydrate	Pure	1.55	2.75	2.50

***Zehner and Schlunder (1970).**

In the present thesis, the effect of the void fraction on the thermal conductivity and the effect of the particle shape are investigated considering that the system is composed of three phases, i.e. solids, water and air. This is processed by combining the two models from Zehner and Schlunder (1970) and Somerton et al. (1974). In ambient conditions, a water saturation of 3% (i.e. s in Equation (4.2.6)), is used here, since it is found that in average (with different void fractions) a water content of 1.5% by mass of the gypsum board is absorbed during the cooling/exposure time. Incorporating Equations (4.2.4) and (4.2.5) into Equation (4.2.6), the parameters (λ_{solid} and C) are obtained by optimization employing the "Solver" tool from Microsoft Excel and the experimental data (Table 4.1 and Table 4.2), yielding 1.55 W $(m\ K)^{-1}$ (λ_{solid}) and 2.75 (C) for pure gypsum, respectively. The results are listed in Table 4.3. The derived thermal conductivity for pure dihydrate is in line with that of Horai and Simmons (1969) who presented a value of 1.26 W $(m\ K)^{-1}$. The obtained value for the shape factor of dihydrate is in line with that of Zehner and Schlunder (1970) who reported a shape factor value of 2.50 for cylinders and tubes. This is also confirmed by the SEM analysis as shown in Figure 4.8a and Figure 4.8c, where it can be seen that the dihydrate crystals are mainly composed of cylinders.

The thermal conductivity calculated from the model by substituting the optimized parameters (C and λ_{solid}) and the experimental data (Tables 4.1 and 4.2) is shown in Figure 4.4a versus the void fraction of the gypsum boards. The good agreement between the model predictions and experimental data indicates the validity of the model. One point that needs to be mentioned here is that the composition of the gypsum boards (Mehaffey et al., 1994; Sultan, 1996; Ghazi Wakili et al., 2007; Ghazi Wakili and Hugi, 2008) varies, which is also the reason, in addition to the measurement difference, that the thermal conductivity varies somewhat. However, in this model, due to the limited information from literature (Mehaffey et al., 1994; Sultan, 1996; Ghazi Wakili et al., 2007; Ghazi Wakili and Hugi, 2008), the influence of the composition is not considered.

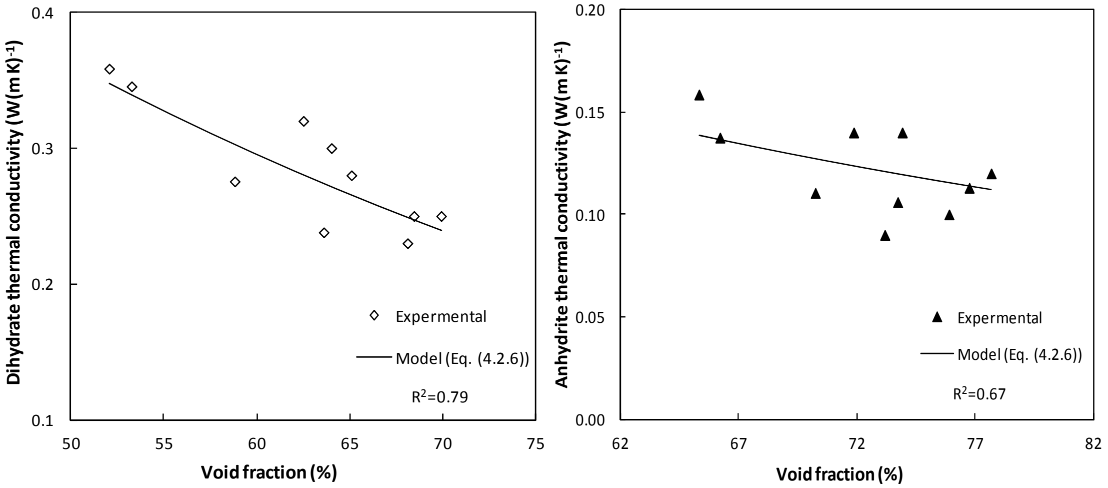

(a) (b)

Figure 4.4: Thermal conductivity of $CaSO_4 \cdot H_2O$ systems (a: $CaSO_4 \cdot 2H_2O$; b: $CaSO_4 \cdot H_2O$), (model predictions versus experimental data (from own tests and Refs. (Mehaffey et al., 1994; Sultan, 1996; Ghazi Wakili et al., 2007; Ghazi Wakili and Hugi, 2008))).

As introduced in the previous section, the heat transfer analyzer employed here can only be operated below 40 °C; therefore, the thermal conductivity measured in the present study at elevated temperatures only represents the microstructure change because of the dehydration reaction of the calcium sulfate dihydrate. The measured thermal conductivity of the gypsum board upon dehydration and the experimental data from literature are listed in Tables 4.1 and 4.2, respectively. As introduced before, here in the dehydrated system, only calcium sulfate anhydrite is available, and the void fraction is also changed, which explains the variation of the measured thermal conductivity. As one can see from Table 4.2, in the case of the same void fraction, the thermal conductivities of calcium sulfate dihydrate and dehydrated system (calcium sulfate anhydrite) are very different, which also indicates the effect of the particle shape in the matrix on the thermal conductivity in addition to the difference between the materials.

The parameters (λ_{solid}, C, and s) in Equations (4.2.4) and (4.2.5) for the dehydrated system are obtained again by optimization employing the “Solver” tool from Microsoft Excel and the experimental data (Tables 4.1 and 4.2), yielding 0.9 W $(m\ K)^{-1}$ (λ_{solid}), 1.3 (C) and 1% (s), respectively, for calcium sulfate anhydrite, as listed in Table 4.3. The obtained value for the shape factor of anhydrite is in line with that of Zehner and Schlunder (1970) who reported a shape factor value of 1.40 for broken particles. This is also confirmed by the SEM analysis as shown in Figures 4.8b and 4.8d. In the present study, the gypsum boards are first always heated up until a full dehydration occurs and then cooled down at ambient conditions until room temperature. A very small amount of moisture is absorbed into the gypsum boards again, which is confirmed by the small derived value of water saturation here. The derived thermal conductivity here can be understood as the thermal conductivity of pure/nonporous anhydrite. However, further research is still necessary to prove this because it has still not been confirmed in literature. Finally, the thermal conductivity calculated from the model by substituting the optimized parameters (C, λ_{solid}, and s) and the experimental data (Tables 4.1 and 4.2) is shown in Figure 4.4b as a function of the void fraction. The fair agreement between the model predictions and experimental data confirms the validity of the followed approach.

4.3 Microstructure

4.3.1 Ambient conditions

The microstructure of the hydrating system is varying during the hydration period, as analyzed in the previous sections. The microstructure governs the final properties of the system such as the mechanical and thermal properties. Therefore, in this section the microstructure of the hydrating system is addressed.

The microstructure is studied from a point of view of the void fraction of the hydrating system. A model is applied here and validated by the performed experiments. Scanning electron microscopy is also used to study the matrix of the hydrating system and the effect of the initial water content on the microstructure.

Modeling and validation

Figure 4.5 shows the schematic volume composition of the hydrating system. Before the hydration, the total volume is composed of only water (V_w) and calcium sulfate β-hemihydrate (V_{hh}) as shown in Figure 4.5a. During the hydration reaction, as shown in Equation (3.3.3), part of the water and the β-hemihydrate are consumed as reactants and the dihydrate is produced, so the total volume is composed of the chemical shrinkage due to the hydration reaction, the water that remains beyond the hydration reaction, the generated dihydrate, and the remaining β-hemihydrate, as shown in Figure 4.5b.

The void fraction of the hydrating system here is defined as the fraction of the void space in the hydrating system, where the void may contain air or water. Therefore, the void fraction of the system upon hydration is described as the sum of the volume caused by the reaction shrinkage and the remaining water as shown in Figure 4.5c.

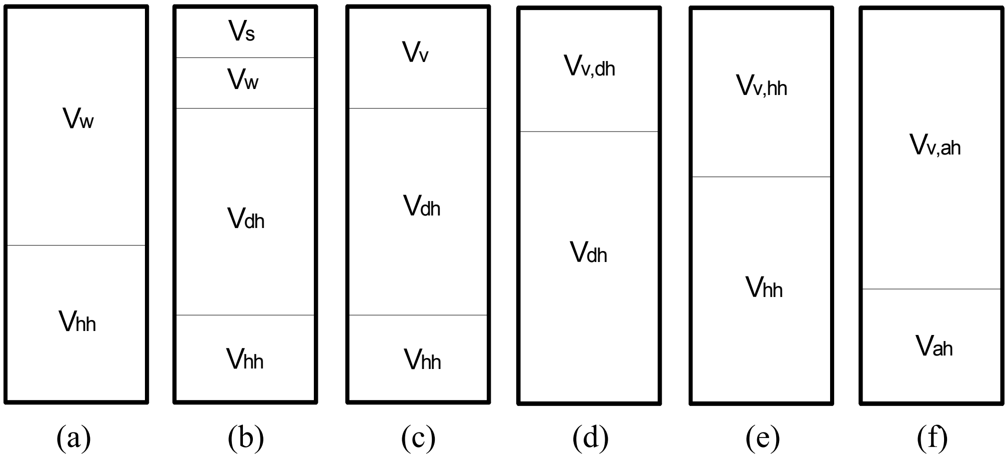

Figure 4.5: Schematic diagram of the volume composition of the $CaSO_4 \cdot H_2O$ system (a: before hydration; b: during hydration; c: during hydration; d: after full hydration, before dehydration (dihydrate); e: upon first dehydration step (hemihydrate); f: upon second dehydration step (anhydrite)).

The chemical shrinkage of the hydrating system is computed from the difference between the reactant water and the chemically bound water, following Equation (3.3.3). In this study, a model proposed by Brouwers (2011) is applied to describe the volume fraction of the chemical shrinkage as:

$$\varphi_s = \frac{n\left(1 - \frac{v_n}{v_w}\right)\frac{w_n}{h}}{\frac{v_{hh}}{v_w} + \frac{w_0}{h_0}} \tag{4.3.1}$$

where φ is volume fraction, n is hydration degree, υ is specific volume ($cm^3\ g^{-1}$), w is water content (g), h is the mass of reacted hemihydrate (g), w_0/h_0 is initial water/hemihydrate ratio by mass, subscripts s is shrinkage, n is non-evaporable water, hh is hemihydrate and w is water. The values of v_n/v_w, w_n/h, v_{hh}/v_w for $CaSO_4$ systems are listed in Table 4.4.

Table 4.4: Parameters of the applied paste model (Yu and Brouwers, 2011a).

substance	M $g\ mol^{-1}$	ρ $g\ cm^{-3}$	ω $cm^3\ mol^{-1}$	υ_{hh}/υ_w	w_n/h	υ_n/υ_w	$\upsilon_n w_n/\upsilon_w h$	υ_s/υ_{hh}
anhydrite	136.14	2.58	52.77	0.39	0.265	0.60	0.16	0.106
β-hemihydrate	145.15	2.62	55.40	0.38	0.186	0.71	0.13	0.054

Here the void fraction of the chemical shrinkage is defined as the proportion of the reaction shrinkage to the total volume which is constant during the whole reaction process, which is in line with Schiller (1957) who also studied the void fraction of gypsum based on the same assumption. The specific volume ($cm^3\ g^{-1}$) of the chemically bound water (υ_n) used here is computed from the difference of the specific volume between the generated calcium sulfate dihydrate and the β-hemihydrate.

As discussed in Chapter 3, due to the requirement of a sufficient fluidity, an extra amount of water is needed. During the hydration, this water works as transport liquid, and then it is evacuated during the curing period, which in turn leads to an open space in the generated matrix. The void fraction caused by this unhydrated water is described by:

$$\varphi_w = \frac{\frac{w_0}{h_0} - n(\frac{w_n}{h})}{\frac{\nu_{hh}}{\nu_w} + \frac{w_0}{h_0}} \tag{4.3.2}$$

Therefore, the total void fraction of the system during the hydration reads:

$$\varphi_v = \varphi_w + \varphi_s = \frac{\frac{w_0}{h_0} - n\frac{\nu_n}{\nu_w}\frac{w_n}{h}}{\frac{\nu_h}{\nu_w} + \frac{w_0}{h_0}} \tag{4.3.3}$$

where subscript *v* is void and *s* is shrinkage. Substituting the values of the β-hemihydrate for the υ_n/υ_w, w_n/h, υ_{hh}/υ_w from Table 4.4, the following expression is obtained:

$$\varphi_v = \varphi_w + \varphi_s = \frac{\frac{w_0}{h_0} - 0.13n}{0.38 + \frac{w_0}{h_0}} \tag{4.3.4}$$

It is evident from Equation (4.3.4) that the void fraction is related to the water content and to the hydration degree of the hydrating system. Unlike cement, β-hemihydrate hydration occurs very quickly, for instance in the present study with the w_0/h_0 of 0.65 the full hydration ends within 10 minutes (see Figure 3.7). Therefore, the investigation of the influence of water on the void fraction here is mainly focused on the case that the hydration degree (n) is unity, i.e. the system undergoes full hydration, yielding

$$\varphi_v = \frac{\frac{w_0}{h_0} - 0.13}{0.38 + \frac{w_0}{h_0}} \tag{4.3.5}$$

Schiller (1957) proposed a void faction model for gypsum, which is in accordance with the model applied here, valid for the case of full hydration (n=1) and α-hemihydrate only. The applied model is verified by experiments in the case of β-hemihydrate and full hydration. The measured void fraction of the calcium sulfate dihydrate is plotted versus w_0/h_0, together with the computed values from the applied model (Equation (4.3.5)) shown in Figure 4.6a. The good agreement between predicted value from the model and experimental data reveals its validity.

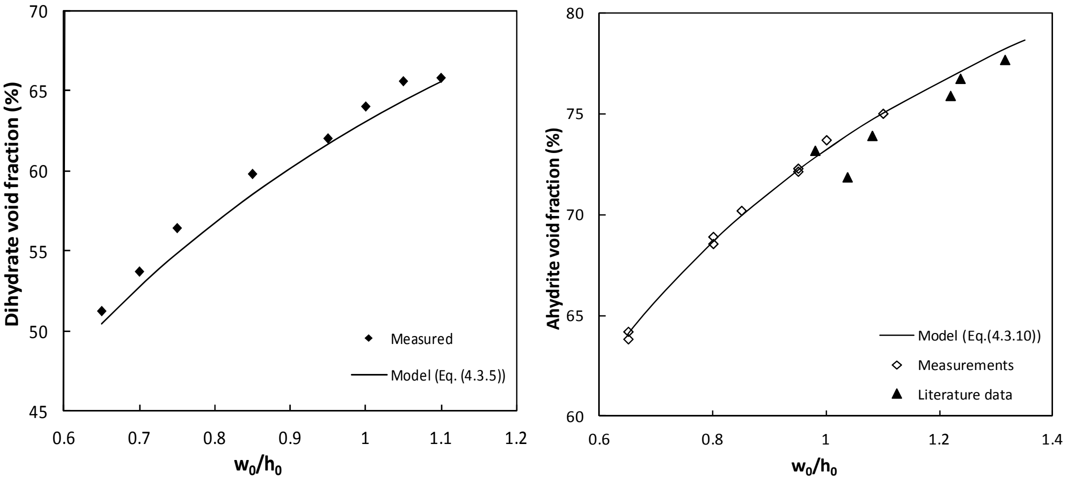

(a) (b)

Figure 4.6: Void fraction versus the water-hemihydrate ratio (w_0/h_0) (a: $CaSO_4 \cdot 2H_2O$; b: $CaSO_4$, experimental data taken from own tests and refs. (Mehaffey et al., 1994; Sultan, 1996; Ghazi Wakili et al., 2007; Ghazi Wakili and Hugi, 2008)).

Microstructure analysis

The microstructure of the hydrating system is studied experimentally applying scanning electron microscope. The hydration test of the β-hemihydrate with different initial water contents is performed at room temperature (about 19-22 °C). Due to the very short period of the hydration process, here the emphasis is put on the fully hydrated system.

The microstructure of the generated gypsum is shown in Figure 4.7. The gypsum in Figure 4.7a and Figure 4.7b is prepared with a w_0/h_0 of 0.65 and 0.80, respectively. It is clear that the crystals in Figure 4.7a are much smaller and tighter and more homogeneous compared to the crystals shown in Figure 4.7b. This shows that the gypsum produced with lower water content has a better bonding between the gypsum crystals, which should lead to better mechanical properties. The gypsum in Figure 4.7a also shows a smaller void fraction compared to the gypsum in Figure 4.7b, which is also in line with the predicted values from the model applied above.

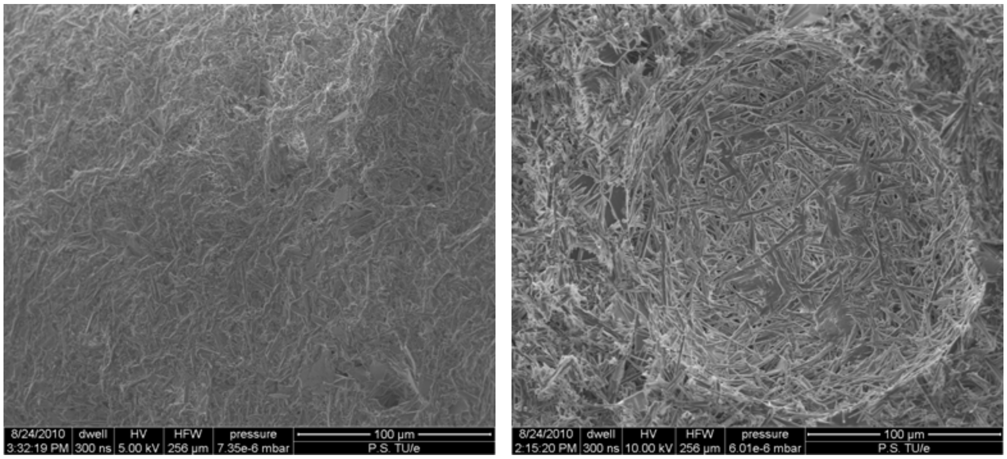

(a) (b)

Figure 4.7: SEM picture of the calcium sulfate dihydrate produced with (a: $w_0/h_0 = 0.65$; b: $w_0/h_0 = 0.80$).

4.3.2 Elevated temperatures

Figures 4.5d-4.5f schematically show the composition of the $CaSO_4·H_2O$ systems by volume at elevated temperatures. The system consists of dihydrate and voids before the dehydration, as shown in Figure 4.5d. During the dehydration process, as indicated in Equations. (4.2.1) and (4.2.2), the chemically combined water in the matrix is gradually released. The dehydrating system is composed of the void space, the dihydrate, and the regenerated hemihydrate, then the anhydrite, as shown in Figure 4.5e and Figure 4.5f. The temperature reaches 200 °C in less than 1 min under real fire test following ISO 834-1 (1999). Therefore, here the focus is only on the fully dehydrated system.

The microstructure of the dehydrating system is investigated both by modeling and by experiments. SEM analysis is performed on two gypsum board samples prepared with different initial water contents to study the crystal shape of the particles, as well as the void fraction of the system. Furthermore, the strength of the dehydrated system is also tested on gypsum prisms according to EN 13279-2 (2004) to investigate the effect of the microstructural change. The flexural strength is measured with the three-point bending test, and the compressive strength is determined by applying a load to the two broken parts of the specimen obtained from the flexural strength test.

Modeling and validation

As illustrated by Equations (4.2.1) and (4.2.2), calcium sulfate hemihydrate and then calcium sulfate anhydrite are generated from calcium sulfate dihydrate during the dehydration reaction. Therefore, the volume composition of the fully dehydrated system consists of only anhydrite and void fraction, that is, air, as shown in Figure 4.5f. During the dehydration process the molar amount of $CaSO_4$ remains constant; therefore, the following expression is obtained

$$\frac{\varphi_{ah}}{\omega_{ah}} = \frac{\varphi_{dh}}{\omega_{dh}} \tag{4.3.6}$$

where φ is the volume fraction, and ω is the specific molar volume (cm^3 mol^{-1}), subscripts *ah* and *dh* are anhydrite and dihydrate, respectively.

Under the assumption that the volume of the system remains constant during the dehydration, Equation (4.3.6) becomes

$$\varphi_{ah} = \frac{\varphi_{dh}}{\omega_{dh}} \times \omega_{ah} = (1-\varphi_{v,dh}) \times \frac{\omega_{ah}}{\omega_{dh}} \tag{4.3.7}$$

and hence,

$$\varphi_{v,ah} = 1-\varphi_{ah} = 1-(1-\varphi_{v,dh}) \times \frac{\omega_{ah}}{\omega_{dh}} \tag{4.3.8}$$

Substituting the void fraction model for dihydrate presented in the previous section (Equation (4.3.5)) in the case of full hydration, yields

$$\varphi_{v,ah} = 1-\varphi_{ah} = 1-(1-\varphi_{v,dh}) \times \frac{\omega_{ah}}{\omega_{dh}} = 1-\left[1-\frac{\frac{w_0}{h_0}-\frac{v_n}{v_w}\frac{w_n}{h}}{\frac{v_h}{v_w}+\frac{w_0}{h_0}}\right] \times \frac{\omega_{ah}}{\omega_{dh}} \tag{4.3.9}$$

Substituting the values for β-hemihydrate from Table 4.4 into Equation (4.3.9), $\varphi_{v,ah}$ is obtained as:

$$\varphi_{v,ah} = \frac{0.01+\frac{w_0}{h_0}}{0.38+\frac{w_0}{h_0}} \tag{4.3.10}$$

Equation (4.3.10) gives the relation between the void fraction of the dehydrated system and the initial water/hemihydrate (w_0/h_0) ratio of the gypsum board. In the present thesis, experiments are carried out with different w_0/h_0 to study the void fraction of the system beyond dehydration. The results are shown in Figure 4.6b. The good agreement between the proposed model (Equation (4.3.10)) and the experimental values (from Mehaffey et al., 1994; Sultan, 1996; Ghazi Wakili et al., 2007; Ghazi Wakili and Hugi, 2008; and own performed experiments) indicates the validity of this microstructural model.

Values from literature (Mehaffey et al., 1994; Sultan, 1996; Ghazi Wakili et al., 2007; Ghazi Wakili and Hugi, 2008) are calculated from the following method. Firstly, the initial water/hemihydrate ratios are assessed using the given density values and the void fraction expression for gypsum (dihydrate) (see Section 4.3.1), assuming no impurities. Then, the void fraction of the gypsum board after dehydration is calculated on the basis of the relation between the given density and the density of the pure anhydrite (Table 4.4), assuming no impurities as well. Because of the assumption of no impurities in the gypsum board, there are some errors in the calculated values, which can be observed in Figure 4.6. As can be seen, the calculated values from literature (Mehaffey et al., 1994;

Sultan, 1996; Ghazi Wakili et al., 2007; Ghazi Wakili and Hugi, 2008) are in general slightly smaller than the model predictions, but still in line with the model presented here.

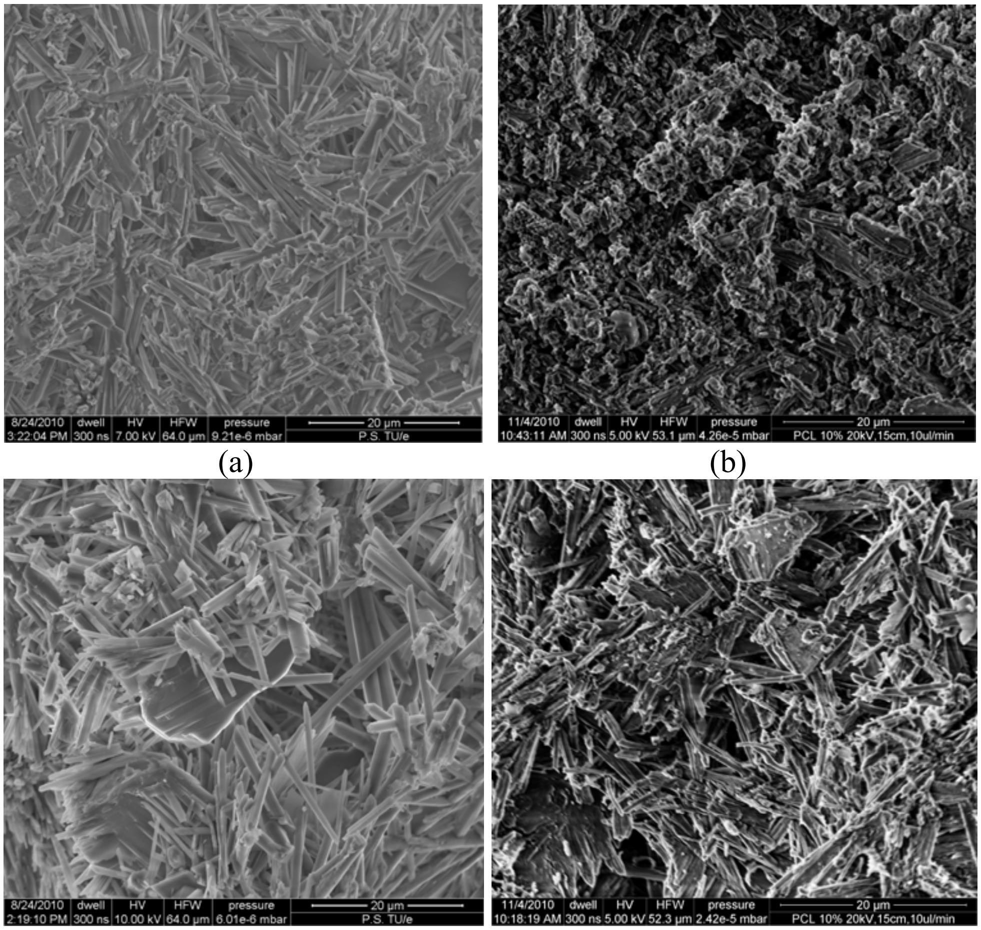

(a) (b)

(c) (d)

Figure 4.8: SEM pictures of the $CaSO_4{\cdot}H_2O$ system (a: $CaSO_4{\cdot}2H_2O$ ($w_0/h_0=0.65$); b: $CaSO_4$ ($w_0/h_0=0.65$); c: $CaSO_4{\cdot}2H_2O$ ($w_0/h_0=0.80$); d: $CaSO_4$ ($w_0/h_0=0.80$)).

Microstructure analysis

The microstructure of the dehydrated system is also investigated by SEM, and the results are shown in Figure 4.8. Figures 4.8a and 4.8c show the SEM images of the gypsum boards prepared with different initial water/hemihydrate ratio of 0.65 and 0.80, respectively. It is obvious that the calcium sulfate dihydrate crystals are regularly formed needles/cylinders, and the porosity of the calcium sulfate dihydrate with a w_0/h_0 of 0.65 in Figure 4.8a is clearly lower than that of the gypsum in Figure 4.8c.

However, after the dehydration reaction, or after the anhydrite is produced, the microstructure of the system changed considerably from regularly shaped needles or tubes to irregularly broken fine particles (Figures 4.8b and 4.8d). This change indicates a reduced bonding between the crystals. Also, it is clear from the SEM pictures that the void fraction significantly increases after dehydration.

The strength loss of the samples produced with different w_0/h_0 beyond dehydration is shown in Figure 4.9. The strength (both the compressive and flexural strength) decreases more than 75% after dehydration in both gypsum boards prepared from an initial w_0/h_0 of 0.65 and 0.80. Results show that the strength of the gypsum with an initial higher void fraction decreases more than that of gypsum with a lower void fraction. These findings indicate evidently that the matrix of the gypsum with a higher void fraction becomes weaker compared to that of the gypsum with a lower void fraction. They also indicate that the strength of the gypsum depends on the bonding between the crystals, and the water release of the gypsum has a larger influence when it has a higher void fraction.

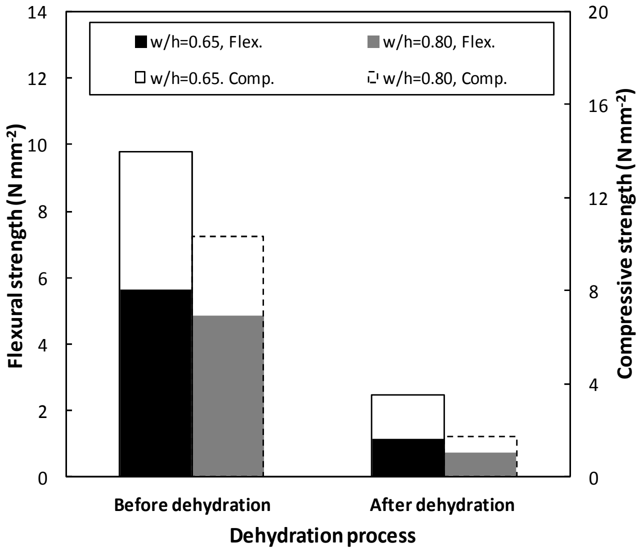

Figure 4.9: Strength of the gypsum boards versus the void fraction (before and after dehydration).

4.4 Conclusions

This chapter addresses the thermal properties and the microstructure of the $CaSO_4 \cdot H_2O$ system in different conditions. The following conclusions are formulated:

- A model is applied to describe the microstructure of the hydrated system and it is validated experimentally.
- The microstructure of the hydrated system is studied by applying scanning electron microscopy (SEM).
- Dehydration of calcium sulfate dihydrate occurs via two steps of first to hemihydrate and then to anhydrite according to TGA; however, these two steps are hardly distinguishable in the case of a high heating rate. The heating rate does not affect the starting dehydration temperature, but it influences the ending temperature. The study from both macroscale and microscale levels shows that given enough time, gypsum can finish the first step dehydration at 80 °C and full dehydration at 120 °C.
- A model is proposed to describe the void fraction of the dehydrated $CaSO_4 \cdot H_2O$ system (calcium sulfate anhydrite), and it is validated by both own experiments and values taken from literature.
- The microstructure of the $CaSO_4 \cdot H_2O$ system experiences a considerable change upon dehydration. The regularly formed gypsum crystals change to

irregularly broken particles, which consequently leads to reduced mechanical properties of the dehydrated system.

- A link between the volumetric specific heat capacity of the gypsum boards and the initial water content is found. A model is derived to describe the thermal conductivity of the gypsum boards and the void fraction, considering both particle shape and free moisture content in the system, and it is validated by experiments.
- The change of the thermal properties of gypsum boards under dehydrated conditions is not only caused by the change of the void fraction, but also considerably by the change of the particle shape in the system. A thermal conductivity value and a particle shape factor (C) are derived for both nonporous dihydrate and nonporous anhydrite. Also, the derived particle shape factor is in line with SEM observations and values presented by Zehner and Schlunder (1970).

Chapter 5

Design of $CaSO_4 \cdot H_2O$-based lightweight composite

5.1 Introduction

As can be concluded from the previous chapter, a high amount of excess water is usually needed for the β-hemihydrate hydration to produce gypsum plasterboards, while stoichiometrically for a full hemihydrate hydration only an initial water amount of 0.186 by mass of hemihydrate (w_0/h_0) is needed. The removal of the excess water during the curing period leads to some conflicting consequences to the generated gypsum, such as a great consumption of heat, which is not desired and a high porosity which contributes to a good indoor thermal insulation property (Yu and Brouwers, 2011a). As will be demonstrated in this chapter as well as in the following chapter, a high porosity is strongly related to a low density and poor mechanical properties such as low strength, and good thermo physical properties such as low thermal conductivity. The resulted low thermal conductivity contributes to a slow heat transfer between the indoor and the outdoor environment, which leads to a better indoor thermal comfort, as well as a good fire resistance. However, a low strength causes not only a limitation of the application of gypsum boards but also very swift strength degradation during a fire, which then even leads to a quick failure of the structure it covers.

Numerous efforts have already been made to address this challenge. Fibers such as glass fiber (Evans et al., 1981; Sing and Garg, 1992), carbon fiber (Tagge, 2005), polypropylene fiber (Deng and Furuno, 2001; Eve et al., 2004), polyamide fiber (Eve et al., 2007), and polyester fiber (Dweck et al., 2002) are applied extensively to improve the properties of gypsum boards. These reinforcements contribute somewhat to the improvement of the gypsum plasterboard in terms of mechanical or thermal properties, but they also have certain drawbacks. Evans et al. (1981) designed a lightweight glass fibers reinforced gypsum panel with a density of about 600-800 kg m^{-3}; however, the compressive strength of this developed panel is very low, only about 0.35 N mm^{-2}, which definitely limits its application. Singh and Garg (1992) reported that glass fibers could not contribute to the strength improvement if shorter than 12 mm. However, for gypsum plasterboards, the normal thickness is about 12 mm, which indicates that applying longer fibers will cause mixing problems. Eve et al. (2004, 2007) reported a reduction of both Young's modulus and strength of the gypsum composite when increasing the content of polyamide fibers and polypropylene fibers. Colak (2001) investigated the methylmethacrylate polymer reinforced gypsum composites and reported that no strength improvement is achieved when the polymer content is lower than 10% by mass. Deng and Furuno (2001) reported that, with a length of 12 mm and a content of 12% by mass, polypropylene fiber reinforced gypsum particleboards (gypsum as binder, and wood particles as the strengthening material) can achieve an optimal performance (physical and mechanical properties), but such a high amount of fiber reinforcement would cause a considerable cost increase and also mixing difficulties. Hernandez-Olivares et al. (1992)

reported that short sisal fibers could not contribute to the fire resistance of the reinforced gypsum board.

The present chapter aims at the development of an environmentally friendly $CaSO_4{\cdot}H_2O$-based lightweight composite with a good fire resistance, sufficient strength, and indoor air quality improvement properties. To obtain a low thermal conductivity, a regenerated lightweight material is used into this new composite as lightweight aggregate. The particles of the lightweight material are rather closed hollow spheres (Chapter 2), assuring a low density and a good thermal insulation. A β-hemihydrate ($CaSO_4{\cdot}0.5H_2O$) produced from flue gas desulfurization (FGD) gypsum is used here as binder.

The mix is designed using a methodology based on the packing theory of the applied solids applying the modified Andreasen and Andersen (A&A) grading model. In this chapter, firstly, the packing theory is reviewed and a mix design algorithm based on the packing theory is introduced. Then, several mixes designed using different distribution moduli are presented and discussed and the fresh state behavior of the produced composites is investigated. After that, the porosity and density of the developed composites in hardened state is investigated by both modeling and experiments. In the following step, the mechanical properties of the developed composites are analyzed. Subsequently, the thermo physical properties of the designed mixes are studied, and finally the fire behavior of the designed composites is investigated by performing the fire test according to ISO 834-1.

5.2 Mix design methodology

5.2.1 Introduction

In this section, the design methodology of the solid ingredients in this lightweight composite using β-hemihydrate as binder is discussed. Section 5.2.2 provides an overview of the packing theory of the applied solids in the mix. As already known, the packing of the granular solid ingredients obviously affect the properties of designed composites such as concrete. Section 5.2.3 introduces a design method applying the packing theory for the development of $CaSO_4{\cdot}H_2O$-based lightweight composites. Section 5.2.4 gives a discussion about the used distribution modulus in the applied mix design model and the used lightweight aggregates.

5.2.2 Grading theory

It is already well accepted that the performance of composite materials such as concrete is strongly linked to their porosity, i.e. the void fraction, which is related to the sizes and the composition of all the applied solid ingredients in the mix (Brouwers, 2011). It was already reported that the maximum strength is attained when the porosity of a granular structure is minimal more than one century ago (Feret, 1892). A minimal porosity can be theoretically achieved by an optimal particle size distribution (PSD) of all the applied solid materials in the mix, which has been addressed by researchers such as Fuller and Thompson (1907) and Andreasen and Andersen (1930), and given by

$$P(D) = \left(\frac{D}{D_{\max}}\right)^{q} \tag{5.2.1}$$

where *P(D)* is a fraction of the total solids being smaller than size D, *D* is the particle size (μm), D_{max} is the maximum particle size (μm), and *q* is the distribution modulus.

Equation (5.2.1) is known as the Fuller curve in the case of a q of 0.5, while according to Andreasen and Andersen (1930) the distribution modulus should be in the range of 1/3 to 1/2 for the densest packing. However, in this expression, the minimum particle size is not incorporated, while in reality there must be a finite lower size limit, which is considered by Funk and Dinger (1994). They proposed a modified model based on the Andreasen and Andersen Equation, which is usually called the modified Andreasen and Andersen model, reading

$$P(D) = \frac{D^q - D_{\min}^q}{D_{\max}^q - D_{\min}^q} \tag{5.2.2}$$

where D_{min} is the minimum particle size (μm).

Funk and Dinger (1994) reported a value of 0.37 for q in Equation (5.2.2) for an optimal packing of continuous particle distribution, which is confirmed by Villar et al. (2000). Brouwers (2006) further demonstrated that theoretically a q value range of 0-0.28 would result in an optimal packing.

5.2.3 Mix design methodology

As discussed above, applying the PSD theory, the particles can be better packed, which results in improved hardened state properties as well as an improved workability, since more water is available to act as lubricant between the particles (Brouwers and Radix, 2005). In this mix design method, the modified Andreasen and Andersen model acts as a target function for the optimization of the composition of individual granular materials. The proportions of the individual materials in the mix are adjusted until an optimum fit between the composed mix and the target curve is reached, using an optimization algorithm based on the Least Squares Method (LSM), i.e. the deviation between the target curve and the composed mix expressed by the sum of the squares of the residuals (RSS) at defined particle sizes (Hüsken, 2010) is minimized:

$$RSS = \sum_{i=1}^{n} \left(P_{mix}\left(D_i^{i+1}\right) - P_{tar}\left(D_i^{i+1}\right) \right)^2 \tag{5.2.3}$$

where P_{mix} is the composed mixture, and $P_{tar}\left(D_i^{i+1}\right)$ is the target grading, calculated from Equation (5.2.2). Figure 5.1 shows an example of the mix design methodology.

The quality of the curve fit can be evaluated by the coefficient of determination (R^2), reading

$$R^2 = 1 - \frac{\sum_{i=1}^{n} \left(P_{mix}\left(d_i^{i+1}\right) - P_{tar}\left(d_i^{i+1}\right) \right)^2}{\sum_{i=1}^{n} \left(P_{mix}\left(d_i^{i+1}\right) - \overline{P_{mix}} \right)^2} \tag{5.2.4}$$

where $\overline{P_{mix}} = \frac{1}{n}\sum_{i=1}^{n} P_{mix}(D_i^{i+1})$ is the arithmetic mean of the entire distribution.

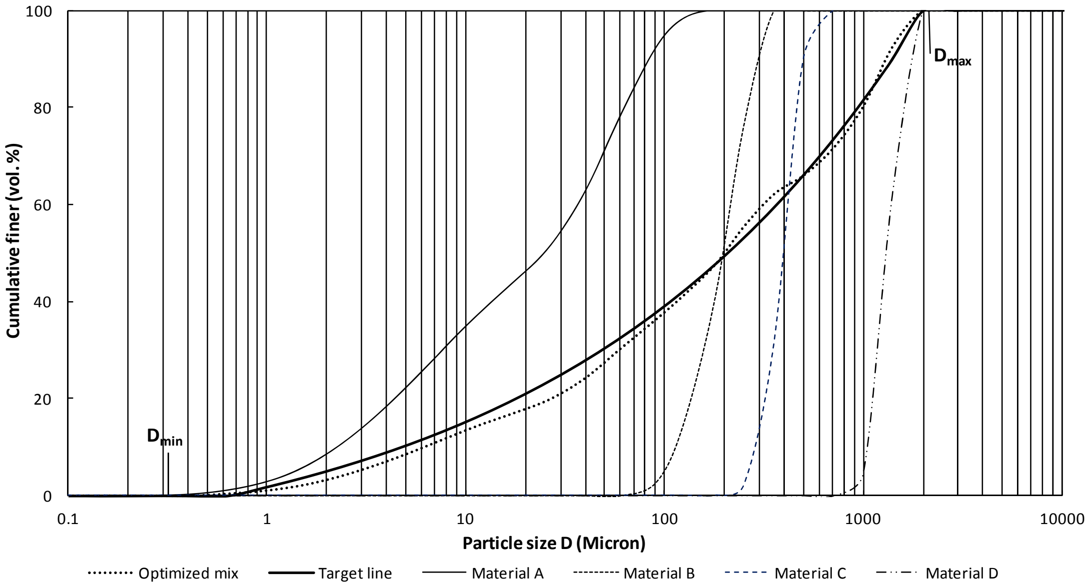

Figure 5.1: PSDs of the involved ingredients, the target line and the resulting integral grading line of the mix.

The variables in Equation (5.2.3) are the respective proportions of the solid materials, reading

$$\varphi_{solid,k} = \frac{V_{solid,k}}{\sum_{k=1}^{m} V_{solid,k}} \tag{5.2.5}$$

where $\varphi_{solid,k}$ is the individual volumetric proportion and $V_{solid,\ k}$ is the volume of each solid material in the total type of m (m^3), respectively.

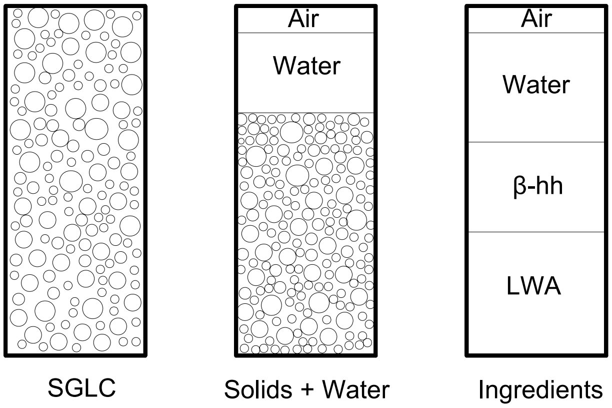

Figure 5.2: Schematic diagram of the volume composition of the SGLC.

The boundary conditions to the variables can be explained as follows: the proportion of each solid material as shown in Equation (5.2.5) should not be negative, while the total volume of the designed composite is the sum of all the solid materials, the used water and the assumed air content, as shown in Figure 5.2 (here SGLC denotes self-compacting gypsum-based lightweight composite). The water content is related to the powder amount. With all the known constraints, the equation can be solved by employing the Solver tool in Microsoft Excel$^{@}$ or other similar tools.

5.2.4 Discussion

This optimization algorithm was initially developed for concrete design and was successfully used to design concrete of different types such as self-compacting concrete (Hunger, 2010) and earth-moist concrete (Hüsken and Brouwers, 2008; Hüsken, 2010). Calcium sulfate hemihydrate (in β-type), instead of cement, is used here as binder for the development of the lightweight composite, but the design methodology is the same as the concrete design, applying the packing theory using this optimization algorithm.

The distribution modulus *q* affects the amount of the coarse and fine particles in the mix. Hüsken and Brouwers (2008) reported that the paste content increases from around 150 L m^{-3} to 350 L m^{-3} when the distribution modulus decreases from 0.50 to 0.35, applying the modified Anderasen and Andersen model, while the paste content is calculated based on the constant water to powder ratio of 0.35 with a maximum and minimum particle size of 16 mm and 0.01 μm, respectively. Here the A&A model and the modified A&A model are also compared using different distribution moduli, as shown in Figure 5.3. It shows clearly that the computed cumulative curve shifts to the left when the distribution modulus becomes smaller. Also it indicates that the correction effect of the modified Andreasen and Andersen model turns negligible when the applied minimum particle size is very small, for instance 0.01 μm in Figure 5.3, as indicated by the almost identical curves resulted from the modified A&A model and the A&A model when both models use the same q (e.g. 0.5 and 0.37).

Hunger (2010) recommended an optimal range of $0.21 < q < 0.25$ for self-compacting concrete (SCC) mix design, considering the workability effect. One objective of the new composite development here is the self-compacting property, i.e. the generated composite can flow freely under its own weight into any shape such as wall board or ceiling. Hence, the distribution modulus here will be also considered using a small value, following the self-compacting concrete mix design as a reference.

As analyzed above, an optimal packing density can be obtained by applying this mix design concept. Density, however, is strongly related with thermo physical properties such as the thermal conductivity of gypsum plasterboard (Yu and Brouwers, 2011b). Ryan (1962) also reported that the thermal conductivity is proportional to the density of gypsum based composites such as gypsum-vermiculite, gypsum-perlite, and gypsum-sand composites. Hence, the new composite developed applying this design concept will have an opposite effect, i.e. a resulted high thermal conductivity as the void content is minimized. However, a low thermal conductivity is another desired objective in the development of this new composite. This chapter tries to tackle this problem by applying a lightweight material as aggregate (LWA). The used LWA, made from recycled glass, are in form of closed hollow spheres, which allow a good thermal insulation property while keeping a low density. The used LWA here have size ranges of 0.1 - 0.3 mm, 0.25 - 0.5 mm, 0.5 - 1.0 mm, and 1.0 - 2.0 mm, and named LWA 0.1-0.3, LWA 0.25-0.5, LWA 0.5-1.0, LWA 1.0-2.0, respectively.

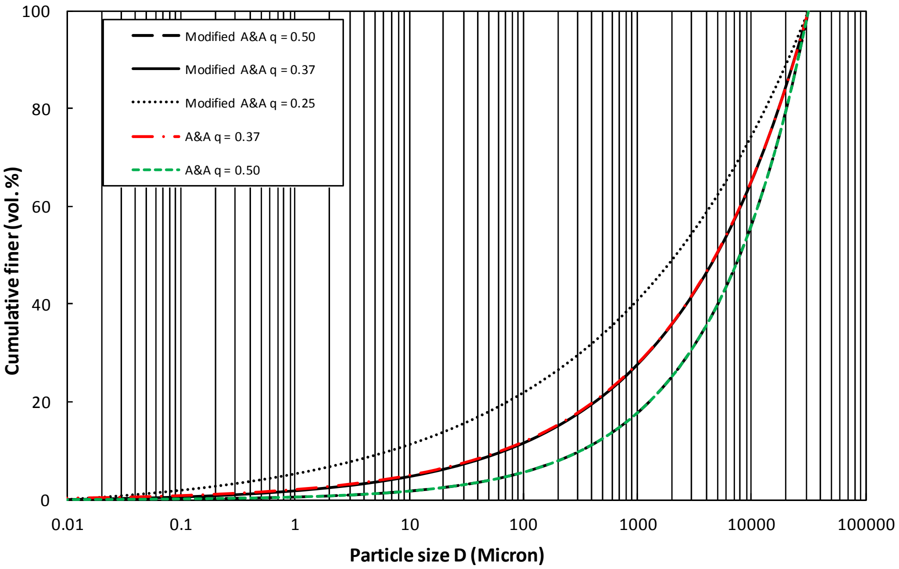

Figure 5.3: Influence of the distribution modulus on the target value (D_{min} = 0.01µm, D_{max} = 32mm).

Therefore, by using β-hemihydrate as binder, lightweight material as aggregates and applying the mix design concept, the obtained self-compacting gypsum-based lightweight composite (SGLC) will have a compact structure/matrix but large unconnected pores, which theoretically will lead to sufficient mechanical properties as well as good thermal insulation properties.

5.3 Mix design

5.3.1 Introduction

As shown in Figure 5.2, the volume-based composition of the developed SGLC is composed of binder (β-hemihydrate), aggregates (LWA), water (including additives such as superplasticizer) and air. Obviously the performance of the composite is related to all the ingredients. The proportions of all the solid materials are determined by the modified A&A model, whereas the distribution modulus has a significant effect. To ensure the mixed system is fluid, a thin layer of adsorbed water molecules around the particles and an extra amount of water to fill the intergranular voids of the system are necessary (Brouwers and Radix, 2005; Hunger and Brouwers, 2009; Fennis, 2011), as investigated in Chapter 3. The water content is strongly linked to both the flowability of the mixture in its fresh state (Yu and Brouwers, 2011a; Fennis, 2011), and the strength of the mixture in its hardened state (Yu and Brouwers, 2011a). Therefore, to design a composite with improved mechanical and thermal properties, the water content, the used solid materials, the possible admixture such as the superplasticizer will be considered simultaneously.

5.3.2 Mix design procedure

Using the self-compacting concrete mix design methodology from a guideline given by EFNARC (2002; 2005) for SCC regarding specification, production and use, and Hunger (2010) as reference, a mix design procedure for SGLC is derived and shown in Table 5.1.

Table 5.1: Description of the mix design procedure.

Design procedure	Notes
Materials characterization	Particle size distribution, specific surface area, density, etc.
Particle size distribution optimization	Mix design methodology (Section 5.2.3).
Water content determination	Mini-slump flow test.
Flowability adjustment	Water content, superplasticizer.

The first step is to collect and compute all the needed input parameters, such as the particle size distribution, the specific surface area, the density of all the materials, etc. The PSD of the β-hemihydrate is measured using a Mastersizer 2000, as described in Chapter 2, and shown in Figure 5.4, with the surface weighted mean of 6.07 μm. The specific surface area is calculated from the measured PSD results based on an assumption that all the particles are spheres (Chapter 2), yielding 0.377 $m^2 g^{-1}$ (9877.4 $cm^2 cm^{-3}$). Here the PSDs of the LWA, measured by sieving tests, are shown in Figure 5.4. The chemical composition of the β-hemihydrate measured with energy-dispersive X-ray spectroscopy (EDX) is listed in Table 2.4 (Chapter 2), and the chemical and physical properties of the LWA taken from the data sheet from the provider are listed in Table 2.7, respectively.

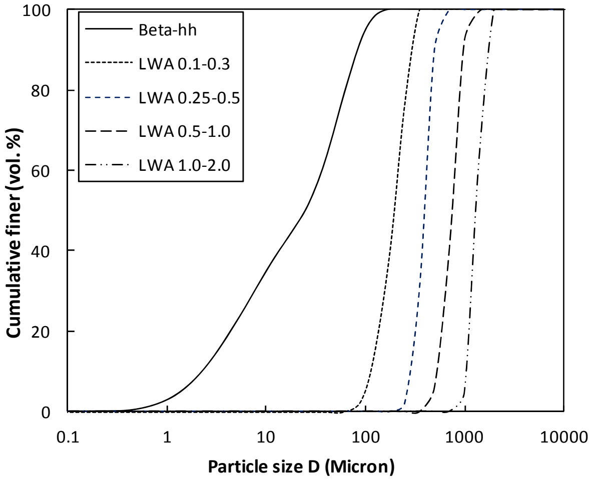

Figure 5.4: Particle size distribution of the used solids.

The second step is the optimization of the proportion of all the solid materials applying the optimization algorithm. As discussed before, the distribution modulus affects greatly the designed mix proportion. Therefore here the effect of the distribution modulus on the final properties of the developed composite is studied. Applying the optimization algorithm introduced in the previous section, four mixes are developed using the same solid ingredients but different distribution moduli, which will be modified and finalized according to the desired workability, as will be discussed in the next section.

Following the optimization of the solid ingredients, the third step is the determination of the water content, or here the water dosage based on the amount of β-hemihydrate (water/hemihydrate by mass). In SCC mix design, a fixed water content of about 0.30 (water/powder by mass) is usually chosen as a starting value and then adjusted according to the required flowability and viscosity (Hunger, 2010). Due to the obvious difference between the properties of cement and β-hemihydrate, while taking into account the LWA, this value is not suitable to be used as a reference. The water content here is first determined applying the mini-slump flow test, as presented in Chapter 3, which will be investigated intensively in the next section.

With the determined water demand, the preliminary mix design, i.e. the determination of solid materials and water content, is completed. However, it should be noted that with this water content the slump flow of the mixture is zero. The next step is to adjust the flowability of the developed mix by applying superplasticizer (SP) and slightly adjusting the water content if necessary until a desired design target.

It can be noticed that the mix design procedure can be treated as a design loop. The determined water content is dependent on the designed solid materials mix, while the solid materials are determined by the optimization program. The amount of the superplasticizer is related to the target flowability as well as to the water content. Therefore, the mix design applying this procedure will be accomplished usually after several loops until the target is achieved based on experimental observation and theoretical computation, which will be discussed in the next section.

5.3.3 Fresh state behavior analysis

Water demand

The water demand of the solid ingredients of the designed composite is determined by the mini-slump flow test using a Hägermann cone. A detailed description of the mini-slump flow test and the calculation procedure is already presented in Chapter 3. Nevertheless, the difference here is that the tested sample is composed, besides water, of binder (β-hemihydrate) and LWA, so not β-hemihydrate alone. Firstly, the slump flows of four mixes with the same designed solid proportions but different water contents are tested. Then, the computed relative slump flow values are plotted versus the respective water/solid volume ratios, and a linear trend line is fitted through the plotted values. Therefore, the water demand (β_s, which represents that here the slump flow is zero, Equation (3.2.3)) and the deformation coefficient (E_s) are derived accordingly as the intercept and slope of the obtained trend line.

Figure 5.5 shows the water demand results from the designed mixes using different distribution moduli. It can be seen that increasing the distribution modulus results in a reduction of the water demand, although the total volume of the solids increases. This can probably be explained by the reduction of the amount of β-hemihydrate, which also reflects the high water demand of β-hemihydrate that is in line with the previous research (see Chapter 3; and Yu and Brouwers, 2011a). On the other hand, this also indicates that the water absorption of the used lightweight aggregates within a short time (i.e. here during the spread flow test time) is rather low, which is confirmed by the LWA water absorption study performed here (see Chapter 2) and Liu et al. (2010).

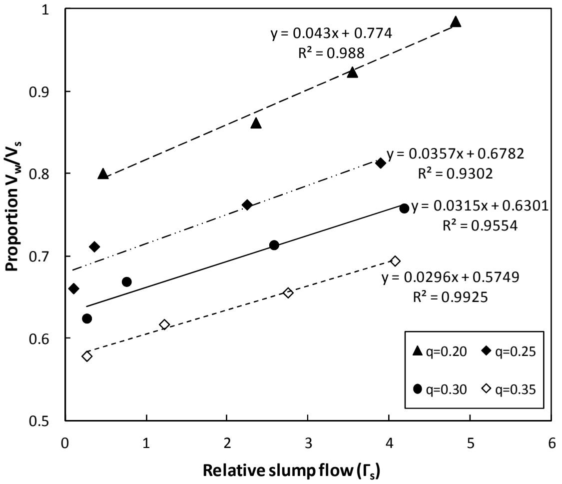

Figure 5.5: V_w/V_s versus relative slump values applying the mini-slump flow test.

The deformation coefficients (E_S, Equation (3.2.3)) of the solid ingredients in each mix are also obtained from the calculation (the slope of the trend lines in Figure 5.5). The SSAs of the solid ingredients are calculated based on the measured PSD of the used solid ingredients and their volume proportion in the mix, as listed in Table 5.2. The derived deformation coefficients are plotted versus their specific surface area, as shown in Figure 5.6. It can be clearly observed that the deformation coefficients of the mixes are linearly related to their specific surface areas. Furthermore, a water layer thickness of 66 nm is obtained from the derived trend line. The specific surface areas are modified by multiplying the shape factor of the used materials. Here the LWA used in the mixture have quite spherical shapes thus their shape factors are assumed as 1.0, which in fact will not cause considerable error since it can also be seen from Table 5.3 that the total specific surface area of the LWA is rather small compared to that of β-hemihydrate.

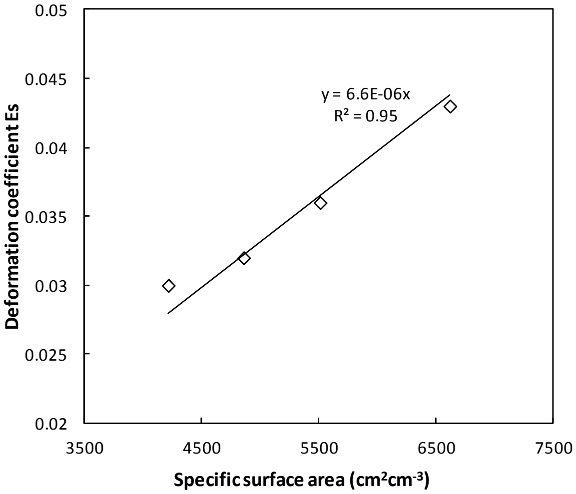

Figure 5.6: Derived deformation coefficients of the solids in the mixes (Table 5.2) versus their specific surface areas.

Compared to the water layer thickness for a pure β-hemihydrate slurry (39.3 nm, detailed presented in Chapter 3), one can see that the water layer thickness needed for the solids in the mixture derived here is larger (66 nm). Hunger (2010) investigated the water layer thickness of a cement based mortar (cement as binder and normal sand as aggregates) and reported as well a larger value than the values for powders such as cement. It can be noticed that even with such different mixes (here in the mix β-hemihydrate is used as binder and a lightweight material as aggregates), the findings from these two studies have a similar feature. The reasons for this can be, as reported by Hunger (2010), the PSD measurement methodology difference between the powders and aggregates and the shared volume of the water layers of the neighboring particles. Further investigation is still necessary to explain this more reasonably in the future.

Table 5.2: Specific surface areas (SSA) calculated from each mix.

Material	SSA ($cm^2\ cm^{-3}$)	Volume proportion				SSA ($cm^2\ cm^{-3}$)			
		Mix1	Mix2	Mix3	Mix4	Mix1	Mix2	Mix3	Mix4
β-hh	9877	0.47	0.388	0.340	0.294	6313.4	5211.9	4567.1	3949.2
LWA 0.1-0.3	337.4	0.15	0.218	0.202	0.190	68.8	100.0	92.7	87.2
LWA 0.25-0.5	156.0	0.056	0.050	0.163	0.127	11.9	10.6	34.6	26.9
LWA 0.5-1.0	82.8	0.237	0.151	0.098	0.127	26.7	17.0	11.0	14.3
LWA 1.0-2.0	45.3	0.087	0.193	0.197	0.262	5.4	11.9	12.1	16.1
Σ		1.0	1.0	1.0	1.0	6426.1	5351.4	4717.6	4093.8

Flowability analysis

- Target flow value

The mini-slump flow test is used to investigate the water demand on both powder and mortar level, i.e. the water content at the onset of the flowing of the spread sample, in the previous sections. In this section the mini-slump flow test is further used to study the flow behavior of the designed composites and the effect of the used superplasticizer.

According to the standard EN 13454-2 (2004), a flowable mortar and a highly plastic mortar based on hemihydrate should have a slump flow not less than 190 mm and 130 mm, respectively, while from EFNARC (2005) the slump flow of cement mortar should be between 240 and 260 mm. Here, using these two standards as references, the slump flow value is set as 200-250 mm, which is shown as a fair target value from the tests.

- The used superplasticizer

As discussed before, this chapter tries to minimize the water content in the mix due to the significant effect it has on the properties of the designed composite. The idea is to start from a water amount determined by the mini-slump flow test, and then to modify it by incorporating the superplasticizer (SP) and by adjusting the water content until the desired flow value is achieved.

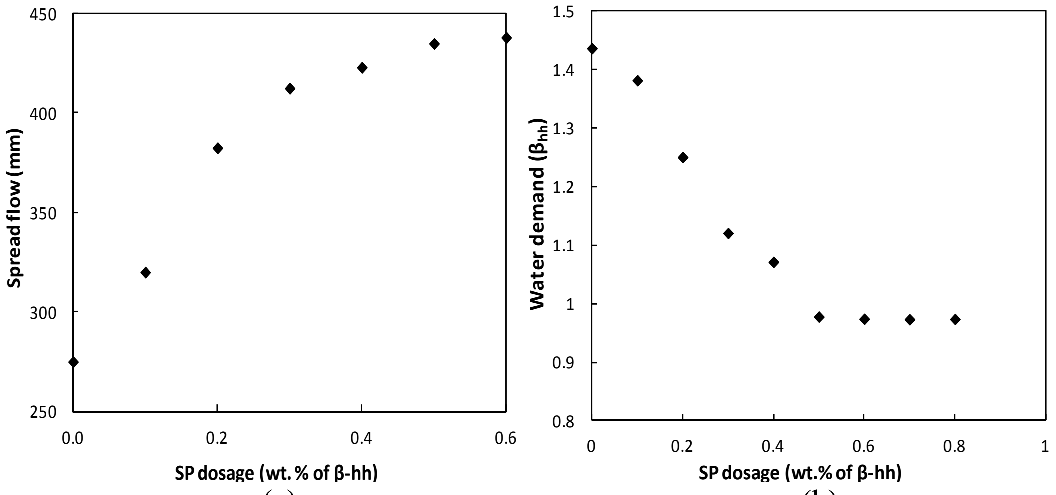

(a) (b)

Figure 5.7: Effect of the SP on the flowability on β-hemihydrate slurry (a: the spread flow versus the SP dosage with fixed water content; b: the determined water demand versus the SP dosage).

A new polycarboxylate (PCE)-based superplasticizer especially designed for gypsum plasterboard production is used here (GPV12, Sika). PCE-based dispersants are commonly used in concrete production, but less for gypsum board. PCE has an effect of retarding the setting, which has a significant effect on gypsum board production, since compared to cement slurry, gypsum setting occurs in a very short period (see Chapter 3). The new SP used here (GPV12) is developed by Sika (Hample, 2010) to tackle this problem. The GPV12 is a transparent solution with a specific density of 1.08 g cm^{-3} and a solids content of 30-40% depending on batches.

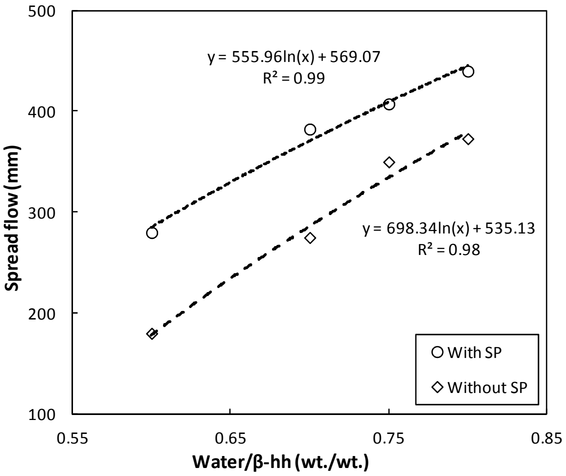

Figure 5.8: Comparison of the spread flow with and without superplasticizer (dosage of 0.2 wt.% of β-hemihydrate) as a function of the water content.

The effect of GPV12 on the flowability of β-hemihydrate slurry is investigated. The spread flow experiment is performed using a Hägermann cone by applying the superplasticizer with different dosages. Figure 5.7a shows the spread flow of the β-hemihydrate slurry with a fixed water/hemihydrate ratio of 0.7 but with different superplasticizer dosages. It is shown that, until the dosage of 0.2% by mass of the β-hemihydrate, the slump flow increases linearly, and then the increase rate reduces fast and finally the slump flow reaches a constant value at the dosage amount 0.5% by mass of the β-hemihydrate. Figure 5.7b shows the water demand determined by the mini-slump flow test at different superplasticizer dosages. It is indicated from both Figures 5.7a and 5.7b that the superplasticizer has an optimal dosage amount of 0.5% by mass of β-hemihydrate from the point of view of flowability.

Table 5.3: Compositions of four mixes designed applying this mix design concept (per 1 m^3).

Material	Mix 1		Mix 2		Mix 3		Mix 4	
	Mass (kg)	**Volume (m^3)**	**Mass (kg)**	**Volume (m^3)**	**Mass (kg)**	**Volume (m^3)**	**Mass (kg)**	**Volume (m^3)**
β-hemihydrate	687.0	0.262	593.8	0.227	532.6	0.203	474.0	0.181
LWA 0.1-0.3	67.9	0.084	102.9	0.127	97.5	0.121	94.8	0.117
LWA 0.25-0.5	16.9	0.031	15.8	0.029	52.5	0.097	42.1	0.078
LWA 0.5-1.0	59.4	0.132	39.6	0.088	26.3	0.058	35.1	0.078
LWA 1.0-2.0	17.0	0.049	39.6	0.113	41.3	0.118	56.2	0.160
Water	412.2	0.412	385.9	0.386	372.8	0.373	355.5	0.356
air	0.0	0.030	0.0	0.030	0.0	0.030	0.0	0.030
SP/hemihydrate (wt./wt.)	0.20%		0.25%		0.30%		0.30%	
Water/hemihydrate (wt./wt.)	0.60		0.65		0.70		0.75	
Distribution modulus	0.20		0.25		0.30		0.35	

A further study on the effect of the SP is carried out by comparing the slump flow of the β-hemihydrate slurry with different water contents but with a fixed superplasticizer dosage of 0.2% by mass of hemihydrate. The results are shown in Figure 5.8. It can be seen that the relation between the spread flow and the water content follows the same law with and without dosing superplasticizer under the investigated water content range. Hampel (2010) reported that a water reduction up to 20% is possible while getting the same flow performance by applying the GPV12 with an amount of 0.2% by mass of β-hemihydrate, which is in line with the current results.

- Flowability analysis

The flowability test performed on the designed composite is the mini-slump flow test using the Hägermann cone. The sample preparation procedure is the same as described in Chapter 3 (Section 3.2.3). The flowability of the composite with the determined water content as described above is tested by dosing different amounts of superplasticizer. The results of the determined SP dosage as well as the final determined mix proportions are listed in Table 5.3.

5.4 Porosity and density

5.4.1 Introduction

The property of being lightweight or low density of the newly developed composite in the hardened state is one of the main objectives; therefore, it is addressed at first here. In this section, the porosity of the SGLC is studied by modeling, and the proposed model is then validated by the performed experiments. The porosity and density of the designed composite is compared with traditional gypsum board, and the effect of the used distribution modulus in the mix design model is discussed.

5.4.2 Porosity and density modeling

The porosity of the developed composite is caused by three main phenomena, i.e. the chemical shrinkage during the hydration of the β-hemihydrate, the evaporation of the excess water during the curing period, and the internal open space caused by the used lightweight aggregates. The first two parts have already been investigated in Chapter 4.

The internal porosity of the LWA particles can be calculated from their apparent density and the specific density of the solid material, reading

$$\varphi_{v,lwa,i} = 1 - \frac{\rho_{lwa,i}}{\rho_{slwa}} \tag{5.4.1}$$

where $\varphi_{v,lwa,i}$ is the porosity introduced by the lightweight aggregates of different size fractions (i), ρ_{lwa} is the apparent density of aggregate particles (g cm^{-3}), and ρ_{slwa} is the specific density of the solid material (glass) (g cm^{-3}).

The specific density of the solid material (ρ_{slwa}) in the present study is measured using a gas Pycnometer (AccuPyc II 1340, Micromeritics) on crushed and ground samples that are obtained from ball milling, resulting in 2.458 g cm^{-3} in average (see Chapter 2). The specific density of the aggregate particles (ρ_{lwa}) is taken from the data sheet of the provider (see Chapter 2). Hence the total porosity caused by the LWA particles of different particle size ranges is calculated from

$$\varphi_{v,lwa} = \sum_{i=1}^{n}\left[\frac{V_{lwa,i}}{V_{SGLC}} \times (1-\frac{\rho_{lwa,i}}{\rho_{slwa}})\right] \tag{5.4.2}$$

where $V_{lwa,i}$ and V_{SGLC} are the volumes of the used LWA in different size ranges and the volumes of the designed SGLC composite, respectively (m^3).

Therefore, the total porosity of the designed composite is obtained by adding the two porosities, contributed by the calcium sulfate dihydrate and the LWA, reading

$$\varphi_{v,sglc} = \varphi_{v,dh} + \varphi_{v,lwa} = \frac{\frac{w_0}{h_0} - 0.13}{\frac{\rho_w}{\rho_{hh}} + \frac{w_0}{h_0}} \times \frac{V_w + V_{hh}}{V_{SGLC}} + \sum_{i=1}^{n}\left[\frac{V_{lwa,i}}{V_{SGLC}} \times (1-\frac{\rho_{lwa,i}}{\rho_{slwa}})\right] \tag{5.4.3}$$

where V_w and V_{hh} are the volumes of initial water and the used β-hemihydrate, respectively. Incorporating the relation

$$\frac{w_0}{h_0} = \frac{\rho_w V_w}{\rho_{hh} V_{hh}} \tag{5.4.4}$$

and using $\rho_{hh}/\rho_w = 2.62$, the following expression is obtained:

$$\varphi_{v,sglc} = 2.62 \times \left(\frac{w_0}{h_0} - 0.13 \right) \times \varphi_{hh} + \sum_{i=1}^{n} \left[\varphi_{lwa,i} \times (1 - \frac{\rho_{lwa,i}}{\rho_{slwa}}) \right] \tag{5.4.5}$$

where φ_{hh} and φ_{lwa} are the volume fraction of the used β-hemihydrate and LWA in the designed composite, respectively.

It shows that the void fraction of the composite is related to the paste content (here paste is defined as the sum of water and β-hemihydrate) and the used lightweight aggregates. One can see that if the density of the LWA is the same as of the solid material, i.e. in case of the normal aggregates, Equation (5.4.5) becomes the void fraction expression for normal gypsum board assuming the aggregates as impurities (here meaning nonreactive material).

The apparent density of the composite after removal of the free water can be calculated from the used β-hemihydrate and the LWA, reading

$$\rho_{SGLC} = \frac{\sum_{i=1}^{n} m_{lwa,i} + 1.186 \times m_{hh}}{V_{SGLC}} \tag{5.4.6}$$

where ρ_{SGLC} is the apparent density of the designed composite (g cm^{-3}), $m_{lwa,i}$ is the mass of the LWA of fraction size *i* (g), m_{hh} is the mass of the used hemihydrate (g), V_{SGLC} is the volume of the designed composite (cm^3), the factor 1.186 originates from the mass of water retained by dihydrate (based on hemihydrate mass, see Chapter 4).

5.4.3 Model validation

The derived density expression is validated by the experimental results. Here the measured density is calculated from the measured mass and size. The samples are prepared from different mix designs, whereas some of them are designed using the same distribution modulus but with different initial water content and some are designed using different distribution moduli. All the samples are cured at ambient conditions for 7 days after demolding (here demolding is performed usually 2 hours after casting the samples), and then dried in a ventilated oven at 40 °C until constant mass.

The results are shown in Table 5.4. It is obvious that the measured density values are in excellent agreement with the calculated values, which indicates the validity of the derived density model as well as the used paste models (see Chapter 4).

Table 5.4: Density comparison between the model predictions and experimental results.

Distribution modulus (q)	Density (g cm^{-3})	
	Computed	Measured
0.20	0.98	0.97
0.25	0.93	0.93
0.30	0.88	0.89
0.35	0.81	0.82

Figure 5.9a shows the relation between the void fraction and density and distribution modulus. The density decreases with the increase of the void fraction, which increases with the increase of the applied distribution modulus. This can be explained from Equation (5.4.5): the increase of the distribution modulus leads to the reduction of the paste amount and to an increase of the LWA amount. Although the reduction of the paste content results in a decrease of the void fraction of the generated dihydrate, the void fraction caused by the increase of the LWA has a larger effect, which also indicates the influence of the applied distribution modulus. A further observation on Figure 5.9a reveals another interesting finding, i.e. the relation between the density and the void fraction of the new composite is in line with the pure gypsum board (see Chapter 4).

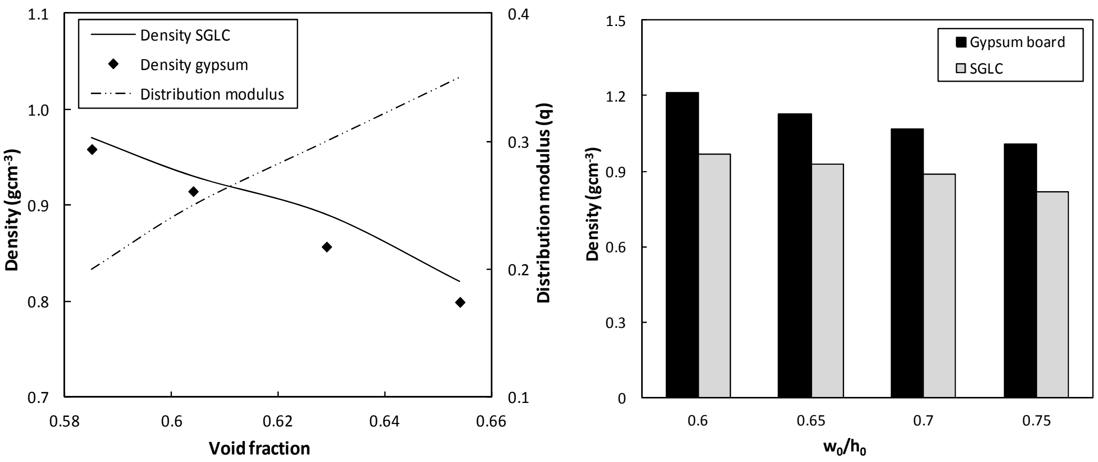

(a) (b)

Figure 5.9: Comparison between the SGLC and traditional gypsum board: (a) The density and the used distribution modulus versus the void fraction; (b) The density versus the water content.

The density of the newly developed composite is compared to the traditional gypsum board (Yu and Brouwers, 2011a). The comparison is carried out based on the initial water content, and the results are shown in Figure 5.9b. It is shown that, under all water content conditions, the density of the new composite is clearly lower than that of the traditional gypsum board; for instance, a reduction of 20% is obtained at a w_0/h_0 of 0.60. This provides a possibility to produce a much lighter building material using this mix design concept.

5.5 Mechanical properties

5.5.1 Introduction

The strength of composite materials such as concrete or gypsum is linked with their densities. For a better understanding of the strength in the newly developed composite, the strength development of the pure gypsum board is firstly studied here. The effect of the density, or alternatively the void fraction, on the strength is investigated. A relation between the void fraction and the strength of the gypsum board is found based on the performed experiments. The strength of the newly developed composite is then analyzed, and the influence of the applied distribution modulus is discussed. Finally, the strength of the pure gypsum board and the developed composite is compared on different parameters such as density and void fraction.

5.5.2 Traditional gypsum board

As typical for many building materials, gypsum behaves elastically under load before reaching its elastic limit. However, it is obvious that the gypsum is not a compact solid due to its high void fraction. Lewry and Williamson (1994b) reported that the gypsum strength develops during setting via a three-stage process: first a development of an interlocking matrix of dihydrate needles, then the relief of internal stress due to the build-up of pressure and finally by a strength increase during the removal of the excess water.

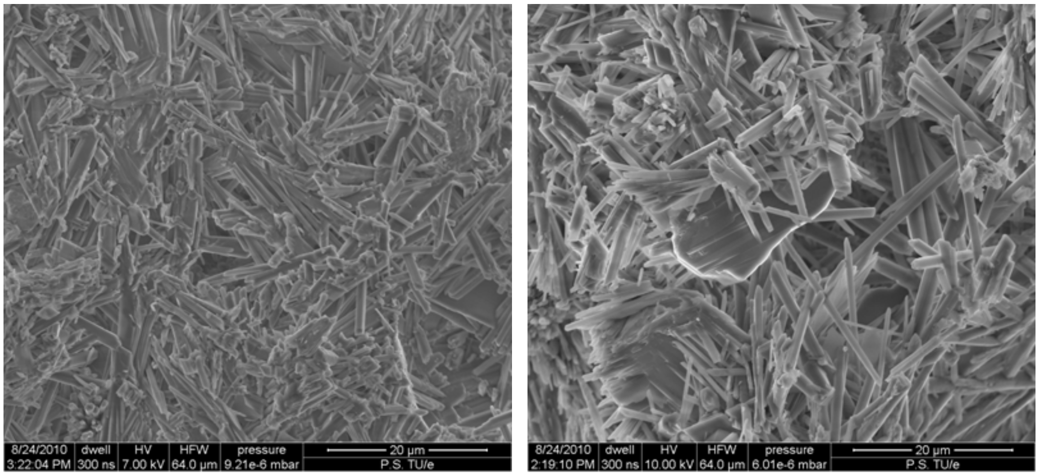

(a) (b)

Figure 5.10: SEM picture of the gypsum produced with (a: $w_0/h_0 = 0.65$; b: $w_0/h_0 = 0.80$).

From the strength development process, one can see that the final strength of gypsum is related to the formation of the produced gypsum crystals and the bond between them. From here we can assume that the water amount influences the strength of gypsum by creating the voids since it influences the formation of the gypsum crystals and their bonds, which is confirmed by the SEM pictures as shown in Figure 5.10.

The strength tests are performed using a Zwick test device according to EN 13279-2 (2004). Here the size of the samples is controlled strictly according to EN 13279-2 (2004) to ensure a representative value since Coquard et al. (1994) reported that the sample size has an obvious influence on the strength of gypsum.

The flexural strength test is performed on samples with dimensions of 160 mm × 40 mm × 40 mm using the three-point bending method. The load is applied vertically by means of a loading roller to the lateral side of the prism with a rate of (50 ± 10) Ns^{-1} until fracture. The flexural strength is calculated from

$$\sigma_f = \frac{3F_{rupt}L_0}{2WH^2} \tag{5.5.1}$$

where σ_f is the flexural strength (N mm^{-2}), F_{rupt} is the breaking load (N), L_0 is the distance between the supports of the bending machine (mm), and W and H are the width and length of the sample (mm), respectively.

The compressive strength is determined by applying a load to the broken part of the specimen used for the flexural strength test, on the molded side over an area of 40 mm × 40 mm. A load is applied and increased smoothly at the rate of (2400 ± 200) N s^{-1} over the entire load application until the fracture. The compressive strength is calculated from

$$\sigma_c = \frac{F_c}{1600mm^2} \tag{5.5.2}$$

where σ_c is the compressive strength (N mm^{-2}) and F_c is the maximum load at fracture (N).

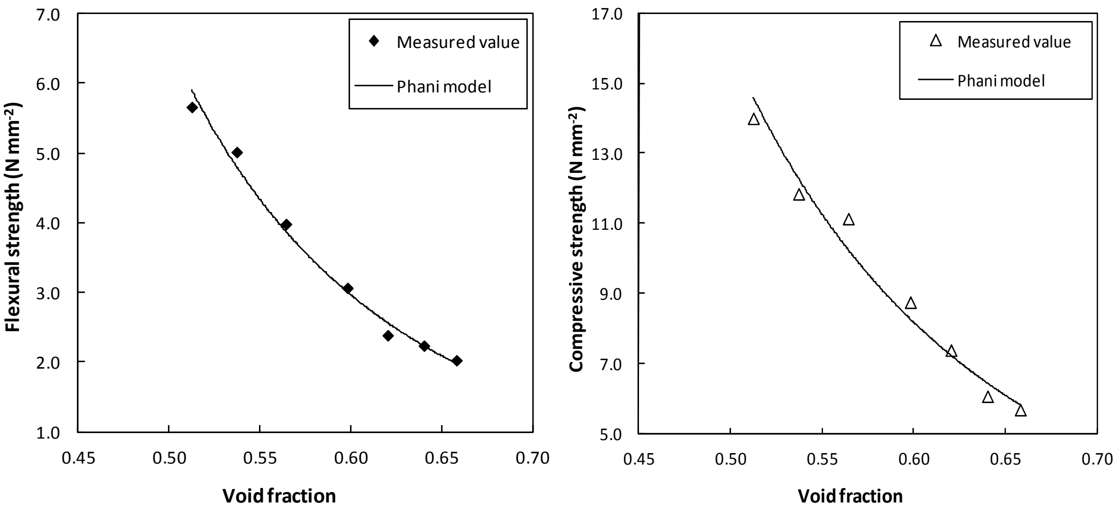

(a) (b)

Figure 5.11: Strength of the gypsum versus the void fraction (a: flexural strength; b: compressive strength).

The influence of the water content on the strength of the gypsum is investigated and the flexural and compressive strength values are plotted versus the void fraction, as shown in Figure 5.11. A detailed analysis of the void fraction of the gypsum board is presented in Chapter 4. It is evident that the strength decreases with the increase of the void fraction, which can be explained by the bonds between the crystals. When the water amount increases, the void fraction of the generated gypsum increases as analyzed above which in turn leads to a weaker bond between the gypsum crystals, which finally results in a decreased strength.

Several models have been proposed and applied to describe the relation between the void fraction and the strength of gypsum, such as

$$\sigma = \sigma_0(1 - b_0\varphi_v) \tag{5.5.3}$$

$$\sigma = \sigma_0(1 - b_0\varphi_v)^{a_0} \tag{5.5.4}$$

$$\sigma = a_0 \ln(\frac{1}{b_0\varphi_v}) \tag{5.5.5}$$

$$\sigma = \sigma_0 \exp(-b_0\varphi_v) \tag{5.5.6}$$

where φ_v is void fraction, and a_0, b_0, σ_0 are parameters.

Here Equation (5.5.3) is referred to as the linear model, Equation (5.5.4) as the Phani model (Phani et al. 1986), Equation (5.5.5) as the Schiller model (Schiller, 1958), and Equation (5.5.6) as the exponential model.

Table 5.5: Comparison of the four applied models.

Model	Flexural strength (σ_f, N mm^{-2})				Compressive strength (σ_c, N mm^{-2})			
	R^2	a_0	b_0	σ_0	R^2	a_0	b_0	σ_0
Linear (Eq.5.5.3)	0.97	--	1.38	18.94	0.98	--	1.33	43.33
Phani (Eq.5.5.4)	0.98	1.20	1.35	23.10	1.00	1.16	1.30	48.70
Schiller (Eq. 5.5.5)	0.98	15.33	1.35	--	0.99	33.65	1.30	--
Exponential (Eq.5.5.6)	0.99	--	7.49	269.60	0.98	--	6.33	369.31

These models are applied and compared, and the obtained coefficient of determination (R^2) and relevant parameters (a_0, b_0, and σ_0) are listed in Table 5.5. One point that should be mentioned here is that both models of Schiller (1958) and Phani et al. (1986) are proposed based on α-hemihydrate produced gypsum. Actually the linear model (Equation (5.5.3)) is one special case of the Phani model (Equation (5.5.4)), i.e. the exponent equals unity. The Phani model (i.e. power model) provides the best predictions in the present study. A critical void fraction value of 0.73~0.77 of the gypsum is obtained here ($1/b_0$ in Equations (5.5.3-5.5.5)). This value indicates that the produced gypsum will lose its strength at this void fraction, which is in line with Schiller (1957) who reported a critical void fraction value of 0.79 for gypsum produced from α-hemihydrate. This finding also indicates that the strength is independent of the type of the used hemihydrate. An extreme strength (σ_0, flexural strength and compressive strength), i.e. the strength of gypsum at zero void fraction, is also derived from the models, as listed in Table 5.5. It can be seen that the Schiller model (Equation (5.5.5)) has a limitation since it only can predict the critical void fraction but not the maximum strength, while the exponential model (Equation (5.5.6)) only generates an extreme strength but not the critical void fraction.

5.5.3 The designed composite SGLC

In this section, the mechanical properties of the developed composite SGLC are investigated, also from the point of view of its strength including the compressive and flexural strengths. Different distribution moduli lead to different mix designs, while a smaller q results in a mixture rich in finer solid ingredients, which obviously influences the mechanical properties such as the strength of the developed composite. Hence, the effect of the distribution modulus is investigated as well. The flexural strength and compressive strength tests are carried out using the same procedure/equipment and the results are computed following the same equations as presented in the previous section.

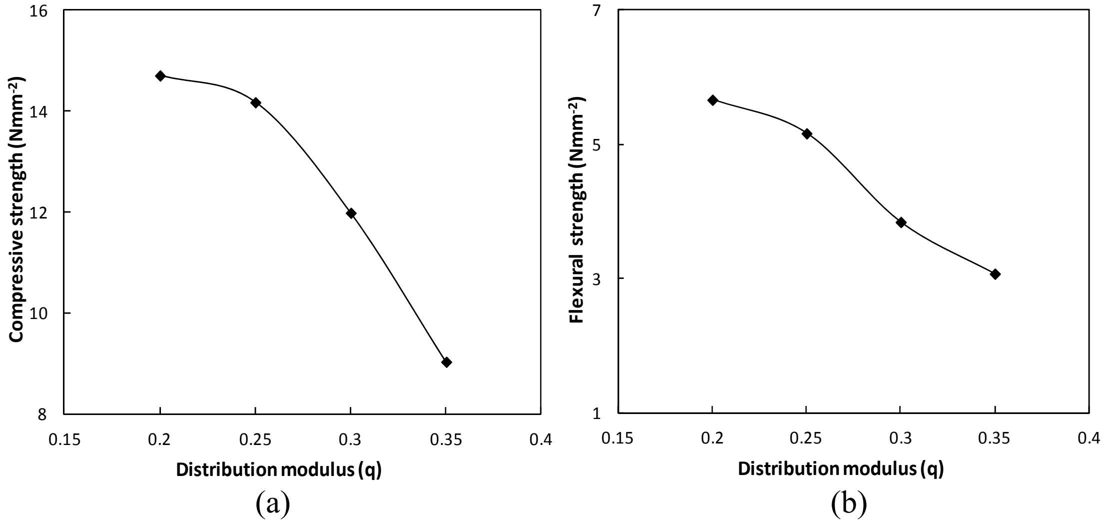

(a) (b)

Figure 5.12: Strength of the SGLC versus the distribution modulus (a: compressive strength; b: flexural strength).

The results are shown in Figures 5.12. Both the compressive and the flexural strength decrease with the increase of the distribution modulus (q), but the strengths are influenced more significantly at a bigger q range. The compressive strength decreases only with 3.6% when the q increases from 0.20 to 0.25, but it decreases with 18.5% when the q increases to 0.30, while the related flexural strength decrease is 8.8% and 32.2%, respectively. This finding indicates from the point of view of strength that a smaller q is more suitable and recommended.

5.5.4 Discussion

As shown in the previous section, the effect of the void fraction of gypsum on its strength is investigated and a power relation between them is found. It is indicated that the effect of the void fraction on the developed composite is also significant. It is therefore that it is first investigated in the present study. The results are plotted in Figure 5.13. It is shown that the strength (both the compressive and flexural strength) has a power law relation with the void fraction. This is in line with the finding of the void fraction and the strength of pure gypsum above.

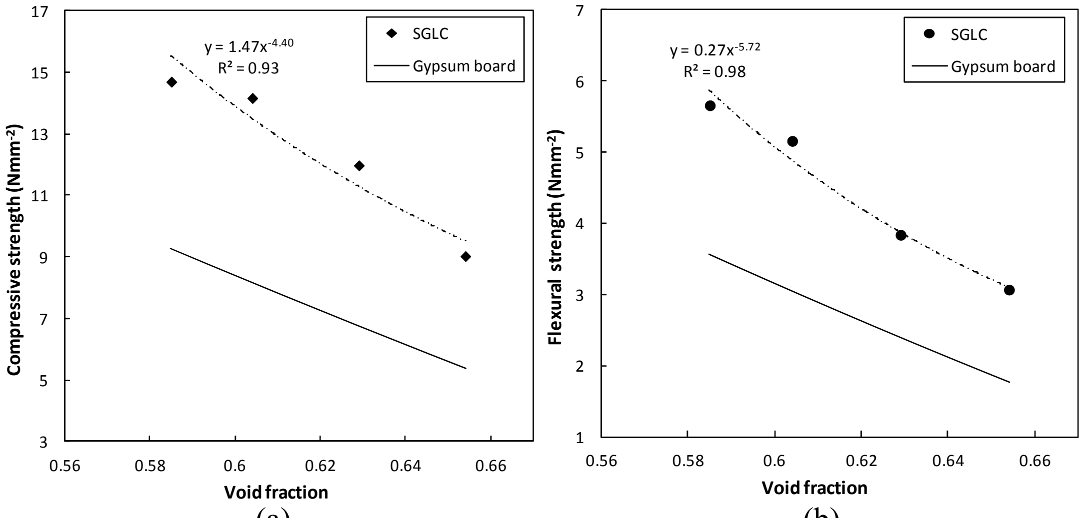

(a) (b)

Figure 5.13: Strength comparison of the SGLC and pure gypsum board versus the computed void fraction (a: compressive strength; b: flexural strength).

The strengths of the SGLC and pure gypsum boards are also compared, and the results are shown in Figure 5.13. Here the strength value for pure gypsum board is taken from the power model derived from the previous section. It can be seen, for instance with a void fraction of 0.60, that an improvement of 73.3% and 70.0% in compressive and flexural strength, respectively, is obtained with the developed composite (designed with the distribution modulus of 0.25 with a similar density as the traditional gypsum board of 0.93 g cm^{-3}).

Hence it is demonstrated here that, although the strength of the new composite holds the same rule, i.e. the relation between the strength and the void fraction is a power law, a much higher strength is reached in the present study while keeping a similar density/porosity in the developed composite SGLC.

5.6 Thermal properties

5.6.1 Introduction

The thermal properties of gypsum plasterboard have been presented in Chapter 4 in detail. In this section, the thermal properties of the developed gypsum based lightweight composite (SGLC) will be addressed. In Section 5.6.2, the thermo physical properties such as the thermal conductivity and volumetric heat capacity of the SGLC will be discussed, and in Section 5.6.3, the thermal degradation under high temperature will be studied.

5.6.2 Thermo physical properties

As one of the key topics in building technology research, fire resistance is always receiving special attention due to the very important role it plays in the safety of human beings. To prevent the premature collapse when heated, the main building structures should have good fire separations. To ensure an excellent fire resistance of a building structure, good thermo physical properties such as a low thermal conductivity are very important to be obtained. On the other hand, a low thermal conductivity of the building structure also contributes to a good thermal comfort, due to the low heat transfer through it between the indoor and outdoor conditions. Hence, here the specific heat capacity and the thermal conductivity of the designed composites are measured, using the same heat transfer analyzer (ISOMET Model 2104) already presented in Chapter 4.

The measured thermal conductivity versus the applied distribution modulus is shown in Figure 5.14a. The thermal conductivity first decreases and then remains stable with the increase of the distribution modulus, whereas a minimum value of 0.19 W (m K)$^{-1}$ is reached at a distribution modulus of 0.30. Figure 5.14b shows the relation between the densities of the composites and their thermal conductivities. It is shown that the thermal conductivity remains stable at a lower density and then increases quickly with the increase of the density. This is in line with Zehner and Schlunder (1970) and De Korte and Brouwers (2010), who reported that the thermal conductivity is related not only with the density, but also strongly with the composition. It should also be pointed out that, to reach a lower thermal conductivity, it is not enough only to consider the reduction of the density. Here, a thermal conductivity of 0.21 W (m K)$^{-1}$ is obtained at a void fraction of 0.60 (with the density of 0.93 gcm^{-3}), while in the previous section a thermal conductivity of 0.30 W (m K)$^{-1}$ is obtained at the same void fraction for pure gypsum board (see Chapter 4). Hence, it can be concluded that a 30% improvement of the thermal conductivity is reached with the SGLC.

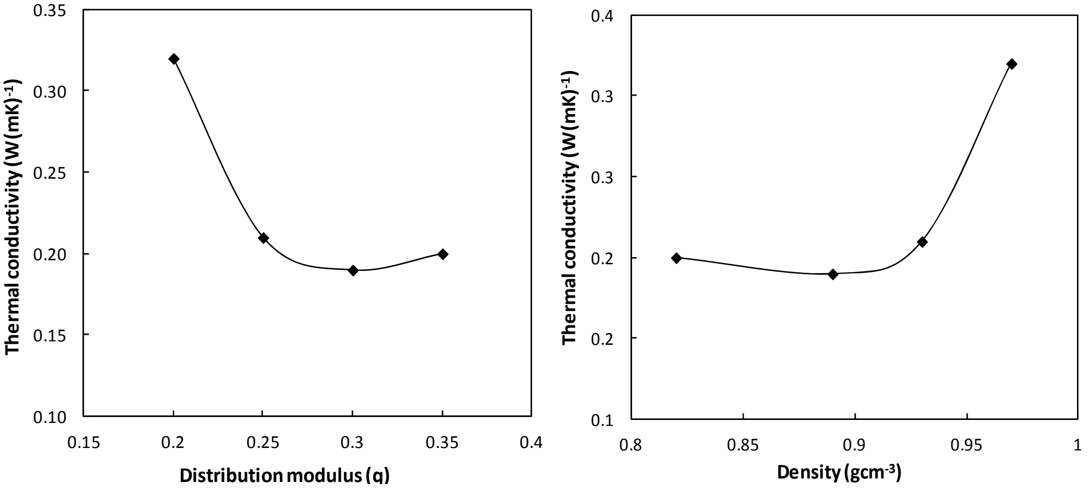

(a) (b)

Figure 5.14: Measured thermal conductivity of the SGLC: (a: versus the used distribution modulus; b: versus the density).

The measured volumetric specific heat capacity is listed in Table 5.6. It can be noticed that the density is again not linked linearly with the volumetric specific heat capacity, and an optimal value is obtained at a distribution modulus of 0.25. Compared to the normal gypsum board, the volumetric specific heat capacity of the SGLC is slightly lower at the same void fraction (density), for instance, the volumetric specific heat capacity is 1.05×10^6 J (m^3 K)$^{-1}$ with a density of 0.93 g cm^{-3}, whereas it is 1.20×10^6 J (m^3 K)$^{-1}$ with a similar density (0.96 g cm^{-3}) in the case of a normal gypsum board. This probably can be explained by the difference between the composition of normal gypsum board and the developed SGLC, especially the applied LWA.

Table 5.6: Thermo physical properties of the SGLC at room temperature.

Distribution modulus (q)	Density (g cm^{-3})	Volumetric heat capacity (J (m^3 K)$^{-1}$)
0.20	0.97	1.04×10^6
0.25	0.93	1.05×10^6
0.30	0.89	0.89×10^6
0.35	0.82	0.73×10^6

5.6.3 Thermal degradation at high temperature

As shown in Equations (4.2.1) and (4.2.2), when exposed to fire or under high temperature, the chemically combined water in gypsum ($CaSO_4 \cdot 2H_2O$) dissociates from the crystal lattice and vaporizes. During this process, gypsum absorbs a large amount of heat that drastically delays the process of heat transfer through the plasterboard (Yu and Brouwers, 2011b and Chapter 4), which is also the reason why gypsum boards are usually used as a fire retardants to protect components of wall assemblies from overheating.

In the investigated SGLC, the change of the mass upon the dehydration of gypsum is only caused by the release of the chemically combined water, because the used LWA is made of glass, which will not lose any weight in this temperature range. Therefore, the density of the composite at high temperature (here emphasis is put on the dehydration temperature of dihydrate) can be theoretically calculated using the same method as discussed in the previous section, reading

$$\rho_{SGLC,220} = \frac{\sum_{i=1}^{n} m_{lwa,i} + 0.938 \times m_{hh}}{V_{SGLC}} \tag{5.6.1}$$

where $\rho_{SGLC,220}$ is the density of the developed composite at 220 °C (g cm^{-3}), the factor 0.938 originates from the water release during the dehydration of dihydrate to anhydrite (as shown in Equations (4.2.1) and (4.2.2)).

However, as already presented in Chapter 4, due to the dehydration reaction, the matrix in the gypsum is changed, which results in a reduced mechanical property, e.g. strength. Here, a lightweight material is used as aggregate. Due to the stability of its microstructure at the dehydration temperature of dihydrate, i.e. below 300 °C (Yu and Brouwers, 2011b), it will contribute to reduce the thermal degradation of the developed composite, i.e. the thermal mass loss and the strength reduction beyond the gypsum dehydration, which is addressed in the present study. Both the thermal mass loss and strength tests are carried out on the samples with a size of 160 mm × 40 mm × 40 mm, using the same procedure as introduced in the previous section. The dehydration experiments are performed following this procedure, i.e. firstly the samples are cured at ambient conditions for 7 days after demolding, and then heated at 220 °C until the mass is constant. According to the previous study (see Chapter 4), this temperature ensures a full dehydration reaction of gypsum given sufficient time.

Table 5.7: Thermo physical properties of the SGLC after dihydrate dehydrated to anhydrite.

Distribution modulus (q)	Density ($g\ cm^{-3}$) Computed	Measured	Thermal conductivity ($W\ (m\ K)^{-1}$)	Volumetric heat capacity ($J\ (m^3\ K)^{-1}$)
0.20	0.81	0.80	0.15	0.62×10^6
0.25	0.75	0.78	0.13	0.63×10^6
0.30	0.74	0.74	0.12	0.55×10^6
0.35	0.71	0.69	0.12	0.54×10^6

The measured and the theoretical mass loss due to the dehydration of the gypsum at high temperature are listed in Table 5.7. It can be seen that the measured values are in good agreement with the computed values. The thermal mass loss leads to the microstructure change of the dihydrate in the matrix of the composite, as presented in Chapter 4: the regular gypsum crystals change to irregular broken anhydrite particles, which results in a weaker bonding between the particles. The measured thermal conductivity and the volumetric specific heat capacity of the composites after dehydration are also listed in Table 5.7. It is obvious that the thermal conductivity becomes lower after the gypsum dehydration due to the extra voids caused by the release of the chemically combined water in gypsum, as well as the change of the matrix. Moreover, it is very clear that the thermal conductivity of the dehydrated composite has a similar feature as the composite before dehydration, i.e. it decreases and then reaches a stable condition within the investigated distribution modulus range.

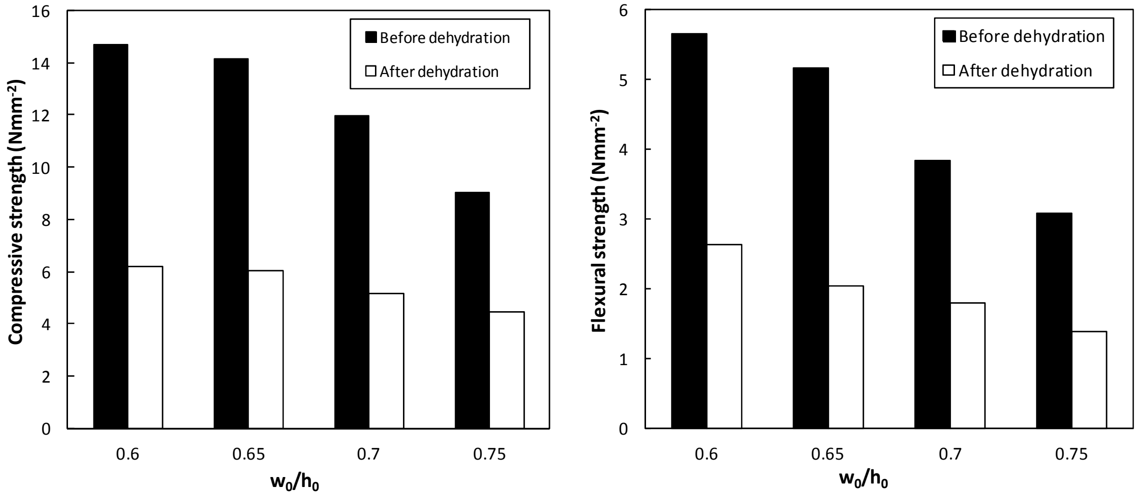

(a) (b)

Figure 5.15: Strength reduction after the gypsum in the SGLC is dehydrated to anhydrite (a: compressive strength; b: flexural strength).

The measured strength values (both the compressive and flexural strength) are shown in Figure 5.15. It can be noticed that a reduction of about 50% in both compressive and flexural strength occurs after the dehydration of gypsum, i.e. the binder in the matrix. However, compared to the current composite, the pure gypsum board loses more than 80% of its strength in this temperature range (see Chapter 4). Hence, one can see that, although there is obvious strength degradation, a considerable improvement has already been reached in the new composite. Once again the improvement obtained here can be explained by the application of the LWA. This improvement can definitely help to delay the failure of the structure itself, and then even the whole building structure it protects.

5.7 Fire behavior

The fire behavior of the developed SGLC is investigated by performing the real fire test on the designed samples. The furnace employed in this study is developed by AIDICO in Spain (Lopez Buendia and Suesta Falco, 2011), as shown in Figure 5.16a. The furnace is built vertically with a surface of exposure of 9 m^2 according to standard EN 1363-1 (1999) and EN 1363-2 (1999). The wall of the furnace is made of bricks and coated with refractory cement mortar. Along the wall 7 burners (14 burners in both left and right sides) are assembled vertically, and the burners are 38 cm away from the wall, as shown in Figure 5.16b.

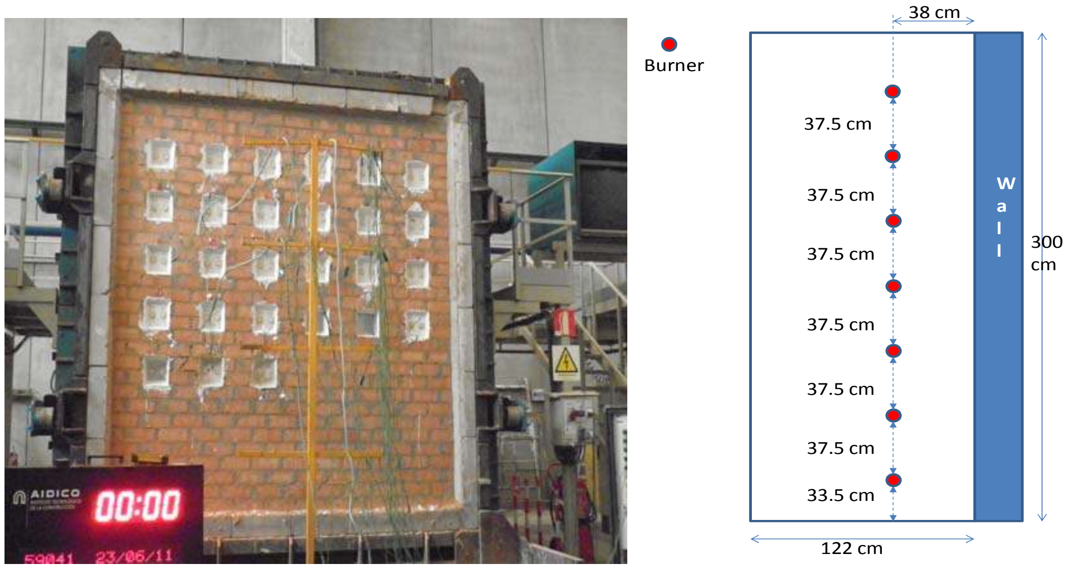

(a) (b)

Figure 5.16: Furnace employed for the fire test (a: picture of the test set-up; b: arrangement of the burners) (Lopez Buendia and Suesta Falco, 2011).

Here samples prepared from 6 different mixes are tested, including four mixes of SGLC and two pure gypsum plasterboards. The mix design of these four gypsum based composites is presented in Table 5.2, while the two pure gypsum plasterboards are produced with an initial water/hemihydrate ratio of 0.65 and 1.00, respectively. Three samples of each mix are tested. Samples are placed in the cavities of the wall of the furnace, as shown in Figure 5.16a. The thicknesses of all the samples are precisely controlled to be the same (20.0 mm) in order to obtain representative results (the reason will be analyzed below). The temperature of the sample in the non-exposed side is monitored by 2 thermocouples. The thermocouples, which are copper disc (12 mm in diameter and 0.2 mm in thickness) type K, are fixed using an adhesive tape and plaster to the samples. The exposed side of the sample is pre-cleaned and free of obstacles.

The fire test is performed following the ISO standard 834-1 (1999). The average temperature of the furnace increases following

$$T_{834-1} = 345\log_{10}(8t+1)+20 \tag{5.6.2}$$

and is monitored by the interior thermocouples, where $T_{834\text{-}1}$ is the average furnace temperature (°C), and t is the time (min).

The temperature in the fire exposed side of the samples is not monitored since in the present study the heat transfer rate of the developed composites is the focus. The distances between the burner and the fire exposed side are the same for all the samples, as shown in Figure 5.16b. Therefore, the heat is transferred from the burner to the fire exposed side with the same rate and the temperature of the fire exposed side is assumed to be the same for all samples. The duration of the fire test is 110 minutes. The temperature values are recorded continuously online, and the results are shown in Figure 5.17.

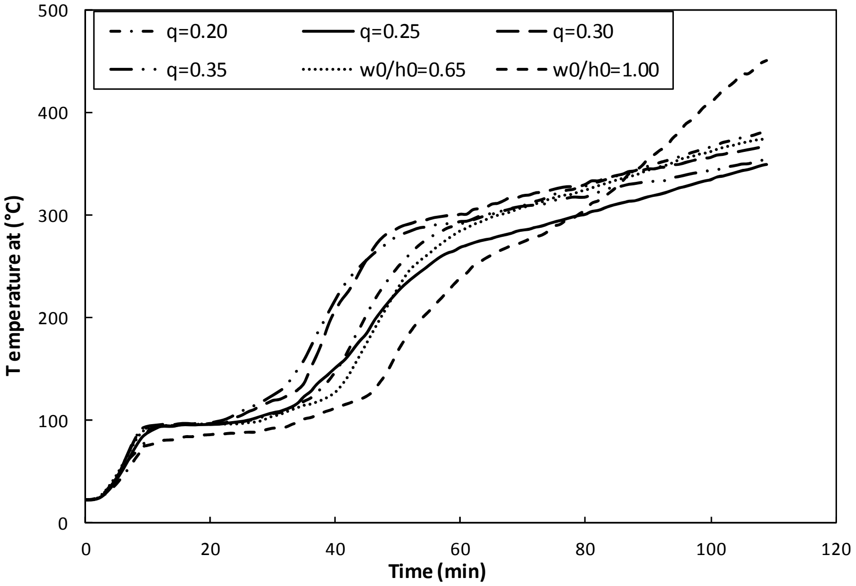

Figure 5.17: Temperature increase at the non-exposed side of the samples during the fire test.

Heat transfer through the samples (here SGLC and gypsum boards) is governed by the following partial differential equation, reading

$$\rho C_{T,p}\frac{\partial T}{\partial t} = \frac{\partial}{\partial x}\left(k\frac{\partial T}{\partial x}\right)+Q_h \tag{5.6.3}$$

where T is the temperature (°C), ρ is the apparent density (kg m^{-3}), $C_{T,p}$ is the temperature related specific heat capacity (J (kg °C)$^{-1}$), k is the thermal conductivity (W (m K)$^{-1}$), t is the time (s), x is the direction of the heat transfer along the sample, Q_h is the internal heat generation rate (W m^{-3}).

Here Q_h is only related to the dehydration of the dihydrate under the tested temperature range, which has been investigated in Chapter 4. It is obvious that the product of the density (ρ) and the specific heat capacity ($C_{T,p}$) is the volumetric heat capacity, which is used in the present thesis to investigate the thermal properties of the material (see Chapter 4 as well as the previous sections in this chapter). So, the measured thermo physical properties of the tested samples can be used as an indicator for the heat transfer through the solid materials, termed heat transfer indicator, reading

$$i_{heat} = \frac{k}{\rho C_{T,p}} \tag{5.6.4}$$

The values for the tested samples can be calculated here, noting at room temperature or before the dehydration reaction of the dihydrate. The relevant values of the thermal conductivity and volumetric heat capacity of the SGLC are presented in the previous section. The average value of the specific heat capacity of pure gypsum plasterboard (1355 J (kg K)$^{-1}$) presented in Chapter 4 is used here to obtain more representative results. The density and the thermal conductivity values of the tested dihydrate are taken from Table 4.2 in Chapter 4. The calculated i_{heat} is listed in Table 5.8. It can be seen that, during the first 20 minutes, the temperature increase in all the samples is similar, which is in line with the similar obtained values here considering the possible measure error during the fire test.

Table 5.8: Calculated heat transfer indicator.

Sample No.	Type	i_{heat}	
		Before dehydration	**After dehydration**
q = 0.20	SGLC	0.308×10^{-6}	0.242×10^{-6}
q = 0.25	SGLC	0.200×10^{-6}	0.206×10^{-6}
q = 0.30	SGLC	0.213×10^{-6}	0.218×10^{-6}
q = 0.35	SGLC	0.274×10^{-6}	0.222×10^{-6}
$w_0/h_0 = 0.65$	Gypsum plasterboard	0.238×10^{-6}	0.224×10^{-6}
$w_0/h_0 = 1.00$	Gypsum plasterboard	0.207×10^{-6}	0.200×10^{-6}

However, this indicator becomes invalid from the time that dihydrate starts losing the chemically combined water, which leads to the change of the physical properties of the tested materials including densities, thermal conductivities and specific heat capacities. However, the physical properties are measured in the case of the samples after the full dehydration (i.e. the complete loss of the chemically combined water from dihydrate, presented in Chapter 4 and previous section in this chapter). Therefore, the heat transfer indicator can be calculated again, and the results are also listed in Table 5.8. The thermo physical properties here are measured by a procedure of heating the samples in the oven at the dehydration temperature until the mass becomes constant (detailed information is presented in Chapter 4).

During the fire test, the crystallized water is gradually lost from the matrix; therefore the thermo physical properties are changing as a function of time. However, this has not been addressed so far (Mehaffey et al., 1994; Ghazi Wakili et al., 2007), and is not addressed in the presented thesis as well, so it is not possible to assess when the samples become fully dehydrated here. Nevertheless, one can see the agreement between the calculated results and the temperature increase in time (Figure 5.17). In the case of a pure gypsum board, in Figure 5.17 it can also be seen that the heat transfer is becoming faster and faster, especially in the case of the gypsum board produced from a w_0/h_0 of 1.00, the temperature increases sharply from 80 minutes on. This is in line with Mehaffey et al. (1994), who reported a swift increase of the thermal conductivity when the temperature increases above 400 °C. It is also evident that the sample (SGLC, q=0.25) has the lowest temperature increase rate from Figure 5.17, which is also confirmed by the calculated heat transfer indicator (Table 5.8).

5.8 Discussion

Distancing from traditional methods to reinforce gypsum boards, the present Thesis aims to develop a type of novel lightweight composite using β-hemihydrate as binder with an improved performance to be used as indoor wall board, fire separation structures, ceiling etc. The modified A&A grading curve has already been applied extensively for concrete mix design, while here it is applied to design this composite with β-hemihydrate as binder instead of cement. To the author’s knowledge, this has never been reported before. Depending on the desired performance, different distribution moduli were recommended for the concrete mix design (Villar and Baret, 1997; Hüsken, 2010; Hunger, 2010; Fennis, 2011). As a binder, hemihydrate behaves very differently from cement, therefore in the present study the effect of the distribution modulus is investigated as well.

The experiments are performed focusing on the targeted objectives: low density, good mechanical properties, and good thermal properties (e.g. low thermal conductivity). As indicated by the results presented in the previous sections, the distribution modulus indeed influences the designed composite significantly. As indicated from Figure 5.9, increasing the distribution modulus leads to a reduction of the density of the composite. Hence, it seems wise to use a larger distribution modulus if we only consider the density as the key factor. However, as shown in Figure 5.12, an increase of the distribution modulus results in a swift decrease of both the compressive and flexural strength of the composite. Thus, a smaller value of q should be considered if only strength is the target value. Therefore, taking both density and strength into account, one already can see that an intermediate value of q should be used. Then, considering a thermo physical property such as thermal conductivity, as shown in Figure 5.14a, it is obvious that we should not use the smallest distribution modulus investigated here, since at that value the composite has the highest thermal conductivity. So taking all these three factors into consideration, it is already very clear that a distribution modulus of 0.25 provides optimal results.

The question then rises here, whether it is useful to apply this mix design method for the calcium sulfate-based composite design when we have already found an optimal value for the distribution modulus. This can be answered from the comparison of strength, density, and thermal conductivity between the currently developed composite and the normal or traditional gypsum board, as shown in Figures 5.9b and 5.13, as well as in Figure 5.15. The significant improvement of all the investigated properties clearly indicates that this mix design method works not only for concrete mix design but also for this calcium sulfate-based composite design. The fire behavior presented in Section 5.7 confirms the novel mix design idea. It is clearly shown that even after 100 minutes (fire test following ISO 834-1), the temperature increase is lower in the case of the designed SGLC.

It is different from concrete design where some constraints usually have to be considered from the point of relevant regulations or practical situation. In the present study all the considerations are only taken from the point of view of the performance of the designed composite. For instance, in concrete design the used cement content should not reach a minimum or maximum given value. Here, a large amount of β-hemihydrate is used; on one hand it provides more binder as well as fine powders to ensure a good viscosity to resist the floating of the applied lightweight aggregates in fresh state, and on the other hand it helps to reduce the cost of the composite.

5.9 Conclusions

In this chapter, a new design method of the calcium sulfate-based lightweight composite is presented. The following conclusions are drawn:

- A mix design methodology originally for concrete design is introduced. The mix design applies the geometric packing theory as the basic principle and the effect of the parameters in the mix design model is discussed; several mixes of the composite designed using different distribution moduli are presented.
- The water demand of the solid ingredients is determined applying the mini-slump flow test; a water layer thickness is found for the designed mixes for the onset of flowing and its difference between the composite mixes and pure calcium sulfate hemihydrate is analyzed.
- The fresh behavior of the designed mixes is investigated, the effect of the used superplasticizer is studied and an optimal superplasticizer dosage is found.
- The density as well as the void fraction of the developed composite in its hardened state is studied by both modeling and experiments; a relation between the void fraction and the density is derived.
- The mechanical properties of the new composite are investigated, a comparative study on strength is performed on the composite and traditional gypsum board; and the effect of the applied distribution moduli on the strength is discussed; a critical void fraction of 0.73-0.77 for dihydrate produced from β-hemihydrate to retain the minimum strength is found.
- The thermo physical properties of the new composite are investigated. The effect of the used distribution moduli is analyzed; a link between the density and the thermal properties is derived.

- The thermal degradation of the designed samples beyond the dihydrate dehydration temperature is studied. The comparison between the developed SGLC and traditional gypsum plasterboards from both the thermo physical properties and the thermal degradation behavior indicates the superiority of the developed SGLC.
- The fire behavior of the developed composite is studied by performing the real fire test following ISO standard 834-1. The lower temperature increase rate compared to the reference gypsum plasterboard confirms again the validity of the mix design method applied here.

Chapter 6

A comparative study on the binders cement and calcium sulfate

6.1 Introduction

In this chapter, different from the previous chapters where calcium sulfate is studied, cement is addressed, which is used as binder to develop a cement-based lightweight composite. The reason here is to provide an insight from a different angle into the performance of the designed calcium sulfate-based lightweight composite.

Concrete, by far, is one of the most used manmade building materials. Lightweight aggregates concrete (LWAC) has its roots in the ancient period about 3000 years ago when volcanic materials were used as lightweight aggregates (Chandra and Berntsson, 2003). Because of its many advantages such as low density, good thermal insulation and good fire resistance, LWAC has been widely developed and applied as both structural and nonstructural material recently. However, so far there is still no systematic study on LWAC regarding mix design methodology. Furthermore, there are usually two objectives to the design of the LWAC, either to achieve as low thermal conductivity or as low density as possible or to achieve as strong mechanical properties as possible, but no studies have been reported, to obtain a LWAC with a low density while retaining sufficient mechanical properties.

Among various types of lightweight aggregates (LWA), LWA produced from a special industrial process such as Leca (UK), Liapor (Germany) and Liaver (Germany) are widely used in LWAC production because of certain special features created during this production process (EuroLightCon, 2000). Here, a lightweight material produced from recycled glass via a special procedure is used as LWA. The addressed products are defined as composites rather than concrete because the largest particle size used in the mixes is only 4 mm.

In Section 6.2, the mix design as well as the properties of the developed cement-based lightweight composites (CLC) will be presented and analyzed. Two different types of CLC, including self-compacting cement-based lightweight composite (SCLC) and vibrated cement-based lightweight composites (VCLC), are developed to compare the properties and the applied mix design methodology. In Section 6.3, a comparative study on the used binder type, whether hemihydrate or cement, is presented.

6.2 Design of cement-based lightweight composites

6.2.1 Introduction

The mixes of the CLC are designed applying the same design methodology as presented in Chapter 5. Nevertheless there is a clear difference, as already discussed before, as the water content in the present mix design is determined following the normal concrete design method, which will be discussed in the following sections.

Firstly the proportion of the solid ingredients will be preliminarily determined in Section 6.2.2, using the same design algorithm as presented in Chapter 5; in Section 6.2.3 the fresh state behavior of the developed mixes is investigated, including the effect of water content and dosage of the superplasticizer, and the final mix design is derived based on this analysis; in Section 6.2.4 the properties of the designed CLC in its hardened state are analyzed including porosity, mechanical property and thermal property; and in Section 6.2.5 a discussion is presented.

6.2.2 Design of the solid ingredients

Materials

The cement used in this study is Ordinary Portland Cement (OPC) CEM I 52.5 N, provided by ENCI (the Netherlands). A polycarboxylic ether based superplasticizer is used to adjust the workability. The lightweight aggregates (the same materials as used in the previous chapter) used here are produced from recycled expanded glass. Limestone is used as filler to increase the powder amount. Normal aggregates used are broken sands with two different fractions of 0-1 mm and 0-4 mm and micro-sand with the maximum particle size of 1 mm (Graniet-Import Benelux, the Netherlands). Detailed properties of all the used materials are already analyzed and are presented in Chapter 2. The used materials are summarized in Table 6.1 and Figure 6.1.

Table 6.1: Properties of materials used (*see detailed information in Table 6.2).

Material	Type	Specific density (kg m^{-3})
Cement	CEM I 52.5 N	3180
Filler	Limestone powder	2710
Fine sand	Micro-sand	2720
Fine sand	Sand 0-1 mm	2650
Coarse sand	Sand 0-4 mm	2650
LWA	Expanded glass	310-810*
Superplasticizer	Polycarboxylate ether	1100

The water absorption of LWA is normally an influential factor in the lightweight aggregates concrete design and production, since LWA absorb a certain amount of free water from the mixture before setting. It is shown that the water absorption of lightweight aggregates has a negative influence on the workability, if mixing them with other materials under dry conditions prior to adding water (Neville, 1995; EuroLightCon, 1998; Chandra and Berntsson, 2003; Liu et al., 2010). However, this negative effect is depending not only on the used amount of the lightweight aggregates, but also clearly on their type and production process. There are two mixing methods which are widely used to address this issue, i.e. either to presoak the LWA in water for a certain period, usually 30 minutes to 1 hour (Chandra and Berntsson, 2003, Zhang and Gjorv, 1991), or to add a certain amount of extra water which is calculated normally based on 1 hour water absorption (Liu et al., 2010). Both methods have disadvantages especially regarding the LWA used in this work. The presoaked LWA should be surface dried before mixing with other materials for the concrete production. But for the lightweight aggregates used here, this could cause considerable errors due to their very small particle size. Adding extra water from the beginning of the mixing process can easily cause segregation or bleeding of the mixture, especially in the case of self-compacting lightweight mortar or concrete. However, as listed in Table 6.2, the water absorption of the used LWA is quite low, especially in the first hour (approximately 1.0 wt. %), due to their quite closed external surfaces (see more detailed analysis of the water absorption of the used LWA in Chapter 2). Hence, the applied LWA will not affect the workability significantly, and on the other hand, the absorbed free water will contribute to the hydration process due to the so called internal curing effect. Therefore, in the present study, the LWA are applied in dry conditions directly to the mixture and no extra water is added.

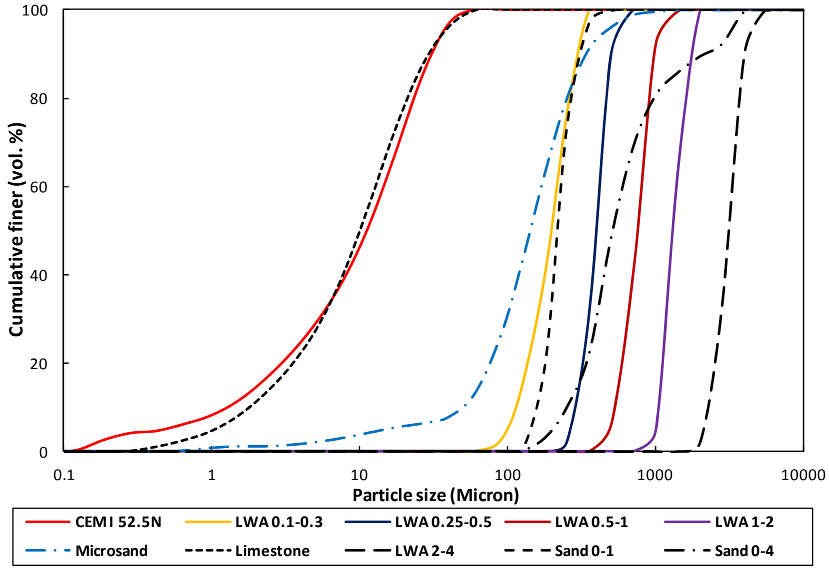

Figure 6.1: Particle size distribution of the used materials.

Preliminary design of the solid ingredients

Densities are strongly linked with thermal properties of lightweight concrete. Neville (1995) reported that there is an almost linear relation between the thermal conductivity and the density of lightweight concrete produced with different types of lightweight aggregates such as pumice, permite, vermiculite, cinders, expanded shale, and expanded slag. Loudon (1979) also reported that, despite the effect of the type of the used lightweight aggregates, the thermal conductivity of lightweight concrete decreases when its density decreases. Therefore, here the effect of density on the investigated properties is taken into consideration. Two types of composites with different workability properties are developed here, which are self-compacting and conventionally vibrated, to investigate the influence of the water content and the used distribution modulus. As from Neville (1995) and Lydon (1982), the strength of concrete is related with the cement content in the matrix. The compressive strength of lightweight concrete produced from expanded clay and sand increases from 12 to 25 N mm^{-2} when the cement content increases from 250 to 480 kg m^{-3} (Neville, 1995). Therefore, in the present study the used cement content is set as a fixed, economically acceptable value, in order to minimize the effect of its dosage on the investigated targets.

Table 6.2: Characteristics of lightweight aggregates used (*taken from the provider).

LWA type	Particle size (mm)	Dry particle density* (kg m^{-3})	1 h water absorption (wt.%)	24 h water absorption (wt.%)
LWA 0.1-0.3	0.1-0.3	810	1.06	2.81
LWA 0.25-0.5	0.25-0.5	540	0.88	3.90
LWA 0.5-1.0	0.5-1.0	450	1.59	8.50
LWA 1.0-2.0	1.0-2.0	350	1.71	7.63
LWA 2.0-4.0	2.0-4.0	310	0.55	7.80

It is recommended (EFNARC, 2005) that a water/powder ratio by volume of 0.85-1.10 is a suitable starting value for the water content determination in order to design self-compacting concrete, which is also confirmed by Hunger (2010) who reported an optimal water/powder ratio by mass of 0.30. Due to the high fluidity, self-compacting concrete/mortar normally has a risk of segregation and blockage, which can be prevented by the use of a sufficient amount of fines (defined as particles with a size smaller than 125 μm). Hence, in the present study, the water amount, i.e. water/powder ratio is chosen as one of the research topics, and different water contents are used to investigate its effect.

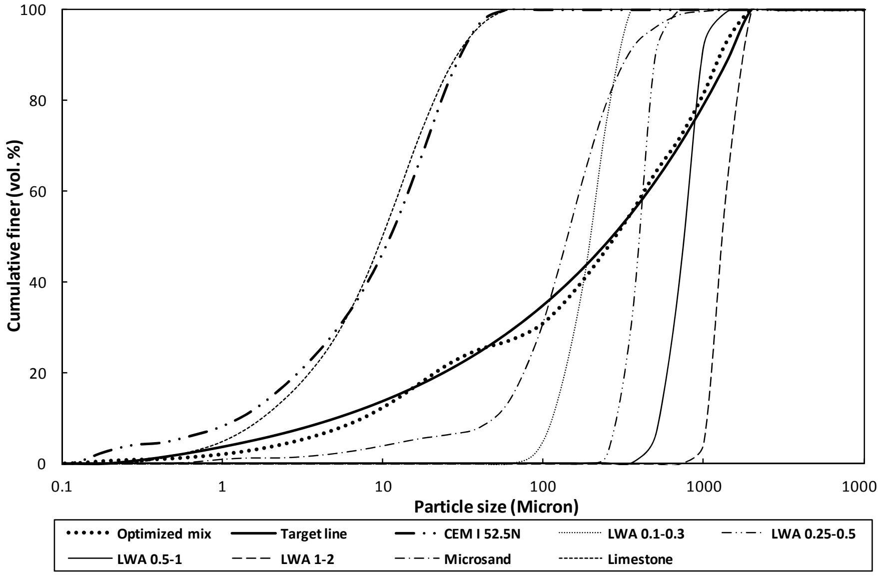

Figure 6.2: Particle size distribution of the used materials and the composed mix SCLC1 and target line with q=0.32.

For the distribution modulus used in the A&A grading equation, Hunger (2010) recommended a value of 0.25 for the mix design of self-compacting concrete. As discussed previously, a smaller distribution modulus leads to a mixture with a larger amount of fines. Thus, here two different values of 0.25 and 0.32 are applied in SCLC mixes as the preliminary design values to study their effect. For the vibrated lightweight composite design, a larger distribution modulus value of 0.35 is used, which is usually suitable for conventional vibrated concrete design (Villar et al., 1997). A much lower water content is chosen (water/cement ratio of 0.35 by mass), because on one hand this value is often used in conventional vibrated concrete design, and on the other hand a comparable density of this mix to mix SCLC2 is set in order to study the relation between density and other properties.

Therefore, applying the optimization algorithm, a preliminary design of the solid materials of three mixes is derived here. The designed grading line as well as the PSD of the used materials is shown in Figure 6.2, using mix SCLC1 as an example (Table 6.3), with the absolute amount of all the materials ready to be varied by adjusting the water content and superplasticizer (SP) dosage in order to achieve the desired flowability.

6.2.3 Fresh state behavior

The fresh state behavior analysis of the designed mixtures, especially in the case of the self-compacting composites, is essential because only by this step the final water content as well as the dosage of the superplasticizer can be determined. To reach the desired workability, the designed mix must have an optimal balance between the water content and the SP dosage. Insufficient dosage of the SP results in insufficient flowability; however, overdosing SP may lead to segregation, bleeding, blockage or to a negative influence on the hydration process. For normal weight self-compacting mortar, two workability parameters are usually investigated, i.e. the slump flow and the funnel time, which are used to assess the flowability and relative viscosity of the mixture, respectively. In the present study, these two parameters are also employed for the mix development.

Normally, lightweight aggregates absorb a certain amount of water due to their open pores, but the LWA used in the present study have a very low water absorption, especially in the early stage due to their rather closed external surfaces (Table 6.2). The water absorption of the LWA after contacting with water for 6 min, which is about the time to perform the mini-slump flow and V-funnel test, is only approximately 0.2% by mass, which indicates that the influence of the water absorption on the measured slump flow spread and V-funnel time can be neglected.

The mini-slump flow test, performed in order to investigate the flowability of the designed composite, is carried out employing the Hägermann cone. Tregger et al. (2008) investigated the rheological properties of self-compacting cement paste using the mini-slump flow test, and reported that the spread of the sample becomes stable at the time of 20 sec, which is in line with the duration of the measurement performed here. The relative viscosity and blocking behavior of the sample is investigated by carrying out the V-funnel test with sizes shown in Figure 6.3, following the procedure described in EFNARC (2005) for mixes with the maximum particle size smaller than 4 mm.

Varied slump flow values from 240 mm to 330 mm and V-funnel times from 4 s to 11 s are reported for self-compacting normal weight aggregates concrete production (Walraven et al., 1999; Ankone, 2000; BFBN, 2001; EFNARC, 2002; EFNARC, 2005; Brouwers and Radix, 2005; Hunger, 2010). Different from self-compacting normal weight aggregates concrete, a great amount of fines is needed to bound the LWA in order to avoid the segregation of the developed composite due to the very low density of the LWA (see Table 6.2). Therefore, the viscosity of the mixture can be higher than for normal SCC concrete. Hence, in the present study a slump flow value of 300 mm and V-funnel time value of 9-11 s are chosen as the target values.

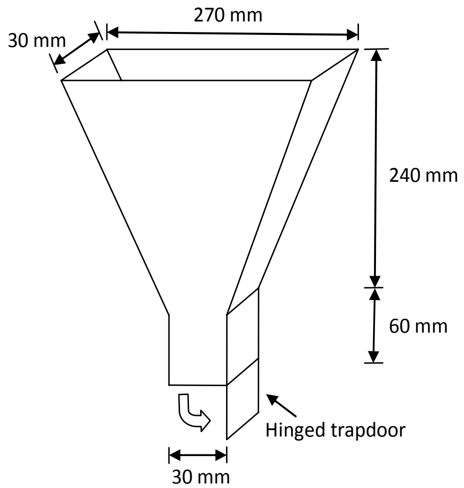

Figure 6.3: Sizes of used V-funnel with the volume of 1.13 L.

By slightly modifying the proportion of the solid ingredients and changing the amount of SP or the water content, trial experiments are performed in order to achieve the above mentioned target values. A maximum effective SP dosage of 1.0% by mass of the cement content is found here. The slump flow remains constant when increasing the SP amount from 1.0% up to 1.5% by mass of cement. Actually, this addition (1.0%) is also the recommended value by the SP producer. This is in line with Hunger (2010), who reported that from a certain dosage of superplasticizer (1.5% based on the cement content), the mixture (self-compacting mortar) will not respond anymore with an increase of the slump flow. This indicates that overdosing SP will not contribute to the flowability; on the contrary, it might cause problems such as segregation and delayed setting time.

The water content is modified in order to reach the desired density and the target flowability. The spread flow increases from 250 mm to 300 mm and V-funnel time decreases from 11 s to 6 s when the water/cement ratio increases from 0.45 to 0.60 with a fixed SP dosage of 1.0% by mass of cement; a water/cement ratio of 0.59 is finally selected to be used in the mix of SCLC1. The spread flow increases from 300 mm to 340 mm while the V-funnel time decreases from 16 s to 10 s when the water/cement ratio increases from 0.51 to 0.60 with a fixed SP dosage of 1.0% by mass of cement. A water/cement ratio of 0.54 is finally selected for the mix of SCLC2 based on these results.

Hunger (2010) reported a V-funnel value between 4 and 6 s for a self-compacting cement mortar using normal weight aggregates, and he reported that a value of around 7.5 s already causes the blockage of the V-funnel, which apparently is shorter than the time obtained here, especially in the case of mix SCLC2. This can be explained by the large amount of powders used in these two mixes compared to the powder content used in the self-compacting mortar in Hunger (2010). The distribution modulus of 0.25 is used for the design of the mix SCLC2, which results in an even larger powder content in this mix than that of SCLC1, as can be seen in Table 6.3. However, to use such a large amount of fine materials is necessary to avoid the segregation of the mixture. This also indicates that the low values recommended by Hunger (2010) are less suitable for self-compacting lightweight mortar design.

Table 6.3: Dosages of the developed mixes.

Material	SCLC1 (kg m^{-3})	SCLC2 (kg m^{-3})	VCLC (kg m^{-3})
CEM I 52.5 N	425.3	423.5	419.7
Limestone powder	111.9	259.6	0
Sand 0-4	0.0	0	407.0
Sand 0-1	0.0	95.6	0
Microsand	381.5	424.6	306.0
LWA 0.1-0.3	56.0	68.3	0
LWA 0.25-0.5	44.8	0	0
LWA 0.5-1.0	56.0	54.9	0
LWA 1.0-2.0	44.8	39.4	63.6
LWA 2.0-4.0	0.0	0	71.6
Water	250.9	230.3	159.4
Superplasticizer (wt. % of cement)	1.0%	1.0%	0.8%
Water/cement ratio	0.59	0.54	0.38
Water/powder ratio	0.35	0.26	0.29
Distribution modulus	0.32	0.25	0.35

For the VCLC, two target values are used here, i.e. the density and the flow determined on a jolting table. The target density of the VCLC is chosen to be similar to the SCLC2 in order to compare their properties in hardened state. The flow test is carried out using a Hägermann cone and a jolting table (15 jolts) with a target flow value of 150 mm. Based on these, a final water/cement ratio of 0.38 is chosen and a SP dosage of 0.8 wt.% of cement. Hence, the final determined mixes of these composites are listed in Table 6.3.

6.2.4 Hardened state properties

Porosity

Figure 6.4 shows the schematic diagram of the designed CLC. As can be seen, the CLC is composed of lightweight aggregates, cement paste, sand, inert filler, and air. In the matrix, the porosity originates from both the internal porosity of LWA and from the porosity of the cement paste. Chandra and Berntsson (2003) reported that the exchange of air and water during the water absorption resulted in a rim of air bubbles in the interfacial transition zone (ITZ) of the lightweight aggregates concrete. However, this does not seem to occur here, which will also be analyzed later. So here the porosity of the ITZ in the composite is assumed to be very small and therefore not considered in the calculation.

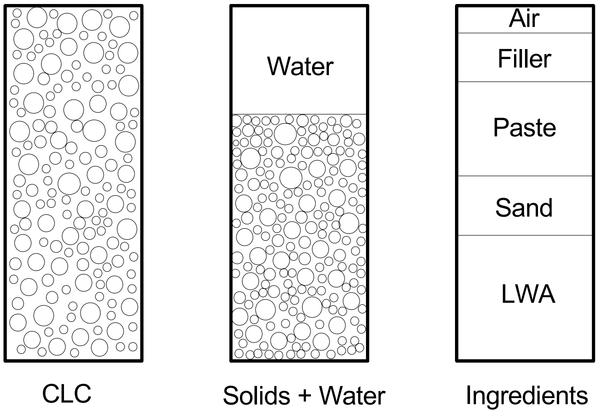

Figure 6.4: Schematic diagram of the volume composition of the CLC.

The internal porosity of the LWA is calculated from Equation (5.4.2) presented in Chapter 5, which is rewritten as follows:

$$\varphi_{v,lwa} = \sum_{i=1}^{n} \varphi_{v,lwa,i} \times \varphi_{lwa,i} = \sum_{i=1}^{n} \left[\frac{V_{lwa,i}}{V_{CLC}} \times (1 - \frac{\rho_{lwa,i}}{\rho_{slwa}}) \right] \tag{6.2.1}$$

where $\varphi_{v,lwa}$ is the porosity introduced by LWA in the designed composites, $\rho_{lwa,i}$ (g cm^{-3}) is the apparent density of aggregate particles in fraction i, ρ_{slwa} (g cm^{-3}) is the specific density of the aggregate raw material, $V_{lwa,i}$ and V_{CLC} are the volumes of the used LWA in different size ranges and volume of the designed CLC, respectively.

The porosity resulted from the hydration of cement consists of two parts: the capillary porosity and the chemical shrinkage porosity due to cement hydration, which can be described using a model proposed by Brouwers (2004), reading

$$\varphi_v = \varphi_w + \varphi_s = \frac{\frac{w_0}{c_0} - n(\frac{w_d v_d}{v_w c})}{\frac{v_c}{v_w} + \frac{w_0}{c_0}} \tag{6.2.2}$$

where φ is the volume fraction, w_0/c_0 is the initial water/cement ratio by mass, c is the hydrated cement content, υ_d is the specific volume of the compressed water (here meaning gel water + nonevaporable water) (cm^3 g^{-1}), υ_c is the specific volume of the cement (cm^{3}g^{-1}) (here a value of 0.314 cm^{3}g^{-1} is obtained from the specific density of the used cement, see Table 6.1), υ_w is the specific volume of water (cm^3 g^{-1}) (here a value of 1.0 cm^3 g^{-1} is used), w_d is the reacted water (g), n is the hydration degree, subscript v is the void fraction, w is the capillary water and s is the chemical shrinkage.

Brouwers (2011) proposed an expression to compute $(w_d v_d)/(v_w c)$ in Equation (6.2.2) under the assumption of congruent hydration, reading

$$\frac{w_d v_d}{v_w c} = 0.284x_{C_3S} + 0.301x_{C_2S} + 1.141x_{C_3A} + 0.387x_{C_4AF} + (0.320\alpha_0 - 0.082)x_{C\overline{S}} \qquad (6.2.3)$$

where x is the mass fraction, subscripts C_3S, C_2S, C_3A, C_4AF, $C\overline{S}$ are alite, belite, aluminate, ferrite and anhydrite, respectively and α_0 is the degree of carbonation of the monosulfate phase. The mass fraction of the above mentioned five phases are calculated using the Bogue method and the chemical composition of the used cement obtained from the provider ENCI (Hunger, 2012) (see Table 2.3 in Chapter) assuming a free lime content of 0.7%, and the results are listed in Table 6.4. The degree of carbonation of the monosulfate phase (α_0) is assumed as zero due to the short curing period of 28 days. Hence $(w_d v_d)/(v_w c)$ is calculated, yielding 0.330.

Table 6.4: Composition of the used CEM I 52.5 N.

Cement type	x_{C_3S}	x_{C_2S}	x_{C_3A}	x_{C_4AF}	$x_{C\bar{S}}$
CEM I 52.5 N	0.571	0.142	0.082	0.091	0.039

Therefore the porosity of the designed lightweight composites can be calculated from

$$\varphi_{v,CLC} = \varphi_{v,lwa} + \varphi_{v,paste} \qquad (6.2.4)$$

where $\varphi_{v,CLC}$ is the porosity of the designed composites, $\varphi_{v,lwa}$ is the porosity contributed by the LWA, and $\varphi_{v,paste}$ is the porosity contributed by the paste, and $\varphi_{v,paste} = \varphi_v \times \varphi_{paste}$. The results are listed in Table 6.5. Here the hydration degree is assumed as 0.7 based on a curing age of 28 days (Chandra and Berntsson, 2003).

Table 6.5: Theoretical porosity of the designed CLC (here φ_{paste} is calculated from the paste volumetric proportion in the mix design).

Mix	$\varphi_{v,LWA}$ (%)	φ_v (%)	φ_{paste} (%)	$\varphi_{v,CLC}$ (%)
SCLC1	32.23	39.71	0.385	47.50
SCLC2	25.25	36.18	0.363	38.40
VCLC	35.76	21.47	0.291	42.01

The porosity of the designed CLC is measured applying the vacuum-saturation technique, i.e. to saturate the accessible pores with water, as this method is referred to as the most efficient saturation method (Safiuddin and Hearn, 2005). Samples with a format of a disc (with a height of 10 - 15 mm, and a diameter of 100 mm) are extracted from the inner layer of three 150 mm cubes for each prepared lightweight composite.

The test is carried out on 3 samples for each mix, following the standards NT Build 492 (1999) and ASTM C1202 (2005). The following test procedure is employed:

- Place the samples in a dessicator and apply a pressure of 40 mbar (the pressure should be lower than 50 mbar according to the standard) for three hours;

- Fill in slowly the dessicator with water (with the pump still connected and running) until approximately 10 mm more than the top surface of the samples;
- Maintain the pressure for an additional hour, then turn the pump off;
- Let the samples soak in water for 18 hours;
- Measure the mass of the surface dry samples in air;
- Measure the hydrostatic mass of the samples (in water);
- Dry the sample in an oven at 105 °C until a constant mass is reached, then measure the mass.

The water permeable porosity is calculated from

$$\varphi_{v,water} = \frac{m_s - m_d}{m_s - m_w} \times 100, \tag{6.2.5}$$

where $\varphi_{v,water}$ is the water permeable porosity (%), m_s is the surface dried mass of water-saturated sample in air (g), m_w is the mass of water-saturated sample in water (g), and m_d is the mass of oven dried sample (g).

Table 6.6: Porosity results measured using vacuum-saturation method.

Mix	Sample number	m_s (g)	m_w (g)	m_d (g)	Porosity $\varphi_{v,water}$ (%)	Average $\varphi_{v,water}$ (st. dev.) (%)
SCLC1	1	140.78	56.74	111.42	34.94	34.31 (1.62)
	2	140.90	53.45	109.84	35.52	
	3	137.00	49.97	108.74	32.47	
SCLC2	1	180.28	81.72	145.37	35.42	34.97 (2.05)
	2	199.51	101.32	167.38	32.72	
	3	187.37	88.77	151.13	36.75	
VCLC	1	168.29	71.87	138.95	30.43	30.65 (0.26)
	2	168.61	72.72	138.94	30.94	
	3	172.67	74.86	142.75	30.59	

The results are listed in Table 6.6. It can be seen that all the values are larger compared to conventional concrete, for instance Safiuddin and Hearn (2005) reported a porosity of 20.5% of the concrete produced with a water/cement ratio by mass of 0.60 employing the same measurement method, i.e. vacuum-saturation technique. This is attributed to the large internal porosity of the LWA (Table 6.5). Although the external shell of the used LWA is rather closed and impermeable, it still contains some interconnected openings (Figure 6.5, and also analysis in Chapter 2), through which liquids can enter the aggregates. The inflow of water into the LWA is even more efficient during the vacuum-saturation process, however there is also a risk that the applied low pressure will damage the outer shells of the aggregates, exposing closed pores and increasing the real permeable porosity.

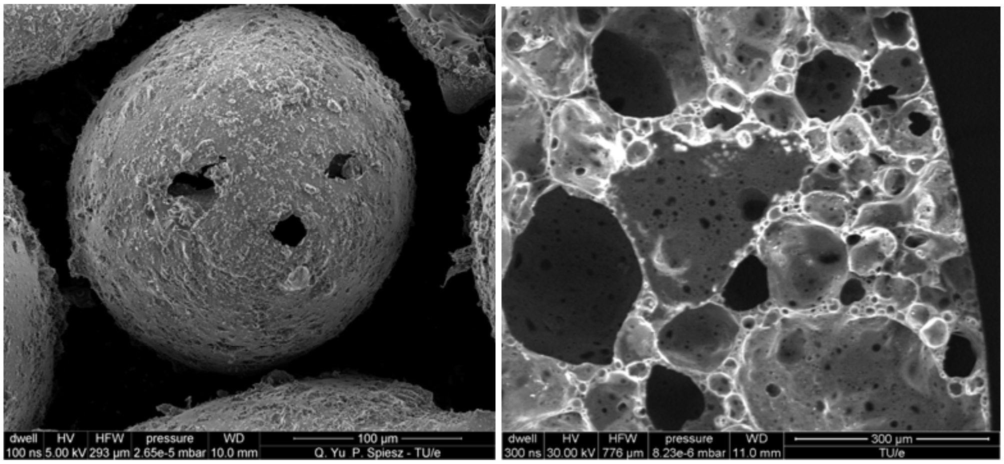

(a) (b)

Figure 6.5: SEM pictures of LWA (a: open pores seen from outside; b: interconnected pores).

The measured water permeable porosities are similar for the two self-compacting composites, 34.31% and 34.97% in average for SCLC1 and SCLC2 respectively; while for the VCLC it is slightly lower, 30.65% in average, as shown in Table 6.6. Nevertheless, all the measured values of the permeable porosities are smaller than the calculated corresponding values, as listed in Table 6.5. This indicates that some of the pores in the used LWA are closed and not accessible to water transport.

It is shown in Table 6.5 that both SCLC1 and SCLC2 have similar porosities contributed by the paste due to the similar water/cement ratios used in these two mixes, while the calculated total porosity of SCLC1 is larger than SCLC2. However, their measured water permeable porosities are similar. As can be seen from Table 6.3, 82.90 dm^3 LWA with the size of 0.25-0.5 mm are used in mix SCLC1 while zero in mix SCLC2, besides a similar amount of the used LWA in the fractions of 0.5-1 mm and 1-2 mm in both SCLC, which results in the porosity difference of these two SCLC. This indicates that the used LWA with the size of 0.25-0.5 mm is quite water impermeable, and the pores inside the particles are mostly closed pores, and this is in line with the water absorption test results (see Table 6.2). Another possible reason is attributed to the larger amount of the LWA 0.1-0.3 used in mix SCLC2. It can be seen that the particle sizes of fraction LWA 0.1-0.3 are very small (40% of the particles are smaller than 125 µm, as seen from Figure 6.1), which creates more chances to be interconnected through the permeable paste.

The measured water-permeable porosity of VCLC is the smallest for all three mixes, which can also be explained by the mix design. As shown in Table 6.3, only fractions of LWA with the larger size of 1-2 mm and 2-4 mm are used in the VCLC. Therefore the interconnection possibilities between particles are reduced to some extent, and besides the water transport route is reduced also due to the small capillary porosity of the paste (see Table 6.5).

Mechanical properties

Figure 6.6 shows the compressive and flexural strength development of the lightweight aggregates composites as a function of the curing age. All these three mixes have a similar feature of a quite fast early stage strength development. The compressive strength of the mixes SCLC1 and SCLC2 after 24 hours curing reaches 58.8% and 57.1% of their compressive strength at 28 days, respectively, while the compressive strength of VCLC reaches even 74.5% of its value at 28 days after 24 hours curing.

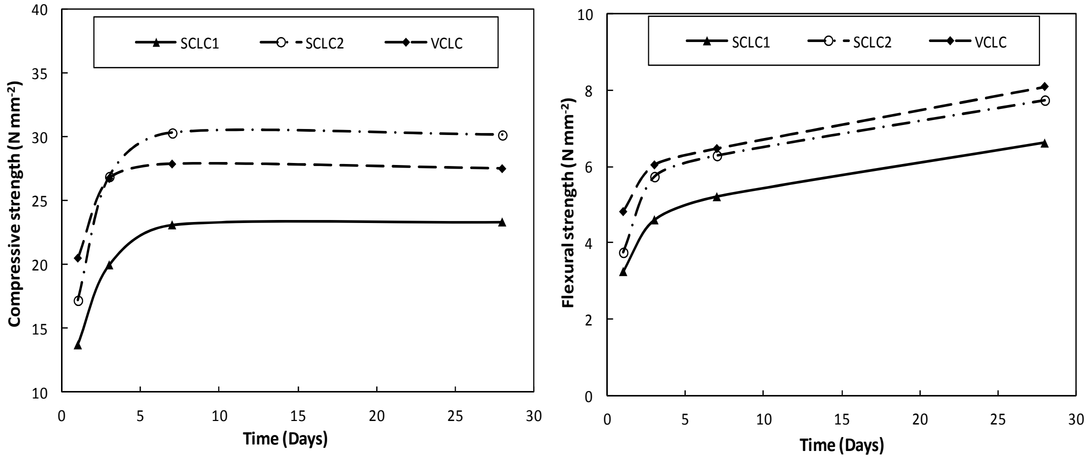

(a) (b)

Figure 6.6: Strength of the CLC (a: compressive strength; b: flexural strength).

The fast strength development during the early stage probably can be explained by the used lightweight aggregates. The porous structure of the used LWA allows absorption of water into their pores, so then the absorbed water can be used later for “internal curing” during the hardening process (Chandra and Berntsson, 2003). Chandra and Berntsson (2003) reported that the exchange of air and water during the water absorption resulted in a rim of air bubbles in the interfacial transition zone (ITZ) of lightweight aggregates concrete. However, this does not occur in the present study, as shown in Figure 6.7. This contributes to a better strength development of the designed composites.

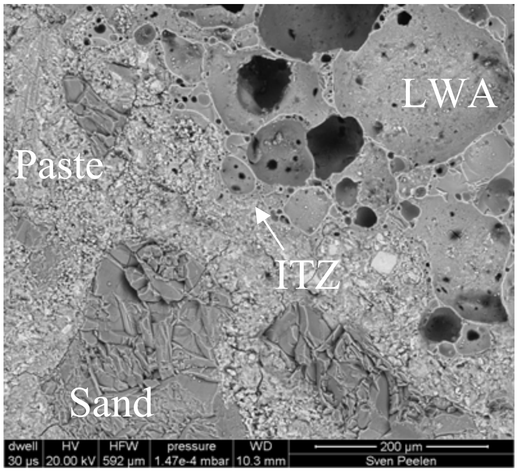

Figure 6.7: SEM picture of the transition zone of VCLC.

Another remarkable finding is that the compressive strength of all the three mixes already reaches the maximum value at the age of only 7 days, as can be seen in Figure

6.6a. This is confirmed by Liu et al. (2010), who observed very similar phenomena using the same type of expanded glass as aggregates. A statistic comparison of the strength development of the lightweight concrete containing different types of LWA is presented here, and the results are shown in Figure 6.8.

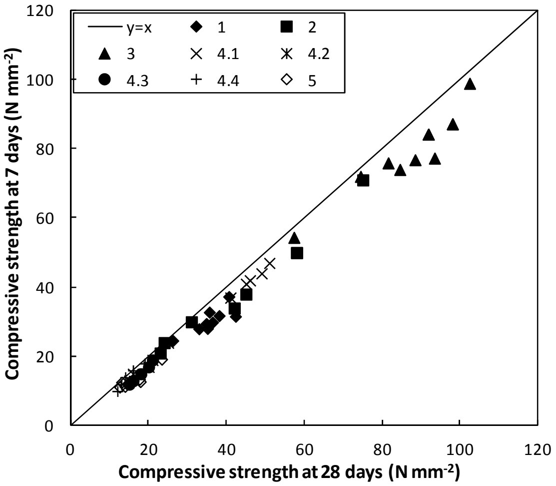

Figure 6.8: Strength comparison between the age of 7 days and 28 days of lightweight concrete using different types of LWA: 1: Expanded clay (Chandra and Berntsson, 2003); 2: Expanded clay (Liu et al., 2010); 3: Expanded clay (Zhang and Gjorv, 1991); 4.1: Recycled stone (Topcu and Uygunoglu, 2010); 4.2: Pumice (Topcu and Uygunoglu, 2010); 4.3: Tuff (Topcu and Uygunoglu, 2010); 4.4: Diatomite (Topcu and Uygunoglu, 2010); 5: Expanded polystyrene (Kan and Demirboga, 2009).

It is clearly shown that the lightweight concrete, although produced from different types of LWA, has the similarity of fast strength development at early ages. This feature becomes more significant especially in the case of the compressive strength at 28 days of lightweight concrete being lower than 30 Nmm^{-2}. This probably can be attributed to the effect of the lightweight aggregates, i.e. the compressive strength of the lightweight composites is dominated by the strength of the used LWA and not the strength of the cement matrix anymore. This is also confirmed by the flexural strength results, as shown in Figure 6.6b. It clearly shows that the flexural strength of the three mixes is continuously increasing until the age of 28 days, which indicates that the hydration process is still progressing although the compressive strength does not increase anymore.

Table 6.7: Compressive strength, density and calculated structural efficiency of the lightweight aggregates composites.

Mix	Compressive strength (N mm^{-2})	Density (kg m^{-3})	Structural efficiency (N m kg^{-1})
SCLC1	23.3	1280	18.2
SCLC2	30.2	1460	20.2
VCLC	27.5	1490	18.8

As discussed in the previous section, for lightweight concrete or mortars, the compressive strength is strongly linked with the density, i.e. the compressive strength decreases with the decrease of the density. This relation is usually investigated using the so called structural efficiency, which is calculated from the ratio of the compressive strength at 28 days to the density. The structural efficiencies, as well as the values of the density of these three developed mixes and their relevant compressive strengths at 28 days are listed in Table 6.7. It can be clearly seen that, although the compressive strength and densities of the three mixes are different from each other, the calculated structural efficiencies are very close to each other. This may be explained by the used cement content in the lightweight composites. As presented in Table 6.3, the cement content in the present study is kept at the same low level, around 420 kg m^{-3}, for all the three mixes.

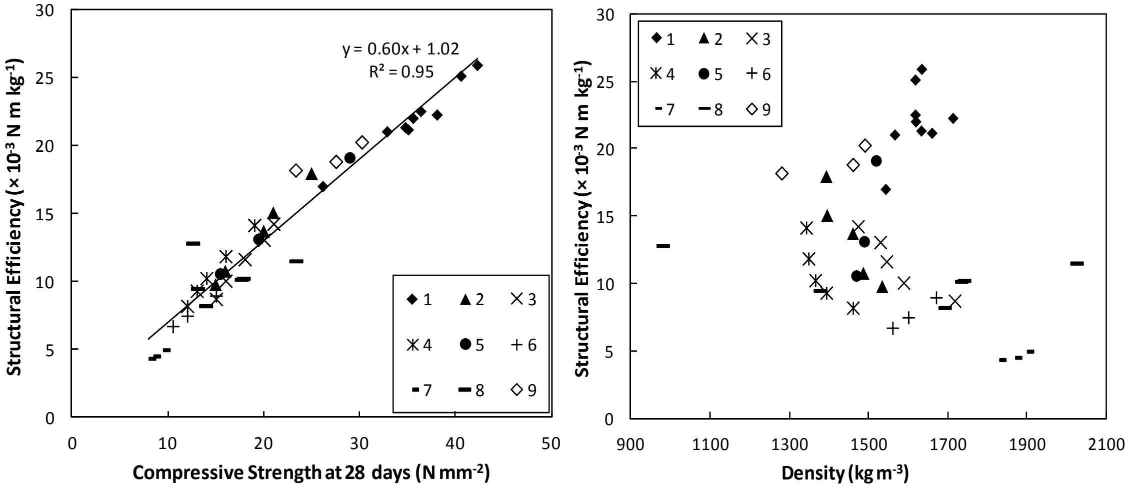

(a) (b)

Figure 6.9: Structural efficiency of lightweight concrete using different types of LWA ((a): versus compressive strength at 28 days; (b): versus density), note: 1: Expanded clay (Chandra and Berntsson, 2003); 2: Pumice (Topcu and Uygunoglu, 2010); 3: Tuff (Topcu and Uygunoglu, 2010); 4: Diatomite (Topcu and Uygunoglu, 2010); 5: Expanded clay (Alduaij et al., 1999); 6: Recycled bricks (Alduaij et al., 1999); 7: No fines (Alduaij et al., 1999); 8: Expanded polystyrene (Kan and Demirboga, 2009); 9: Present experimental results.

Further analysis of the structural efficiency is carried out using the lightweight aggregates concrete/mortar produced with different types of LWA, such as expanded clay, pumice, tuff, diatomite, recycled bricks etc. (Alduaij et al., 1999; Chandra and Berntsson, 2003; Kan and Demirboga, 2009; Topcu and Uygunoglu, 2010), and the results are shown in Figure 6.9. Surprisingly, it can be seen in Figure 6.9a that the structural efficiency has a rather good linear relation with the compressive strength of the lightweight concrete, although produced from different types of LWA. However, the structural efficiency of the lightweight aggregates concrete does not have any clear relation with their density, as can be seen from Figure 6.9b. This demonstrates that the compressive strength of lightweight concrete is not necessarily linked with its density, but more with the type of lightweight aggregates used. It also indicates that the structural efficiency is more dominated by the compressive strength of the lightweight concrete/mortar rather than its density.

Thermal properties

Thermal behavior is a key factor in the development and application of lightweight concrete. The thermal behavior of lightweight aggregates concrete is related to its thermal conductivity and its density, which in turn is influenced by its pore structure, i.e. the air-void system, aggregates and the matrix (Chandra and Berntsson, 2003). Therefore, the thermal conductivity is addressed in the present study as well.

The thermal conductivities of the three developed mixes are measured using the same heat transfer analyzer (ISOMET Model 2104) as presented in the previous chapters. Here the samples are first dried in an oven at 105 °C until the mass becomes constant, and then cooled down to room temperature for executing the thermal conductivity measurement. The average results are listed in Table 6.8.

Table 6.8: Thermo physical properties of the lightweight aggregates composites (*reference self-compacting concrete prepared with normal weight aggregates).

Mix	Density (kg m^{-3})	Thermal conductivity (W (m K)$^{-1}$)
SCLC1	1280	0.485
SCLC2	1460	0.738
VCLC	1490	0.847
Reference*	2300	1.700

It can be seen that, with the increase of the density, the thermal conductivity of the two SCLC increases. ACI committee 213R-03 (2003) and Topcu and Uygunoglu (2010) reported that the relation between the thermal conductivity and density follows an exponential relationship, which reads as:

$$\lambda = a_0 \times e^{b_0 \times \rho} \tag{6.2.6}$$

where λ is the thermal conductivity (W (m K)$^{-1}$), ρ is the density (kg m^{-3}) and a_0 and b_0 are parameters. ACI committee 213R-03 (2003) proposed the values of 0.072 and 0.00125 for a_0 and b_0, respectively, based on an investigation by Valore (1980).

Using the experimental values from Table 6.8 for SCLC1, SCLC2 and reference concrete, the values of a_0 and b_0 can be obtained employing the Solver function from Microsoft Excel$^{@}$, yielding a_0 and b_0 of 0.11 and 0.0012 respectively, with the coefficient of determination (R^2) of 0.99. The results are shown in Figure 6.10. It can be seen that the value of a_0 is larger than the recommended value from ACI committee 213R-03 (2003), but it is in line with the value reported by Topcu and Uygunoglu (2010), who derived a_0 (0.1242) and b_0 (0.0011) also based on self-compacting lightweight concrete.

However, the thermal conductivity of a material is related not only to the porosity or density of the matrix, but also to the thermal conductivity and particle shape of all the materials in the matrix. Therefore, the proposed expression (Equation (6.2.6)) can only be used to estimate the relation between density and thermal conductivity, which is also in line with many researchers such as Loudon (1979), and Chandra and Berntsson (2003) who reported a significant influence of the LWA type on the thermal conductivity.

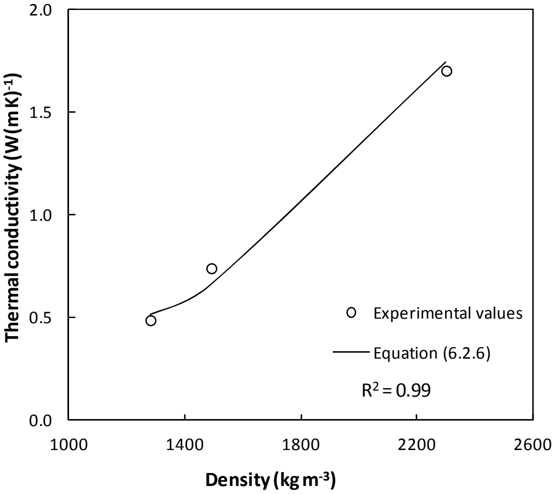

Figure 6.10: Thermal conductivity versus density (a = 0.11and b = 0.0012).

This is also confirmed by the thermal conductivity value of the VCLC, as listed in Table 6.8. With a similar density as SCLC2, the thermal conductivity of VCLC is 14.8% larger than that of SCLC2. This indicates that the expression (Equation (6.2.6)) is not suitable to compare concretes/mortars of different types; here the type means the design method. The larger thermal conductivity of the VCLC can be explained by the used mix design. Although the total porosity of SCLC2 and VCLC are comparable (see Table 6.5), it is obvious that the paste porosity of VCLC is much smaller, which is not surprising due to the low w_0/c_0 used in the mix of VCLC (see Table 6.3). This results in a much faster transport route for heat. Despite the fact that the internal porosity of LWA in VCLC is larger than that of SCLC2, the LWA in SCLC2 are better distributed because they are smaller, which contributes finally to the lower heat transfer rate. This is confirmed by the pictures of cut surfaces of the three composites shown in Figure 6.11, where it can be seen for instance that the LWA are denser and more homogeneously distributed in the case of SCLC1.

6.2.5 Discussion

In the above sections, three mixes are developed and investigated. In order to study the effect of the density on strength and thermal conductivity, two self-compacting mixes (SCLC1 and SCLC2) and one vibrated mix (VCLC) are designed. Two mixes with self-compacting properties are designed applying different distribution moduli in order to study their influences.

The smaller distribution modulus applied in design of mix SCLC2 compared to that in SCLC1 results in a smaller porosity (see Table 6.5) due to the large amount of inert fines used in that mix (see Table 6.3). This smaller porosity should theoretically lead to a larger strength, which is confirmed by the experimental results, as shown in Figure 6.6, and to a larger thermal conductivity which is also confirmed by the value listed in Table 6.7. Therefore, the selection of a suitable distribution modulus should be taken into consideration in order to obtain an optimal balance between strength and thermal conductivity.

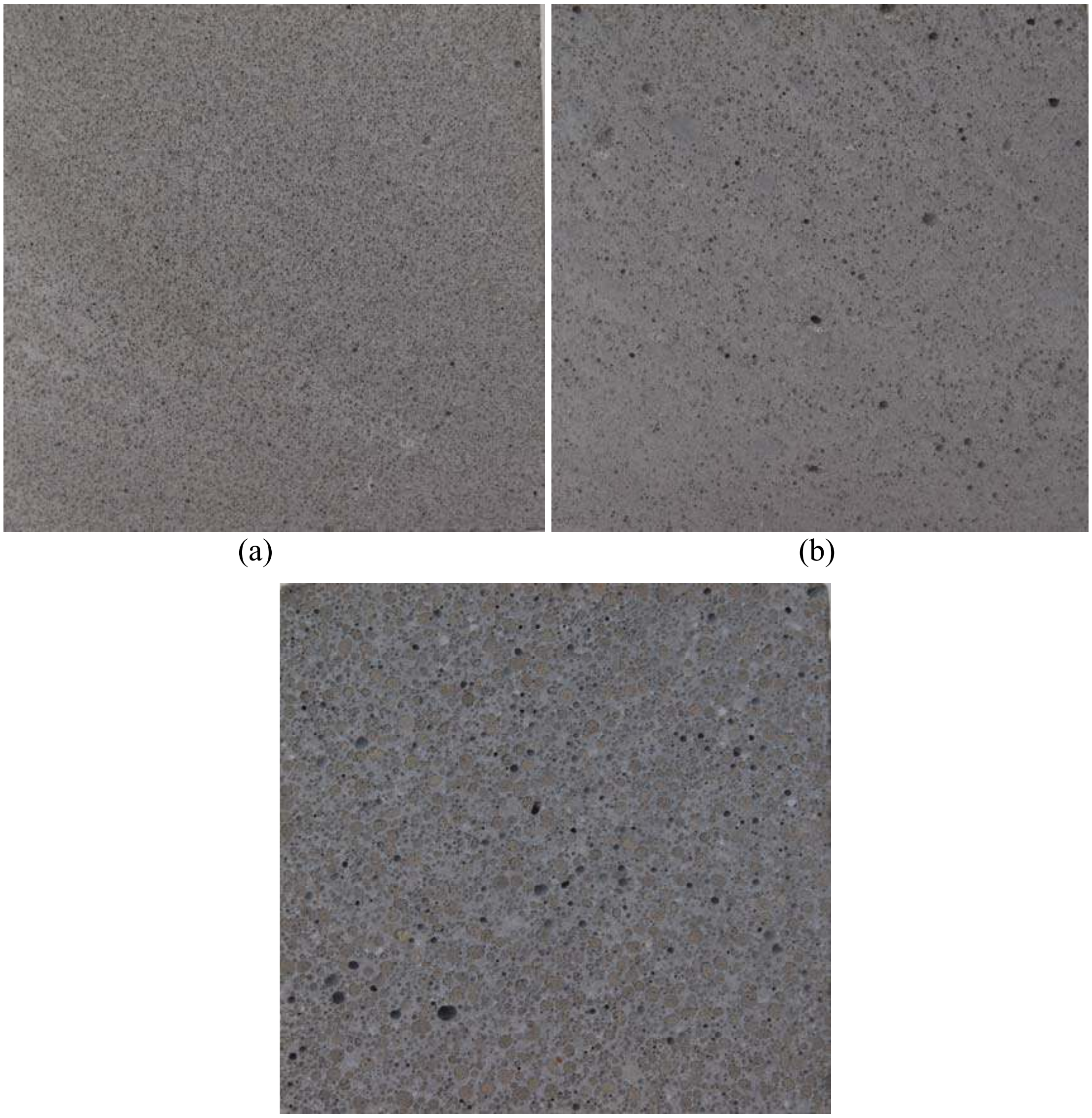

(a) (b)

(c)

Figure 6.11: Pictures of the cut surface of the three composites (a: SCLC1; b: SCLC2; c: VCLC).

SCLC2 and VCLC, designed following different distribution moduli and using different materials, have comparable densities. Surprisingly, these two composites have quite different thermal conductivities, which are in conflict with the well accepted opinion, i.e. the direct relation between the thermal conductivity and density (see Equation (6.2.6)). However, this finding confirms the analysis presented in Yu and Brouwers (2012). The difference in the measured thermal conductivity between these two mixes can actually be explained by the permeable porosity (see Table 6.6), i.e. the small permeable porosity of VCLC leads to a larger thermal conductivity, and also by the distribution of the lightweight aggregate particles in the matrix.

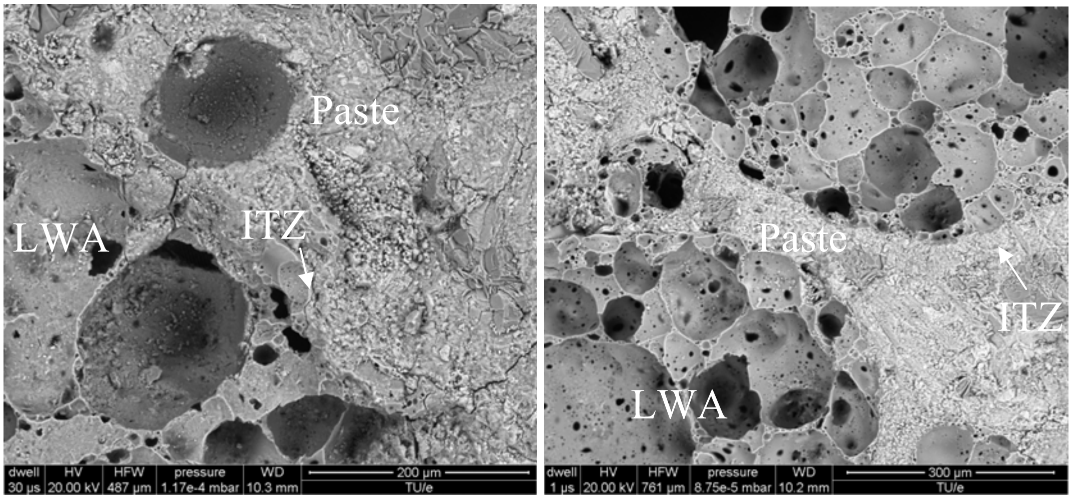

(a) (b)

Figure 6.12: SEM pictures of the composites using back scatter mode (a: VCLC; b: SCLC1).

The LWA used is produced from recycled glass (see the chemical composition analysis in Chapter 2). Therefore, there is a possibility of alkali-silica reactivity because of the high SiO_2 content in LWA (about 70% by mass, see Chapter 2). Ducman et al. (2002) reported that, although the expanded glass aggregates are reactive, they do not cause either expansion or cracks in concrete. This is attributed to the very porous structure of the aggregates, which provides sufficient space for hydration products, which is also confirmed by Chandra and Berntsson (2003). Zhang and Gjorv (1990) also reported that, although there is a certain degree of pozzolanic reaction between the cement paste and the LWA, which contain SiO_2, Al_2O_3, and Fe_2O_3 up to 85% in total, the effect is very small and can be neglected. The present chapter studies the possible chemical reaction between the LWA and cement paste by analyzing SEM images in back-scattered mode. No characteristic reaction "rings" are observed around LWA at the interfacial zone, as can be seen in Figure 6.7 and Figure 6.12. Therefore, it can be concluded that there is no determined chemical reaction between the LWA and the cement matrix at the test age. The ASR may still occur later, which could affect the properties of the developed composites, and further and long term investigation is needed.

6.3 Portland cement or calcium sulfate hemihydrate - a discussion

The binders, i.e. cement or calcium sulfate, can now be compared. In Chapter 5, the development of self-compacting lightweight composites using calcium sulfate hemihydrate (SGLC) as binder is presented, while in this chapter cement-based lightweight composites (CLC) are developed. In this section, a detailed comparison between them will be presented.

6.3.1 Water demand

Water demand determination of powders is essential in designing concrete especially with self-compacting features (Hunger, 2010). The water demand of both β-hemihydrate and cement can be performed by using the same mini-slump flow test (see analysis presented in Chapter 3). The investigated β-hemihydrate has a much larger water demand compared to that of cement CEM I 52.5, which is caused by the large difference between their specific surface areas (BET surface area of β-hemihydrate is 7.5 m^2 g^{-1} compared to CEM I 52.5 N of 0.9 m^2 g^{-1}, see analysis also in Chapter 2). The larger water demand of β-hemihydrate leads to a large difference between the calcium sulfate-based composite and the cement-based composite design.

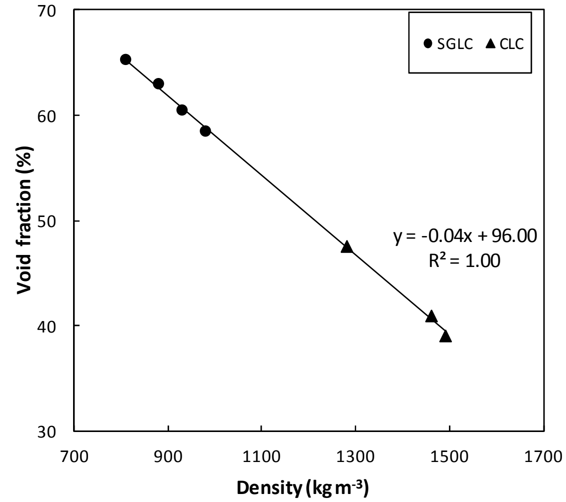

Figure 6.13: Porosity of SGLC and CLC versus density.

6.3.2 Density and porosity

In Chapter 5, a model is proposed to describe the porosity of the SGLC and it is validated by the present experiments. In this chapter, the theoretical porosity of the CLC is also calculated. Figure 6.13 shows the porosity of both SGLC and CLC versus density. It is obviously shown that the porosity and density of both SGCL and CLC follow the same rule, although the values of each material are in different ranges. This probably can be explained by the same mix design method, and the same type of the used LWA.

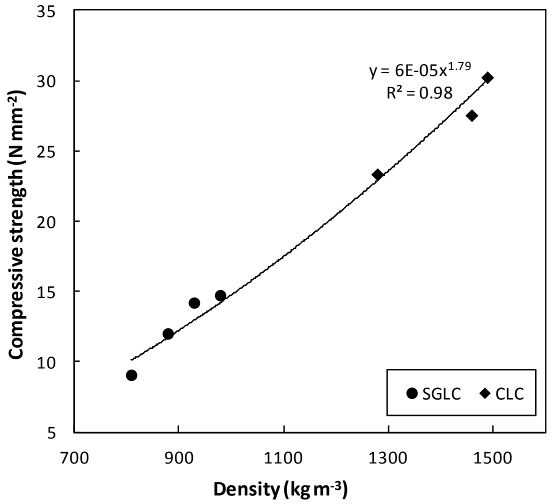

Figure 6.14: Compressive strength of SGLC and CLC versus density.

6.3.3 Strength and density

Figure 6.14 shows the results of the compressive strength plotted against the density of SGLC and CLC. Surprisingly, these two composites have the same power law between the compressive strength and the density. This finding is very interesting, from here it can be concluded that the SLGC can have a much better strength when its porosity can be reduced. This means a proper design, implying more efficient SP dosage, should be taken into account.

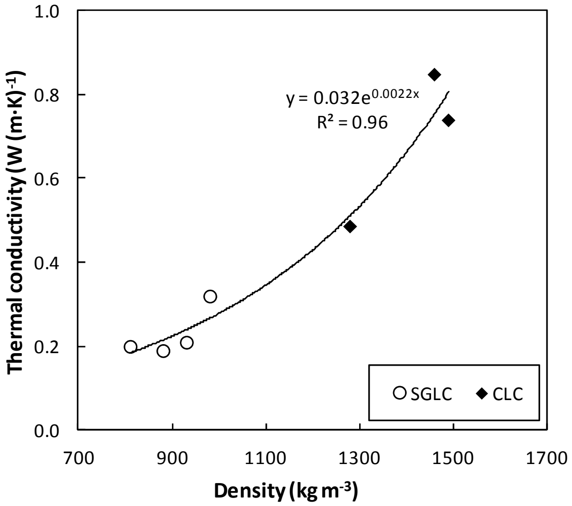

Figure 6.15: Thermal conductivity of SGLC and CLC versus density.

6.3.4 Thermal conductivity and density

Figure 6.15 shows the relation between the thermal conductivity and density of both SGLC and CLC. It shows that the exponential relation between the thermal conductivity and the density in the case of both composites still hold. Nevertheless the deviation is larger, compared to the porosity and strength and density, as indicated from the coefficient of determination shown in Figure 6.15. This also confirms the analysis in the previous sections that the thermal conductivity is complicatedly related not only to the density, but also to many other factors.

6.3.5 Discussion

The above sections analyzed the SGLC and CLC in terms of both fresh behavior of cement and β-hemihydrate and the properties of SGLC and CLC in their hardened state, including density/porosity, strength and thermal conductivity.

Results show that, despite the clear difference between the used binders, β-hemihydrate and cement, in SGLC and CLC, the two composites have quite similar characteristics between the density and other properties including porosity, strength and thermal conductivity. This generates an idea of using β-hemihydrate as binder to produce high strength composites in order to replace concrete to some extent, for example to be used as structural material in indoor conditions. But, as discussed before, the large porosity of the composite caused by the large water demand of β-hemihydrate is a challenge that should be overcome.

6.4 Conclusions

This chapter addresses the design of cement-based lightweight composites (CLC), and a comparison with the calcium sulfate-based composites. The following conclusions are drawn:

- Three mixes of cement-based lightweight composites using the design methodology presented in Chapter 5 are developed; these mixes are different in terms of the applied distribution modulus, density, and materials (the size fraction of LWA).
- The fresh behavior of these three mixes is investigated. An effective maximum superplasticizer dosage is found; beyond this maximum value the flowability remains constant when the SP content is further increased.
- V-funnel tests indicate that the CLC needs a longer V-funnel time compared to self-compacting mortar with normal weight aggregates.
- The water-accessible porosity of the three CLC, measured using the vacuum-saturation method, indicate that some of the pores in the used LWA are closed, which contributes to the lower thermal conductivity of the CLC.
- The fast early age strength development of CLC is attributed to the applied LWA, which on one hand causes the so-called internal curing effect, but on the other hand limits the final strength of the composites.
- The structural efficiency, although calculated from the ratio of the compressive strength and the density of one material, is linearly related to the compressive strength and not to the density according to a statistical analysis of lightweight aggregates concrete using different types of LWA.
- Thermal conductivity is related to the density: with the same type of CLC, it shows an exponential relation with the density, which however becomes complicatedly when the concrete is produced from different types of materials as well as a different design method.
- Although the LWA used here contain a high amount of SiO_2, there is no chemical reaction between them and the cement paste in the interfacial transition zone at the age of 28 days.
- Composite produced using β-hemihydrate as binder has similar characteristics as the present CLC; for example, their porosity, compressive strength and thermal conductivity follow similar rules as density; this indicates an ample room for the application of calcium sulfate as binder to produce load bearing composites to replace concrete in some extent.

Chapter 7

Indoor air purification applying heterogeneous photocatalytic oxidation

7.1 Introduction

Indoor air quality (IAQ) has received great attention because of the very important role the indoor environment plays on human comfort and health. Nitric oxides (NO and NO_2, also written as NO_x), Sulfur dioxide (SO_2) and Volatile organic compounds (VOCs), as typical inorganic and organic indoor air pollutants, can be emitted from cooking, combustion, exhaust gases, tobacco smoke, furniture, building materials, even traffic pollutants from outside of buildings, and can cause serious health problems such as drowsiness, headache, sore throat and mental fatigue (Obee and Brown, 1995). So, it is of vital importance to remove these pollutants to improve the indoor air quality.

Traditional methods of reducing indoor air pollution include controlling pollutant sources, increasing air exchange and using air purifiers, which have certain disadvantages. Source control is difficult to achieve in many places. Increasing the air exchange may even transport more pollutants from the outdoor environment (Jones, 1999). Common air purifiers often use sorption materials to adsorb gases or odors which only transfer the contaminants to another phase rather than eliminating them and additional disposal or handling steps are subsequently required.

Heterogeneous photocatalytic oxidation (PCO) has been studied for several decades (Fujishima and Honda, 1972), and shown as an effective method for water or air purification. Studies on photocatalytic oxidation of NO_x and VOCs have been carried out intensively (Turchi and Ollis, 1990; Obee and Brown, 1995; Devahasdin et al., 2003; Ao and Lee, 2004; Wang et al., 2007; Hüsken et al., 2007). Although certain progress has been achieved on the air purification employing photocatalytic oxidation, the differences in the findings or conclusions among these studies are still significant (Devahasdin et al., 2003; Ao and Lee, 2004; Wang et al., 2007; Hüsken et al., 2007). A further study is still very necessary, especially in indoor air quality improvement as discussed above.

The present chapter addresses the indoor air purification applying photocatalytic oxidation under indoor conditions. NO is chosen as the target pollutant in the first stage of this study since it is a typical indoor air pollutant that can be emitted from many sources. A mixture of NO and NO_2 (NO_x) is chosen in the second stage as the target pollutant to investigate the interrelation of the pollutants during the PCO reaction. Visible light (VIS) is used as the light source in this research, which is different from most of the available literature, among which UV light is still extensively used as the light source of the PCO, although studies on modifying TiO_2 to make it photoactive in visible light range has been widely carried out (Yu et al., 2002; Yang et al., 2007; Wang et al., 2007). Here a modified TiO_2 is used as the photocatalyst, which can be activated by visible light. The experimental study is carried out using the standard ISO 22197-1: 2007 as a basic reference. The experimental conditions that influence the photocatalytic oxidation such as light intensity, initial pollutant concentration, flow rate, water vapor, and the dosage of photocatalyst are investigated in detail.

7.2 Indoor air quality

7.2.1 Introduction

Human beings need a regular supply of food, water and air, with a relatively constant amount of 10-20 m^3 of air and 1-2 liters of water per day, respectively (WHO, 2000). People, especially in modern urban areas, spend most of their time (70 to 90%) in indoor conditions (Brown et al., 1994), exposing themselves much more to the indoor environment than to the outdoors. It is clearly indicated the important role that indoor air quality plays.

Indoor air quality, a term referring to the air quality within and around buildings and structures, especially as it relates to the health and comfort of building occupants, is strongly associated with indoor air pollution by chemicals, and its adverse effect on human health is becoming a global subject of public concern. The US Environmental Protection Agency (1987) pointed out that indoor air pollution poses a greater risk than outdoor air pollution. The European Union has set standards for the maximum levels of several gases in the atmosphere for the protection of human health and vegetation. The World Health Organization (WHO) has also set universal standards and recommendations for the indoor environment (WHO, 2000).

7.2.2 The Sick Building Syndrome

The sick building syndrome (SBS), as indicated from its name, is a syndrome related with buildings, including as headache, nausea, fever, eye or skin irritation, dry cough or fatigue. A World Health Organization report suggested that up to 30% of new and remodeled buildings worldwide may be subjected to complaints related to the indoor air quality (EPA, 1991).

The following parameters are attributed to the causes or the contributing factors to the SBS (EPA, 1991):

- Inadequate ventilation: both inadequate outdoor and indoor ventilation, usually resulting from improper building design, cause health and comfort problems to the building occupants (Emmerich et al., 2005).
- Chemical pollutants: can be emitted from both indoor and outdoor sources. Various indoor sources such as adhesives, carpeting, furniture, and human activities like cooking, heating and smoking are responsible for emitting chemical pollutants. The emissions can be organic gases such as formaldehyde and toluene, or inorganic gases such as carbon monoxide, nitrogen oxides, as well as particles. The chemical pollutants in outdoor environment can enter the indoor conditions by routes such as ventilation, windows and other openings. For instance, nitrogen oxides can be introduced into the indoor environment by the combustion products from the neighboring garages. Even worse, these pollutants are in even higher concentrations when they are located in indoor air conditions (Brown et al., 1994).
- Biological pollutants: bacteria, molds, pollens and viruses are typical biological pollutants which breed in stagnant water that has accumulated in humidifiers, drain pans and ducts, or where water is collected.

Therefore, the indoor air quality is complexly associated with many factors. Even these factors may work in combination, for instance inadequate ventilation introduces pollutants from outdoor to indoor conditions. It is also associated with other complaints regarding for instance temperature, humidity, or lighting.

7.2.3 Indoor air pollutants

As described above, the sick building syndrome is linked with many factors; among them gas pollutants act as one of the main roles in the indoor air quality degradation. WHO has already summarized the types of these pollutants and given the guideline of the limit concentration, which is briefly introduced here (WHO, 2000).

Organic gas pollutants

Typical organic air pollutants such as benzene, formaldehyde, toluene, etc. can be emitted from cigarette smoke, combustion, and evaporation of benzene-containing petrol, petrochemical industries and combustion processes. Brown et al. (1994) reported a maximum benzene concentration of 500 μgm^{-3} based on a survey in several countries such as US, Canada, Netherlands, Germany and Italy.

Among the organic air pollutants, volatile organic compounds (VOCs) especially cause health problems of human being. VOCs can be emitted from many sources such as paints, cleaning supplies, building materials, furnishings, office equipments like photocopy machines and printers etc. VOCs include a variety of chemicals, which may have short or long term adverse health effects. It is also shown that the VOC concentration in indoor air is much higher compared to that in outdoor air. For instance, the United States Environmental Protection Agency reported that the concentration of VOCs in indoor air is 2 to 5 times greater than in outdoor air and sometimes even far greater (EPA, 1991). Brown et al. (1994) reported a ratio of indoor VOCs concentration and outdoor concentration up to 20.

Table 7.1: WHO guidelines for organic pollutants.

Pollutants	Guideline
Benzene	No safe level can be recommended due to its carcinogenic risk
Carbon monoxide	100 mg m^{-3} as a 15-min mean; 60 mg m^{-3} as a 30-min mean; 30 mg m^{-3} as a 60-min mean; 10 mg m^{-3} as a 8-hour mean;
Toluene	0.26 mg m^{-3} as a weekly mean.
Formaldehyde	0.1 mg m^{-3} as a 30-min mean.
Trichloroethylene	No safe level can be recommended due to its carcinogenic risk

Due to the difference between the characteristics of the organic pollutants, the guidelines set by the WHO differ significantly, as shown from Table 7.1. The varied values also indicate the complexity of organic pollutants.

Inorganic gas pollutants

Classical inorganic gas pollutants include nitrogen oxides, ozone, sulfur dioxide etc. Sulfur dioxide is mainly emitted from the combustion of coal. In many countries in Western Europe and North America the utilization of coal as fuel has been limited, but in countries where coal is still being used for domestic heating or cooking, the concentration of sulfur dioxide can still reach even 2000 μg m^{-3}. Ozone and other photochemical oxidants are formed by the action of short-wavelength radiation from the sun on nitrogen dioxide. In the presence of VOCs, the equilibrium favors the formation of even higher levels of ozone. Nitrogen oxides are usually produced from the reaction of nitrogen and oxygen in air during combustion, especially at high temperature. The two major emission sources are transportation vehicles and stationary combustion sources such as electric utilities and industrial boilers (Butler et al., 2010), and they can be widely found indoors through cooking, heating, smoking and air infiltration (EHVAC, 2010).

Guidelines to these pollutants separately based on short term and long term exposure are given by WHO (2000), as listed in Table 7.2. The two guiding values for the short and long terms indicate the effect of the exposure time to these pollutants. The very low set values also indicate the toxicity of these pollutants.

Table 7.2: WHO guidelines for particulates and inorganic pollutants.

Pollutants	Guideline (μg m^{-3})	
	24-hour mean	Annual mean
Particulates ($PM_{2.5}$)	25	10
Particulates (PM_{10})	50	20
Ozone	100*	--
Nitrogen dioxide	200	40
Sulfur dioxide	500	20

***8-hour mean.**

7.2.4 Indoor air quality improvement

The health impact caused by poor IAQ has been extensively investigated. Common methods of improving the IAQ include controlling pollution sources, increasing ventilation rates or using air purifiers. Controlling pollution sources can often be difficult. For instance, although awareness of the potential harm of many products such as fire-retarding and stain-resistant formulations which emit pollutants has been noticed, they are still applied to furnishings for both the commercial and domestic market.

The ingress of poor-quality outdoor air into the indoor air is clearly undesirable. In Europe for example, much attention has been focused on the local air quality in urban areas. Increasing ventilation rates is a common strategy to improve IAQ but it can propagate the outdoor pollution indoors while increasing energy demand (Jones, 1999).

Gas pollutants removal generally is not highly effective when using standard particle filtration devices. The usage of air purifiers gains more acceptance nowadays due to less complications but its principle lies on only transforming contaminants from gas phase to another phase rather than eliminating them, so additional disposal steps are required (Kim et al., 2008).

A novel methodology, which addresses these issues, is the application of heterogeneous photocatalytic oxidation (PCO). Operating at ambient conditions, PCO can degrade a wide range of air pollutants into innocuous products solely with the energy input of light radiation, which will be investigated in detail in the next section.

7.3 Heterogeneous photocatalytic oxidation

7.3.1 Introduction

The history of the research on the heterogeneous photocatalytic oxidation (PCO) can be traced back to the 1970s, when Fujishima and Honda (1972) observed the water splitting effect by the electrochemical photocatalysis process at a semiconductor electrode. Interest from both scientific and industrial community in heterogeneous photocatalysis has greatly increased, including the fields such as self-cleaning, water purification, air purification etc. It is indicated from, for instance, the related publications which were less than 100 annually before 2000 but were already about 1000 in 2010 (Augugliaro et al., 2010).

7.3.2 Photocatalyst

The photocatalyst plays a key role in the process of the photocatalytic oxidation. It is used to absorb the radiation energy and transform it to generate highly reactive species. Some metal oxide semiconductors such as TiO_2 and ZnO are commonly used as the photocatalyst in PCO reactions. Among them, TiO_2 is widely applied because of its many appropriate characteristics: (a) it is inexpensive, safe, very stable, and has high photocatalytic efficiency; (b) it promotes the ambient temperature oxidation of the major indoor air pollutants; (c) no chemical additives are required (Obee and Brown, 1995).

Titanium, the world's fourth most abundant metal (exceeded only by aluminum, iron, and magnesium) and the ninth most abundant element (constituting about 0.63% of the Earth's crust), was discovered in 1791. TiO_2 has two main crystal modifications, anatase and rutile, with a band gap of 3.2 eV and 3.0 eV, respectively. Anatase has some better features than rutile, for instance the conduction band location is more favorable for conjugate reactions and very stable surface peroxide groups can be formed during the PCO reaction, which make it the preferable choice to be used as photocatalyst. TiO_2 can be prepared in the form of powder, crystals or thin films, and both powders and films can be built up from crystallites ranging from a few nanometers to several micrometers (Augugliaro et al., 2010).

However, TiO_2 can only be activated by UV light which is only 0.001-0.05 W m^{-2} in indoor illumination (Kuo et al., 2007). To use TiO_2 as photocatalyst in the visible light range, it is necessary to enlarge the photo absorption of TiO_2 into the visible light range (wavelength of 400-700 nm). The usual method is to modify TiO_2 by creating intra-band gap states that are close to the conduction or valence band edges and adsorb visible light at sub-band gap energies of less than 3.2 eV, such as the sol-gel method and doping metal or nonmetal materials onto the surface of TiO_2 (Kraeutler and Bard, 1978; Choi et al., 1994; Anpo, 1997; Yamashita et al., 1999; Asahi et al., 2001; Sano et al., 2003).

7.3.3 PCO working principle

The photocatalytic oxidation mechanism has been extensively investigated (Turchi and Ollis, 1990; Choi et al., 1994; Dalton et al., 2002; Devahasdin et al., 2003; Wang et al., 2007). The photocatalytic oxidation of gases can be divided into three main steps: (1) mass transport and adsorption of pollutants from the bulk air to the surface of the catalyst; (2) photocatalytic reaction on the catalyst; (3) desorption and mass transport of the reaction products from the surface of the catalyst to the air. In a photocatalytic system the behavior of each photocatalyst particle can be treated as a photo-electrochemical cell, where the oxidation and reduction reactions may occur on the photocatalyst electrode, with the principle shown in Figure 7.1 and the following equations.

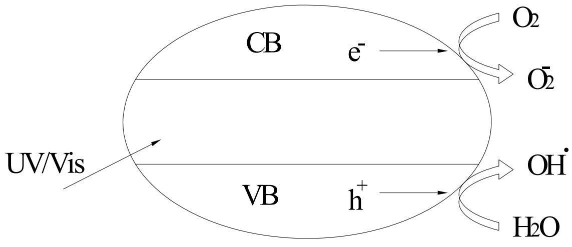

Figure 7.1: Working principle of the photocatalyst.

Equation (7.3.1) shows the photon generation of electron/hole pairs:

$$TiO_2 + hv \rightarrow e^+ + h^- \tag{7.3.1}$$

Under the irradiance of light with sufficient energy, the electron is excited from the valance band (VB) of the photocatalyst to its conduction band (CB), leaving a hole there, as described by Equation (7.3.1).

Equations (7.3.2) - (7.3.4) show the adsorption of the reactants onto the photocatalyst:

$$TiO_2 + H_2O \Leftrightarrow TiO_2\_H_2O \tag{7.3.2}$$

$$TiO_2 + O_2 \Leftrightarrow TiO_2\_O_2 \tag{7.3.3}$$

$$TiO_2 + X \Leftrightarrow TiO_2\_X \tag{7.3.4}$$

where X denotes pollutant.

Equation (7.3.5) shows the recombination of the generated electron and hole pairs:

$$e^- + h^+ \rightarrow heat \tag{7.3.5}$$

Equations (7.3.6) and (7.3.7) show the trapping of the generated holes and electrons:

$$h^+ + H_2O \rightarrow OH^\bullet + H^+ \tag{7.3.6}$$

$$e^- + O_2 \rightarrow O_2^- \qquad (7.3.7)$$

Then the pollutants can be oxidized by the generated radicals, which will be specifically addressed in the next section. From these equations it is evident that the absorbed oxygen and water play a very important role in PCO reaction. Oxygen is used to trap the generated electrons on the TiO_2 surface. Hydroxyl radicals are produced from water by trapping the generated holes on TiO_2 surface, which then lead to the oxidation of the pollutants.

7.3.4 Application of PCO

PCO, although it is still a quite novel research topic and many efforts are yet to be spent on it, has already been widely investigated on many materials such as glass, building materials, plastic, textile, metal, paper etc. (Augugliaro et al., 2010).

TiO_2-containing glass is already commercially available on the market (Pilkington, 2001), and usually has the characteristics of being photocatalytic, self-cleaning, hydrophilic, as well as even improved optical properties.

Cementitious materials-related products, for instance concrete as one of the most used manmade materials, are also modified by, for example, simply mixing with small amounts of TiO_2. It has been demonstrated (Beeldens, 2007; Hunger, 2010; Hüsken, 2010; Ballari and Brouwers, 2011) that the outdoor air purification is achieved by the TiO_2-incorporating concrete pavestones, and some patents (Muruta et al., 1999; Kimura et al., 2001) regarding these photocatalytic products have been granted. In addition, photocatalytic concrete has another big advantage of maintaining its surface clean, i.e. the self-cleaning property. The application of recycled glass to photocatalytic concrete is a novel idea to address on one hand the sustainability and on the other hand to improve the PCO efficiency, since more light can reach the photocatalyst due to the transparency of the glass (Chen and Poon, 2009). Ceramic tiles, another widely used building material, are also introduced into the photocatalytic world (Augugliaro et al., 2010).

7.4 Indoor air quality assessment

7.4.1 Introduction

The importance of the indoor air quality (IAQ) has been described in the previous sections. The application of the photocatalytic oxidation has also been introduced. In this section, the application of the PCO technology to improve the indoor air quality will be addressed.

Relevant available standards on the assessment of the air quality applying the PCO will be discussed in Section 7.4.2. A model pollutant is chosen as the target pollutant and the detailed information is given in Section 7.4.3. A test set-up is developed here to perform the PCO experiments, which will be introduced in Section 7.4.4. The methodology and the preparation of the samples for the PCO tests will be introduced in Section 7.4.5. The experiment performed as well as the results analysis will be given in Section 7.4.6.

7.4.2 Relevant standards comparison

Several national and international standards are available to assess the performance of the photocatalytic materials, including international standards ISO 22197-1:2007; ISO

22197-2:2011, and ISO 22197-3: 2011, and national standard UNI 11247:2007. However, they significantly differ from each other. Different pollutants from inorganic to organic gases are employed as model pollutants to perform the PCO tests, and the specified test conditions vary greatly as well. More detailed information about these standards specifications is presented in Appendix C.

Table 7.3: Comparison of the experimental conditions set by different standards.

Conditions	ISO 22197-1:2007	UNI 11247:2007	ISO 22197-2:2011	ISO 22197-3:2011
Model pollutant	NO	NO_x	Acetaldehyde	Toluene
Inlet concentration (ppm)	1.0	0.55^*	5.0	5.0
Irradiance (UVA) (W m^{-2})	10	20	10	10
Flow rate (L min^{-1})	3.0	5.0	1.0	0.5
Relative humidity (%)	50	50	50	50

***composed of 0.4 ppm NO and 0.15 ppm NO_2.**

The three ISO standards (ISO 22197-1; 22197-2; 22197-3) employ the same reactor with a surface area allowing a test sample with a size of 50 × 100 mm^2 to be embedded into the reactor, which is then covered with an optical glass for photo-irradiation with a distance of 5 mm in between. The standard UNI 11247:2007 employs a reactor made of Pyrex-glass with a total volume of 3 l and a height of 13 cm, allowing a test sample with size of 65 cm^2 to be embedded in. The above introduced standards differ greatly also by the recommended test conditions, as listed in Table 7.3.

Furthermore, it is also clear that there are distinct differences in the results calculation method among these standards, as shown in Equations (AC.1) - (AC.6) in Appendix C. It can be seen from Equations (AC.1) and (AC.2), that in ISO 22197-1:2007 the absolute amount of NO removed or NO_2 produced during the PCO reaction period is taken into consideration. However, in UNI 11247:2007, the concentration difference between the initial condition and after the PCO reaction, the flow rate, and the surface area as well as the light intensity are considered together, while in both ISO 22197-2:2011 and ISO 22197-3:2011, only the concentration difference between the inlet and outlet of the reactor during the PCO reaction is used as an indicator.

It should be mentioned here that all these four standards use UV light as the light source, i.e. with the normal TiO_2 as the photocatalyst. However, for the indoor air quality improvement, there is no UV light available in indoor conditions as discussed before, hence here visible light is used as the light source to simulate the indoor air conditions.

7.4.3 Model pollutants selection

NO_x are generated from the reaction of nitrogen and oxygen gases in the air during combustion, especially at high temperatures. The two major emission sources are transportation vehicles and stationary combustion sources such as electric utilities and industrial boilers, as well as indoor sources such as cooking, heating and smoking.

NO_x emissions contribute to the formation of fine particulates and ozone smog. Even worse, NO_x together with SO_x (sulfur dioxide and sulfur trioxide) are the major contributors to the “acid rain”, one of the most serious environmental problems across the world.

Extensive research has been carried out on the photocatalytic degradation of NO_x. Hashimoto et al. (2001) studied the effect of titania-zeolite composite catalyst for the photocatalytic oxidation of NO and found that a combination of TiO_2 and zeolite of 7:3 by weight results in the highest PCO rate. Lee and his coworkers studied the PCO of NO and VOCs in a typical indoor concentration of ppb level (Ao and Lee, 2003; Ao et al., 2003; Ao and Lee, 2004). The effect of using active carbon to improve the PCO efficiency was investigated, and a NO degradation improvement of 20% was found. Devahasdin et al. (2003) studied the reaction kinetics of the NO photocatalytic oxidation with an inlet concentration of 20 - 200 ppm, and the effect of the applied experimental conditions on the PCO efficiency is investigated. Ichiura et al. (2003) studied the PCO of NO_x using composite sheets containing TiO_2 and metal compounds such as CaO and MgO. Results indicate the CaO-treated TiO_2 has the greatest NO_x conversion rate. Wang et al. (2007) studied the reaction mechanism of PCO of NO_x with an inlet concentration of 20-168 ppm using TiO_2 supported on woven glass fabric, and reported a 27% NO degradation at an initial NO concentration of 147 ppm. Kuo et al. (2007) studied the PCO of NO_x under visible light using carbon-containing TiO_2 and investigated the effect of the wavelength of the light. Results show that a 70% NO degradation is achieved under the UV light and 50% under the blue LED irradiation. Shelimov et al. (2008) studied the enhancement effect of using alumina as the support of TiO_2 on the photocatalytic removal of NO_x. The sample was prepared using a sol-gel method and the enhancement of the PCO efficiency is attributed to a faster generation of the electron and hole pairs to produce the hydroxyl radicals for the NO degradation reaction. Dalton et al. (2002) studied the PCO of NO_x using TiO_2 as photocatalyst with a surface spectroscopic approach and proposed a NO_x degradation mechanism in which the function of the generated hydroxyl radicals is confirmed.

Although great progress has been achieved, the differences in the findings or conclusions among these studies are still evident. For instance, in Devahasdin et al. (2003), the increase of the relative humidity leads to a higher PCO conversion rate while in Ao and Lee (2003) it results in a lower PCO conversion rate. Reaction kinetics of the PCO of NO has been investigated as well; however, as an undesired intermediate, NO_2 is seldom considered in literature. In addition, using NO and NO_2 together as target pollutants as well as their interrelation during the PCO reaction have not been addressed. Thus, further study is still very necessary to be carried out, especially for indoor air quality improvement as discussed above.

Therefore, with the consideration that NO_x are typically available in both indoor and outdoor conditions and they are very harmful to human beings, here NO_x are chosen as the target pollutants to assess the PCO performance. The ISO standard 22197-1: 2007 is used as a reference to perform the PCO experiments. In the first stage, NO is used as a single target pollutant and in the second stage NO and NO_2 together are used as the target pollutants to investigate the interrelation of the pollutants during the PCO.

7.4.4 PCO test set-up

Here two test set-ups are used for the PCO experiments. The first test set-up, developed originally by Hunger (2010) and Hüsken (2010) for a study on the PCO of concrete pavements, is employed where NO is used as target pollutant. The second set-up is developed here and NO_x (NO and NO_2) are used as pollutants. The set-ups are developed using the ISO standard 22197-1: 2007 as a reference. The set-up is composed of the reactor, visible light source, target gas pollutant supply, transport gas supply, analyzer, flow rate valves/mass controller meters, relative humidity valve, and parameter measurement apparatus such as temperature and relative humidity. The schematic diagrams of the PCO set-ups are shown in Figure 7.2 and Figure 7.3, respectively.

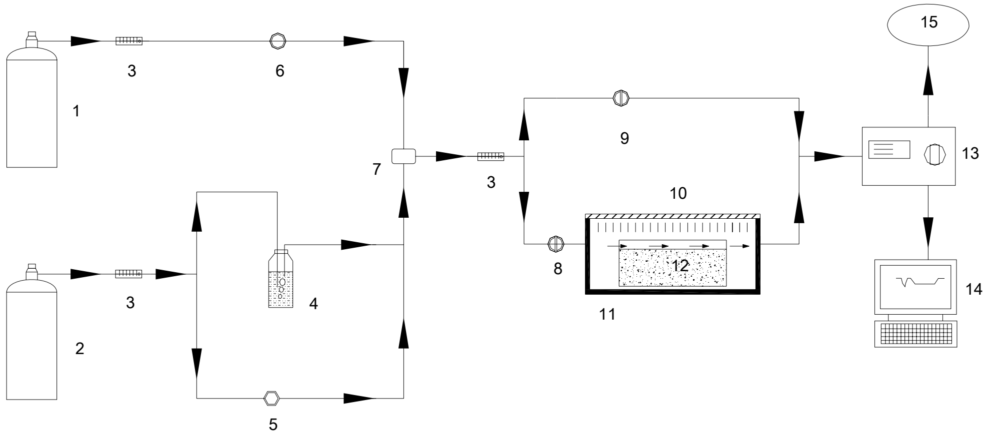

Figure 7.2: Schematic diagram of the photocatalytic degradation set-up. 1. NO gas supply. 2. Synthetic air. 3. Flow rate meter. 4. Humidifier. 5. Humidity controller. 6. NO concentration controller. 7. Temperature and relative humidity sensor. 8. Valve. 9. Valve. 10. Light source. 11. Reaction chamber. 12. Reactor. 13. NO_x analyzer. 14. Computer. 15. Vent.

The reactor, made from non-adsorbing plastic materials with a size of 100 × 200 mm^2 (W × L), allows a flat sample to be embedded, as shown in Figure 7.4 (Hüsken et al., 2007). After placing the test sample inside, the top of the reactor is tightly covered with a plate made from borosilicate glass allowing UV and/or visible light to pass through with almost no resistance. A more detailed description is presented in Hüsken et al. (2007) and Yu and Brouwers (2009). The reactor's height, which is the distance between the paralleled surface of the test sample and the covering glass plate, can be adjusted by screws in the bottom of the reactor. The target pollutant gas can only pass through the reactor along the longitudinal direction by means of appropriate sealing.

Visible light is used in the experiment. The applied light source consists of three cool day light lamps of 25 W each (Philips, the Netherlands), emitting a visible radiation in the range of 400-700 nm. The irradiance can be adjusted by a light intensity controller. The light intensity is measured with a VIS-BG radiometer (Dr. Gröbel UV-Elektronik GmbH, Germany). The VIS-BG radiometer measures a wavelength range of 400-600 nm with the maximum relative sensitivity at about 460 nm. The reason that the VIS-BG radiometer with this range is chosen lies in the characteristics of the photocatalyst used in the experiment. The used carbon-doped TiO_2 can be activated until the bluish green light region which is the same as the measurement range that the radiometer has. The VIS-BG has a measuring range of 2000 Wm^{-2} with the resolution of 0.1 W m^{-2}.

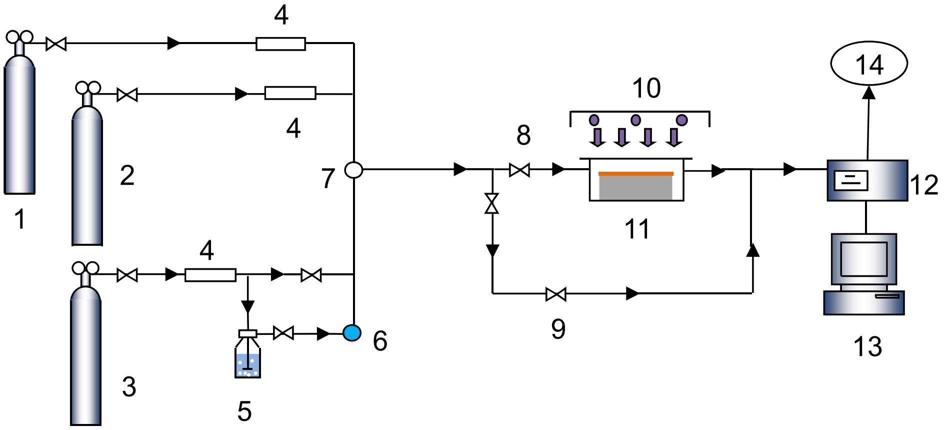

Figure 7.3: Schematic diagram of photocatalytic degradation set-up. 1. NO gas supply. 2. NO_2 gas supply. 3. Synthetic air supply. 4. Mass controller meter. 5. Humidifier. 6. Humidity controller. 7. Temperature and relative humidity sensor. 8. Valve. 9. Valve. 10. Light source. 11. Reactor. 12. NO_x analyzer. 13. Computer. 14 Vent.

NO_x is used as target pollutant. The used gas consists of 10 - 50 ppm NO or 10 - 50 ppm NO_2 stabilized in nitrogen (N_2). Because the final target NO_x concentration ranges in the order of ppb with the maximum concentration of 1.0 ppm, a transport fluid synthetic air which is composed of 20.5 vol.% of oxygen (O_2) and 79.5 vol.% of N_2 is employed, which is humidified by flowing through a demineralized water filled bottle. The target concentration of NO (or NO_x) is adjusted by the NO concentration control and flow rate valves, or the mass controller meters depending on the set-up.

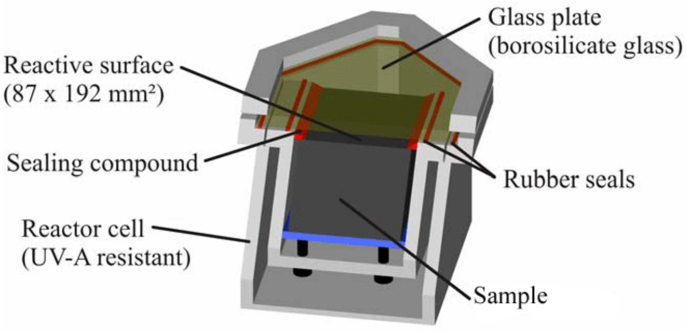

Figure 7.4: Schematic diagram of the reactor (Hüsken et al., 2007).

Pollutant (NO or NO_x) and intermediate product (NO_2) are analyzed using a chemiluminescent NO_x analyzer (HORIBA 370, Japan). The analyzer, with a detection limit of 0.5 ppbv, measures the concentration in steps of 5 seconds. During the measurement, the analyzer constantly samples gas with a rate of 0.8 $Lmin^{-1}$.

7.4.5 PCO experiment

Photocatalyst applied

As analyzed before, photocatalyst plays a key role in the PCO reaction. Also as discussed above, traditional TiO_2 could not be activated under visible light range due to its larger band gap. Accordingly, a modified TiO_2 is used as the photocatalyst here. Here two commercially available modified TiO_2 are chosen and compared from their physical properties (see Chapter 2) and photocatalytic degradation performance (detailed results are presented in Ballari et al., 2012) and finally a carbon-doped TiO_2 (K-7000) is chosen as the photocatalyst used in the present study.

Table 7.4: Physical properties of the used photocatalyst.

Parameter	Photocatalyst
TiO_2 content (ISO 591)	>87.5%
Crystal structure	anatase
Density (ISO 787, Part 10)	3.9 g cm^{-3}
Crystallite size	approx. 15 nm
Specific surface area (BET)	>225 m^2 g^{-1}
Bulk density	350 g L^{-1}
Max. processing temperature	150 °C

The K-7000 is produced by mixing a fine grained titanium compound with an organic carbon compound and subsequent thermal treatment at temperatures up to 350 °C (Orth-Gerber and Kisch, 2005). By doping the anatase phase with carbon, the cut-off wavelength is shifted from 388 nm (band gap of 3.20 eV) to 535 nm (band gap of 2.32eV) which corresponds to bluish green light (Blöß and Elfenthal, 2007). The modification indicates that only 2.32 eV needs to be absorbed, which means that visible light can be used to activate this material as catalyst. The basic physical properties of the employed photocatalyst are shown in Table 7.4 (values taken from the data sheet of the provider).

Photocatalytic materials development

As introduced in the previous section, so far many materials such as concrete, plastic and glass have been used as substrates for the photocatalyst, however mainly only for the outdoor air quality improvement and/or self-cleaning property. Here, the research emphasis is focused on the photocatalytic oxidation behavior under indoor air conditions, and several different materials are used and studied as substrates for the photocatalyst application, whereas they are all related to the soul of this research, i.e. the $CaSO_4{\cdot}H_2O$ based composite, as will be discussed below.

- Gypsum board cover paper

A new type of gypsum plasterboard covering paper with nonwoven glass wool fabric, instead of traditional gypsum paper, is used as substrate for the application of the photocatalyst.

This newly designed paper can also be further used as normal wall covering. Firstly, a slurry is prepared by mixing water with the carbon-doped TiO_2. Subsequently, glass fibers are coated by dipping them into the carbon-doped TiO_2 slurry. Finally, the glass fibers are sprayed onto the wool fabric with a good adhesion between them after curing.

- Gypsum plaster

The PCO performance of photocatalytic gypsum plaster is also investigated. The research development aims at an improvement of the traditional gypsum board, i.e. the gypsum core is covered by gypsum paper from both sides. Nevertheless, gypsum plaster is also widely applied as interior wall furnishing material. Therefore, the application of PCO technology to the furnishing gypsum plaster is also addressed.

Here the used photocatalyst is applied to the gypsum plaster by simply mixing it with the solid ingredients in water. The dosage of the photocatalyst is calculated based on the proportion of the used binder (i.e. β-hemihydrate here). The mixing procedure and the curing method are the same as introduced previously (see Chapter 3).

- Wall covering

A commercially available wall paper is also used as the substrate, considering that the developed composite can be directly decorated by for instance wall covering.

The used photocatalyst is mixed with water and an inorganic binder. Then the photocatalyst slurry is painted onto the wall covering followed by curing in ambient conditions for at least 2 days before any PCO experiment is carried out.

PCO test procedure and experiment

NO_x is used as the target indoor air pollutant in the present research. The average NO_x concentrations are in the range of 9.4-596 μgm^{-3} in a week in houses with kitchens equipped with gas cookers in the UK, and peak values of up to 3800 μgm^{-3} for 1 min have been reported in the Netherlands in kitchens with unvented gas cooking (Hoskins, 2003). Based on this, a ppb level of the initial NO_x concentration is chosen to represent the real indoor air condition, as 1 ppm is about 1300 μgm^{-3} (20 °C, 1 bar).

The photocatalytic oxidation experiments are carried out using a standard procedure illustrated as follows. The first step is to warm up the NO_x analyzer to a stable condition for about 1-3 hours, here a 1.5-hour warm up time is usually used. In the meantime the reactor is prepared, including the preparation of the testing sample, placing the sample into the reactor, sealing the reactor and placing the reactor into the reaction chamber with the reactor covered by an opaque material. Then the gas is allowed to flow through the system using a bypass (with valve 9 open and valve 8 closed, see Figures 7.2 and 7.3), and the concentration is adjusted with the concentration valve (in the case of set-up in Figure 7.2) or the mass controller meter (in the case of set-up in Figure 7.3) to the desired value while monitored by the NO_x analyzer. Then the visible light lamp is switched on to get a stable radiation and adjusted to the desired experimental light intensity value with the lamp control valve while the reactor remains covered, followed by the adjustment of the relative humidity to the desired value with the humidity control valve.

When these experimental conditions become stable, the photocatalytic oxidation reaction can be started first by opening valve 8 and then closing valve 9, while keeping the reactor covered. The NO_x concentration decreases immediately when it flows through the reactor because of the adsorption of NO_x onto the surface of the sample. Then the concentration increases again to the former concentration within several minutes, 5 - 10 minutes is usually enough in the present research, although it can be influenced by the NO_x initial concentration, flow rate, and the surface structure of the tested sample. This phenomenon also indicates that no photocatalytic oxidation reaction takes place in the dark. After this the photocatalytic oxidation reaction is started by uncovering the reactor to allow the visible light to irradiate the sample. The PCO reaction lasts for 30 minutes and is ended by covering the reactor with an opaque material to stop the light irradiation.

Table 7.5: Experimental conditions employed in the tests.

Parameter	Standard conditions	Varying conditions
Reactor Height H (mm)	3	2 - 9
Initial NO concentration (ppmv)	0.5	0.1-1.0
Volumetric flow rate Q (L min^{-1})	3	1-5
Relative humidity RH (%)	50	10 - 70
Light intensity E (W m^{-2})	10	1-13

Here experiments are performed on different materials as described above using the standard ISO 22197-1:2007 as a reference. The emphases on these targets are different, as will be discussed and analyzed below.

- PCO gypsum board covering paper

Standard test conditions are set here: an initial NO concentration of 500 ppb and a volumetric flow of 3.0 $Lmin^{-1}$; the visible light intensity is chosen as 10.0 Wm^{-2} and a relative humidity of 50%. All the experiments are carried out at room temperature (here the room temperature is always about 19.0 - 20.0°C). To study the influence of the experimental conditions on the photocatalytic oxidation rate, the parameters mentioned above are varied to carry out the PCO test. The detailed information is shown in Table 7.5 and will be discussed in the following sections.

Table 7.6: Chemical composition of the test samples (Pöllmann, 2009).

Sample	TiO_2 (%)	SiO_2 (%)	CaO (%)	MgO (%)	LOI (%)	Others (%)	Total (%)
A	1.00	5.70	46.50	2.86	41.50	2.44	100
B	5.00	3.79	46.00	2.76	40.80	1.65	100
C	18.60	2.33	40.90	2.18	34.70	1.29	100
D	54.10	22.00	2.13	1.60	10.00	10.17	100

Here, four PCO samples are tested to study the effect of the photocatalyst dosage on the PCO efficiency. The chemical composition of the samples is measured by means of

X-ray fluorescence (XRF) to provide deeper understanding of the employed materials. The results are listed in Table 7.6.

- PCO gypsum plaster

As introduced above, the emphasis is not on the PCO gypsum plaster/composite because this new developed composite will normally be covered or furnished with for instance wall paper. However, since gypsum plaster as well as the new gypsum composite can be used as ceiling or wall partition without covering with anything, their PCO effect is studied as well. The mixes are listed in Table 7.7.

Table 7.7: Mix design of the PCO gypsum plaster.

Materials	β-hemihydrate (g)	Photocatalyst (g)	Water (g)	Accelerator (g)
Mix 1	255.9	7.68	166.3	0
Mix 2	255.9	12.8	166.3	0
Mix 3	224.1	6.73	190.4	1.68
Mix 4	224.1	11.21	190.4	1.68
Ref	255.9	0.0	166.3	0

The standard experimental conditions are set the same as above. An initial NO concentration is chosen as 500 ppb and the volumetric flow rate of 3.0 $Lmin^{-1}$; the visible light intensity is 10.0 Wm^{-2} and the relative humidity of 50%. The experiments are carried out at room temperature.

- PCO wall covering

The emphasis of the PCO behavior is on the interrelation of the different pollutants during the PCO reaction. NO and NO_2 are chosen as the target pollutants in different proportions but always with a total concentration of 500 ppb.

Table 7.8: Experimental conditions employed in the tests.

Description	Operating conditions
Photocatalyst dosage (mg cm^{-2})	0.25
Volumetric low rate Q (L min^{-1})	1.0-3.0
Relative humidity RH (%)	40 -70
Light intensity E (W m^{-2})	1 - 12
NO inlet concentration (ppb)	0 - 500
NO_2 inlet concentration (ppb)	0 - 500

The other experimental parameters are set the same as above, i.e. the volumetric flow rate as 3.0 $Lmin^{-1}$; the visible light intensity is chosen as 10.0 Wm^{-2} and a relative humidity of 50%. All the experiments are carried out at room temperature. To study the influence of the experimental conditions on the photocatalytic oxidation efficiency, the parameters mentioned above as well as the proportion of the NO and NO_2 are varied to carry out the PCO tests, and the detailed information is shown in Table 7.8.

7.4.6 Results analysis

Reaction mechanism of PCO of NO_x

In the previous section, the photo-activation of the photocatalyst, the adsorption of the reactants such as H_2O and O_2, and the generation of the hydroxyl radicals are discussed. Here, with NO_x as pollutant, the following reactions are presented, including the adsorption and the oxidation of NO_x.

$$TiO_2 + NO \Leftrightarrow TiO_2\_NO \tag{7.4.1}$$

$$TiO_2 + NO_2 \Leftrightarrow TiO_2\_NO_2 \tag{7.4.2}$$

$$NO + OH^{\bullet} \rightarrow HNO_2 \tag{7.4.3}$$

$$HNO_2 + OH^{\bullet} \rightarrow NO_2 + H_2O \tag{7.4.4}$$

$$NO_2 + OH^{\bullet} \rightarrow NO_3^- + H^+ \tag{7.4.5}$$

Here the generated superoxide can be also attacked by the following routes:

$$O_2^- + H^+ \rightarrow HO_2 \tag{7.4.6}$$

$$NO + HO_2 \rightarrow NO_3^- + H^+ \tag{7.4.7}$$

However, firstly due to the lack of sufficient acidic environment and secondly the superoxide is generated in the conduction band while the NO is adsorbed in the valence band of the catalyst, it is very difficult for the superoxide to undergo the reaction. Hence, in the present study the proposed mechanisms in Equations (7.4.6) and (7.4.7) are not considered. Therefore, it can be seen from the mechanism proposed above that NO is oxidized by the produced hydroxyl radicals firstly to NO_2 and finally to NO_3^-. The generation of HNO_2, also referred to as HONO, is also confirmed by Laufs et al. (2010). The study of the photocatalytic decomposition of NO (Yamashita et al., 1999; Lim et al., 2000) in absence of oxygen and water also indicates their role in the NO photocatalytic oxidation. Here it is also shown that only one oxidation step is needed in the case of NO_2 as sole pollutant, which indicates that the PCO efficiency of NO_2 should be better than that of NO, which will be demonstrated as well.

Photocatalytic oxidation of NO_x

The photocatalytic oxidation reaction takes place immediately when the sample is exposed to the visible light. In the case of NO as sole pollutant, the concentration of NO_2 increases and reaches stable conditions quickly. After reaching the maximum degradation rate, the process will slightly slow down and reach a stable conversion condition finally. Figure 7.5 shows a typical concentration change of NO_x during the photocatalytic oxidation reaction.

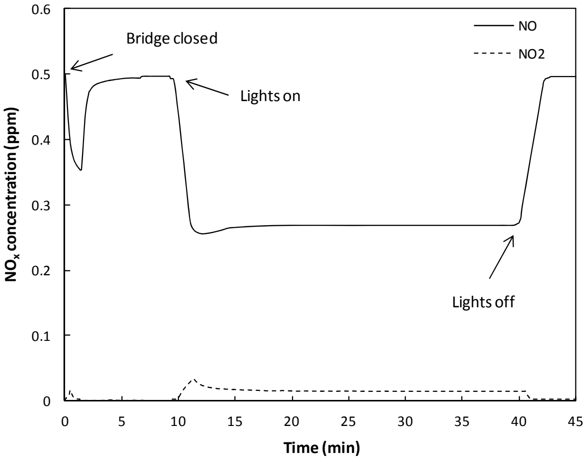

Figure 7.5: Schematic diagram of the NO concentration change during a measurement.

The photocatalytic oxidation efficiency of NO is calculated from:

$$NO_{con}(\%) = \frac{C_{NO,in} - C_{NO,out}}{C_{NO,in}} \times 100\% \qquad (7.4.8)$$

where $C_{NO,out}$ is defined as the average NO concentration during the last 5 minutes of the measurement (ppb).

In the case of NO_2 as pollutant, the PCO efficiency of NO_2 is calculated from:

$$NO_{2,con}(\%) = \frac{C_{NO_2,in} - C_{NO_2,out}}{C_{NO_2,in}} \times 100\% \qquad (7.4.9)$$

where $C_{NO2,out}$ is defined as the average NO_2 concentration during the last 5 minutes of the measurement (ppb).

Equation (7.4.4) shows the formation of NO_2 during the oxidation reaction of NO. However, not all the produced NO_2 can be oxidized to HNO_3 because a small part of it is released into the air due to desorption. So even when NO is used as single pollutant, the pollutants at the exit are composed of undegraded NO and the formed intermediate NO_2. Therefore, the NO_x conversion is used to study the influence of the experimental conditions since NO_2 is an undesired intermediate pollutant. The NO_x conversion is calculated from:

$$NO_{x,con}(\%) = \frac{C_{NO_x,in} - C_{NO_x,out}}{C_{NO_x,in}} \times 100\% \tag{7.4.10}$$

where $C_{NO_x,out}$ is defined as the average NO_x concentration during the last 5 minutes of the measurement (ppb).

PCO results analysis

The results can be divided into three parts according to the different PCO samples described above. The varied experiments with the PCO gypsum wall board paper and PCO wall covering are also performed in order to investigate the effect of the applied test conditions on the PCO efficiency, and the detailed results regarding these two parts will be specifically addressed in the next section (Section 7.5). In this section, only the results of the PCO gypsum plaster are analyzed, as listed in Table 7.9.

Table 7.9: PCO test results with the photocatalytic gypsum plaster.

Sample No.	NO_{con} (%)	$NO_{X,con}$ (%)
Mix 1	15.0	8.9
Mix 2	33.2	23.7
Mix 3	22.0	14.9
Mix 4	32.5	22.7
Reference	0.0	0.0

It can be clearly observed that the idea of dosing photocatalyst to degrade the indoor air pollutant is working. With a dosage of TiO_2 of 3% by mass of the β-hemihydrate, samples of Mix 1 and Mix 3 already show considerable NO and NO_x conversion rates. This indicates that the photocatalytic oxidation technique can be a promising technology for the indoor air quality improvement.

Table 7.10: Dosage of the used photocatalyst.

Sample No.	w_0/h_0	Photocatalyst	
		Dosage (%)	Volumetric proportion (%)
Mix 1	0.65	3.0	0.74
Mix 2	0.65	5.0	1.23
Mix 3	0.85	3.0	0.62
Mix 4	0.85	5.0	1.03

The photocatalytic oxidation reaction is a surface reaction, i.e. the reaction only occurs on the surface of the photocatalyst. Therefore, the PCO performance would increase if the dosage of the photocatalyst increases, which is confirmed by the present result (see results of Mix 1 and Mix 2, and Mix 3 and Mix 4, respectively in Table 7.9). However, this does not mean that the more photocatalyst is used, the higher PCO efficiency is resulted. The PCO is also related to many other factors such as the photocatalyst surface area, the porosity of the substrate, surface roughness of the substrate etc.

Table 7.10 shows the volumetric proportion (VP) of the used photocatalyst in the matrix of the produced PCO gypsum plaster. It can be seen that although the VP of Mix 3 is lower than that of Mix 1, the PCO efficiency of Mix 1 is higher. This probably can be explained by the larger porosity of the gypsum plaster produced from Mix 3 (a larger w_0/h_0), which contributes to a higher pollutant absorption which in turn leads to a higher degradation rate of NO_x.

7.5 Influential factors analysis

7.5.1 Introduction

As reported in literature (Ao and Lee, 2003; Ao and Lee, 2004; Ao et al., 2003; Hashimoto et al., 2001; Ichiura et al. 2003; Wang et al., 2007), the test conditions significantly affect the PCO efficiency; however, their effect so far is still not agreed upon. Hence, in this section the influence of experimental conditions including initial pollutant concentration, volumetric flow rate, irradiance, water vapor or relative humidity, dosage of the photocatalyst on the PCO efficiency is addressed.

This section is divided into two parts. In the first part, a novel PCO gypsum plasterboard cover paper is used as the test target. NO is used as a single pollutant. All other factors remain as standard condition when investigating one test parameter by varying its value. The experimental results are listed in Table 7.11. In the second part, a PCO wall covering is used in the tests. NO_x (both NO and NO_2) is used as the target pollutant to investigate the interrelation of them during the PCO reaction. The overall initial concentration of NO_x is kept constant at 0.5 ppm, but the proportions of NO and NO_2 are varied. Also all the other factors remain as standard condition when investigating one test parameter. The experimental results are listed in Table 7.12.

Table 7.11: Experimental results of the PCO of NO under different test conditions.

E (W m^{-2})	Q (L min^{-1})	RH (%)	$C_{NO,in}$ (ppb)	$C_{NO_2,in}$ (ppb)	$C_{NO,out}$ (ppb)	$C_{NO_2,out}$ (ppb)	NO_{con} (%)	$NO_{x,con}$ (%)
3.0	3.0	50.0	983.1	10.2	877.3	33.6	10.8	8.3
5.0	3.0	50.0	975.5	9.7	832.7	41.2	14.6	11.3
8.0	3.0	50.0	999.3	11.6	820.0	51.3	18.0	13.8
10.0	3.0	50.0	976.6	11.6	779.1	52.4	20.2	15.9
13.0	3.0	50.0	980.5	12.9	766.9	58.2	21.8	16.9
1.0	3.0	50.0	482.7	4.7	433.0	16.1	10.3	7.9
2.0	3.0	50.0	496.7	7.7	408.9	27.3	17.7	13.5
4.0	3.0	50.0	493.3	3.6	392.2	29.6	20.5	15.1
6.0	3.0	50.0	482.8	3.6	362.6	34.4	24.9	18.4

8.0	3.0	50.0	469.1	10.9	341.9	44.3	27.1	19.5
10.0	3.0	50.0	493.3	13.6	356.5	49.3	27.7	19.9
13.0	3.0	50.0	476.0	16.2	325.7	51.9	31.6	23.3
10.0	1.0	50.0	472.7	1.5	141.6	36.8	70.0	62.4
10.0	2.0	50.0	487.6	4.7	270.3	48.0	44.6	35.4
10.0	5.0	50.0	492.9	0.0	399.1	27.7	19.0	13.4
10.0	3.0	50.0	96.0	2.6	28.0	10.7	70.8	60.8
10.0	3.0	50.0	293.0	4.1	151.9	30.6	48.1	38.6
10.0	3.0	10.0	489.5	0.0	435.9	11.0	10.9	8.8
10.0	3.0	20.0	497.6	4.5	420.7	21.1	15.5	12.0
10.0	3.0	30.0	485.2	0.0	400.3	17.6	17.5	14.0
10.0	3.0	40.0	496.4	5.4	377.6	34.9	23.9	17.8
10.0	3.0	60.0	484.6	11.6	306.4	53.6	36.8	27.5
10.0	3.0	70.0	485.9	4.2	287.2	49.3	40.9	31.3

Table 7.12: Experimental results of the PCO of NO_x under different test conditions.

Exp. #	RH (%)	E (W m^{-2})	Q (L min^{-1})	$C_{NO,in}$ (ppb)	$C_{NO_2,in}$ (ppb)	$C_{NO,out}$ (ppb)	$C_{NO_2,out}$ (ppb)	$NO_{x,con}$ (%)
1	50.0	10.0	3.0	491.5	1.4	445.5	16.0	6.4
2	50.0	10.0	3.0	399.7	104.9	365.3	106.9	6.4
3	50.0	10.0	3.0	301.1	189.4	278.4	175.4	7.5
4	50.0	10.0	3.0	203.6	292.5	189.3	263.3	8.8
5	50.0	10.0	3.0	105.3	381.5	100.3	340.0	9.6
6	50.0	10.0	3.0	10.3	482.4	16.3	426.7	10.1
7	50.0	10.0	1.0	391.0	62.1	299.1	77.5	16.9
8	50.0	10.0	1.5	388.5	76.4	326.9	86.0	11.2
9	50.0	10.0	2.0	391.7	85.5	343.6	91.8	8.8
10	50.0	10.0	2.5	398.3	86.7	358.2	92.0	7.2
11	50.0	10.0	1.0	110.6	352.4	90.5	262.5	23.8
12	50.0	10.0	1.5	107.5	370.3	91.5	303.0	17.4
13	50.0	10.0	2.0	106.2	384.5	91.4	325.5	15.0
14	50.0	10.0	2.5	105.6	386.6	98.0	340.2	11.0
15	50.0	3.0	3.0	400.0	115.7	381.2	114.4	3.9

16	50.0	5.0	3.0	402.2	97.1	367.2	103.8	5.7
17	50.0	7.0	3.0	402.3	94.6	366.3	99.4	6.3
18	50.0	12.0	3.0	401.2	96.4	360.7	99.7	7.5
19	50.0	1.0	3.0	110.1	409.5	103.8	399.3	3.2
20	50.0	3.0	3.0	108.7	399.2	98.9	377.8	6.1
21	50.0	5.0	3.0	98.7	404.3	95.2	371.7	7.2
22	50.0	7.0	3.0	98.5	399.1	93.9	362.4	8.3
23	50.0	12.0	3.0	98.6	401.8	93.1	357.8	9.9
24	40.0	10.0	3.0	399.7	97.3	361.7	101.7	6.8
25	50.0	10.0	3.0	400.0	106.1	365.1	109.4	6.2
26	60.0	10.0	3.0	400.9	103.0	361.7	112.3	5.9
27	70.0	10.0	3.0	400.9	102.9	363.2	115.7	4.9
28	40.0	10.0	3.0	98.5	378.2	90.3	336.1	10.6
29	50.0	10.0	3.0	99.4	385.0	91.5	347.5	9.4
30	60.0	10.0	3.0	99.4	388.2	91.1	354.5	8.6
31	70.0	10.0	3.0	99.9	388.0	91.1	359.2	7.7

7.5.2 NO as single pollutant

Effect of the initial NO concentration

The level of NO concentration in the indoor air environment is in a range of several hundred ppb (Ao and Lee, 2003) and can reach a peak of ppm level in some places such as a car garage (Maggos et al., 2007). The photocatalytic oxidation experiments are carried out using different initial NO concentrations ranging from 100 ppb to 1.0 ppm to study its effect on the photocatalytic oxidation rate, while other conditions are the same as the standard experimental conditions introduced above.

The effect of the initial concentration on the NO$_x$ conversion rate is shown in Figure 7.6. The lower initial NO concentration results in a higher conversion rate. The conversion rate is 60.8% when the initial NO concentration is 0.1 ppm while the conversion rate is only 15.9% when the initial concentration increases to 1.0 ppm, which is also confirmed by Devahasdin et al. (2003) who found a conversion of 70% and 15% with the initial concentration of 5.0 ppm and 60.0 ppm, respectively. This can probably be explained by the adsorption ability of the fixed active sites of TiO$_2$ on the surface of the sample, which is in accordance with Ao and Lee (2004) who reported the NO$_x$ removal rate is improved with the use of activated carbon to help absorbing the NO onto the surface of the sample.

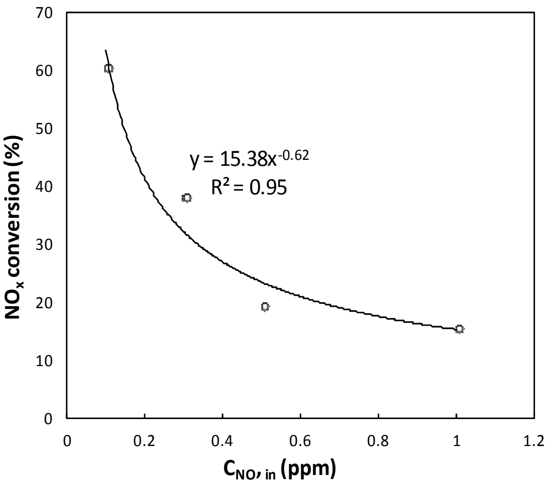

Figure 7.6: Effect of the initial pollutant concentration on the NO$_x$ conversion rate (Q = 3 L min^{-1}; RH = 50%; I = 10 W m^{-2}).

The Langmuir-Hinshelwood model has been widely investigated (Obee and Brown, 1995; Devahasdin et al., 2003; Zhao and Yang, 2003; Hunger and Brouwers, 2008; Yu et al., 2009) to describe the photocatalytic reaction rate with different pollutants such as VOCs and NO. The model applies the Langmuir adsorption isotherm to describe the disappearance rate of reactant, and reads:

$$r = \frac{kKC}{1+KC} \Leftrightarrow \frac{1}{r} = \frac{1}{kKC} + \frac{1}{k} \tag{7.5.1}$$

where r is the reaction rate, k is the reaction rate constant, K is the absorption rate constant and C is the concentration.

The reaction rate in Equation (7.5.1) is of the first order at low concentrations and of the zero order at high concentrations, which is confirmed by Obee and Brown (1995) and Emeline et al. (2000). Yu et al. (2007) also reported a linear increase of the initial reaction rate at a lower initial concentration of PCO of formaldehyde in indoor air. So, although the conversion of NO is higher with a smaller initial concentration, the lower initial reaction rate means that a longer reaction time is needed for the photocatalytic oxidation.

Effect of the flow rate

Varying the flow rates result in different photocatalytic oxidation reaction periods, since they influence the mass transfer and adsorption of NO onto the surface of the photocatalyst. The residence time, also known as the space time, is defined as the reactor's volume divided by the volumetric gas flow rate. Experiments are performed using different volumetric flow rates varying from 1.0 to 5.0 L min^{-1} to study the effect of the flow rate. The Reynolds number of the flow is used to describe the style of the flow:

$$\mathrm{Re} = \frac{v_{air} D_h \rho_{air}}{\eta_{air}} = \frac{D_h v_{air}}{\mu_{air}} = \frac{2Q}{(W+H)\mu_{air}} \tag{7.5.2}$$

where D_h is the hydraulic diameter, which is defined as 4 times the cross-sectional area (W×H), divided by the wetted perimeter (2(W+H)), $\mu_{air} = 1.80 \times 10^{-5}$ (20 °C, 1 bar) (Ns m^{-2}).

Within the used flow rates, the Reynolds number ranges from 21 to 105, which indicates the flow is laminar (Levenspiel, 1999).

Figure 7.7 shows the photocatalytic oxidation results using the different flow rates. It is evident from the results that a lower flow rate results in a higher conversion. Ao and Lee (2003) reported a steady decrease of NO conversion from 88% to 68% when the flow rate increases from 5 $Lmin^{-1}$ to 30 $Lmin^{-1}$. Devahasin et al. (2003) and Wang et al. (2007) reported that the conversion increases with an increase of the residence time until a value from which the conversion remains stable. This is different from the present thesis, in which the results show that the lower the flow rate is, the faster the conversion speed increase is obtained. The system here becomes a batch reactor when the volumetric flow rate decreases to zero, which means that a 100% of the conversion will be obtained given a sufficient reaction time. However, the applicable lowest flow rate is 1 $Lmin^{-1}$ due to the limitation of the test set-up. The influence of the mass transfer between the reactants and the catalyst is not studied when the flow decreases to a very low value.

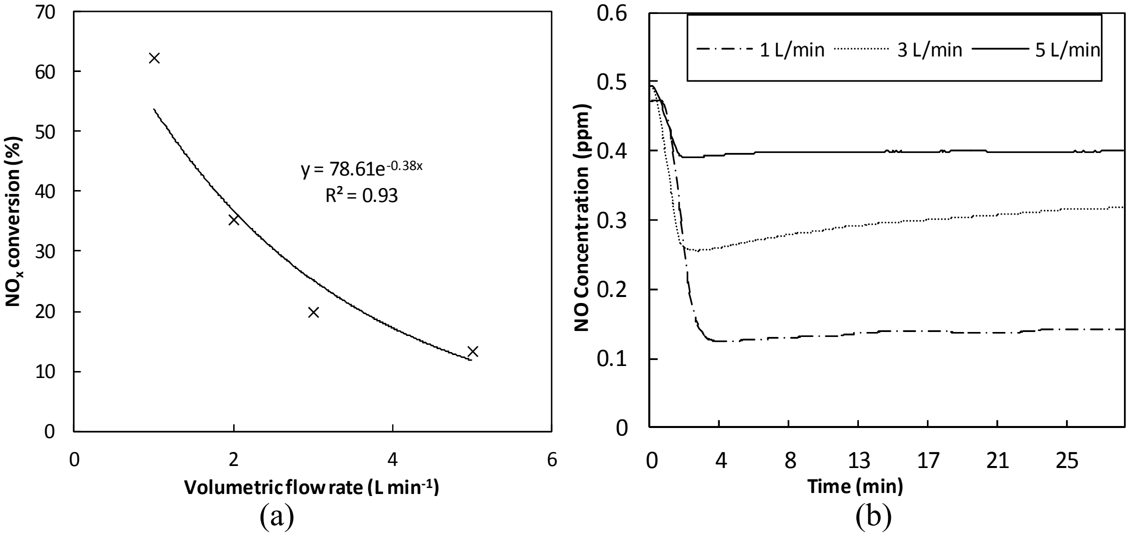

Figure 7.7: Effect of the volumetric flow rate on the NO_x conversion rate (a: NO_x conversion versus the flow rate, $C_{NO,\,in}$ = 0.5 ppm; RH = 50%; I = 10 W m^{-2}; b: The NO concentration change during measurement with different volumetric flow rates, $C_{NO,\,in}$ = 0.5 ppm; Q = 3 L min^{-1}; RH = 50%).

Effect of the light source

UV light is extensively used to activate the photocatalytic oxidation reaction. With enough activation energy provided by photons from the UV light, the electron and hole pairs will be generated on the catalyst surface, which leads to the photocatalytic oxidation of pollutants. The light intensity influences the PCO effect because more photons are produced when the light intensity becomes stronger.

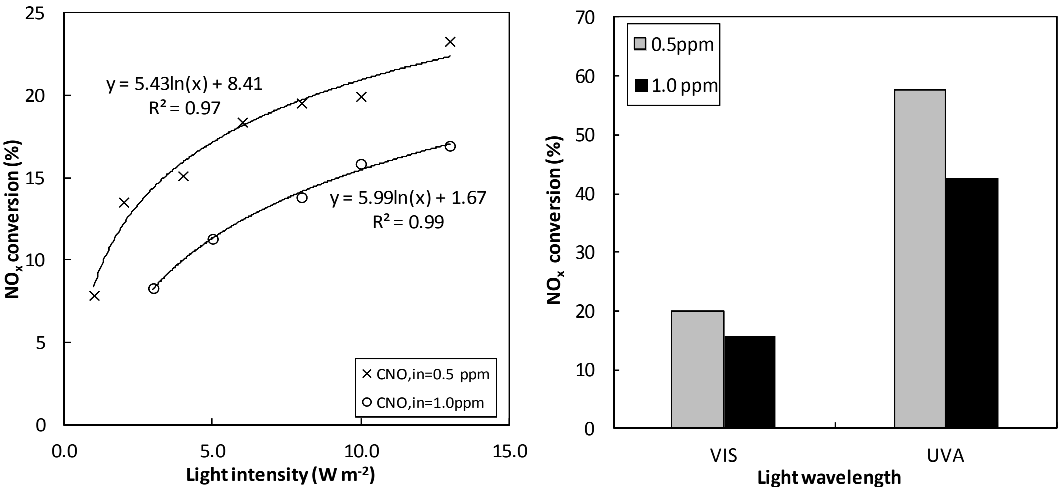

(a) (b)

Figure 7.8: Effect of light on the NO_x conversion (a: light intensity, $C_{NO,\,in} = 0.5$ ppm; $Q = 3$ L min^{-1}; RH = 50%; b: light wavelength, $C_{NO,\,in} = 0.5$ ppm or 1.0 ppm; $Q = 3$ L min^{-1}; RH = 50%; $I = 10$ Wm^{-2}).

Egerton and King (1979) pointed out that the PCO rate increases linearly with the light intensity at low values while it follows a square root law at high values, which is also confirmed by Herrmann et al. (2007) who reported a turning point of the light intensity at 250 Wm^{-2}. The reason is that in the first regime, i.e. first order regime, the generated electron-hole pairs are consumed more rapidly by the PCO reaction than by the recombination, whereas in the second order regime the recombination rate is dominant which results in a decrease of the photocatalytic oxidation. Kim and Hong (2002) reported a linear increase of the PCO rate with the increase of the UV light intensity within 40 Wm^{-2} using VOCs like trichloroethylene and toluene as pollutants. This is in line with Yu et al. (2007) who reported a linear increase of the PCO conversion of formaldehyde with an increase of the light intensity from 0.5 to 2.5 Wm^{-2}. Devahasdin et al. (2003) found a combination effect of the NO initial concentration on its conversion with the light intensity varying from 20 to 70 Wm^{-2}. The conversion rate does not change with an initial concentration of 5 ppm, but it steadily increases with an initial concentration of 40 ppm.

Visible light is used as the light source for the photocatalytic oxidation of NO using the carbon-doped TiO_2 as the photocatalyst, considering the extremely low UV light intensity in indoor conditions. By doping with carbon, the band gap between the valence band and conduction band of TiO_2 is modified, which allows it to be activated by the visible light in the bluish light range. However, to the author's knowledge, no study has been carried out on the effect of the visible light intensity on the PCO of NO. A range of 1.0 - 13.0 Wm^{-2} of the visible light intensity is used to study its effect on the photocatalytic oxidation rate. The results are shown in Figure 7.8a. The NO_x conversion rate increases with an increase of the light intensity according to a logarithmic relation, which is different from all available literature. The NO_x conversion rate increase has the same logarithmic rule with the increase of the light intensity using two different initial NO concentrations, which is also different from Devahasdin et al. (2003).

Compared to the undoped TiO_2, the cut-off wavelength of the carbon-doped TiO_2 extends to the visible bluish light range (Blöß and Elfenthal, 2007), which indicates that the doped TiO_2 should still have a similar absorption ability in the UV light range. Experiments are carried out to study the effect of the light wavelength here. Results are shown in Figure 7.8b, and they are in accordance with Blöß and Elfenthal (2007), who reported a 53.8% PCO degradation rate using the carbon-doped TiO_2 and 59.1% degradation rate using the undoped TiO_2 respectively, applying UV light as the light source. The photocatalytic degradation effect of materials in the UV light range is more than two times that of visible light in bluish green region with the same experimental conditions. However, as mentioned before, there is very little UV light irradiance in indoor air conditions, so the combined effect of UV light and visible light to activate the photocatalytic reaction remains an important open topic in applying the photocatalytic oxidation technology in indoor air conditions.

Effect of the relative humidity

Water plays a very important role in PCO because it is the only source of the hydroxyl radicals, which then oxidizes NO into NO_2 and then to the final product NO_3^-. Numerous studies have been carried out on its effect on the photocatalytic oxidation. Although the opinion that the competition between the pollutant and water adsorption onto the photocatalyst surface greatly influences the PCO is quite popular, no conclusive agreement has been reached to the author's knowledge.

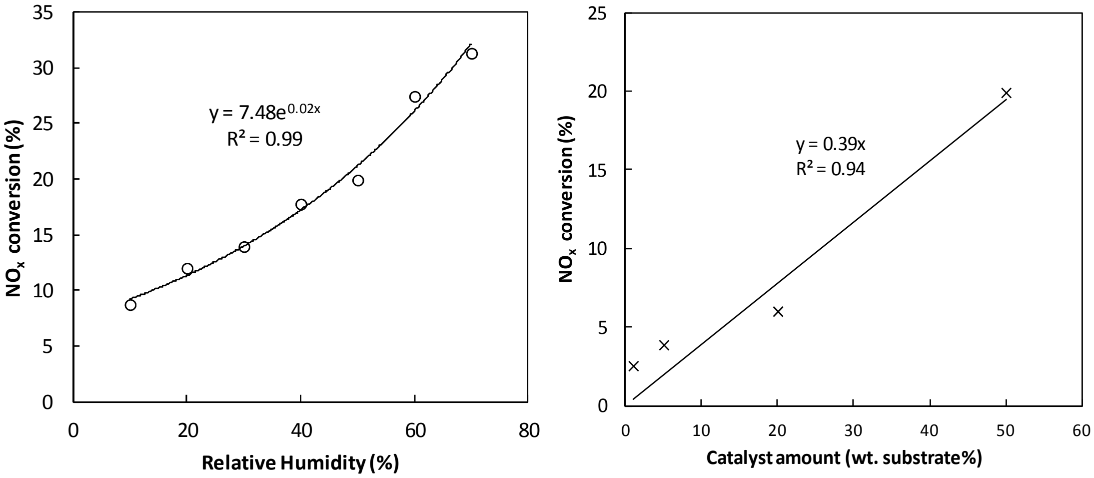

(a) (b)

Figure 7.9: NO$_x$ conversion versus: a: the relative humidity, $C_{NO,\ in}$ = 0.5 ppm; Q = 3 L min^{-1}; I = 10 W m^{-2}; b: the photocatalyst dosage, $C_{NO,\ in}$ = 0.5 ppm; Q = 3 L min^{-1}; RH = 50%; I = 10 W m^{-2}.

Obee and Brown (1995) reported that the effect of the water vapor on the photocatalytic oxidation of three pollutants (toluene, formaldehyde, and 1, 3-butadiene) is dependent on both the humidity and the initial pollutant concentrations, which can be explained as a result of competitive adsorption on the available hydroxyl adsorption sites and of changes in the hydroxyl radical population levels. Kim and Hong (2002) reported that the influence of water vapor on the photocatalytic oxidation depends on the species of pollutant. The effect of water on photocatalytic oxidation also is influenced by the substrate of the photocatalyst. Ao and Lee (2003) reported an almost constant NO conversion with the increase of the relative humidity from 10% until 70% using Teflon film as substrate. Devahasdin et al. (2003) reported that the conversion increases with the increase of the relative humidity from 0 until 50%, and then it becomes constant with NO as pollutant and using Pyrex as substrate. Wang et al. (2007) reported a steady increase of the NO conversion with an increase of the relative humidity from 8% until 100% using a woven glass fabric as substrate for the TiO_2. Beeldens (2007) and Hüsken et al. (2007) reported a steady decrease of the NO conversion with the increase of the RH using a concrete pavestone as substrate.

The effect of water on the photocatalytic oxidation is investigated by varying the relative humidity from 10% to 70%, since according to ASHRAE 30% to 60% of the relative humidity is recommended for a good indoor air quality. The experimental results are shown in Figure 7.9a. It is very clear that the NO_x conversion rate increases with an increase of the relative humidity, which is in line with Wang et al. (2007). The results indicate that the problem of the competition between the NO and water adsorption onto the photocatalyst surface does not exist at the low initial concentrations used here, which is also confirmed by Ao and Lee (2003).

Effect of the photocatalyst dosage

Photocatalysts are needed for the photocatalytic oxidation reaction of NO. The generated electron and hole pairs participate in the oxidation reaction with the adsorbed pollutant and water on the photocatalyst surface. The effect of the photocatalyst amount is studied since it influences the surface area, which will result in a different photocatalytic oxidation rate. The dosage of the photocatalyst is based on the total weight of the investigated photocatalytic paper. Experimental results of the photocatalytic oxidation of NO with different dosages of the photocatalyst are shown in Figure 7.9b.

From the results it is obvious that the dosage of the photocatalyst influences very much the photocatalytic oxidation rate. The NO_x conversion increases linearly with the increase of the photocatalyst amount, which is in line with Hüsken et al. (2007).

7.5.3 NO_x as pollutants

Effect of the initial NO and NO_2 concentrations

The PCO tests are performed using different initial concentration proportions of NO_x, but always with a total amount of 500 ppb. Figure 7.10a shows the influence of varying the initial pollutant concentration on the outlet concentration of both nitrogen oxides.

Increasing the initial concentrations results in higher removal rates for NO and NO_2, indicating that the PCO process does not privilege the degradation of one molecule over the other. This is one characteristic of the hydroxyl radicals, as they can oxidize a wide number of chemicals. Nevertheless, there is one difference between the PCO of the two molecules: increasing the NO concentration yields more NO_2, up to a point where the outlet concentration of NO_2 is higher than at the inlet. This behavior reduces significantly the overall NO_x conversion, as shown in Figure 7.10b. This happens because the complete oxidation of NO takes two intermediate steps of first to NO_2 (Equations (7.4.3) and (7.4.4)), which then can either be oxidized to NO_3^- or be desorbed into the carrier gas.

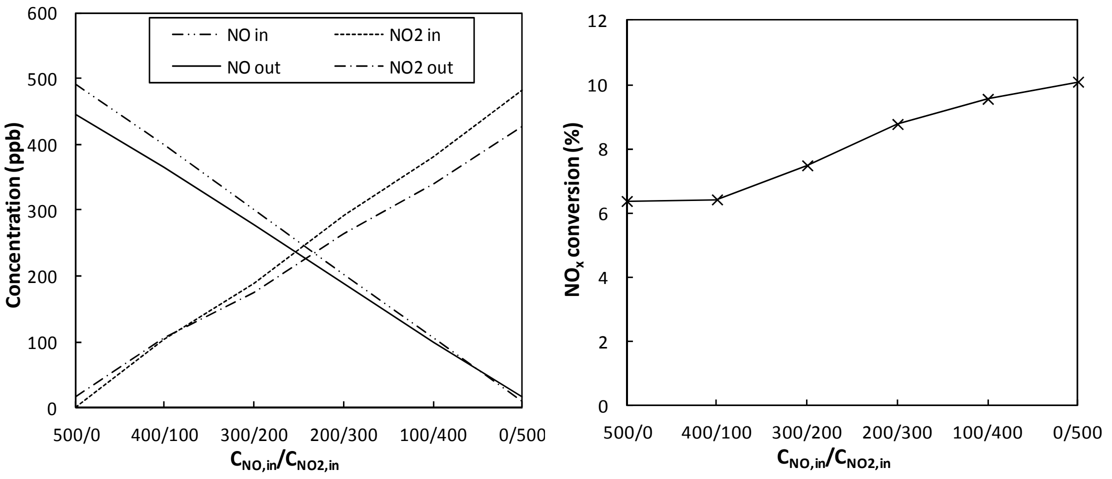

(a) (b)

Figure 7.10: (a) Effect of the initial pollutant concentration on the NO_x conversion; (b): NO_x conversion versus NO_x concentration.

Another difference can be noticed from Figure 7.10a when the inlet air stream carries only NO or NO_2. When there is only NO at the inlet, there is a significant production of NO_2. When the inlet air stream carries only NO_2 at 500 ppb, there are still traces of NO at the inlet. The initial amount of NO appears due to the fact that the NO_2 supply cylinder contains trace amounts of NO, and is shown in the analyzer as well as confirmed by the certificate from the gas provider. However, the outlet NO concentration slightly increases from 10.3 to 16.3 ppb. The generation of NO may occur because NO_2 can react with water vapor producing nitric oxide as well as nitric acid, reading

$$3NO_2 + H_2O \rightarrow NO + 2HNO_3 \tag{7.5.3}$$

Although the formation of NO by the homogeneous reaction shown in Equation (7.5.3) may occur, it is very small compared to the photocatalytic reactions (see experiment $^{\#}$6 in Table 7.12).

Effect of the flow rate

The residence time is the average amount of time that a particle spends in a particular system, defined as:

$$\tau = \frac{V}{Q} \tag{7.5.4}$$

where τ is the residence time, V is the volume of the system (L) and Q is the volumetric flow rate (L min^{-1}).

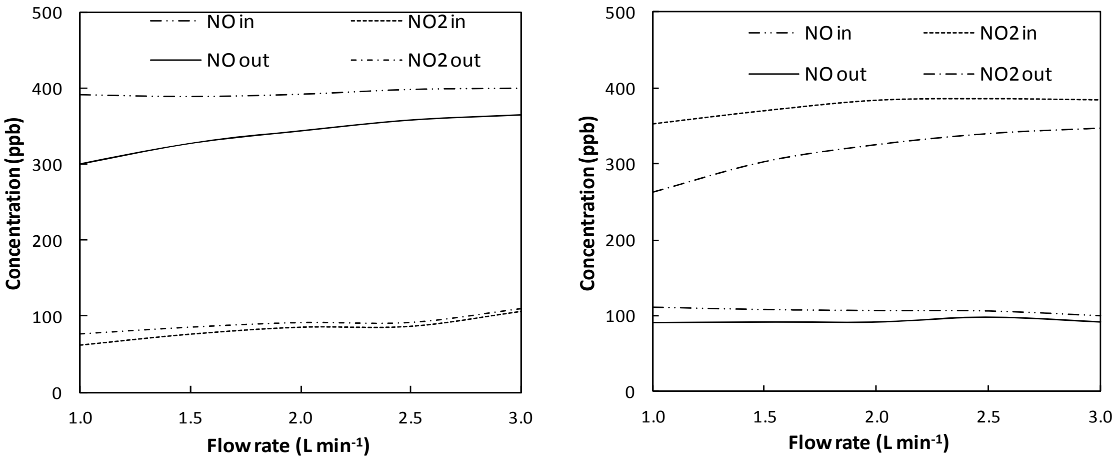

(a) (b)

Figure 7.11: Effect of the flow rate on the NO_x conversion (a: $C_{NO,in}$ = 400 ppb, $C_{NO_2,in}$ = 100 ppb; b: $C_{NO_2,in}$ = 400 ppb, $C_{NO,in}$ = 100 ppb).

The residence time of a pollutant molecule in the system and the pollutant concentration influence the number of available molecules with possible contacts to the active sites of the photocatalyst. Figure 7.11 shows the experimental results for varying the flow rates and their influence on the nitrogen oxides concentration. In the entire experimented range there is a degradation of both nitrogen oxides, except for the case when the initial concentration of NO_2 is 100 ppb (Figure 7.11a). In this case, NO_2 is produced and even increases at lower flow rates, confirming the analysis made in the previous section: part of the intermediate product (NO_2) of the oxidation of NO is desorbed into the carrier gas. This affects the overall NO_x conversion, as seen in Figure 7.12, where the conversion is significantly higher when NO_2 is the abundant pollutant. The relation between the flow rate and NO_x conversion is also clear: high flow rates reduce the residence time of the pollutant molecules on the active sites of the photocatalyst, thus reducing the reaction rate.

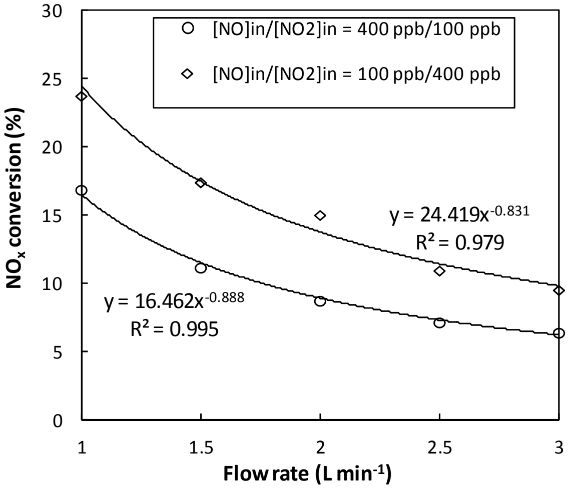

Figure 7.12: Flow rate versus overall NO_x conversion.

It can also be seen from Figure 7.12 that the conversion of NO_x follows a power law. The flow rate plays a significant role on the efficiency of the PCO: decreasing its value from 3.0 to 1.0 $Lmin^{-1}$ increases the NO_x conversion from 6.2% to 16.9% when the dominant pollutant is NO; when the abundant pollutant is NO_2 it increases from 9.37% to 23.8%. At a flow rate value of $Q = 1.0$ $Lmin^{-1}$ the highest NO_x conversion is reached in all the experiments performed, showing that this is the most sensitive parameter of the pollutant oxidation. This is in line with the study presented in the previous section, i.e. an increase of NO_x conversion of around 40% is noticed when decreasing the flow rate from 5 to 1 $Lmin^{-1}$ in the case of NO as a single pollutant.

Effect of the light intensity

The effect of the light intensity on the photocatalytic reaction has been studied extensively (Hashimoto et al., 2001; Kim and Hong, 2002; Hoskins, 2003; Wang et al., 2007). As mentioned in the previous sections, the PCO reaction is caused by the optoelectronic properties of titanium dioxide in the anatase form. Due to the modification of the photocatalyst, the electron-hole pairs can now be generated with the irradiation of visible light. However, not only the wavelength of the light shows an influence on the PCO efficiency, but also the intensity, E. The light intensity influences the PCO efficiency because the produced electrons become higher when the light intensity becomes stronger.

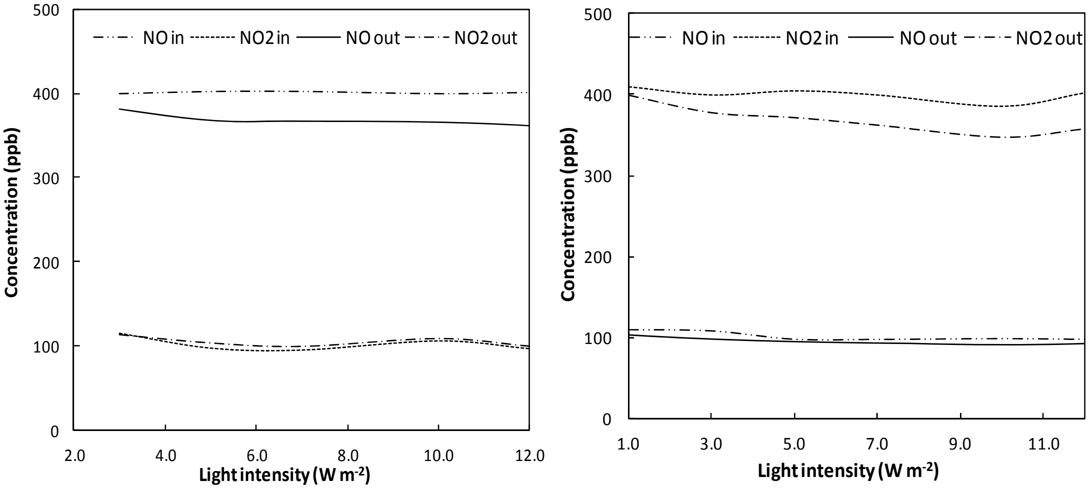

(a) (b)

Figure 7.13: Influence of the light intensity on the NO_x conversion (a: $C_{NO,in}$=400 ppb, $C_{NO_2, in}$=100 ppb; b: $C_{NO_2,in}$=400 ppb, $C_{NO, in}$=100 ppb).

The results are shown in Figure 7.13. It can be seen that, when NO is at a majority concentration (400 ppb), the effect of the light intensity is more obvious: the NO conversion increases from 4.7% at 3 Wm^{-2} to 10.1% at 12 Wm^{-2}. However, when the concentration of the pollutant is low (100 ppb), the effect of the light intensity on the outlet concentration is insignificant: at the lowest irradiation value the NO conversion is 5.7% and at the highest irradiation it remains at 5.6%. The same behavior is observed when NO_2 is the abundant pollutant (Figure 7.13b).

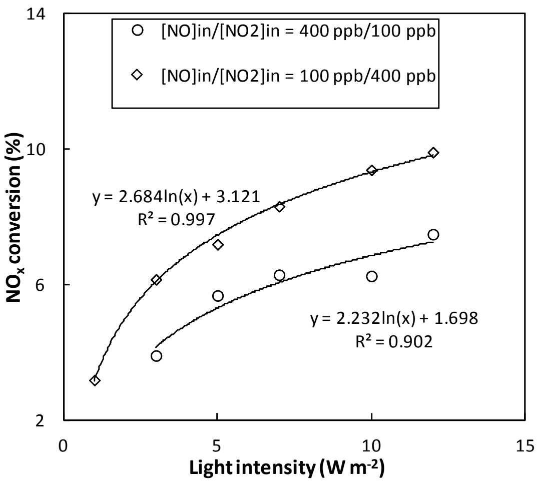

Figure 7.14: Light intensity versus NO_x conversion.

Figure 7.14 shows the NO_x conversion as a function of the light intensity in two different cases. When the abundant pollutant is NO_2, the overall NO_x conversion is higher in every value of light intensity. This also happens when reporting the effect of the concentration and of the flow rate. The increase of the NO_x conversion with the increase of the light intensity follows a logarithmic law, which is in line with the findings reported in the previous section. The logarithmic trend fits quite well to the experimental results with an R^2 value of 0.997 and 0.902 for the two different concentration mixtures.

Effect of the relative humidity

The molecular water adsorbed on the photocatalyst reacts with the hole and generates hydroxyl radicals (OH·), which then oxidizes pollutants. It has been reported that the PCO reaction is typically governed by the generation of the hydroxyl radicals (Herrmann et al., 2007), although reactions that generate other radicals, like chlorine, could also display high reaction rates (Lim et al., 2000). When there is an absence of water vapor, the PCO is seriously retarded, for instance when the target pollutant is formaldehyde (Tompkins and Anderson, 2001) or acetone (Yamazaki et al., 1996). However, it has also been stated that an excessive amount of water vapor on the catalyst surface will inhibit the reaction rate, because the water vapor competes with pollutants for adsorption sites on the photocatalyst, thus reducing the pollutant removal rate (Ao et al., 2004).

The ASHRAE standard 55-2004 (2003) specifies that to decrease the possibility of discomfort due to low humidity, the dew point temperature should not be less than 2.8°C, which equals to 31% RH in 21°C. The upper dew point limit is specified to 16.7°C, which equals to 76% RH in 21°C. Therefore, in this research the relative humidity is varied between 40% and 70% to investigate its effect on the PCO behavior.

Figure 7.15 shows the influence of the relative humidity on the outlet concentrations of both nitrogen oxides. The relative humidity however, within the range specified, does not have any significant influence on the outlet concentration of NO: the NO conversion remains at stable levels of 9.5% at 40% RH to 9.4% at 70% RH when the initial concentration is 400 ppb. In the case of NO initial concentration of 100 ppb, the NO conversion very slightly varies from 8.3% at 40% RH to 8.8% at 70% RH. For NO_2, the relative humidity indeed influences its conversion: at 400 ppb, NO_2 degradation decreases from 11.1% at 40% RH to 7.4% at 70% RH. This behavior could be explained by the fact that water vapor molecules compete with NO_2 for the adsorption of active sites, decreasing the reaction efficiency. However, when NO_2 is at 100 ppb, something different happens: the NO_2 conversion is always negative, meaning there is more production of the nitrogen dioxide rather than its degradation. This is explained by the generation of more NO_2-intermediate molecules. The conclusion from this phenomena is that at increasing RH, the water vapor is inducing desorption of the NO_2 molecules from the surface.

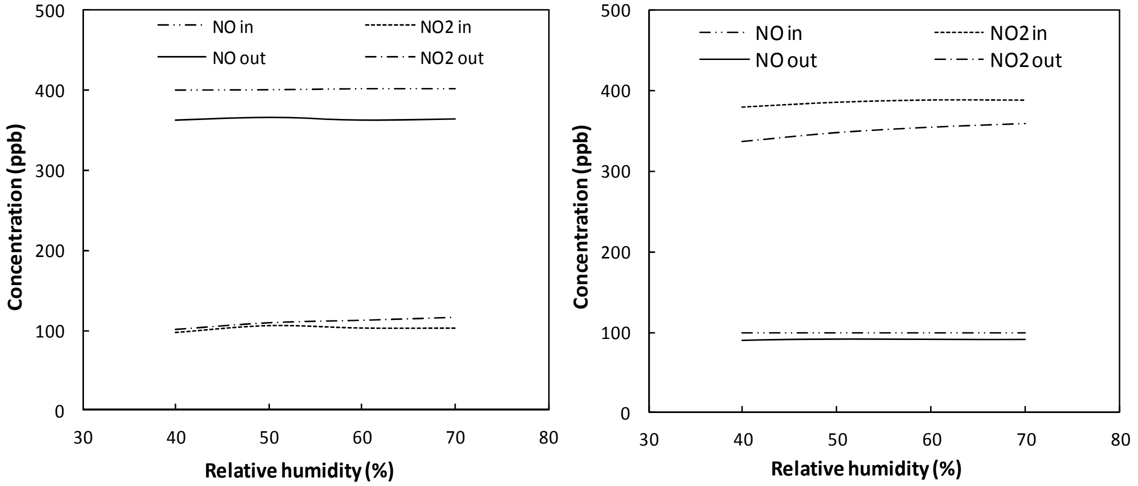

(a) (b)

Figure 7.15: Influence of relative humidity on the NO_x conversion (a: $C_{NO,in} = 400$ ppb, $C_{NO_2,in} = 100$ ppb; b: $C_{NO_2,in} = 400$ ppb, $C_{NO,in} = 100$ ppb).

The overall degradation of the NO_x is shown in Figure 7.16. The degradation rate is always higher when NO_2 is the abundant molecule in the mixture, and this behavior also occurs when varying flow rate and light intensity, as shown in Figures 7.12 and 7.14, respectively. The slope of the abundant-NO_2 trend line is steeper than the one with abundant NO, which also confirms the higher influence water vapor plays on NO_2 than on NO degradation. This generalized decrease in the NO_x conversion has also been reported (Ao and Lee, 2003; Maggos et al., 2007; Hunger et al., 2009). Hunger et al. (2009), for instance, reported a linear decrease in the NO conversion, within an investigation range of 10% to 80% RH. They also reported that the RH values higher than 45% result in higher NO_2 concentrations, which is exactly the same behavior as found here. In contrast, the results presented in the previous section indicated a PCO efficiency improvement with more moisture, in line with Devashadin et al. (2003). What could be explained here is that the author used a higher concentration of pollutants, so the pollutant molecules have a larger chance of reaching the active sites, decreasing the molecular competition and increasing the reaction rates. The difference of results in literature may be due to the influence of different substrates used. Martinez et al. (2011) compared the photo-degradation of NO using glass and mortar as substrates and found different results: within a RH range of 0-74%, the optimal humidity level for the degradation of NO using glass as the substrate is found to be 32%. Using mortar, no optimal humidity level could be identified due to the fact that the excess water is absorbed by the substrate, reducing molecular competition. In this research a paper-based wall covering is used, which could be the reason why the decrease in the NO_x concentration is small when varying the RH: when NO is the dominant pollutant, the NO_x conversion decreases from 6.8% at 40% RH to 4.9% at 70% RH. When NO_2 is the abundant pollutant the NO_x conversion decreases from 10.6% at 40% RH to 7.7% at 70% RH. While in both cases there is a decreasing trend of the NO_x conversion, the variation is small, and may indicate that the adsorption of excess water on the substrate decreases the impact of the molecular competition on active sites.

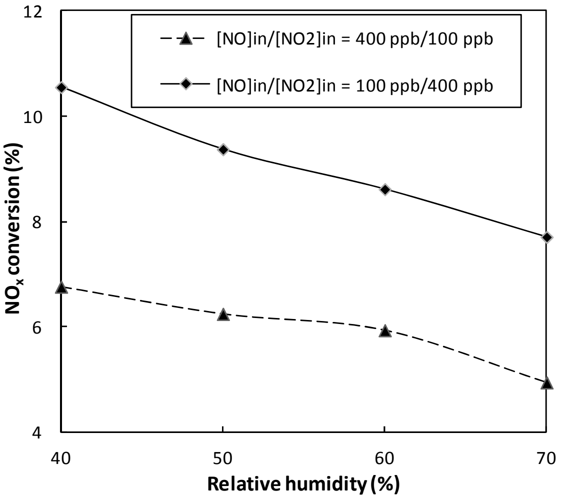

Figure 7.16: Relative humidity versus NO_x conversion.

After reviewing the influence of certain variables on the NO_x conversion, it is clear that in every case, the conversion is considerably higher when the NO_2 is the dominant nitrogen oxide in the mixture. The purpose of maintaining the concentration of NO_x fixed at 500 ppb every time while varying the pollutants proportions is more to assess mixture variations rather than to assess the absolute bulk concentration of pollutants. The result is clear that NO_2 is degraded more efficiently than NO. The pathway to a nitrate oxidation takes just one reaction step, while the oxidation of NO has first to undergo a conversion to NO_2.

7.6 Conclusions

This chapter addresses the indoor air purification using heterogeneous photocatalytic oxidation. Two photocatalytic oxidation test set-ups are developed in the present study following the ISO standard 22197-1:2007 as a reference. To use the visible light activated catalyst in indoor air conditions, a carbon-doped TiO_2 is chosen as photocatalyst. Different materials such as newly developed gypsum plasterboard cover paper, gypsum plaster, and wall covering are used as substrate for the photocatalyst. Using NO_x as the target pollutant, the photocatalytic oxidation experiments are carried out in indoor air conditions. The following conclusions are drawn:

- The experimental results indicate that the photocatalytic oxidation is an effective indoor air purification technology. All photocatalytic oxidation experiments are carried out at ambient conditions under visible light, which shows its convenience for the indoor air purification.
- Visible light is chosen as the light source for the photocatalytic oxidation of NO_x and the results show its efficiency. The NO_x conversion increases with an increase of the light intensity according to a logarithmic rule, which is different from the available literature so far. Furthermore, the effect of the light wavelength is studied and the NO_x conversion is more than two times higher in the UVA range than in the visible bluish light range, which brings an open research topic on how to use the photocatalyst in indoor conditions more effectively.
- Lower initial NO concentration shows a higher NO_x conversion. However, a longer reaction time is needed for the photocatalytic oxidation of NO with a very low initial concentration.
- Decreasing the volumetric flow rate of the pollutant results in a longer residence time that in turn leads to a longer reaction time of the pollutant, which finally leads to a higher NO_x conversion rate. The reactor becomes a batch reactor when the volumetric flow rate decreases to zero, which means that a 100% of the conversion will be obtained given a sufficient reaction time.
- Water plays a very complex role in the PCO process. It is the source of the hydroxyl radical generation, but it also competes with other reactants for the active surface occupation. Current experiments show controversial results, i.e. depending on different materials as substrate, a higher or lower NO_x conversion results when increasing the relative humidity. In the case of NO_x as the target pollutants, the effect of the water vapor is even more complex.
- The photocatalytic oxidation of NO_x takes place on the photocatalyst surface. The higher the exposed surface area of the photocatalyst is, the higher NO_x conversion should be, which can be used to explain the higher NO_x conversion in this study when the amount of the photocatalyst increases.
- In the case of NO_x as the target pollutants, the overall NO_x conversion is always higher when NO_2 is the abundant pollutant no matter which test parameter is varied, which is a favorable outcome since NO_2 is more toxic than NO. The difference in conversion occurs because NO_2 only needs to undergo, during the PCO reaction, one oxidation step to reach the nitrate form, while NO is oxidized via the intermediate NO_2 to nitric acid. Also, when NO_2 is the only pollutant in the stream, there is a slight generation of NO, indicating the possible presence of homogeneous reactions.

Chapter 8

Modeling of photocatalytic oxidation under indoor air conditions

8.1 Introduction

Heterogeneous photocatalytic oxidation (PCO) has been shown to be a successful technology for water or air purification in outdoor conditions and to date the photocatalytic oxidation has been investigated intensively (Fujishima and Honda, 1972). The PCO experiments performed under different indoor air conditions and results presented in the previous chapter prove that the PCO is also suitable for the indoor air quality improvement.

Besides the laboratory-scaled experimental research on the PCO, investigations have also been performed to numerically model the reactions. These models predict not only the underlying kinetic processes, but also the involved transport phenomena (mass, heat and momentum). Hoffmann et al. (1995) reviewed the photocatalytic reaction mechanism and especially studied the application of the Langmuir-Hinshelwood (L-H) model. Obee and Brown (1995) applied the L-H model to study the oxidation rate of some VOCs such as formaldehyde, toluene, and 1,3-butadiene using an indoor air concentration of sub-ppm level and the effect of the humidity and pollutants concentration is considered in their model. They found that the effect of humidity on the oxidation rate is dependent critically on the concentration of the pollutant and the L-H model was successfully used to correlate the oxidation rate data. Dalton et al. (2002) investigated the PCO reaction mechanism of NO_x using TiO_2 as photocatalyst with a surface spectroscopic approach. Devahasdin et al. (2003) studied the reaction kinetics of NO photocatalytic oxidation and the effect of the residence time and inlet pollutant concentration on the PCO efficiency. Wang et al. (2007) reported a reaction mechanism of the PCO of NO_x with an inlet concentration of 20-168 ppm using TiO_2 supported on a woven glass fabric, and they reported that NO is oxidized to NO_2 both by the generated hydroxyl radicals and electron trapped oxygen. Kuo et al. (2007) studied the PCO of NO_x under visible light using carbon-doped TiO_2 and they proposed a reaction mechanism in which NO is oxidized to NO_2 by the generated hydroxyl radicals and HO_2 radicals.

Computational Fluid Dynamics (CFD), a branch of fluid mechanics, uses numerical methods and algorithms to solve and analyze problems that involve fluid flows. It is widely applied to different fields such as combustion, airplane design, submarines etc. CFD has been also applied to reactor modeling in the chemical engineering field. Jarandehei and Visscher (2009) made a three-dimensional model of a flat-plate photocatalytic reactor by applying commercial CFD software. Their work is of particular interest, since they found that the flow and mass phenomena involved in the gas phase plays an important role in the entire photocatalytic process. Salvadó-Estivill et al. (2007) used CFD modeling to evaluate the PCO of trichloroethylene (TCE) and came to a similar conclusion about the importance of the mass transport. Xu et al. (2009) carried out the actual measurements and built a CFD room model to understand the dispersion of contaminants when there is personal displacement ventilation. Kao et al. (2009) compared the airflow and the particulate matter transport in multi-room buildings for different natural ventilation patterns, also involving CFD modeling. Hayashi et al. (2002) performed a CFD analysis on the characteristics of contaminated indoor air ventilation and its application in the evaluation of the effects of contaminant inhalation by a human occupant. Murakami et al. (2003) presented a CFD model for analyzing the transport of various pollutants from building materials inside a room. The room consists of a floor covered with an emission material made of polypropylene styrene-butadiene rubber and the side walls are made of coal-based activated carbon spread over the walls, which adsorbs pollutants.

However, so far the modeling of the PCO of NO under indoor air conditions has not been reported. As the influential parameters, the effects of the experimental conditions on the photocatalytic oxidation are rarely considered into the pollutant reaction. Most researchers believe that NO is oxidized to NO_3^- via the intermediate product NO_2, however, the influence of this undesired intermediate product NO_2 is seldom investigated (Ballari et al., 2010).

This chapter addresses the modeling of the PCO of NO under indoor air conditions. A kinetic model is proposed to describe the process of PCO of NO, and a reactor model is built applying CFD commercial software. The reaction rate of the NO oxidation is derived from the PCO reaction mechanism of NO_x and the kinetic parameters are optimized using the experimental results presented in Chapter 7. The proposed model and the built reactor model are validated against the experimental data, and the good agreement between the predicted values and the experimental results indicates their validity. Furthermore, the influence of the experimental conditions such as the NO inlet concentration, the volumetric flow rate of the NO, the relative humidity, the irradiance, the dosage of the photocatalyst, as well as the effect of the intermediate product NO_2 are investigated.

8.2 Proposal of a kinetic model

8.2.1 Introduction

A kinetic model is proposed in this section based on the PCO mechanism presented in the previous chapter (see Sections 7.3.3 and 7.4.6 in Chapter 7). In the following sections, the proposed model will be derived step by step: in Section 8.2.2 an adsorption model will be presented; in Section 8.2.3 a reaction rate model of NO_x will be proposed; in Section 8.2.4 the mass balance of NO_x along the PCO reactor will be provided; and in Section 8.2.5 the results will be presented and the proposed model will be validated by experiments.

8.2.2 Adsorption model

For the occurrence of the PCO reaction, the first essential step is the adsorption of the reactants onto the surface of the test sample (photocatalyst). The adsorption/desorption process reaches equilibrium when the adsorption and desorption rate of a particular gas on the superficial active sites of photocatalyst are equal (Ballari et al., 2009):

$$r_{+} - r_{-} = k_{+}C_{TiO_2\_free}C_{GAS} - k_{-}C_{TiO_2\_GAS} = 0 \tag{8.2.1}$$

Thus,

$$C_{TiO_2\_GAS} = K_{GAS}C_{TiO_2\_free}C_{GAS} \tag{8.2.2}$$

where *r* is the reaction rate (with r_+ the adsorption rate and r_- the desorption rate), *k* is the reaction rate constant, *C* is the superficial concentration in the valance band, *GAS* stands for NO, NO_2, or H_2O, and $K_{GAS}=k_{+}/k_{-}$.

The total superficial concentration of active sites is composed of the concentration of the free sites and the occupied sites due to the adsorption of NO, NO_2 and H_2O:

$$C_{TiO_2} = C_{TiO_2\_free} + C_{TiO_2\_NO} + C_{TiO_2\_NO_2} + C_{TiO_2\_H_2O} \tag{8.2.3}$$

Here Equation (8.2.3) is deduced based on the consideration that the adsorption of NO, NO_2, and H_2O does not compete with oxygen adsorption (Turchi and Ollis, 1990). The reason lies in that O_2 is trapped in the conduction band of the photocatalyst, while other gases (here NO, NO_2 and H_2O) are trapped in the valence band of the photocatalyst (Blöß and Elfenthal, 2007).

Substituting the adsorbed gas concentration given by Equation (8.2.2) in the case of NO, NO_2 and H_2O, respectively, into Equation (8.2.3) generates,

$$C_{TiO_2} = C_{TiO_2\_free} + K_{NO}C_{TiO_2\_free}C_{NO} + K_{NO_2}C_{TiO_2\_free}C_{NO_2} + K_{H_2O}C_{TiO_2\_free}C_{H_2O} \tag{8.2.4}$$

where *K* is the adsorption constant.

Thus, $C_{TiO_2\_free}$ is obtained by rewriting Equation (8.2.4), which reads:

$$C_{TiO_2\_free} = \frac{C_{TiO_2}}{1 + K_{NO}C_{NO} + K_{NO_2}C_{NO_2} + K_{H_2O}C_{H_2O}} \tag{8.2.5}$$

Substituting the obtained expression for $C_{TiO_2\_free}$ (Equation (8.2.5)) back into Equation (8.2.2), the adsorption equilibrium concentrations of all the gases are obtained:

$$C_{TiO_2\_NO} = \frac{K_{NO}C_{TiO_2}C_{NO}}{1 + K_{NO}C_{NO} + K_{NO_2}C_{NO_2} + K_{H_2O}C_{H_2O}} \tag{8.2.6}$$

$$C_{TiO_2\_NO_2} = \frac{K_{NO_2}C_{TiO_2}C_{NO_2}}{1 + K_{NO}C_{NO} + K_{NO_2}C_{NO_2} + K_{H_2O}C_{H_2O}} \tag{8.2.7}$$

$$C_{TiO_2\_H_2O} = \frac{K_{H_2O}C_{TiO_2}C_{H_2O}}{1 + K_{NO}C_{NO} + K_{NO_2}C_{NO_2} + K_{H_2O}C_{H_2O}} \tag{8.2.8}$$

The fundamental adsorption models derived here have the same format as the Langmuir adsorption isotherm, which has already been investigated to describe the adsorption of NO onto the surface of the photocatalyst for the PCO reaction (Hashimoto et al., 2001). In addition, a reaction rate model, Langmuir-Hinshelwood model, developed based on the Langmuir adsorption isotherm, has also been applied successfully to describe the reaction rate of the PCO of NO (Peral and Ollis, 1992; Hunger et al., 2010; Yu et al., 2009).

As discussed above, O_2 here is trapped in the conduction band of the photocatalyst. Therefore, the adsorption model of O_2 can be also obtained following the same procedure to deduce the adsorption model of the reactants that are trapped in the valence band of the photocatalyst, which reads:

$$C_{TiO_2'\_O_2} = \frac{K_{O_2} C_{TiO'_2} C_{O_2}}{1 + K_{O_2} C_{TiO'_2} C_{O_2}} \tag{8.2.9}$$

where $C_{TiO_2'}$ is the superficial concentration in the conduction band (mol dm^{-2}).

8.2.3 Reaction rate model

According to the mass action law and the fundamental reaction given in Equation (7.4.3) (see Section 7.4.6 in Chapter 7), the superficial reaction rate of NO is shown as follows:

$$r_{NO} = - k_{NO} C_{TiO_2\_NO} C_{OH\cdot} \tag{8.2.10}$$

Here it should be pointed out that the reaction mechanism (Equations (7.4.6) and (7.4.7)) proposed in Chapter 7 is not considered due to the very difficult reaction routes which have been discussed in Chapter 7.

Since NO_2 is generated from HNO_2 (here HNO_2 can be also written as HONO (Laufs et al., 2010)) and then oxidized to NO_3^- as shown in Equations (7.4.4) and (7.4.5) respectively, the reaction rate of NO_2 reads:

$$r_{NO_2} = k_{HNO_2} C_{TiO_2\_HNO_2} C_{OH\cdot} - k_{NO_2} C_{TiO_2\_NO_2} C_{OH\cdot} \tag{8.2.11}$$

Assuming a microscopic local equilibrium for unstable intermediates, the superficial reaction rate for hydroxyl radicals reads:

$$r_{OH\cdot} = k_{h^+} C_{TiO_2\_H_2O} C_{h^+} - k_{NO} C_{TiO_2\_NO} C_{OH\cdot} - k_{HNO_2} C_{TiO_2\_HNO_2} C_{OH\cdot} - k_{NO_2} C_{TiO_2\_NO_2} C_{OH\cdot} = 0 \tag{8.2.12}$$

Therefore, $C_{OH\cdot}$ is obtained by rewriting Equation (8.2.12):

$$C_{OH\cdot} = \frac{k_{h^+} C_{TiO_2\_H_2O} C_{h^+}}{k_{NO} C_{TiO_2\_NO} + k_{HNO_2} C_{TiO_2\_HNO_2} + k_{NO_2} C_{TiO_2\_NO_2}} \tag{8.2.13}$$

With the hypothesis that, as an intermediate, HNO_2 is produced and very rapidly consumed (Laufs et al., 2010), $C_{TiO_2\_HNO_2}$ is therefore obtained as follows:

$$r_{HNO_2} = k_{NO}C_{TiO_2\_NO}C_{OH\cdot} - k_{HNO_2}C_{TiO_2\_HNO_2}C_{OH\cdot} = 0 \qquad (8.2.14)$$

$$C_{TiO_2\_HNO_2} = \frac{k_{NO}C_{TiO_2\_NO}}{k_{HNO_2}} \qquad (8.2.15)$$

The reaction rates of the generated electron/hole pairs are expressed as follows:

$$r_{e^-} = r_{act} - k^*_{e^-}C_{e^-} - k_{dea}C_{e^-}C_{h^+} = 0 \qquad (8.2.16)$$

$$r_{h^+} = r_{act} - k_{h^+}C_{TiO_2\_H_2O}C_{h^+} - k_{dea}C_{e^-}C_{h^+} = 0 \qquad (8.2.17)$$

where $k^*_{e^-} = k_{e^-}C_{TiO'_2\_O_2} = k_{e^-}\frac{K_{O_2}C_{TiO'_2}C_{O_2}}{1+K_{O_2}C_{TiO'_2}C_{O_2}}$ (8.2.18)

assuming that $C_{TiO'_2\_O_2}$ is constant, since O_2 in the air is in huge excess compared to the concentration of the pollutant, and k_{ea} is the reaction rate constant of the recombination of the generated electron/hole pairs (Equation (7.3.5)).

The reaction rate of the photocatalyst activation (r_{act}) along the thickness (th) of the photocatalyst and under all wavelengths in the range of the lamps emission that the photocatalyst absorbs can be expressed as a function of the local superficial rate of photon absorption $e^a_{S,\lambda}$ and the primary quantum yield Φ_λ (Imoberdorf et al., 2005; Imoberdorf et al., 2006), reading

$$r_{act} = \int_{y=0}^{y=th}\int_{\lambda} \Phi_\lambda\, e^a_{S,\lambda}(y)\,d\lambda\, dy = \int_{y=0}^{y=th}\int_{\lambda} \Phi_\lambda S_g \rho D_{TiO_2} \kappa_\lambda E_\lambda(y)\,d\lambda\, dy \qquad (8.2.19)$$

where S_g is the specific surface area of the used photocatalyst ($dm^2\ g^{-1}$), ρ is the density of the photocatalyst ($g\ dm^{-3}$), D_{TiO2} is the dosage of the photocatalyst, κ_λ is the radiation absorption coefficient of the photocatalyst (cm^{-1}) and E_λ is the irradiance on the surface of photocatalyst at different wavelength ($W\ m^{-2}$).

Assuming an absorbent medium, the radiation extinction along the thickness of the photocatalyst can be expressed according to the Beer-Lambert law as follows (Siegel and Howell, 1992):

$$E_\lambda(y) = E_\lambda e^{-\kappa_\lambda y} \qquad (8.2.20)$$

where y is the depth along the thickness of the photocatalyst.

Therefore, integrating along the thickness of the photocatalyst and assuming that every property is constant in the uniform thickness, Equation (8.2.19) is rewritten as:

$$r_{act} = \int_{y=0}^{y=th}\int_{\lambda} \Phi_{\lambda}\ S_g \rho D_{TiO_2} \kappa_{\lambda} E_{\lambda} e^{-\kappa_{\lambda}\, y} d\lambda dy = E\int_{\lambda} \Phi_{\lambda}\ S_g \rho D_{TiO_2}\left(1 - e^{-\kappa_{\lambda} th}\right) d\lambda = \alpha E \qquad (8.2.21)$$

where

$$\alpha = \int_{\lambda} \Phi_{\lambda}\ S_g \rho D_{TiO_2}\left(1 - e^{-\kappa_{\lambda} th}\right) d\lambda \qquad (8.2.22)$$

Therefore, C_{h^+} and C_{e^-} are obtained from Equations (8.2.16), (8.2.17) and (8.2.21):

$$C_{e^-} = \frac{\alpha E}{k^*_{e^-} + k_{dea} C_{h^+}} \qquad (8.2.23)$$

$$C_{h^+} = \frac{\alpha E}{k_{h^+} C_{TiO_2\_H_2O} + k_{dea} C_{e^-}} = \frac{\alpha E}{k_{h^+} C_{TiO_2\_H_2O} + k_{dea}\dfrac{\alpha E}{k^*_{e^-} + k_{dea} C_{h^+}}} \qquad (8.2.24)$$

C_{h^+} can be solved from Equation (8.2.24) and the positive sign of the quadratic solution is chosen since C_{h^+} is 0 if E is 0, yielding

$$C_{h^+} = \frac{k^*_{e^-}\left(\sqrt{1 + \dfrac{4 k_{dea} \alpha E}{k^*_{e^-} k_{h^+} C_{TiO_2\_H_2O}}} - 1\right)}{2 k_{dea}} \qquad (8.2.25)$$

Substituting the obtained C_{h^+} from Equation (8.2.25) and Equation (8.2.15) into Equation (8.2.13), $C_{OH^\cdot}$ is obtained

$$C_{OH^\bullet} = \frac{k^*_{e^-} k_{h^+} C_{TiO_2\_H_2O}\left(\sqrt{1 + \dfrac{4 k_{dea} \alpha E}{k^*_{e^-} k_{h^+} C_{TiO_2\_H_2O}}} - 1\right)}{4 k_{dea} k_{NO} C_{TiO_2\_NO} + 2 k_{dea} k_{NO_2} C_{TiO_2\_NO_2}} \qquad (8.2.26)$$

Substituting the obtained $C_{OH^\cdot}$ into Equation (8.2.10) and (8.2.11), the reaction rate models for NO and NO_2 now are derived as

$$r_{NO} = -k_{NO} C_{TiO_2\_NO} \frac{\gamma C_{TiO_2\_H_2O}\left(\sqrt{1 + \dfrac{4 \alpha E}{\gamma C_{TiO_2\_H_2O}}} - 1\right)}{4 k_{NO} C_{TiO_2\_NO} + 2 k_{NO_2} C_{TiO_2\_NO_2}} \qquad (8.2.27)$$

and

$$r_{NO_2}=\frac{(k_{NO}C_{TiO_2\_NO}-k_{NO_2}C_{TiO_2\_NO_2})\gamma C_{TiO_2\_H_2O}}{4k_{NO}C_{TiO_2\_NO}+2k_{NO_2}C_{TiO_2\_NO_2}}\left(\sqrt{1+\frac{4\alpha E}{\gamma C_{TiO_2\_H_2O}}}-1\right) \tag{8.2.28}$$

respectively, where

$$\gamma=\frac{k_{h^+}\times k_{e^-}^*}{k_{dea}} \tag{8.2.29}$$

8.2.4 Mass balances

The following aspects are usually considered in reactor design (Cassano et al., 1995): raw materials, operating conditions, geometry of the reactor, radiation etc. Different types of reactors can be used for photocatalytic reactions (Cassano et al., 2000; de Lasa et al., 2005), and among them three types of reactors are usually considered as ideal reactors (Levenspiel, 1999): batch reactor, plug flow reactor and continuously mixed reactor.

In a plug flow reactor, the fluid flows along the reactor orderly with no element overtaking or mixing with any other element ahead or behind. All reactants in the plug flow reactor have the same residence time (Zhao and Yang, 2003). The reactor used in the present study can be assumed as a plug flow reactor according to the description above and also to the analysis from Ballari et al. (2010). For this kind of reactor configuration, NO and NO_2 are consumed or generated along the reactor as follows:

$$v_{air}\frac{dC_{NO}}{dx}=a_v r_{NO} \tag{8.2.30}$$

$$v_{air}\frac{dC_{NO_2}}{dx}=a_v r_{NO_2} \tag{8.2.31}$$

with the following boundary conditions:

$$C_{NO}(x=0)=C_{NO,in} \tag{8.2.32}$$

$$C_{NO_2}(x=0)=C_{NO_2,in} \tag{8.2.33}$$

Here a_v, the active surface area per unit of reactor volume related with the dosage of the photocatalyst, is introduced in the mass balances given by Equations (8.2.30) and (8.2.31) since the PCO reaction only occurs on the surface of the photocatalyst:

$$a_v=\frac{D_{TiO_2}A}{V_{reactor}}\cong\frac{D_{TiO_2}}{H} \tag{8.2.34}$$

The concentration of NO and NO_2 along the reactor is solved numerically applying the Euler method after substituting Equations (8.2.27) and (8.2.28) into Equations (8.2.30) and (8.2.31) respectively, yielding

$$v_{air}\frac{C_{NO,i+1}-C_{NO,i}}{x_{i+1}-x_i}=\frac{-a_v\gamma k_{NO}C_{TiO_2\_NO,i}C_{TiO_2\_H_2O}\left(\sqrt{1+\frac{4\alpha E}{\gamma C_{TiO_2\_H_2O}}}-1\right)}{(4k_{NO}C_{TiO_2\_NO,i}+2k_{NO_2}C_{TiO_2\_NO_2,i})} \tag{8.2.35}$$

$$v_{air}\frac{C_{NO_2,i+1}-C_{NO_2,i}}{x_{i+1}-x_i}=\frac{a_v\gamma(k_{NO}C_{TiO_2\_NO,i}-k_{NO_2}C_{TiO_2\_NO_2,i})C_{TiO_2\_H_2O}}{(4k_{NO}C_{TiO_2\_NO,i}+2k_{NO_2}C_{TiO_2\_NO_2,i})}\left(\sqrt{1+\frac{4\alpha E}{\gamma C_{TiO_2\_H_2O}}}-1\right) \tag{8.2.36}$$

where $i = 1, 2, \dots, n$, and $x_{i+1}-x_i=L/(n-1)$.

Therefore, the concentrations of NO and NO_2 along the reactor are obtained:

$$C_{NO,i+1}=\frac{(x_{i+1}-x_i)}{v_{air}}\frac{-a_v\gamma k_{NO}C_{TiO_2\_NO,i}C_{TiO_2\_H_2O}\left(\sqrt{1+\frac{4\alpha E}{\gamma C_{TiO_2\_H_2O}}}-1\right)}{(4k_{NO}C_{TiO_2\_NO,i}+2k_{NO_2}C_{TiO_2\_NO_2,i})}+C_{NO,i} \tag{8.2.37}$$

$$C_{NO_2,i+1}=\frac{(x_{i+1}-x_i)}{v_{air}}\frac{a_v\gamma(k_{NO}C_{TiO_2\_NO,i}-k_{NO_2}C_{TiO_2\_NO_2,i})C_{TiO_2\_H_2O}}{(4k_{NO}C_{TiO_2\_NO,i}+2k_{NO_2}C_{TiO_2\_NO_2,i})}\left(\sqrt{1+\frac{4\alpha E}{\gamma C_{TiO_2\_H_2O}}}-1\right)+C_{NO_2,i} \tag{8.2.38}$$

8.2.5 Results and model validation

The concentrations of NO and NO_2 in Equations (8.2.37) and (8.2.38) are described using the superficial adsorbed concentration of reactants (NO, NO_2, and H_2O), and they can be expressed as the volumetric concentration in air by substituting Equations (8.2.6) - (8.2.8) into Equations (8.2.37) and (8.2.38), respectively. Therefore, a full model of the concentration of NO and NO_2 along the reactor during the PCO reaction is obtained:

$$C_{NO,i+1}=\frac{(x_{i+1}-x_i)}{v_{air}}\frac{-a_v k_{NO}\beta K_{NO}K_{H_2O}C_{NO,i}C_{H_2O}\left(\sqrt{1+\frac{4\alpha E(1+K_{NO}C_{NO,i}+K_{NO_2}C_{NO_2,i}+K_{H_2O}C_{H_2O})}{\beta K_{H_2O}C_{H_2O}}}-1\right)}{(4k_{NO}K_{NO}C_{NO,i}+2k_{NO_2}K_{NO_2}C_{NO_2,i})(1+K_{NO}C_{NO,i}+K_{NO_2}C_{NO_2,i}+K_{H_2O}C_{H_2O})}+C_{NO,i} \tag{8.2.39}$$

$$C_{NO_2,i+1} = \frac{(x_{i+1}\text{-}x_i)}{v_{air}} \frac{a_v\beta\left(k_{NO}K_{NO}C_{NO,i}\text{ - }k_{NO_2}K_{NO_2}C_{NO_2,i}\right)K_{H_2O}C_{H_2O}}{(4k_{NO}K_{NO}C_{NO,i}+2k_{NO_2}K_{NO_2}C_{NO_2,i})(1+K_{NO}C_{NO,i}+K_{NO_2}C_{NO_2,i}+K_{H_2O}C_{H_2O})}\times$$
$$\left(\sqrt{1+\frac{4\alpha E(1+K_{NO}C_{NO,i}+K_{NO_2}C_{NO_2,i}+K_{H_2O}C_{H_2O})}{\beta K_{H_2O}C_{H_2O}}}\text{ -1}\right)+C_{NO_2,i} \tag{8.2.40}$$

where

$$\beta = \frac{k_{h^+}\times k^*_{e^-}}{k_{dea}}\times C_{TiO_2} \tag{8.2.41}$$

The kinetic parameters in Equations (8.2.39) and (8.2.40) are then obtained by optimizing these two equations employing the "Solver" tool from Microsoft Excel@ and applying the experimental data presented in Chapter 7 (see Table 7.11). The results are listed in Table 8.1, with the coefficient of determination (R^2) of 0.992.

Table 8:1: Parameters obtained by applying the full model.

Parameter	Value	95% confidence interval
k_{NO} ($dm^2\ mol^{-1}\ min^{-1}$)	3.21×10^{-9}	0.02×10^{-9}
k_{NO_2} ($dm^2\ mol^{-1}\ min^{-1}$)	1.19×10^{-7}	0.11×10^{-7}
K_{NO} ($dm^3\ mol^{-1}$)	2.09×10^{4}	0.02×10^{4}
K_{NO_2} ($dm^3\ mol^{-1}$)	5.38×10^{3}	0.32×10^{3}
K_{H_2O} ($dm^3\ mol^{-1}$)	2.39×10^{0}	0.01×10^{0}
α ($mol\ W^{-1}\ min^{-1}$)	4.32×10^{-2}	0.05×10^{-2}
β ($mol\ dm^{-2}\ min^{-1}$)	6.20×10^{-8}	0.04×10^{-8}
R^2	0.992	

Since in the present study, the concentrations of NO, NO_2, and H_2O are in the order of 10^{-8}, 10^{-9}, and 10^{-4}, respectively, then for the optimized value of K_{NO}, K_{NO_2}, and K_{H_2O} the denominator of Equations (8.2.6) - (8.2.8) can be equaled to unity without causing any significant error. Therefore the complete model (Equations (8.2.39) and (8.2.40)) can be simplified according to this, yielding

$$C_{NO,i+1} = a_v\frac{(x_{i+1}\text{-}x_i)}{v_{air}}\frac{\text{-}k^{'}_{NO}\beta' C_{NO,i}C_{H_2O}\left(\sqrt{1+\frac{4\alpha E}{\beta' C_{H_2O}}}\text{ -1}\right)}{(4k^{'}_{NO}C_{NO,i}+2k^{'}_{NO_2}C_{NO_2,i})}+C_{NO,i} \tag{8.2.42}$$

$$C_{NO_2,i+1} = a_v \frac{(x_{i+1}-x_i)}{v_{air}} \frac{\beta'\left(k'_{NO}C_{NO,i} - k'_{NO_2}C_{NO_2,i}\right)C_{H_2O}}{\left(4k'_{NO}C_{NO,i} + 2k'_{NO_2}C_{NO_2,i}\right)} \left(\sqrt{1+\frac{4\alpha E}{\beta' C_{H_2O}}} -1\right) + C_{NO_2,i} \qquad (8.2.43)$$

where

$$k'_{NO} = k_{NO}K_{NO},\ k'_{NO_2} = k_{NO_2}K_{NO_2},\ \text{and}\ \beta' = \beta \times K_{H_2O} \qquad (8.2.44)$$

The parameters in Equations (8.2.42) and (8.2.43) are again obtained using optimization employing the experimental results from Chapter 7. The results are listed in Table 8.2, with the coefficient of determination (R^2) of 0.993.

Table 8.2: Parameters obtained by applying the simplified model.

Parameter	Value	95% confidence interval
k'_{NO} ($dm^5\,mol^{-2}\,min^{-1}$)	4.50×10^{-5}	0.05×10^{-5}
k'_{NO_2} ($dm^5\,mol^{-2}\,min^{-1}$)	5.02×10^{-4}	0.68×10^{-4}
α ($mol\,W^{-1}\,min^{-1}$)	3.72×10^{-2}	0.08×10^{-2}
β' ($dm\,min^{-1}$)	2.49×10^{-7}	0.09×10^{-7}
R^2	0.993	

Figure 8.1 shows the outlet concentration of NO_x predicted by the simplified model versus their concentration from the experiments. It can be seen that the predicted outlet NO concentration fits very well to the experimental data, while the predicted outlet NO_2 concentration has a larger spread. But overall these predictions show a fair agreement with the experimental data, especially when one considers the very low NO_2 concentrations (a few ppb). This indicates the validity of the proposed kinetic model.

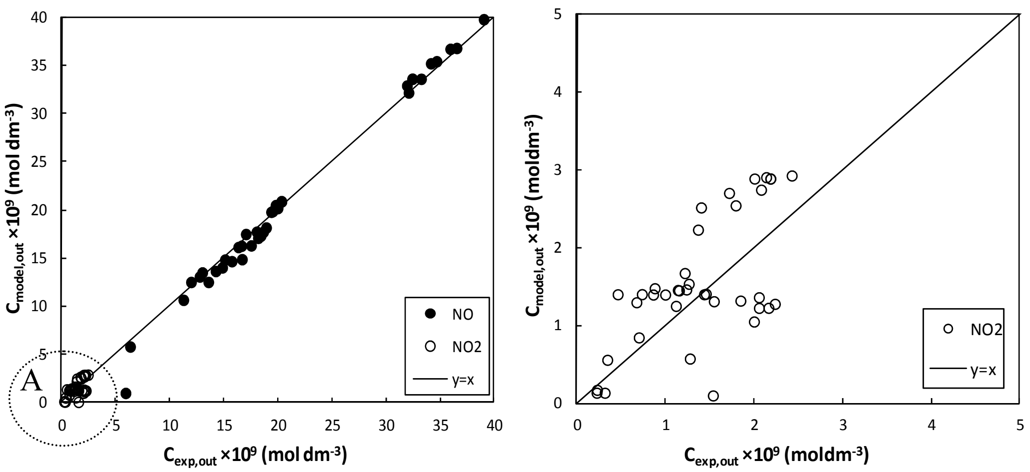

(a) (b)

Figure 8.1: a: Predictions of the NO and NO_2 outlet concentration from the models versus the experimental results; b: Close-up on the NO_2 predictions, zone A in Figure 8.1a.

From Equations (8.2.30) and (8.2.31), a relation between the outlet concentrations of NO and NO2 is obtained, which reads:

$$\frac{dC_{NO}}{dC_{NO_2}} = \frac{-k_{NO}K_{NO}C_{NO}}{(k_{NO}K_{NO}C_{NO} - k_{NO_2}K_{NO_2}C_{NO_2})} = \frac{-k'_{NO}C_{NO}}{(k'_{NO}C_{NO} - k'_{NO_2}C_{NO_2})} \tag{8.2.45}$$

with the following boundary condition:

$$C_{NO_2}(C_{NO} = C_{NO,in}) = 0 \tag{8.2.46}$$

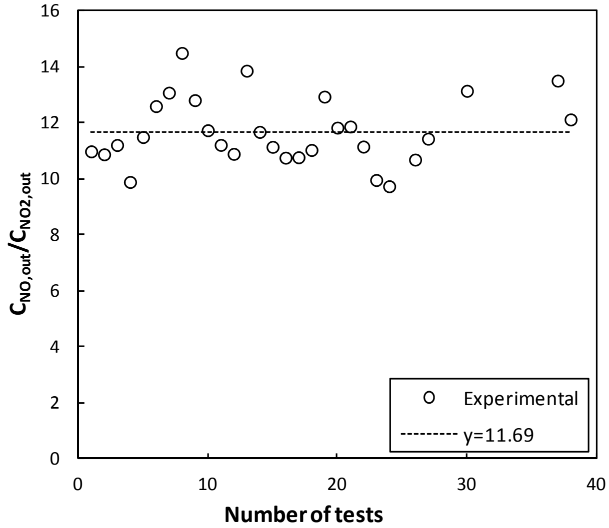

Figure 8.2: Relation between outlet concentration of NO and NO$_2$.

Equation (8.2.45) is solved analytically employing the boundary condition (Equation (8.2.46)), yielding

$$C_{NO_2} = \frac{C_{NO}}{(k'_{NO_2}/k'_{NO} - 1)} - \frac{C_{NO,in}}{(k'_{NO_2}/k'_{NO} - 1)}\left(\frac{C_{NO}}{C_{NO,in}}\right)^{\frac{k'_{NO_2}}{k'_{NO}}} \tag{8.2.47}$$

Equation (8.2.47) can be simplified since $C_{NO} < C_{NO,in}$ and $k'_{NO_2}/k'_{NO} = 11.2$ by taking the values of k'_{NO} and k'_{NO_2} from Table 8.2, hence a linear relation between the outlet concentration of NO and NO2 is derived, reading

$$C_{NO} = 10.2 \times C_{NO_2} \tag{8.2.48}$$

The outlet concentrations of NO and NO2 obtained from experiments are plotted in Figure 8.2. It is shown that the average value of the ratio of the concentrations of NO and NO2 is 11.7, which is compatible with the derived results here.

8.2.6 Discussion

As presented in the previous chapter, as well as in Beeldens (2007) and Hüsken et al. (2009), test conditions significantly influence the PCO performance. Hence, in order to develop a representative model, the incorporation of the experimental conditions is of vital importance. From the developed model (Equations (8.2.42) and (8.2.43)) one can see that all the test conditions such as the initial pollutant (NO) concentration, volumetric flow rate, relative humidity, irradiance, reactor size and catalyst dosage are represented.

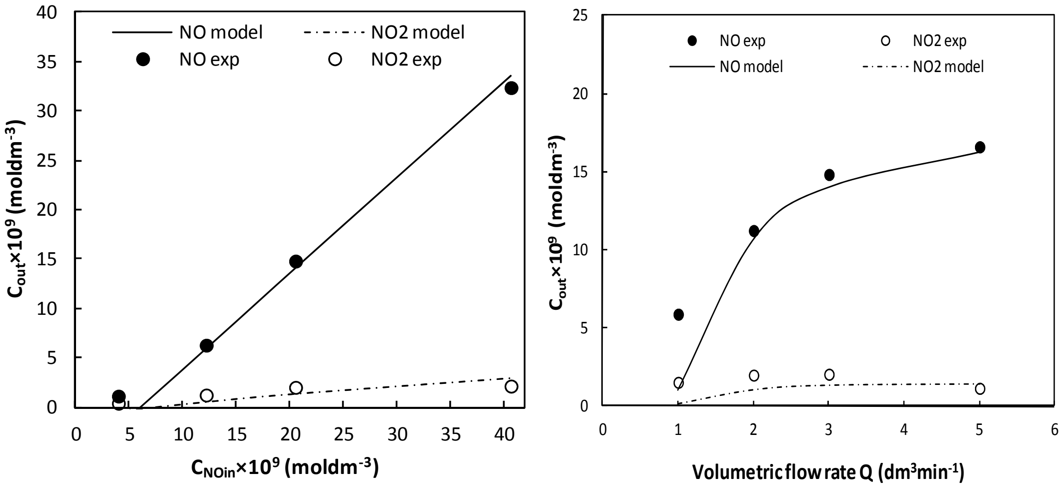

(a) (b)

Figure 8.3: Model predictions versus the experimental results.

Figures 8.3 - 8.5 show the results predicted from the proposed model versus the experimental results under different experimental conditions. It should be mentioned that all other experimental conditions remain standard when one parameter is changed (see Chapter 7). It is evident from Figures 8.3 - 8.5 as well as Figure 8.1 that the proposed model provides correct predictions even under very different test conditions. This shows clearly that the developed model can be applied validly for the conditions described here.

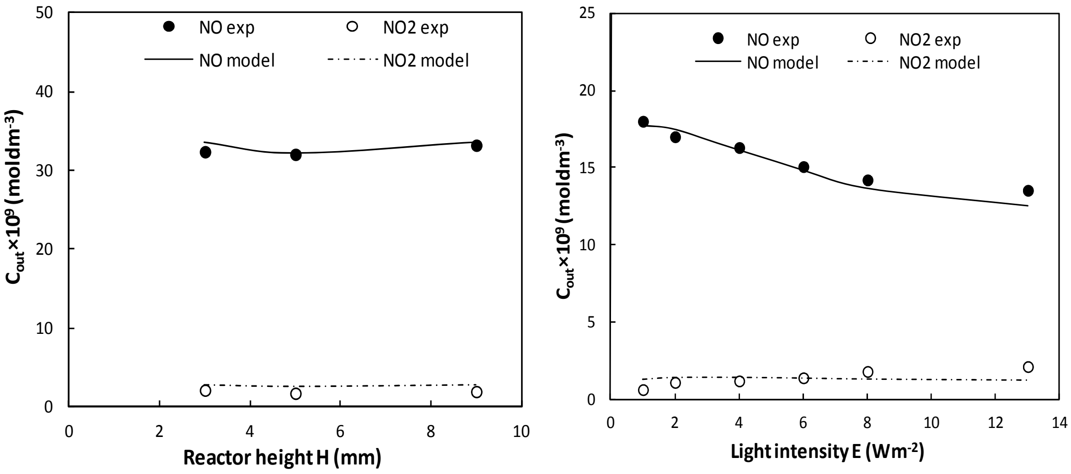

(a) (b)

Figure 8.4: Model predictions versus the experimental results.

As described before, NO_2 is generated during the PCO of NO and it is not oxidized completely in this process, and actually NO_2 is even more toxic than NO (Langridge et al., 2009). Therefore, the proposed model incorporates NO_2 from its reaction mechanism, adsorption isotherm and reaction rate as well. The predicted values versus the measured experimental results of NO_2 presented in Figures 8.3 - 8.5 indicate the validity of the proposed model. The linear relation between the outlet concentration of NO and NO_2 derived here is confirmed by Ballari et al. (2010), who investigated the PCO of NO with the traditional TiO_2 as photocatalyst applying pavestone as substrate for the outdoor air purification and found a linear relation of 11.0~11.9 between the outlet concentration of NO and NO_2.

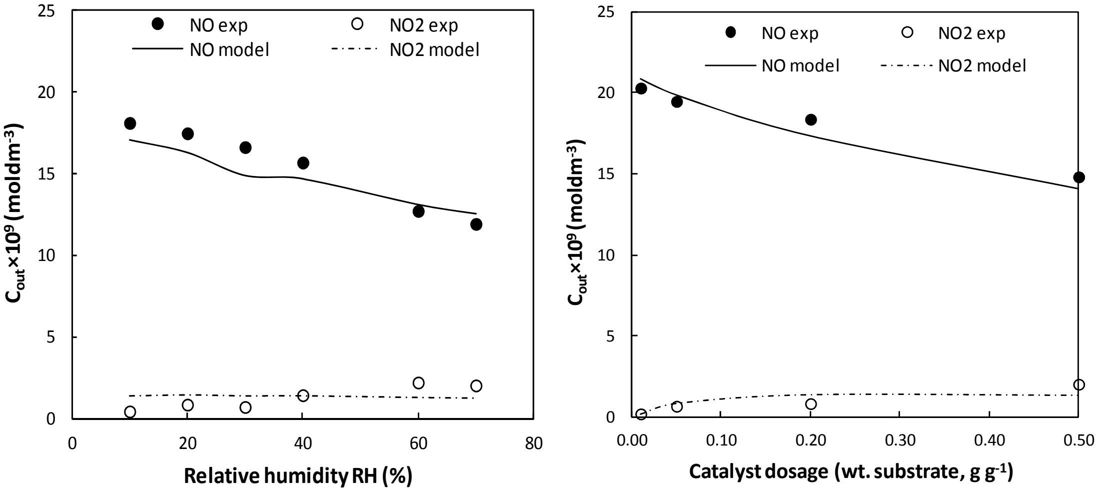

(a) (b)

Figure 8.5: Model predictions versus the experimental results.

Nevertheless, regarding the validity of the proposed models, they hold only for the present experimental conditions, i.e. strict laboratory scale test conditions, as shown in Table 7.5. Further investigations, for instance with a reactor with a larger volume, are still of interest in order to study the behavior of the PCO under real indoor air conditions as well as validate the proposed model.

8.3 Reactor modeling applying CFD

8.3.1 Computational Fluid Dynamics

Computational Fluid Dynamics (CFD) is a branch of fluid mechanics which uses numerical methods and algorithms to analyze and solve problems that involve fluid flows. It is widely applied to numerous fields such as combustion, airplane design, submarines, etc. To solve complicated fluid flow problems, programs are usually structured around the numerical algorithms using a CFD software, which contains three main elements: (i) a pre-processor, (ii) a processor, and (iii) a post-processor (Anderson, 1995).

The pre-processing stage consists of the input of a flow problem to a CFD program by means of an operator-friendly interface and the subsequent transformation of this input into a form suitable for use by the solver, including the definition of the geometry and the subdivision of the domain into smaller sub-domains: a grid (or mesh). The processor consists of the solver, which is based on numerical methods, including approximating the unknown flow variables by means of simple functions, discretizing the approximations into the governing flow equations and subsequent mathematical manipulations, and finally solving the algebraic equations. The last stage is the post-processing stage that consists of versatile data visualization tools.

FLUENT, a CFD package owned by ANSYS, is employed here. FLUENT applies the finite volume method to solve the governing equations. The numerical algorithm steps can be described as: first the integration of the governing equations of the fluid flow; then the discretization including the substitution of a varied approximation for the terms in the integrated equation representing the flow processes such as convection, diffusion and sources; and then the integration of these equations into a system of algebraic equations; finally the solution of the equations by an iterative method (Topp, 1999).

8.3.2 Reactor modeling

Model construction

The reactor model is built in a 2-dimensional structure, because the reactor is completely symmetrical. The 2-D model provides a simpler and less time-consuming approach than the 3-D version. In order to model a fully developed flow over the photocatalytically active surface, the length of the reactor model is extended at the inlet to cope with the transitional behavior. This is also in line with the used real reactor (see Figure 7.4 in Chapter 7), which has a non-reactive surface, before the flow can reach the active material. The geometry of the reactor, along with its boundaries, is shown in Figure 8.6.

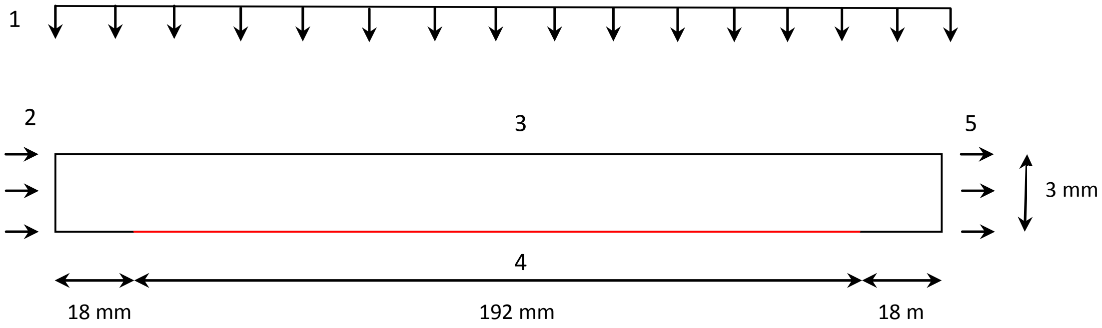

Figure 8.6: Geometry of the reactor model (1. Light source; 2. Inlet; 3. Glass; 4. Photoactive surface; 5. Outlet).

The first step towards the CFD modeling is the creation of the geometry of the reactor. Employing the software Gambit, the geometry is created and meshed to provide sufficient control volumes (CVs) for the CFD simulation in Fluent, as shown in Figure 8.7. It shows only a portion of the horizontal reactor (about one sixth of the total length) to be able to observe more clearly the grid distribution. Horizontally, the CVs are spaced proportionally every 2 mm, yielding 110 cells through the reactor length; while vertically, the CVs are spaced with an exponential space factor of 0.75, which leads to the fact that more CVs are generated near the lower wall where larger variable gradients are expected.

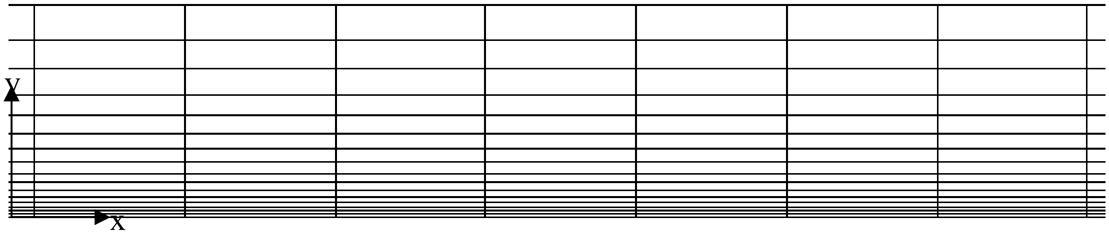

Figure 8.7: Close-up on the distribution of the mesh in the reactor model (x: along the reactor length; y: along the reactor height).

A grid independence test is performed to examine the validity of the number of CVs by simulating the velocity profile and the static pressure distribution inside the reactor with finer grids and calculating their respective differences (Roache, 1994). The grid convergence index (GCI) is calculated from

$$GCI(u) = \frac{3\varepsilon_{rms}}{r^2 - 1} \qquad (8.3.1)$$

where r is the ratio of amounts of fine grid to that of coarse grid and ε_{rms} is defined as:

$$\varepsilon_{rms} = \left(\frac{\sum_{i=1}^{n} \varepsilon_{i,u}^2}{n} \right)^{0.5} \qquad (8.3.2)$$

where $\varepsilon_{i,u}$ is defined as:

$$\varepsilon_{i,u} = \frac{u_{i,coarse} - u_{i,fine}}{u_{i,fine}} \qquad (8.3.3)$$

where u is the variable (x-velocity and static pressure).

Table 8.3: Grid independent test for the validated measurements.

Simulation	Amount of used cells	Amount of cells in fine grid	GCI(u) (%)
x-velocity	4.510	6.765	1.3
x-velocity	4.510	9.020	2.0
x-velocity	4.510	22.550	4.4
static pressure	4.510	6.765	1.4
static pressure	4.510	9.020	2.2
static pressure	4.510	22.550	4.8

The calculated values of GCI(u) are listed in Table 8.3. It is shown that when the grids are five times larger than the amount used here, the GCI index only reaches 4.4% for the x-velocity magnitude simulation and 4.8% for the static pressure simulation, which indicates the mesh is sufficiently dense to provide accurate results (Chen and Zhao, 2010).

Table 8.4: Gambit boundary conditions (Yu et al., 2012).

Edge Number	Name (Figure 8.6)	Boundary Condition
1	Inlet	Mass-Velocity Inlet
2	Glass	Wall
3	Regular Surface	Wall
4	Active Surface	Wall
5	Regular Surface	Wall
6	Outlet	Outflow

The second step in building the reactor model is the definition of the boundary conditions, as listed in Table 8.4. The inlet is defined in FLUENT as a "Mass-Velocity Inlet" boundary condition, which is used to define the flow velocity, along with the relevant scalar properties of the flow inlet. Edges numbers 2 to 5 are defined as "Wall" (see Figure 8.6). Wall boundary conditions are used to bound fluid and solid regions. In viscous flows, the no-slip boundary condition is enforced at walls by default. The edge number 6 is set as an "Outflow" boundary condition which is commonly used to model flow exits where the details of the flow velocity and pressure are not known prior to the solution of the flow problem. Nothing is needed to be defined at the outflow boundaries.

The area inside of the reactor is defined as two different zones, as shown in Figure 8.8. Zone 2 consists of a narrow group of cells adjacent to the active surface to simulate the surface reaction of the PCO of NO_x. This region covering 30 µm vertically (1% of the height of the reactor) and the whole length of the active surface horizontally along the reactor, is the space where the photocatalytic reactions take place.

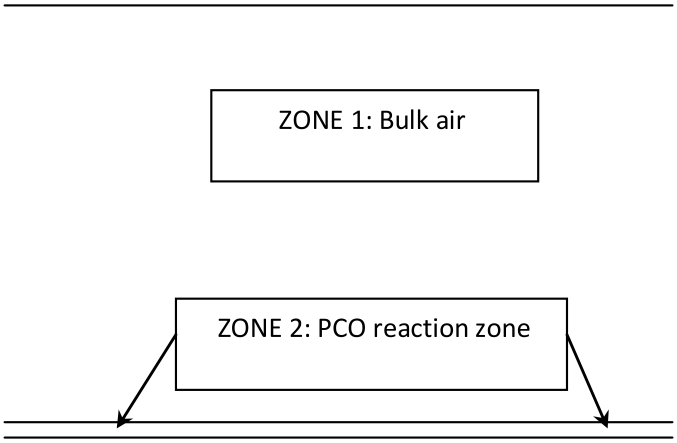

Figure 8.8: Assignment of zones in the geometry of the modeled reactor.

Using Equations (8.3.1) to (8.3.3) again, the space of the reactive zone is checked and compared to the actual length used in the model (30 μm), as shown in Table 8.5. It is shown that the largest error of 1.01% is reached when the height of this zone is decreased to 0.1 μm. This small value indicates the validity of the height approach of this zone.

Table 8.5: Independence test of the PCO reactive area.

Length of reactive zone (μm)	Length of finer reactive zone (μm)	GCI(u) (%)
30	100	0.42
30	10	0.50
30	1	0.90
30	0.1	1.01

Governing equations

FLUENT solves conservation equations for mass and momentum of the flow in the reactor. The flow in the reactor is assumed to be incompressible because of the ambient test conditions and it does not undergo any significant compression or expansion. The reactor is assumed to be isothermal because it always works under room temperature. So any increases in temperature due to the adsorption, desorption and reaction of species is negligible. Thus, the inclusion of equations of energy is not needed. The conservation equations for turbulent modeling are not needed because the flow in the reactor is laminar (see analysis in Section 7.5.2 in Chapter 7).

- Continuity equation

The equation for conservation of mass or continuity equation is valid for both incompressible and compressible flows, and is described as follows:

$$\frac{\partial \rho}{\partial t} + \nabla \cdot \left(\rho \vec{v}\right) = S_m \tag{8.3.4}$$

where ρ is the density of the fluid, t is time and $\vec{v}$ is the velocity vector. The source S_m is the mass added to the continuous phase from a dispersed second phase, which is zero here.

In a 2-dimensional coordinate system, a steady compressible gas flow yields:

$$\frac{\partial u}{\partial x} = -\frac{\partial v}{\partial y} \tag{8.3.5}$$

- Momentum equations

Conservation of momentum in an inertial (non-accelerating) reference frame is described by Topp (1999):

$$\frac{\partial}{\partial t}(\rho\vec{v})+\nabla\cdot(\rho\vec{v}\vec{v})=-\nabla p+\nabla\cdot(\bar{s})+p\bar{g}+\vec{F} \tag{8.3.6}$$

where *p* is the static pressure, *s* is the stress tensor, and *pg* and *F* are the gravitational body force and external body forces, respectively. F also contains other model-dependent source terms such as the user-defined source.

In a Newtonian fluid the viscous stresses are proportional to the rates of deformation. The two-dimensional form of Newton's law of viscosity for compressible flows involves two constants of proportionality: the dynamic viscosity (μ) to relate stresses to linear deformations, and the second viscosity (λ) to relate stresses to the volumetric deformation. The stress components are:

$$S_{xx}=2\mu\frac{\partial u}{\partial x}+\lambda divu, S_{yy}=2\mu\frac{\partial v}{\partial y}+\lambda divu, S_{xy}=S_{yx}=\mu(\frac{\partial u}{\partial y}+\frac{\partial v}{\partial x}) \tag{8.3.7}$$

Although sufficient information is not available about the second viscosity λ, an acceptable approximation for gases can be obtained by taking the value λ = -2/3 μ (Versteed and Malalasekera, 1995). Substitution of the above shear stresses (Equation (8.3.7)) into Equation (8.3.6) in a steady state yields the so-called Navier-Stokes equations:

$$\frac{\partial \rho uu}{\partial x}+\frac{\partial \rho vu}{\partial y}=-\frac{\partial p}{\partial x}+\frac{\partial}{\partial x}\left(2\mu\frac{\partial u}{\partial x}+\lambda divu\right)+\frac{\partial}{\partial y}\left[u\left(\frac{\partial u}{\partial y}+\frac{\partial v}{\partial x}\right)\right] \tag{8.3.8}$$

$$\frac{\partial \rho uv}{\partial x}+\frac{\partial \rho vv}{\partial y}=-\frac{\partial p}{\partial y}+\frac{\partial}{\partial x}\left[\mu(\frac{\partial u}{\partial y}+\frac{\partial v}{\partial x})\right]+\frac{\partial}{\partial y}\left(2\mu\frac{\partial v}{\partial y}+\lambda divu\right) \tag{8.3.9}$$

- Species transport equations

FLUENT solves the species mixing problem with conservation equations by predicting the mass fractions of each species, Y_i, through the solution of a convection-diffusion equation for the ith species, which reads as:

$$\frac{\partial}{\partial t}(\rho Y_i)+\nabla\cdot(\rho\vec{v}Y_i)=\nabla\cdot\vec{J_i}+R_i+\vec{S_i} \tag{8.3.10}$$

where Y_i is the mass fraction of each material, J_i is the diffusion flux due to the concentration gradients, R_i is the production rate of species *i* by chemical reaction and S_i is the rate of reaction by addition from the user-defined source.

By default, FLUENT uses the dilute approximation (Fickian diffusion only), under which the diffusion flux can be written as:

$$\vec{J_i}=-\rho D_{i,m}\nabla Y_i \tag{8.3.11}$$

where $D_{i,m}$ is the diffusion coefficient for species *i* in the mixture and set as a constant value for all the molecules present. Here the dilute approximation is acceptable, since the pollutants are present in very low concentrations of ppb level.

In this reactor model, the production rate of species i by chemical reaction (R_i) is set as zero in both zones because the PCO rates of NO and NO_2 that are only present in zone 2 are given as the rate of reaction by addition (S_i), which read as follows:

$$a_v r_{NO} = \frac{-k_{NO}\beta K_{NO} K_{H_2O} C_{NO,i} C_{H_2O}\left(\sqrt{1+\frac{4\alpha E(1+K_{NO}C_{NO,i}+K_{NO_2}C_{NO_2,i}+K_{H_2O}C_{H_2O})}{\beta K_{H_2O}C_{H_2O}}}-1\right)}{(4k_{NO}K_{NO}C_{NO,i}+2k_{NO_2}K_{NO_2}C_{NO_2,i})(1+K_{NO}C_{NO,i}+K_{NO_2}C_{NO_2,i}+K_{H_2O}C_{H_2O})} \tag{8.3.12}$$

$$a_v r_{NO_2} = \frac{\beta\left(k_{NO}K_{NO}C_{NO,i} - k_{NO_2}K_{NO_2}C_{NO_2,i}\right)K_{H_2O}C_{H_2O}}{(4k_{NO}K_{NO}C_{NO,i}+2k_{NO_2}K_{NO_2}C_{NO_2,i})(1+K_{NO}C_{NO,i}+K_{NO_2}C_{NO_2,i}+K_{H_2O}C_{H_2O})} \times \tag{8.3.13}$$

$$\left(\sqrt{1+\frac{4\alpha E(1+K_{NO}C_{NO,i}+K_{NO_2}C_{NO_2,i}+K_{H_2O}C_{H_2O})}{\beta K_{H_2O}C_{H_2O}}}-1\right)$$

where all the symbols are the same as presented in Section 8.2.

Table 8.6: Chemical species involved in the model.

Number given in FLUENT	Chemical Species	Symbol
0	Nitric Oxide	NO
1	Nitrogen Dioxide	NO_2
2	Water Vapor	H_2O
3	Oxygen	O_2
4	Nitrogen	N_2

Since the mass fraction of the species must sum to unity, the N^{th} mass fraction is determined as one minus the sum of the previous N-1 solved mass fractions. To minimize the numerical error, the N^{th} species is selected as the one with the largest overall mass fraction, here nitrogen (N_2). The numerical order of all the species in Table 8.6 remains unchanged when adding them to FLUENT in the Materials Panel, so that when the concentration of chemical species is called in the user defined function, the data will be processed accordingly. Therefore, the equations of species transport are obtained:

$$\rho u\frac{\partial Y_{NO}}{\partial x}+\rho v\frac{\partial Y_{NO}}{\partial y}=\frac{\partial}{\partial x}(\rho D_{NO,air}\frac{\partial Y_{NO}}{\partial x})+\frac{\partial}{\partial y}(\rho D_{NO,air}\frac{\partial Y_{NO}}{\partial y})+a_v r_{NO}M_{NO} \tag{8.3.14}$$

$$\rho u\frac{\partial Y_{NO_2}}{\partial x}+\rho v\frac{\partial Y_{NO_2}}{\partial y}=\frac{\partial}{\partial x}(\rho D_{NO_2,air}\frac{\partial Y_{NO_2}}{\partial x})+\frac{\partial}{\partial y}(\rho D_{NO_2,air}\frac{\partial Y_{NO_2}}{\partial y})+a_v r_{NO_2}M_{NO_2} \tag{8.3.15}$$

$$\rho u\frac{\partial Y_{O_2}}{\partial x}+\rho v\frac{\partial Y_{O_2}}{\partial y}=\frac{\partial}{\partial x}(\rho D_{O_2,air}\frac{\partial Y_{O_2}}{\partial x})+\frac{\partial}{\partial y}(\rho D_{O_2,air}\frac{\partial Y_{O_2}}{\partial y}) \qquad (8.3.16)$$

$$\rho u\frac{\partial Y_{H_2O}}{\partial x}+\rho v\frac{\partial Y_{H_2O}}{\partial y}=\frac{\partial}{\partial x}(\rho D_{H_2O,air}\frac{\partial Y_{H_2O}}{\partial x})+\frac{\partial}{\partial y}(\rho D_{H_2O,air}\frac{\partial Y_{H_2O}}{\partial y}) \qquad (8.3.17)$$

$$Y_{N_2}=1-Y_{NO_2}-Y_{H_2O}-Y_{NO}-Y_{O_2} \qquad (8.3.18)$$

Introducing PCO reactions to FLUENT

The PCO reaction rates (Equations (8.3.12) and (8.3.13)) are introduced to the FLUENT solver by a user-defined function (UDF). The UDF is a user-programmed function written in the programming language C and defined by using DEFINE macros (named as DEFINE_SOURCE) supplied by FLUENT, and can be dynamically loaded with the FLUENT solver to enhance the standard features of the original code. UDFs are executed as either interpreted or compiled functions in FLUENT, whereas values that are passed to the solver by a UDF or returned by the solver to a UDF must be specified in SI units.

The source codes are listed in Appendix D, where three different DEFINE_SOURCE codes are presented, i.e. “rNO”, “rNO2” and “rtotal”, which returns the reaction rate of NO, NO_2 and the sum of both reaction rates, respectively. ‘rtotal’ is defined because in FLUENT the user gives the program the total mass source along with the individual source of the species NO, NO_2, H_2O and O_2. The software calculates N_2 by subtracting the individual species source from the total mass source. When the source code is uploaded to FLUENT, the three UDFs are found in every drag-down panel in the software.

Table 8.7: Boundary conditions of the governing equations.

	Inlet	Wall	Outlet
Velocity in x	$u = u_o$	$u = 0$	$\partial u/\partial x = 0$
Velocity in y	$v = 0$	$v = 0$	$\partial v/\partial y = 0$
Pressure	$P_{in} = 0$	$\partial P/\partial y = 0$	$\partial P/\partial x = 0$
Y_{NO}	$Y_{NO,in}$	0	$\partial Y_{NO}/\partial x = 0$
Y_{NO_2}	$Y_{NO_2,in}$	0	$\partial Y_{NO_2}/\partial x = 0$
Y_{H_2O}	$Y_{H_2O,in}$	0	$\partial Y_{H_2O}/\partial x = 0$
Y_{O_2}	$Y_{O_2,in}$	0	$\partial Y_{O_2}/\partial x = 0$
Y_{N_2}	$Y_{N_2,in}$	0	$\partial Y_{N_2}/\partial x = 0$

Boundary conditions and initialization

Two more boundary conditions are defined in addition to the Gambit boundary conditions presented in Table 8.4: the characteristics of the inlet flow and the source term in zone 2 (see Figure 8.8). These boundaries are used to describe the flow phenomena.

The inlet, the walls and the outlet have different constraints on the variables involved, as shown in Table 8.7. The variables at the inlet are constants and given by the user depending on the test conditions, except for the pressure and the velocity in the y direction, which are both set as 0. At the wall, all variables are zero, since there are no transport phenomena across this boundary. The outlet conditions are set as a difference in space, since the last variable solution will remain the same.

In every simulation run, the initialization variables are set equal to the inlet ones. This is recommended since the reactor modeled here deals with very low variable gradients.

8.3.3 Modeling results and validation

Model validation

The reactor model is validated against the experimental data presented in Section 7.5.2. The reaction rate kinetic parameters listed in Table 8.1 are applied as the input of the reaction source term (Equations (8.3.12) and (8.3.13)).

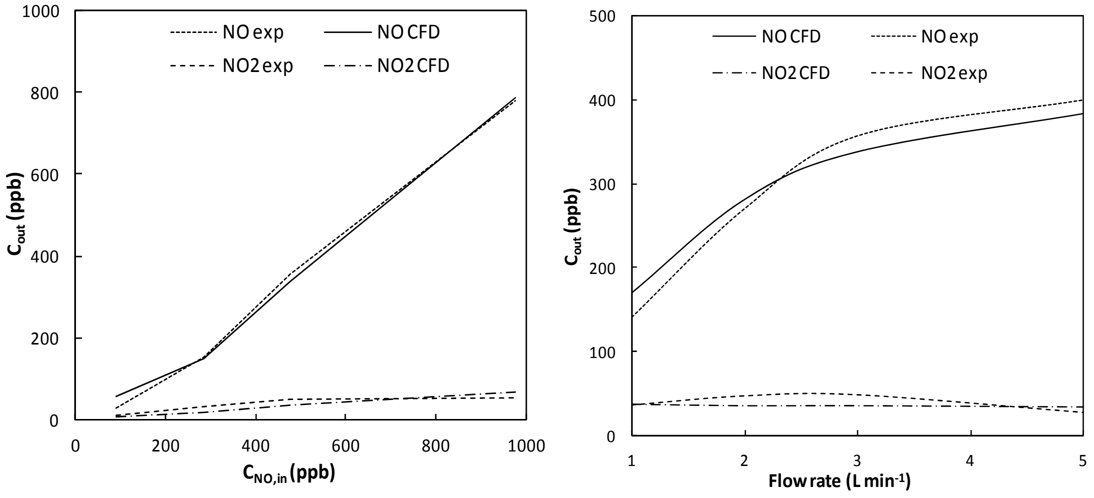

(a) (b)

Figure 8.9: CFD model predictions versus the experimental results (a: effect of the initial NO concentration, Q = 3 L min^{-1}; RH = 50%; I = 10 W m^{-2} ; b: effect of the flow rate, $C_{NO,\,in}$ = 0.5 ppm; RH = 50%; I = 10 W m^{-2}).

The influence of conditions such as pollutant initial concentration, volumetric flow rate, relative humidity, irradiance, dosage of the photocatalyst on the CFD simulations is shown in Figures 8.9-8.10, where also the experimental results are compared.

Throughout the experiment the inlet concentrations of NO_2 are set to zero. Figure 8.9a shows the CFD model predictions when varying the inlet concentrations of NO. The outlet concentrations of both nitrogen oxides are correctly predicted by the CFD model in the test range, with the maximum divergence at the lowest inlet concentration. When varying volumetric flow rate (Figure 8.9b), the CFD model cuts through the middle of the NO experimental results, under-predicting at low values of flow rate and over-predicting at high values. The NO_2 outlet prediction is more stable and only divergent at middle values. These are in the range of 2-3 Lmin^{-1} where the outlet concentration of NO_2 is a little bit under-predicted.

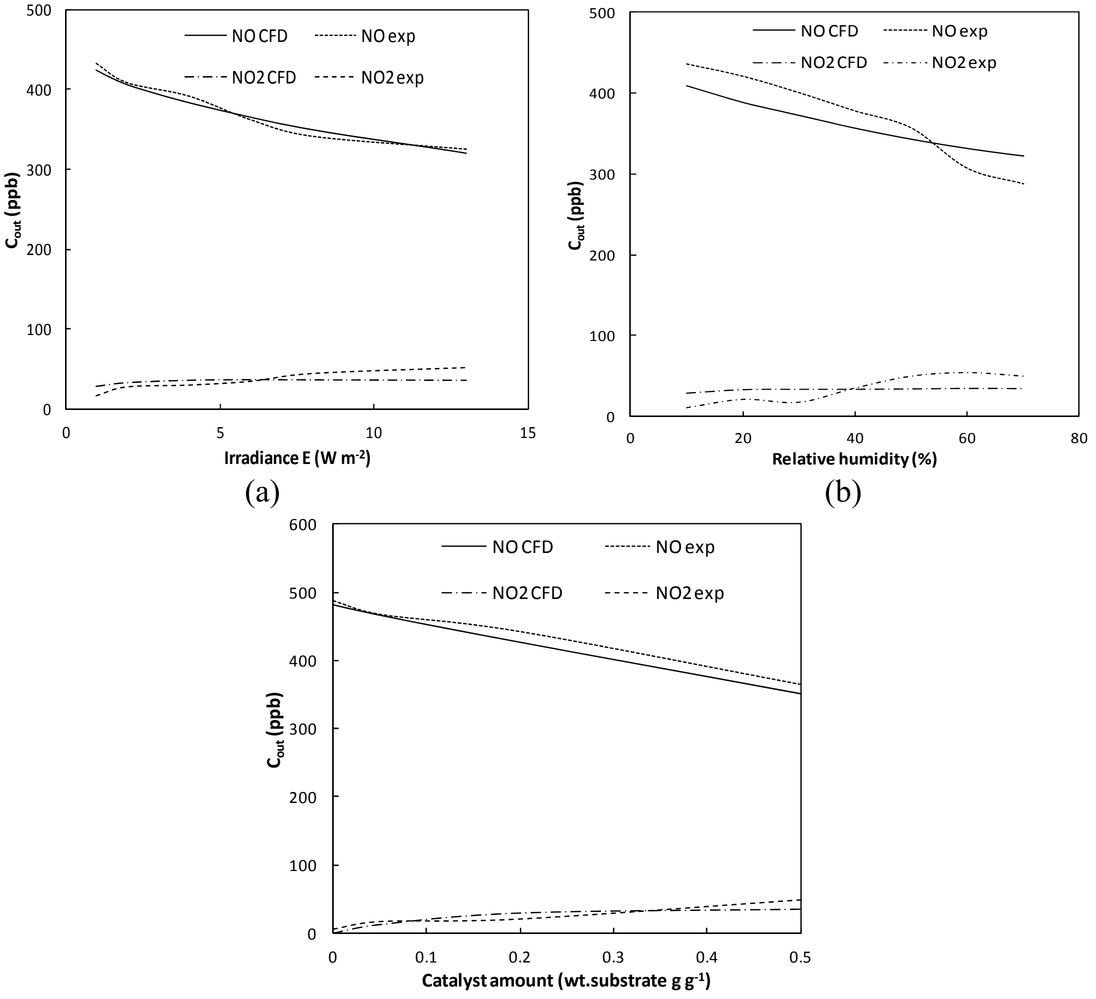

(a) (b)

(c)

Figure 8.10: CFD model predictions versus the experimental results (a: effect of the irradiance, $C_{NO, in}$ = 0.5 ppm; Q = 3 L min^{-1}; RH = 50%; b: effect of the relative humidity, $C_{NO, in}$ = 0.5 ppm; Q = 3 L min^{-1}; I = 10 W m^{-2} ; c: effect of the catalyst dosage) ($C_{NO, in}$ = 0.5 ppm; Q = 3 L min^{-1}; I = 10 W m^{-2}).

Figure 8.10a shows the CFD simulation results contrasted with the experimental data when varying the irradiance. The irradiance is varied between 1 and 13 W m^{-2} and the model predicted accurately throughout the whole range when simulating the NO outlet concentrations. The concentration of NO_2 is over-predicted at 1 Wm^{-2}, and under-predicted at irradiance values higher than 6 Wm^{-2}. Figure 8.10b shows the effect of relative humidity (RH) on the outlet concentrations of nitrogen oxides. The NO and NO_2 concentrations behave in a very similar way as with the flow rate, cutting through the middle of the experimental trend line, but never diverging more than 7% in the case of NO and 20% for NO_2. Figure 8.10c shows the effect of the photocatalyst dosage (D_{TiO_2}) on the outlet concentration of the nitrogen oxides. Here, the experimental results are well predicted by the CFD model for the whole range, having its maximum NO outlet concentration error of 4.1% at 0.5 g g^{-1}, and its maximum error of NO_2 outlet concentration of 20.4% also at 0.5 g g^{-1}.

It can be well stated that the CFD reactor model is a fair predictor through the ranges of the experimental conditions, though there is still room for improvement. Especially, the outlet concentrations of NO_2 may have errors of more than 15%. The complex role of nitrogen dioxide in photocatalytic reactions needs further understanding in order to further improve the model to reach more accurate predictions.

Hydrodynamics

Figure 8.11 shows the velocity development of the flow at the entrance of the reactor with an inlet flow of 0.167 m s^{-1} (3 $Lmin^{-1}$). It shows that it takes only several millimeters to develop a steady-stable laminar flow, which indicates the validity of the added extra length at the entrance of the reactor (regular surface in Figure 8.6). The maximum x-velocity is 0.247 m s^{-1} at the center of the reactor. Figure 8.12 shows the contours of static pressure. It can be seen that the pressure gradient occurs only in the horizontal direction, and a pressure drop of 0.821 Pa along the reactor is resulted.

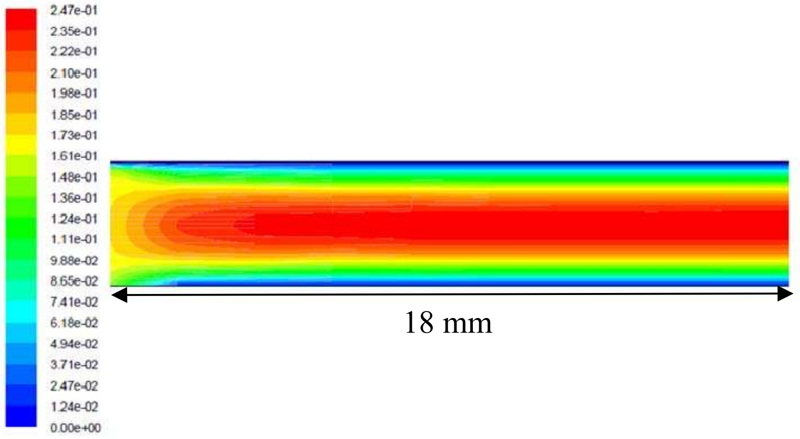

Figure 8.11: Contour plot of velocity magnitude (ms^{-1}) at the entrance of the reactor (first 18 mm).

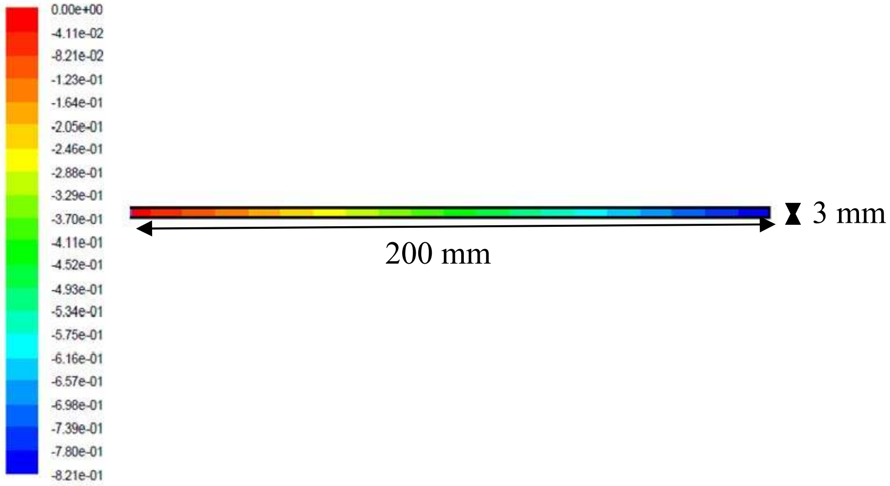

Figure 8.12: Contours of static pressure (Pa) along the reactor.

Both the velocity and the pressure gradient can be also analytically solved, as shown in Equations (8.3.19) and (8.3.20), respectively. The expression of the velocity gradient is the analytical solution for the Navier-Stokes equation (Equation (8.3.6)) assuming that the velocity is a function of the y-direction alone and the velocity u is the only velocity component.

$$u(y) = \left(y^2 - \left(\frac{H}{2} \right)^2 \right) \frac{1}{2\mu} \frac{dp}{dx} \tag{8.3.19}$$

where y is the variable (vertical distance from the middle of the reactor), H is the reactor height (0.003 m), μ is the viscosity of air and dp/dx is the pressure gradient (in Pa m^{-1}).

Here, the pressure drop along the reactor is solved applying the Poiseuille equation, which is dependent on the viscosity of the fluid (Columbia University, 2011) and on the distance between the two plates embedding the fluid and on the initial average velocity u_0:

$$\frac{dp}{dx} = -\frac{3\mu u_0}{(H/2)^2} \tag{8.3.20}$$

where u_0 is the linearly air velocity (0.167 m s^{-1}, i.e. 3 L min^{-1}), μ is the viscosity (1.83×10^{-5} Ns m^{-2}, 20 °C, 1 bar), and H is the reactor height (0.003 m).

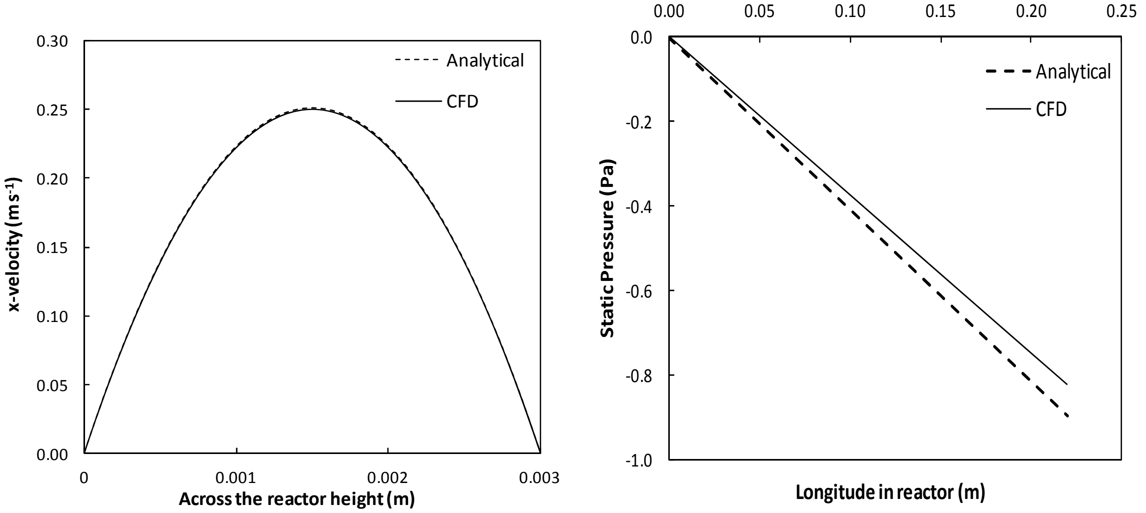

(a) (b)

Figure 8.13: For the analytical and the numerical solutions: (a) Velocity magnitudes across the reactor height; (b) Static pressure versus reactor length.

The analytical solutions of the air velocity and the pressure along the reactor are then compared with the CFD predictions, as shown in Figures 8.13. Figure 8.13a shows the velocity profile as a function of the reactor height. Both the numerical and analytical solutions are almost equal, with an average error of less than 1%. Figure 8.13b shows a slight divergence, giving a pressure drop error of 6.8% at the exit of the reactor.

Reactants distribution in the reactor

Figure 8.14 shows the NO distribution in the reactor, indicating that the NO concentration decreases proportionally along the reactor. It can be seen that in the vertical direction NO concentration changes very slightly due to the small height of the reactor. Figure 8.15 shows the NO_2 distribution in the reactor, indicating that the NO_2 concentration increases along the reactor but not proportionally, remaining almost constant from approximately halfway of the reactor. The reaction rate of NO_2 becomes lower when there is an increasing production from the NO oxidation (see Equation (8.3.13)) and thus hinders its own production.

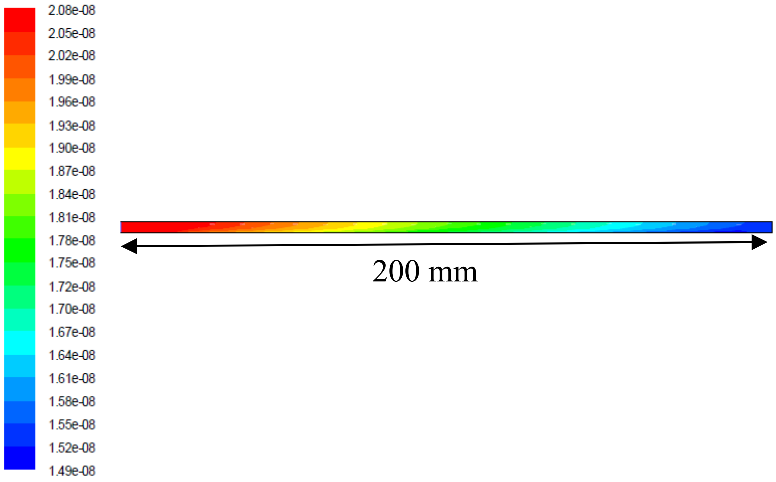

Figure 8.14: Contours of the molar concentration of NO (kmol m^{-3}) along the reactor.

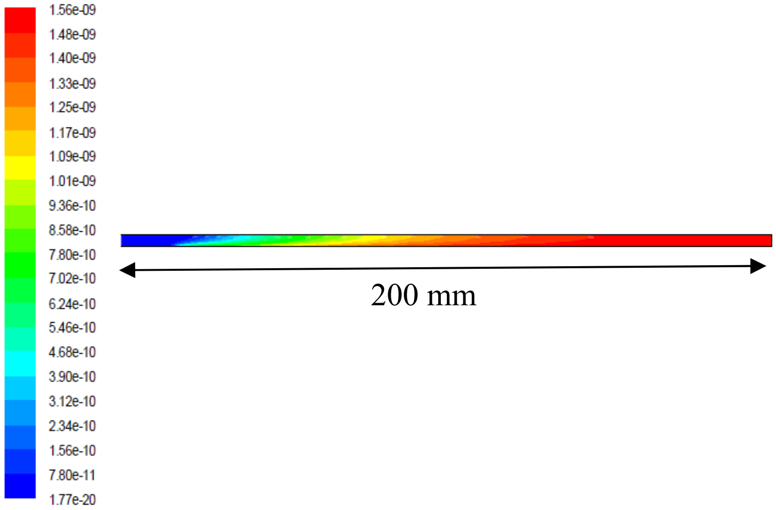

Figure 8.15: Contours of the molar concentration of NO_2 (kmol m^{-3}) along the reactor.

Figure 8.16 shows vertical distribution of both nitrogen oxides in the reactor at two different locations. Figure 8.16a shows the concentration profiles of NO and NO_2 at the outlet of the reactor (x = 220 mm). The NO concentration decreases when approaching the active surface (while NO_2 shows an opposite behavior) due to the fact that at the active surface NO is consumed while NO_2 is first generated. However, the difference is almost negligible at this point of the reactor for both chemicals, since it takes 10 mm after the photocatalytically surface ends. The difference in concentration at the active surface of the reactor compared to the top surface is only 0.39% for NO and 0.03% for NO_2.

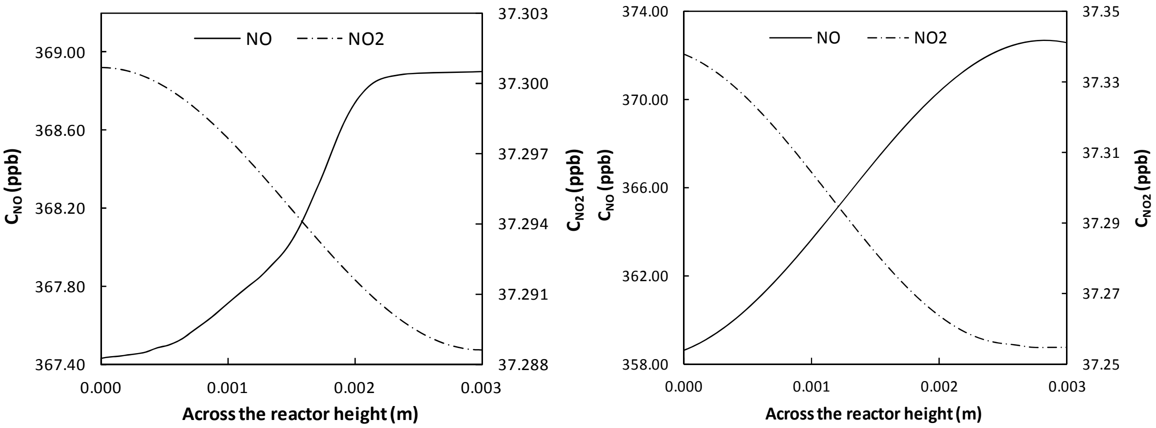

Figure 8.16: Vertical molar concentration of NO and NO_2 profile (a) at x = 220 mm; (b) at x = 210 mm.

Figure 8.16b shows the concentration profiles of NO and NO_2 at the outflow (x = 210 mm, 10 mm before the outlet). Here, as expected, the concentration profile is more pronounced. The difference in vertical concentration at this point is 3.9% for NO and 0.2% for NO_2. This shows that only the 10 mm extra already provides good mixing for both nitrogen oxides. It also illustrates that the vertical diffusion is fast enough to provide an almost negligible concentration gradient. The very thin path that the fluid flows in the reactor and the low viscosity of the fluid are responsible for the relatively high mass diffusivity of the nitrogen oxides in air.

8.4 Conclusions

This chapter addresses the kinetics of the heterogeneous photocatalytic oxidation and the reactor modeling applying CFD for the indoor air purification employing nitrogen oxides as target pollutant. The following conclusions are drawn:

- A kinetic model is proposed to describe the photocatalytic degradation of NO under indoor experimental conditions, and it is validated against the present experimental data.
- The influential experimental conditions such as initial pollutant concentration, volumetric flow rate of the air, relative humidity, irradiance, dosage of the photocatalyst, and reactor size are incorporated in the proposed model; the good agreement between the model predictions and the experimental results indicates that the model works validly in the complex conditions.
- As an undesired intermediate product, NO_2 influences the degradation rate of NO by affecting the adsorption and oxidation process, which is also taken into account in this new model; and a relation of the outlet concentration of NO and NO_2 is found based on the information whereby NO is the single pollutant.

- The CFD model proves to be a reliable prediction tool for the photocatalytic oxidation of NO_x. The model shows slight divergences at some points, especially in the case of NO_2, but in general the prediction is in good agreement with the experimental data.
- The CFD simulation brings new insight about the construction of the reactor. The vertical concentration and velocity profiles are almost constant, although the generation and consumption of different species occur along the surface.
- In the kinetic model proposed, it is assumed that the species concentrations are constant vertically in the reactor and that the species concentrations do not play a role in the velocity profile. Both are confirmed in the CFD simulation.

Chapter 9

Conclusions and recommendations

This Thesis addresses the design and development of novel calcium sulfate-based environmentally friendly building materials. Here “environmentally friendly” refers to environment-related subjects including: (1) the selection of sustainable raw materials to decrease the environmental impact caused by the production process; (2) the enhanced thermal comfort resulted from the newly developed composite; (3) the air pollutants removal function of the development.

Thorough fundamental research on the used core materials (the $CaSO_4 \cdot H_2O$ system) is carried out, from their physical properties to hydration behavior and thermal performance. The water demand of the used $CaSO_4 \cdot 0.5H_2O$ is determined by the mini-slump flow test. The hydration process of the $CaSO_4 \cdot H_2O$ system is studied by the ultrasonic wave velocity method. The thermo physical properties of the $CaSO_4 \cdot H_2O$ system are investigated by both experiments and modeling in different conditions (for instance at room temperature and elevated temperatures).

The indoor thermal comfort related to the indoor temperature, which is strongly affected by the heat transfer between the indoor and outdoor environment, is addressed in the present study. Based on the gained knowledge about the materials, a novel calcium sulfate-based lightweight composite is designed and developed applying a mix design concept which is originally developed for concrete mix design (Hüsken and Brouwers, 2008). Lightweight aggregates are used in the mixture in order to obtain low density and low thermal conductivity. Multiple experiments are performed to investigate the newly developed composite, including its properties in the fresh state such as workability and in the hardened state such as mechanical properties, physical properties, thermal properties and fire behavior. Is it wise to use calcium sulfate as binder? This Thesis tries to answer this question by not only investigating the developed calcium sulfate-based composites, but also through a thorough comparative study with developed cement-based composites. Indoor air pollutants significantly influence the comfort and health of human beings since people spend most of their time indoors. This is addressed by applying heterogeneous photocatalytic oxidation technology (PCO) into the new development to remove indoor air pollutants. Experimental results prove the positive effect of the indoor air purification function of the new development. A kinetic study is subsequently performed to further understand the PCO working principle and computational fluid dynamics is also employed to model the used PCO reactor.

9.1 Conclusions

The main conclusions are drawn from the performed study and elaborated in the following sections.

9.1.1 Fundamental research on the $CaSO_4{\cdot}H_2O$ system

The fundamental study of the properties of the $CaSO_4{\cdot}H_2O$ system presented in this Thesis contributes not only to a deeper understanding of the used materials for their further application, but also brings values to the academic and industrial community since so far there are still very limited publications in this regards (Chapters 3 & 4).

As already discussed in the previous chapters, $CaSO_4{\cdot}0.5H_2O$ in beta type (β-hemihydrate) is used here as binder because of its hydraulic characteristics and binding effect when being in contact with water. The performed mini-slump flow test illustrates not only its water demand but also its flow behavior under different water content conditions. The granular properties of the β-hemihydrate such as the deformation coefficient and the particle shape are derived subsequently from the mini-slump flow test. A minimum thickness of water layer to cover the hemihydrate particles in order to trigger the flow of the system is derived and discussed. The binding effect of the β-hemihydrate is studied from its hydration behavior employing an ultrasonic wave method. The effect of the initial water content and the heat evolution are analyzed. A relation between the initial water amount and the microstructure development, as well as the heat evolution is found accordingly (Chapter 3 & 4).

$CaSO_4{\cdot}H_2O$ systems are excellent building materials also because of their thermal instability, i.e. the chemically combined water in the materials is gradually released at elevated temperatures and a great amount of heat is needed during the process, which makes them proper fire protection materials (Chapter 4). This is investigated by determining their thermo physical properties and microstructure in different conditions. New insights regarding the dehydration process of $CaSO_4{\cdot}2H_2O$ are presented here. A new model is proposed to describe the microstructure of $CaSO_4$ (calcium sulfate anhydrite) and validated by the present experimental results. Thermal conductivities of both $CaSO_4{\cdot}2H_2O$ and $CaSO_4$ are investigated by both modeling and experiments, and new findings are presented. The microstructure change of the $CaSO_4{\cdot}H_2O$ systems at elevated temperature is reported by both performed modeling and experiments.

9.1.2 The concept of $CaSO_4{\cdot}H_2O$-based lightweight composites

After a sound investigation of the material properties, the attention here is shifted to the development of a novel lightweight aggregates composite using calcium sulfate hemihydrate as binder. The composite is designed applying a mix design concept based on the packing theory originally developed for concrete mix design (Chapter 5). The objective of this design is to obtain a composite with excellent thermo physical properties while retaining sufficient mechanical properties. This is addressed by applying lightweight aggregates into the new composite and by optimizing the particle size distribution of all the solid ingredients.

The presented results confirm that this mix design concept is also suitable for the calcium sulfate-based material design. This new product shows a considerable improvement compared to traditional gypsum plasterboards, including mechanical properties, thermal properties and fire behavior. The excellent thermal properties of the newly developed composite contribute to an improved indoor thermal comfort.

For a thorough understanding of using calcium sulfate as binder, the performance of the calcium sulfate-based composite and the cement-based composite (Chapter 6) are compared. The detailed results presented in Chapter 6 confirm the validity of the design concept of the calcium sulfate-based composite, and the results also indicate that the calcium sulfate-based composite would have similar properties as the cement-based composite if the large porosity caused by the large water demand of calcium sulfate β-hemihydrate could be reduced (e.g. by using more efficient water reducing admixtures).

9.1.3 Indoor air purification applying photocatalytic oxidation

This Thesis addresses the indoor air pollutants removal by applying the heterogeneous photocatalytic oxidation (Chapters 7 & 8). A modified TiO_2, which can be activated by visible light, is applied as the photocatalyst to degrade the indoor air pollutants. The positive results indicate the validity of the applied technology.

Indoor air conditions affect not only the residential environment but also significantly the photocatalytic oxidation efficiency of indoor air pollutants. The influential factors include (but are not limited to): light intensity (irradiance), moisture (relative humidity), air flow rate (ventilation), initial pollutants concentration and dosage of the photocatalyst. The relation between these factors and the PCO efficiency is revealed by the performed experiments, as presented and analyzed in Chapter 7.

However, it is not realistic to carry out each test to investigate the PCO performance under various conditions because it is time- and cost-consuming. This is tackled by performing a kinetic study of the photocatalytic oxidation to understand its working principle, in order to predict the PCO efficiency. A fundamental reaction rate model is proposed to describe the PCO reaction. This model incorporates all the above mentioned influential factors and the possible intermediate products and it is validated by the experiments.

Computational fluid dynamics (CFD) is currently extensively used to investigate the air flow problems, and it is also applied in the present study to understand the flow, distribution and removal of the air pollutants and related intermediates/products in the reactor. A CFD reactor model is built using commercial software (Fluent), and it is validated by the test results.

9.2 Recommendations for future research

The present PhD project was triggered by the idea of performance-based design towards novel products, contributing to a better life of human beings. The above presented results positively indicate the achievements and validity of the performed study. Nevertheless, further research is still necessary, based on various investigations and open questions.

The following work is summarized as the recommendations for deeper, future investigations:

1. The effect of the dosed admixture, such as superplasticizer, accelerator etc. on the fresh behavior such as flowability and hydration process of calcium sulfate hemihydrate, as well as their effect on the microstructure development during the hydration process;
2. The overall grading line of a mix serves as a basic law in the present mix design concept. However, in this concept the particle shapes of all the materials are not included. Furthermore, the distribution modulus (q) in the modified Andreasen and Andersen equation significantly affects the overall performance of the designed mixture as already indicted by the present results; more fundamental work is still necessary;

3. The bonding between the lightweight aggregates and matrix (calcium sulfate and/or cement-based) needs further attention. It is very important to further efficiently reduce the porosity of the calcium sulfate-based composite in order to obtain a higher strength while preserving a lower thermal conductivity;
4. Organic pollutants such as volatile organic compounds (VOCs) are evidently present in indoor air. They behave very differently from inorganic pollutants. Therefore, fundamental research and effort should be given to the PCO of organic pollutants as well, especially the PCO of mixture organic pollutants, to study their reaction mechanism as well as their interrelations and intermediate products;
5. In addition to the research on laboratory scale, investigations should be performed to study the PCO efficiency under real indoor air conditions such as a room with larger volume, with/without (mechanical) ventilation, pollutants which are emitted naturally from inside or outside of the environment etc. Furthermore, computational fluid dynamics (CFD) is a very powerful tool to study the air flow and distribution under both indoor and outdoor conditions; therefore, more effort should be devoted to linking CFD to PCO for improving the indoor air quality.

Bibliography

Alduaij, J., Alshaleh, K., Haque, M.N., and Ellaithy, K. (1999). Lightweight concrete in hot coastal areas. *Cement & Concrete Composites* 21: 453-458.

Amathieu, L., and Boistelle, R. (1988). Crystallization kinetics of gypsum from dense suspension of hemihydrate water. *Journal of Crystal Growth* 88: 183-192.

Amziane, S. (2006). Setting time determination of cementitious materials based on measurements of the hydraulic pressure variations. *Cement and Concrete Research* 36(2): 295-304.

Andersson, L., and Jansson, B. (1987). *Analytical fire design with gypsum - a theoretical and experimental study*. Institute of Fire Safety Design, Lund, Sweden.

Anderson, J.D. (1995). *Computational fluid dynamics: the basics with applications.* Science/Engineering/Math. McGrwa-Hill Science.

Andreasen, A.H.M., and Andersen, J. (1930). Über die Beziehungen zwischen Kornabstufungen und Zwischenraum in Produkten aus losen Körnern (mit einigen Experimenten). *Kolloid-Zeitschrift* 50: 217-228 (In German).

Ang, C.N., and Wang, Y.C. (2004). The effect of water movement on specific heat of gypsum plasterboard in heat transfer analysis under natural fire exposure. *Construction and Building Materials* 18: 505-515.

Ankone, S.F.A. (2000). *Zelfverdichtend beton*. Training period report. University of Twente, the Netherlands (in Dutch).

Anpo, M. (1997). Photocatalysis on titanium oxide catalysts approaches in achieving highly efficient reactions and realizing the use of visible light. *Catalysis Surveys from Japan* 1: 169-179.

Ao, C.H., and Lee, S.C. (2003). Enhancement effect of TiO_2 immobilized on activated carbon filter for the photodegradation of pollutants at typical indoor air level. *Applied Catalysis B: Environmental* 44(3): 191-205.

Ao, C.H., Lee, S.C., Mak, C.L., and Chan, L.Y. (2003). Photodegradation of volatile organic compounds (VOCs) and NO for indoor air purification using TiO_2: promotion versus inhibition effect of NO. *Applied Catalysis B: Environmental* 42(2): 119-129.

Ao, C.H., and Lee, S.C. (2004). Combination effect of activated carbon with TiO_2 for the photodegradation of binary pollutants at typical indoor air level. Journal of *Photochemistry and Photobiology A: Chemistry* 161(2-3): 131-140.

Ao, C.H., and Lee, S.C. (2005). Indoor air purification by photocatalyst TiO_2 immobilized on an activated carbon filter installed in an air cleaner. *Chemical Engineering Science* 60(1): 103-109.

Asahi, R., Morikawa, T., Ohwaki, T., Aoki, K., and Taga, Y. (2001). Visible-Light Photocatalysis in Nitrogen-Doped Titanium Oxides. *Science* 293(5528): 269-271.

ASTM C1202 (2005). *Standard Test Method for Electrical Indication of Concrete's Ability to Resist Chloride Ion Penetration*. In Annual Book of ASTM Standards. vol. 04.02. American Society for Testing and Materials, Philadelphia, USA.

Augugliaro, V., Loddo, V., Pagliaro, M., Palmisano, G., and Pamisano, L. (2010). *Clean by light irradiation - practical applications of supported TiO_2*. RSC Publishing ISBN: 978-1-84755-870-1.

Austin, J.C., Holmes, A.K., Tebbutt, J.S., and Challis, R.E. (1996). Ultrasonic wave propagation in colloid suspensions and emulsions: recent experimental results. *Ultrasonics* 34(2-5): 369-374.

Ballari, M.M., Alfano, O.M., and Cassano, A.E. (2009). Photocatalytic degradation of Dichloroacetic acid. A kinetic study with a mechanistically based reaction model. *Industrail & Engineering Chemistry Research* 48: 1847-1858.

Ballari, M.M., and Brouwers, H.J.H. (2011). *Demonstration project of air-purifying pavement in Henglo*. Rep. Nr. BWK 2011. 1098, Eindhoven University of Technology, Eindhoven, the Netherlands.

Ballari, M.M., Hunger, M., Hüsken, G., and Brouwers, H.J.H. (2010). NO_x photocatalytic degradation employing concrete pavement containing titanium dioxide. *Applied Catalysis B: Environmental* 95(3-4): 245-254.

Ballari, M.M., Carballada, J., Yu, Q.L., Brouwers, H.J.H., Alfano, O.M., and Cassano, A.E. (2012). Visible light TiO_2 photocatalysts assessment for the indoor air decontamination. Accepted by *7th European meeting on solar chemistry and photocatalysis: environmental applications (SPEA7)*, June 2012, Porto, Portugal.

Barthelmes, M. (2008). *How to prepare a laboratory gypsum plasterboard*. Knauf Gips KG, Germany, personal communication.

Beeldens, A. (2007). Air purification by road materials: results of the test project in Antwerp. *Proceedings International RILEM Symposium on Photocatalysis, Environment and Construction Materials* Eds. P. Baglioni and L. Cassar, RILEM Publications, Bagneux, France, 187-194.

BFBN (2001). *Cursushandboek Zelfverdichtend Beton*. Bond van Fabrikanten van Betonproducten in Nederland (BFBN), Woerden, the Netherlands (in Dutch).

Blöß, S.P., and Elfenthal, L. (2007). Doped titanium dioxide as a photocatalyst for UV and visible Light. *Proceedings International RILEM Symposium on Photocatalysis, Environment and Construction Materials* Eds. P. Baglioni and L. Cassar, RILEM Publications, Bagneux, France, 31-38.

Bornemann, R. (2005). *Untersuchung zur Modellierung des Frisch- und Festbetonverhaltens erdfeuchter Betone*. PhD Thesis, University of Kassel, Kassel, Germany (in German).

Brouwers, H.J.H. (2004). The work of Powers and Brownyard revisited: part 1. *Cement and Concrete Research* 34: 1697-1716.

Brouwers, H.J.H. (2006). Particle-size distribution and packing fraction of geometric random packings. *Physical Review E* 74: 031309-1-031309-14.

Brouwers, H.J.H. (2010). *Recipes for porous building materials, more with less*. Inaugural lecture, Eindhoven University of Technology, Eindhoven, the Netherlands.

Brouwers, H.J.H. (2011). *A hydration model of Portland cement using the work of Powers and Brownyard.* Eindhoven University of Technology & Portland Cement Association. ISBN: 978-90-6814-184-9, Available on http://www.cement.org.

Brouwers, H.J.H., and Radix, H.J. (2005). Self-compacting concrete: theoretical and experimental study. *Cement and Concrete Research* 35: 2116-2136.

Brown, S.K., Sim, M.R., Abramson, M.J., and Gray, C.N. (1994). Concentrations of volatile organic compunds in indoor air - a review. *Indoor air* 4: 123-134.

Brunauer, S., Emmett, P.H., and Teller, E. (1938). Adsorption of gases in multimolecular layers. *Journal of the American Chemistry Society* 60: 109-117.

Butler, T.J., Vermeylen, F.M., Rury, M., Likens, G.E., Lee, B., Bowker, G.E., and McCluney, L. (2010). Response of ozone and nitrate to stationary source NO_x emission reductions in the eastern USA. *Atmospheric Environment* 45(5): 1084-1094.

Cassano, A.E., Martin, C.A., Brandi, R.J., and Alfano, O.M. (1995). Photoreactor analysis and design: fundamentals and applications. *Industrial & Engineering Chemistry Research* 34: 2155-2201.

Cassano, A.E., and Alfano, O.M. (2000). Reaction engineering of suspended solid heterogeneous photocatalytic reactors. *Catalysis Today* 58: 167-197.

Cazacliu, B., and Roquet, N. (2009). Concrete mixing kinetics by means of power measurement. *Cement and Concrete Research* 39(3): 182-194.

Chandra, S., and Berntsson, L. (2003). *Lightweight aggregate concrete science, technology and applications.* ISBN: 81-8014-052-0. Standard publishers distributors. Delhi, India.

Chen, W. (2007). *Hydration of slag cement: theory, modeling and application*. PhD thesis, University of Twente, Enschede, the Netherlands.

Chen, J., and Poon, C.-S. (2009). Photocatalytic activity of titanium dioxide modified concrete materiasl - influence of uitlizing recycled glass cullets as aggregates. *Journal of Enviornmental Management* 90: 3436-3442.

Choi, W., Termin, A., and Hoffmann, M.R. (1994). The role of metal ion dopants in quantum-sized TiO_2: correlation between photoreactivity and charge carrier recombination dynamics. *The Journal of Physical Chemistry* 98: 13669-13679.

Chen, C., and Zhao, B. (2010). Some questions on dispersion of human exhaled droplets in ventilation room: answers from numerical investigation. *Indoor Air* 20: 95-111.

Choi, Y.W., Kim, Y.J., Shin, H.C., and Moon, H.Y. (2006). An experimental research on the fluidity and mechanical properties of high-strength lightweight self-compacting concrete. *Cement and Concrete Research* 36: 1595-1602.

Cubillos Sanabria, H.A. (2011). *Heterogeneous photocatalytic oxidation of* NO_x *under indoor conditions: experimental and simulation study.* Master thesis. Eindhoven University of Technology, Eindhoven, the Netherlands.

Colak, A. (2001). Physical and mechanical properties of polymer-plaster composites. *Cement and Concrete Research* 31(11): 1539-1547.

Columbia University (2011). Poiseuille flow between parallel plates (laminar). http://www.columbia.edu/cu/gsapp/BT/RESEARCH/Arch-atmos/plates.html.

Cooley, J.D., Wong, W.C., Jumper, C.A., and Straus, D.C. (1998). Correlation between the prevalence of certain fungi and sick building syndrome. *Occupational and Environmental Medicine* 55: 579-584.

Coquard, P., Boistelle, R., Amathieu, L., and Barriac, P. (1994). Hardness, elasticity modulus and flexion strength of dry set plaster. *Journal of Materials Science* 29: 4611-4617.

Cramer, S.M., Friday, O.M., White, R.H., and Sriprutkiat, G. (2003). Mechanical properties of gypsum board at elevated temperatures. *Proceedings of the Fire and Materials 2003 conference*. January 2003, California, USA: 27-42.

Dalton, J.S., Janes, P.A., Jones, N.G., Nicholson, J.A., Hallam, K.R., and Allen, G.C. (2002). Photocatalytic oxidation of NO_x gases using TiO_2: a surface spectroscopic approach. *Environmental Pollution* 120: 415-422.

Devahasdin, S., Fan, C., Li, J.K., and Chen, D.H. (2003). TiO_2 photocatalytic oxidation of nitric oxide: transient behavior and reaction kinetics. Journal of *Photochemistry and Photobiology A: Chemistry* 156: 161-170.

De Belie, N., Grosse, C.U., Kurz, J., and Reinhardt, H.W. (2005). Ultrasound monitoring of the influence of difference accelerating admixtures and cement types for shotcrete on setting and hardening behavior. *Cement and Concrete Research* 35(11): 2087-2094.

Deng, Y.H., and Furuno, T. (2001). Study on gypsum-bonded particleboard reinforced with polypropylene fibers. The Japan Wood Research Society 47: 445-450.

Deutsch, Y., Nathan, Y., and Sarig, S. (1994). Thermogravimetric evaluation of the kinetics of the gypsum-hemidhyrate-soluble anhydrite transitions. *Journal of Thermal Analysis* 42: 159-174.

Domone, P.L., and HsiWen, C. (1997). Testing of binders for high performance concrete. *Cement and Concrete Research* 27(8): 1141-1147.

Ducman, V., Mladenovic, A., and Suput, J.S. (2002). Lightweight aggregate based on waste glass and its alkali-silica reactivity. *Cement and Concrete Research* 32: 223-226.

Dweck, J., Andrade, B.F., Monteiro, E.E.C., and Fischer, R. (2002). Thermal characterization of polymeric plaster composites. *Journal of Thermal Analysis and Calorimetry* 67: 321-326.

EFNARC (2002). *Specification and Guidelines for Self-Compacting Concrete*. EFNARC.

EFNARC (2005). *The European guidelines for self-compacting concrete. Specification, production and use*. EFNARC.

Egerton, T.A., and King, C.J. (1979). The influence of light intensity on photocativity in TiO_2 pigmented systems. *Journal of the Oil and Coloru Chemists Association* 62(10): 386-391.

Elbeyli, I.Y., and Piskin, S. (2004). Thermal dehydration kinectics of gypsum and borogypsum under non-isothermal conditions. *Chinese Journal of Chemical Eingeering* 12: 302-305.

Emeline, A.V., Ryabchuk, V., and Serpone, N. (2000). Factors affecting the efficiency of a photocatalyzed process in aqueous metal-oxide dispersions: prospect of distinguishing between two kinetic models. *Journal of Photochemistry and Photobiology A: Chemistry* 133(1-2): 89-97.

Emmerich, S.J., McDowell, T., and Anis, W. (2005). *Investigation of the impact of commercial building envelope airtightness on HVAC energy use*. Washington D.C.: U.S. Department of Commerce. NISTIR 7238.

EN 13279-2 (2004). European Standard. *Gypsum binders and gypsum plasters*. CEN.

Engelhardt, K. (2009). Personal communication.

EU project (2008). *The Integrated Safe & Smart Built concept (I-SSB)*. URL: http://www.issb-project.com/.

EuroLightCon (1998). *LWAC material properties state-of-the-art.* Document BE96-3942/R2, European Union – Brite EuRam III.

EuroLightCon (2000). *Light weight aggregates*. Document BE96-3942/R15, European Union – Brite EuRam III.

Evans, T.J., Majumdar, A.J., and Ryder, J.F. (1981). A semi-dry method for the production of lightweight glass-fibre-reinforced gypsum. *The International Journal of Cemant Composites and Lightweight Concrete* 3(1): 41-44.

Eve, S., Gomina, M., and Orange, G. (2004). Effects of polyamide and polypropylene fibers on the setting and the mechanical properties of plaster. *Key Engineering Materials* 264-268: 2531-2536.

Eve, S., Gomina, M., Hamel, J., and Orange, G. (2006). Investigation of the setting of polyamide fibre/latex-filled plaster composites. *Journal of the European Ceramic Society* 26: 2541-2546.

Federation of European Heating, Ventilation and Air-Conditioning Associations (2010). *Air filtration in HVAC systems*. Brussels : REHVA. ISBN 978-2-930521-01-5.

Fennis, S.A.A.M. (2011). *Design of ecological concrete by particle packing optimization.* PhD Thesis. Delft University of Technology, Delft, the Netherlands.

Feret, R. (1892). Sur la compactié des mortiers hyrdauliques. *Ann. Ponts Chauss* IV: 5-164 (in French).

Ferraris, C.F. (1999). Measurement of the rheological properties of high performance concrete: state of the art report. *Journal of research of the National Institute of Standards and Technology* 104(5): 461-478.

Finnegan, M.J., Pickering, C.A., and Burge P.S. (1984). The sick building syndrome: prevalence studies. *British Medical Journal (Clinical Research Ed)* 289: 1573–1575.

Fujishima, A., and Honda, K. (1972). Electrochemical Photolysis of Water at a Semiconductor Electrode. *Nature* 238(5358): 37-38.

Fujii, K., and Kondo, W. (1986). Kinetics of hydration of calcium sulphate hemihydrate. *Journal of Chemical Society, Dalton Transactions*: 729-731.

Fuller, W.B., and Thompson, S.E. (1907). The laws of proportioning concrete. *Transactions of the American Society of Civil Engineers* 33: 222-298.

Funk, J.E., and Dinger, D.R. (1994). *Predictive Process Control of Crowded Particulate Suspensions, Applied to Ceramic Manufacturing*. Kluwer Academic Publishers, Boston, the United States.

Ghazi Wakili, K., Hugi, E., Wullschleger, L., and Frank, Th. (2007). Gypsum board in fire - modeling and experimental validation. *Journal of Fire Sciences* 25: 267- 282.

Ghazi Wakili, K., and Hugi, E. (2008). Four types of gypsum plaster boards and their thermophysical properties under fire condition. *Journal of Fire Sciences* 27: 27-43.

Gmouh, A., Eve, S., Samdi, A., Moussa, R., Tricha, L., Aazzab, B., Hamel, J., and Gomina, M. (2004). Development and validation of a dimensional variation measurement set-application to the plaster setting. *Materials Science and Engineering A* 372: 123-127.

Gomez Alvarez-Arenas, T.E., Elvira Segura, L., Riera Franco de Sarabia, E. (2002). Characterization of suspensions of particles in water by an ultrasonic resonant cell. *Ultrasonics* 39(10): 715-727.

Grosse, C.U., Reinhardt, H.W., Kruger, M., and Beutel, R. (2006). Ultrasonic through-transmission techniques for quality control of concrete during setting and hardening, in: H.W. Reinhardt (Ed.), *Advanced Testing of Fresh Cementitious Materials*, Stuttgart, 83-93.

Groves, A.W. (1958). *Gypsum and Anhydrite*. Overseas Geological Surveys, Mineral Resources Division. Her Majesty's Stationery Office: London.

Hampel, C. (2010). *Polymer 1* or 2* produced in full production scale (about 3 tons) for extended production tests of gypsum plasterboards.* EU Project I-SSB report.

Hand, R.J. (1994). The kinetics of hydration of calcium sulphate hemihydrate: a critical comparison of the models in the literature. *Cement and Concrete Research* 24: 885-895.

Haque, M.N., Al-Khaiat, H., and Kayali, O. (2004). Strength and durability of lightweight concrete. *Cement & Concrete Composites* 26: 307-314.

Harker, A.H., and Temple, J.A.G. (1988). Velocity and attenuation of ultrasound in suspensions of particles in fluids. *Journal of Physics D: Applied Physics* 21(11): 1576-1588.

Harrison, J., Pickering, C.A.C., Faragher, E.B., Austwick, P.K.C., Little, S.A., and Lawton, L. (1992). An investigation of the relationship between microbial and particulate indoor air pollution and the sick building syndrome. *Respiratory Medicine* 86(3): 225-235.

Hashimoto, K., Wasada, K., Osaki, M., Shono, E., Adachi, K., Toukai, N., Kominami, H., and Kera, Y. (2001). Photocatalytic oxidation of nitrogen oxide over titania–zeolite composite catalyst to remove nitrogen oxides in the atmosphere. *Applied Catalysis B: Environmental* 30: 429-436.

Hayashi, T., Ishizu, Y., Kato, S., and Murakami, S. (2002). CFD analysis on characteristics of contaminated indoor air ventilation and its application in the evaluation of the effects of contaminant inhalation by a human occupant. *Building and Environment* 37(3): 219-230.

Herrmann, J.M., Péruchon, L., Puzenat, E., and Guillard, C. (2007). Photocatalysis: From fundamentals to self-cleaning glass application. In Baglioni, P., Cassar, L. (eds.). *Proceedings International RILEM Symposium on Photocatalysis, Environment and Construction Materials*-TDP. RILEM Publications: Bagneux, France, 41-48.

Hernandez-Olivares, F., Oterza, I., and Villanueva, L.D. (1992). Experimental analysis of toughness and modulus of rupture increase of sisla short fibre reinforced hemihydrated gypsum. *Composite Structures* 22: 123-137.

Hoffmann, M.R., Martin, S.T., Choi, W., and Bahnemann, D.W. (1995). Environmental applications of semiconductor photocatalysis. *Chemical Review* 95: 69-96.

Horai, K., and Simmons, G. (1969). Thermal conductivity of rock-forming minerals. *Earth and Planetary Science Letters* 6: 359-368.

Hoskins, J.A. (2003). Health effects due to indoor air pollution. *Indoor and Building Environement* 12:427-433.

Hudson-Lamb, D.L., Strydom, C.A., and Potgieter, J.H. (1996). The thermal dehydration of natural gypsum and pure calcium sulphate dihydrate (gypsum). *Thermochimica Acta* 282/283: 483-492.

Hüsken, G. (2010). *A multifunctional design approach for sustainble concrete, with application to concrete mass products.* PhD Thesis. Eindhoven University of Technology, Eindhoven, the Netherlands.

Hüsken, G., and Brouwers, H.J.H. (2008). A new mix design concept for earth-moist concrete: A theoretical and experimental study. *Cement and Concrete Research* 38: 1246-1259.

Hüsken, G., Hunger, M., and Brouwers, H.J.H. (2007). Comparative study on cementitious products containing titanium dioxide as photo-catalyst. In Baglioni, P., Cassar, L. (eds.). *Proceedings International RILEM Symposium on Photocatalysis, Environment and Construction Materials*-TDP. RILEM Publications, Bagneux, France, 147-154.

Hüsken, G., Hunger, M., and Brouwers, H.J.H. (2009). Experimental study of photocatalytic concrete products for air purification. *Building and Environment* 44(12): 2463-2474.

Hunger, M. (2010). *An integral design concept for ecological self-compacting concrete*. PhD Thesis. Eindhoven University of Technology, Eindhoven, the Netherlands.

Hunger, M., and Brouwers, H.J.H. (2009). Flow analysis of water-powder mixtures: application to specific surface area and shape factor. *Cement & Concrete Composites* 31: 39-59.

Hunger, M., and Brouwers, H.J.H. (2008). Self-Cleaning Surfaces as an innovative potential for sustainable concrete. In Limbachiya, M.C., Kew, H.Y. (eds.). *Proceedings International Conference Excellence in Concrete Construction - through Innovation 2008*. CRC Press: United Kingdom, 545-552.

Hunger, M., Brouwers, H.J.H., and Ballari, M.M. (2008). Photocatalytic degradation ability of cementitious materials: A modeling approach. *Proceedings International Conference on Microstructure related Durability of Cementitious Composites*, October 2008, Nanjing, China, 1103-1112.

Hunger, M., Hüsken, G., and Brouwers, H.J.H. (2010). Photocatalytic degradation of air pollutants - from modeling to large scale application. *Cement and Concrete Research* 40: 313-320.

Hunger, M. (2012). Personal communication.

Ichiura, H., Kitaoka, T., and Tanaka, H. (2003). Photocatalytic Oxidation of NO_x Using Composite Sheets Containing TiO_2 and a Metal Compound. *Chemosphere* 51: 855-860.

Imoberdorf, G.E., Irazoqui, H.A. Cassano, A.E., and Alfano, O.M. (2005). Photocatalytic degradation of Tetrachloroethylene in gas phase on TiO_2 films: a kinetic study. *Industrial & Engineering Chemistry Research* 44: 6075-6085.

Imoberdorf, G.E., Cassano, A.E., Alfano, O.M., and Irazoqui, H.A. (2006). Modelling of a multiannular photocatalytic reactor for perchloroethylene degradation in air. *AIChE Journal* 52: 1814-1823.

International Organization for Standardization (2007). *Fine ceramics (advanced ceramics, advancced technical ceramics) - Test method for air-purification performance of semiconducting photocatalytic materials - Part 1: Removal of nitric oxide*: ISO, Switzerland. Reference number: ISO 22197-1:2007.

International Organization for Standardization (2007). *Fine ceramics (advanced ceramics, advancced technical ceramics) - Test method for air-purification performance of semiconducting photocatalytic materials - Part 2: Removal of acetaldehyde*: ISO, Switzerland. Reference number: ISO 22197-2:2011.

International Organization for Standardization (2007). *Fine ceramics (advanced ceramics, advancced technical ceramics) - Test method for air-purification performance of semiconducting photocatalytic materials - Part 1: Removal of toluene*: ISO, Switzerland. Reference number: ISO 22197-3:2011.

International Organization for Standardization (1999). *Particle size analysis - Laser diffraction methods - Part 1: General principles.* ISO, Switzerland. Reference nubmer: ISO 13320-1:1999.

International Organization for Standardization (1999). *Fire-resistance tests - Elements of building construction - Part 1: General requirements*, ISO, Switzerland. Reference number: ISO 834-1:1999.

Jarandehei, A., and de Visscher, A. (2009). Three-Dimensional CFD model for a flat plate photocatalytic reactor: degradation of TCE in a serpentine flow field. *AIChE Journal* 55(2): 312-320.

Jones, A.P. (1999). Indoor air quality and health. *Atmospheric Environment* 33(28): 4535-4564.

Kan, A., and Demirboga, R. (2009). A novel material for lightweight concrete production. *Cement & Concrete Composites* 31: 489-495.

Kantro, D.L. (1980). Influence of water-reducing admixtures on properties of cement paste - a miniature slump test. *Cement, Concrete and Aggregates* 2: 95-102.

Kao, H.-M., Chang, T.-J., Hsieh, Y.-F., Wang, C.H., and Hsieh, C.-I. (2009). Comparison of airflow and particulate matter transport in multi-room buildings for different natural ventilation patterns. *Energy and Buildings* 41(9): 966-974.

Kim, S.B., and Hong, S.C. (2002). Kinetic study for photocatalytic degradation of volatile organic compounds in air using thin film TiO_2 photocatalyst. *Applied Catalysis B: Environmental* 35(4): 305-315.

Kim, S.-S., Kang, D.-H., Choi, D.-H., Yeo, M.-S., and Kim, K.-W. (2008). Comparison of strategies to improve indoor air quality at the pre-occupancy stage in new apartment buildings. *Bulding and Environment* 43: 320-328.

Kimura, N., Abe, S., Yoshimoto, T., and Fukayama, S. (2001). Photocatalyst-carrying structure and photocatalyst coating material, US 6228480, Nippon Soda Co. Ltd., Japan.

Koehler, E.P., and Fowler, D.W. (2003). *Summary of concrete workability test*, Research report ICAR-105-1, International center for aggregates research, The University of Texas at Austin.

Korte, A.C.J. de, and Brouwers, H.J.H. (2008). Hydration of modeling of calcium sulphates. In: Al-Mattarneh H, Mustapha KN, Nuruddin MP, editors. *Proceedings of International Conference on Construction and Building Technology*. Malaysia: Kuala Lumpur. 433-444.

Korte, A.C.J. de, and Brouwers, H.J.H. (2010). Calculation of thermal conductivity of gypsum plasterboards at ambient and elevated temperature. *Fire and Materials* 34: 55-75.

Korte, A.C.J. de, and Brouwers, H.J.H. (2011). Ultrasonic sound speed analysis of hydrating clacium sulphate hemihydrate, *Jounal of Materials Science* 46: 7228-7239.

Kralj, D. (2009). Experimental study of recycling lightweight concrete with aggregates containing expanded glass. *Process Safety and Environmental Protection* 87: 267-273.

Kraeutler, B., and Bard, A.J. (1978). Heterogeneous photocatalytic preparation of supported catalysts. Photodeposition of platinum on titanium dioxide powder and other substrates. *Journal of Amercian Chemistry Society* 100(13): 4317-4318.

Kuntze, R.A. (1965). Effect of water vapor on the formation of $CaSO_4 \cdot 0.5H_2O$ modifications. *Journal of Chemistry* 43: 2522-2529.

Kuo, C.S., Tseng, Y.H., Huang, C., and Li, Y. (2007). Carbon-containing nano-titania prepared by chemical vapor deposition and its visible-light-responsive photocatalytic activity. *Journal of Molecular Catalysis A: Chemical* 270(1-2): 93-100.

Lancia, A., Musmarra, D., and Prisciandaro, M. (1999). Measuring induction period for calcium sulphate dihydrate precipitation. *AIChE Journal* 45(2): 390-397.

Langridge, J.M., Gustafsson, R.J., Griffiths, P.T., Cox, R.A., Lambert, R.M., and Jones, R.L. (2009). Solar driven nitrous acid formation on building material surfaces containing titanium dioxide: a concern for air quality in urban areas? *Atmospheric Environment* 43: 5128-5131.

Lasa, H. de, Serrano, B., and Salaices, M. (2005). *Photocatalytic reaction engineering*. Springer.

Laufs, S., Burgeth, G., Duttlinger, W., Kurtenbach, R., Maban, M., Thomas, C., Wiesen, P., and Kleffmann, J. (2010). Conversion of nitrogen oxides on commercial photocatalytic dispersion paints. *Atmospheric Environment* 44: 2341-2349.

Lebowitz, M.D, and Walkinshaw, D.S. (1992). Indoor Air '90: Health effects associated with indoor air contaminants. *Archives of Environmental Health* 47: 6-7.

Lehmann, F., and Grosse, C.U. (2008). *Ultrasound measurements of hydrating of hemihydrates*. Universitat Stuttgart, personal communication.

Levenspiel, O. (1999). *Chemical reaction engineering*. Willey: New York.

Lewry, A.J., and Williamson, J. (1994a). The Setting of Gypsum Plaster Part I The Hydration of Calcium Sulphate Hemihydrate. *Journal of Materials Science* 29: 5279-5284.

Lewry, A.J., and Williamson, J. (1994b). The Setting of gypsum plaster Part II the development of microstructure and strength. *Journal of Materials Science* 29: 5524-5528.

Lim, T.H., Jeong, S.M., Kim, S.D., and Gyenis, J. (2000). Photocatalytic decomposition of NO by TiO_2 particles. *Journal of Photochemistry and Photobiology A: Chemistry* 134(3): 209-217.

Liu, X., Chia, K.S., and Zhang, M.H. (2010). Development of lightweight concrete with high resistance to water and chloride-ion penetration. *Cement & Concrete Composites* 32: 757-766.

Liu, X., Chia, K.S., and Zhang, M.H. (2011). Water absorption, permeability, and resistance to chloride-ion penetration of lightweight aggregate concrete. *Construction and Building Materials* 25: 335-343.

Liu, S., and Nancollas, G.H. (1971). The kinetics of dissolution of calcium sulphate dihydrate. *Journal of Inorganic and Nuclear Chemistry* 33: 2311-2316.

Lopez Buendia, A.M., and Suesta Falco, C. (2011). Personal communication.

Loudon, A.G. (1979). The thermal properties of lightweight concretes. *The International Journal of Lightweight Concrete* 11(2): 71-85.

Lydon, F.D. (1982). *Concrete mix design*, 2nd edition. Applied Science Publishers, London, UK.

Maggos, T., Bartzis, G.J., Liakou, M., and Gobin, C. (2007). Photocatalytic Degradation of NO_x Gases using TiO_2-Containing Paint: A Real Scale Study. *Journal of Hazardous Materials* 146: 668-673.

Malvern Instruments Ltd. (2007). *Mastersizer 2000 user manual* 73-74.

Manzello, S.L., Gann, R.G., Kukuck, S.R., and Lenhert, D.B. (2007). Influence of gypsum board type (X or C) on real fire performance of partition assemblies. *Fire and Materials* 31: 425-442.

Marquardt, I. (2002). Determination of the composition of self-compacting concretes on the basis of the water requirements of the constituent materials – Presentation of a new mix concept, *Betonwerk + Fertigteiltechnik, Bauverlag* BV GmbH, Gütersloh, Germany 11: 22-30.

Mehaffey, J.R., Cuerrier, P., and Carisse, G. (1994). A model for predicting heat transfer through gypsum-board/wood-stud walls exposed to fire. *Fire and Materials* 18: 297-305.

Murakami, S., Kato, S., Ito, K., and Zhu, Q. (2003). Modeling and CFD prediction for diffusion and adsorption within room with various adsorption isotherms. *Indoor Air* 13(6): 20-27.

Murata, Y., Tawara, H., Obata, H., and Murata, K. (1997). NO_x-Cleaning Paving Block. EP-patent 0786283 A1, Mitsubishi Materials Corporation, Japan.

Neville, A.M. (1995). *Properties of concrete.* Fourth edition. ISBN: 978-0-582-23070-5. Pearson education limited. Harlow, England.

NEN-EN 1097-6 (2000). *Tests for mechanical and physical properties of aggregates – part 6: Determination of particle density and water absorption.*

NEN-EN 1097-7 (1999). *Test for mechanical and physical properties of aggregates – part 6: Determination of particle density of filler-Pycnometer method.*

NT Build 492 (1999). *Concrete, mortar and cement-based repair materials: Chloride migration coefficient from non-steady-state migration experiments*. Nord test method. Finland.

Obee, T.N., and Brown, R.T. (1995). Photocatalysis for indoor air applications: effects of humidity and trace contaminant levels on the oxidation rates of Formaldehyde, Toluene, and 1, 3-Butadiene. *Environmental Science & Technology* 29(5): 1223 - 1231.

Okamura, H., and Ozawa, K. (1995). Mix-design for self-compacting concrete. *Concrete Library, JSCE* 25: 107-120.

Orth-Gerber, J., and Kisch, H. (2005). *Titanium dioxide photocatalyst containing carbon and method for its production.* Patent US 2005/0227857 A1.

Paulik, F., Paulik, J., and Arnold, M. (1992). Thermal decomposition of gypsum. *Thermochimica Acta* 200: 195-204.

Peral, J., and Ollis, D.F. (1992). Heterogeneous photocatalytic oxidation of gas-phase organics for air purification: Acetone, 1-Butanol, Butyraldehyde, Formaldehyde, and m-Xylene oxidation. *Journal of Catalysis* 136: 554-565.

Phani, K.K., Niyogi, S.K., Maitra, A.K., and Roychaudhury, M. (1986). Strength and elastic modulus of a porous brittle solid: an acousto-ultrasonic study. *Journal of Materials Science* 21: 4335-4341.

Pöllmann, H. (2009). Personal communication.

Puntke, W. (2002). Isseranspruch von feinen Kornhaufwerken, *Beton* 52(5): 242-248 (in German).

Quercia, G., Hüsken, G., and Brouwers, H.J.H. (2012a). Water demand of amorphous nano silica and its impact on the workability of cement paste. *Cement and Concrete Research* 42: 344-357.

Quercia, G., Lazaro, A., Geus, J.W., and Brouwers, H.J.H. (2012b). Morphology and texture characteritics of amorphous nano-silica particles used in concrete. Under review.

Reinhardt, H.W., and Grosse, C.U. (2004). Continuous monitoring of setting and hardening of mortar and concrete. *Construction and Building Materials* 18: 145-154.

Richardson, L.F. (1910). The approximate arithmetical solution by finite differencces of physical problems involving differential equations, with an application to the stresses in a masonry dam. *Philosophical Transactions of the Royal Society* 210: 307-357.

Ridge, M.J., and Surkevicius, H. (1961). Hydration of calcium sulphate hemihydrate I. kinetics of the reaction. *Journal of Applied Chemistry* 12: 246-252.

Ridge, M.J. (1964). Hydration of calcium sulphate hemihydrate. *Nature* 204: 70-71.

Roache, P.J. (1994). Perspective: a method for uniform reporting of grid refinement studies. *ASME Journal of Fluids Engineering* 116: 405-413.

Robens, E., Benzler, B., Büchel, G., Reichert, H., and Schumacher, K. (2002). Investigation of characterizing methods for the microstructure of cement. *Cement and Concrete Research* 32(1): 87-90.

Robeyst, N., Gruyaert, E., Grosse, C.U., and De Belie, N. (2008). Monitoring the setting of concrete containing blast-furnace slag by measuring the ultrasonic p-wave velocity. *Cement and Concrete Research* 38: 1169-1176.

Ryan, J.V. (1962). Study of gypsum plasters exposed to fire. Journal of research of the national bureau of standards-C. *Eingineering and Instrumentation* 66C(4): 373-387.

Safiuddin, Md., and Hearn, N. (2005). Comparison of ASTM saturation techniques for measuring the permeable porosity of concrete. *Cement and Concrete Research* 35: 1008-1013.

Salvadó-Estivill, I., Hargreaves, D.M., and Puma, G.L. (2007). Evaluation of the Intrinsic photocatalytic oxidation kinetics of indoor air pollutants. *Environmental Science Technology* 41(6): 2028-2035.

Sano, T., Negishi, N., Uchino, K., Tanaka, J., Matsuzawa, S., and K. Takeuchi (2003). Photocatalytic degradation of gaseous acetaldehyde on TiO_2 with photodeposited metals and metal oxides. *Journal of Photochemistry and Photobiology A: Chemistry* 160(1-2): 93-98.

Schiller, K. (1957). Strength of highly porous brittle materials. *Nature* 180: 862- 863.

Schiller, K. (1958). Porosity and strength of brittle solids (with particular reference to gypsum). In *Mechanical properties of non-brittle materials*. London, UK: Butterworths Scientific Publications, 35-49.

Schiller, K. (1962). Mechanism of re-crystallisation in calcium sulphate hemihydrate plasters. *Journal of Applied Chemistry* 12: 135-144.

Schiller, K. (1963). The setting of a slurry. *Journal of Applied Chemistry* 13: 572-575.

Schiller, K. (1974). The course of hydration: its practical importance and theoretical interpretation. *Journal Applied Chemistry Biotechnology* 24: 379-385.

Shelimov, B.N., Tolkachev, N.N., Tkachenko, O.P., Baeva, G.N., Klementiev, K.V., Stakheev, A.Y., and Kazansky, V.B. (2008). Enhancement Effect of TiO_2 Dispersion over Alumina on the Photocatalytic Removal of NO_x Admixtures from O_2-N_2 Flow. *Journal of Photochemistry and Photobiology A:* Chemistry 195: 81-88.

Siegel, R., and Howell, J.R. (1992). *Thermal radiation heat transfer 3rd edition* Hemisphere: Washington DC.

Sing, M., and Garg, M. (1992). Glass fiber reinforced water-resistant gypsum-based composites. *Cement & Concrete Composites* 12(1): 23-32.

Solberg, C., and Hansen, S. (2001). Dissolution of $CaSO_4 \cdot 1/2H_2O$ and precipitation of $CaSO_4 \cdot 2H_2O$: A kinetic study by synchrotron X-ray powder diffraction. *Cement and Concrete Research* 31(4): 641-646.

Somerton, W.H., Chu, S.L., and Keese, J.A. (1974). Thermal behavior of unconsolidated oil sands. *Society of Petroleum Eingineers of AIME Journal* 14(5): 513-521.

Sultan, M.A. (1996). A model for predicting heat transfer through noninsulated unloaded steel stud gypsum board wall assemblies exposed to fire. *Fire Technology* third quarter: 239-259.

Tagge, C.D., Pollock, J.F., Torres, L., and Soane, D.S. (2005). *Reinforced wallboard.* United States Patent 6841232.

Taplin, J.H. (1973). Kinetics models for the setting of plaster of Paris. *Journal of Applied Chemistry and Biotechnology* 23: 349-355.

Taylor, H.F.W. (1985). The reactions of cement compounds with water, in P. Barret and L.-C. Dufour (eds), *Proceedings of the 10th International Symposium on the Reactivity of Solids*, Vol. A, Elsevier, Dijon, France, 39-45.

Thomas, G. (2002). Thermal properties of gypsum plasterboard at high temperatures. *Fire and Materials* 26: 37-45.

Topcu, I.B., and Uygunoglu, T. (2010). Effect of aggregate type on properties of hardened self-consolidating lightweight concrete (SCLC). *Construction and Building Materials* 24: 1286-1295.

Topp, C. (1999). *Diffusion and evaporation-controlled emission in ventilated rooms*. PhD Thesis. Alaborg University, Denmark.

Tregger, N., Ferrara, L., and Shah, S.P. (2008). Identifying viscosity of cement paste from mini-slump-flow test. *ACI Materials Journal* 558-566.

Turchi, C.S., and Ollis, D.F. (1990). Photocatalytic degradation of organic water contaminants: mechanisms involving hydroxyl radical attack. *Journal of Catalysis* 122(1): 178-192.

United States Environmental Protection Agency (1991). *Indoor air facts No. 4 Sick Building Syndrome*. Research and Development (MD-56).

User's guide, ISOMET model 2104 *heat transfer analyzer*, Applied Precision.

Villar, J., and Baret, J.F. (1997). *Cementing slurry and method of designing a formulation.* United States Patent 6153562.

Walraven, J.C., Takada, K., and Pelova, G.I. (1999). Zelfverdichtend beton, hoe maak je dat? *Cement* 3: 68-72 (in Dutch).

Wang, Sh., Chen, T., Rao, K.K., and Wong, M. (2007). Nanocolumnar titania thin films uniquely incorporated with carbon for visible light photocatalysis. *Applied Catalysis B: Environmental* 76: 328-334.

Wang, H., Wu, Z., Zhao, W., and Guan, B. (2007). Photocatalytic Oxidation of Nitrogen Oxides Using TiO_2 Loading on Woven Glass Fabric. *Chemosphere* 66: 185–190.

Wargocki, P., Wyon, D.P., Sundell, J., Clausen, G., and Fanger, P.O. (2000). The Effects of Outdoor Air Supply Rate in an Office on Perceived Air Quality, Sick Building Syndrome (SBS) Symptoms and Productivity. *Indoor Air* 10(4): 222-236.

Wasserman, R., and Bentur, A. (1996). Interfacial interactions in lightweight aggregate concretes and their influence on the concrete strength. *Cement & Concrete Composites* 18: 67-76.

Wirsching, F. (2005). *Calcium Sulfate*. Wiley-VCH Verlag GmbH & Co. KGaA, Weinheim.

World Health Organization (2006). *Air Quality Guidelines - Global Update 2005*. Druckpartner Moser. ISBN 92 890 2192 6.

Wu, Z., Zhang, Y., Zheng, J. and Ding, Y. (2009). An experimental study on the workability of self-compacting lightweight concrete. *Construction and Building Materials* 23: 2087-2092.

Xu, Y., Yang, X., Yang, C., and Srebric, J. (2009). Contaminant Dispersion with personal displacement ventilation, Part I: Base case study. *Building and Environment* 44(10): 2121-2128.

Yamashita, H., Ichihashi, Y., Takeuchi, M., Kishiguchi, S., and Anpo, M. (1999). Characterization of metal ion-implanted titanium oxide photocatalysts operating under visible light irradiation. *Journal of Synchrotron Radiation* 6(3): 451-452.

Yang, X., Cao, Ch., Hohn, K., Erickson, L., Maghirang, R., Hamal, D., and Klabunde, K. (2007). Highly visible-light active C- and V-doped TiO_2 for degradation of acetaldehyde. *Journal of Catalysis* 252: 296-302.

Yu, Q.L. (2010). *BET specific surface area test method*. Internal report. Eindhoven University of Technology, Eindhoven, the Netherlands.

Yu, Q.L., and Brouwers H.J.H. (2010). Gypsum: an investigation of microstructure and mechanical properties, *Proceedings 8th fib International PhD Symposium in Civil Engineering*, 20-23 June 2010, Lyngby, 341-346, Eds. G. Fischer, M. Geiker, O. Hededal, L. Ottoson and H. Stang, DTU Byg, Lyngby, Denmark.

Yu, Q.L., and Brouwers, H.J.H. (2009). Indoor air purification using heterogeneous photocatalytic oxidation. Part I: experimental study. *Applied Catalysis B: Environmental* 92: 454-461.

Yu, Q.L., and Brouwers, H.J.H. (2011a). Microstructure and mechanical properties of β-hemihydrate produced gypsum: an insight from its hydration process. *Construction and Building Materials* 25: 3149-3157.

Yu, Q.L., and Brouwers, H.J.H. (2011b). Thermal properties and microstructure of gypsum board and its dehydraiton products: a theoretical and experimental investigation. Accepted by *Fire and Materials*, DOI: 10.1002/fam.1117.

Yu, Q.L., and Brouwers, H.J.H. (2011c). The development of self-compacting gypsum based lightweight composite: a theoretical and experimental invesitation. Submitted to *Cement & Concrete Composites*.

Yu, Q.L., Brouwers, H.J.H., and Ballari, M.M. (2009). Experimental study and modelling of the photocatalytic oxidation of NO in indoor conditions, *Proceedings of the 3rd international symposium on nanotechnology in construction*, Springer-verlag, Berlin Heidelberg, 389-394.

Yu, Q.L., Brouwers, H.J.H., and Ballari, M.M. (2010). Indoor air purification using heterogeneous photocatalytic oxidation, Part 2: Kinetic study, *Applied Catalysis B: Environmental*, 99: 58-65.

Yu, Q.L., Brouwers, H.J.H., and Korte, A.C.J. de. (2009). Gypsum hydration: a theoretical and experimental study. In: Fischer HB, editor. *Proceedings of 17th International conference in building materials (Internationale Baustofftagung)*. Germany: Weimar, 1: 783-788.

Yu, Q.L., Cubillos Sanabria, H.A., Loomans, M.G.L.C., and Brouwers. H.J.H. (2012). NO and NO_2 degradation applying a novel photocatalytic wall covering under indoor air conditions - part 2: a CFD modeling approach. To be submitted.

Yu, J.C., Yu, J., Ho, W., Jiang, Z., and Zhang, L. (2002). Effects of F- doping on the photocatalytic activity and microstructures of nanocrystalline TiO_2 powders. *Chemstry of Materials* 14: 3808-3816.

Yu, H., Zhang, K., and Rossi, C. (2007). Experimental Study of the Photocatalytic Degradation of Formaldehyde in Indoor Air using a Nano-particulate Titanium Dioxide Photocatalyst. *Indoor and Built Environment* 16(6): 529-537.

Zehner, P., Schlunder, E.U. (1970). Thermal conducvitiy of granular materials at moderate temperatures. *Chemie Ingenieur Technik* 42(14): 933-941.

Zhang, M.H., and Gjorv, O.E. (1991). Mechanical properties of high-strength lightweight concrete. *ACI Materials Journal* May-June: 240-247.

Zhang, M.H., and Gjorv, O.E. (1990). Microstructure of the interfacial zone between lightweight aggregate and cement paste. *Cement and Concrete Research* 20: 610-618.

Zhang, M.H., and Gjorv, O.E. (1990). Pozzolanic reactivity of lightweight aggregates. *Cement and Concrete Research* 20: 884-890.

Zhao, J., and Yang, X.D. (2003). Photocatalytic Oxidation for Indoor Air Purification: A Literature Review. *Building and Environment* 38(5): 645-654.

List of symbols and abbreviations

Abbreviations

ASR	Alkali-Silica-Reaction
BET	Brunauer-Emmett-Teller
CFD	Computational Fluid Dynamics
CLC	Cement based Lightweight Composite
CV	Control Volume
DSC	Differential Scanning Calorimetry
EDX	Energy-dispersive X-ray spectroscopy
FGD	Flue Gas Desulfurization
GCI	Grid Convergence Index
IAQ	Indoor Air Quality
L-H	Langmuir-Hinshelwood
LLS	Laser light scattering
LSM	Least Squares Method
LWA	Light Weight Aggregates
LWAC	Lightweight Aggregates Concrete
OPC	Ordinary Portland Cement
PCO	Photocatalytic Oxidation
PCE	Polycarboxylates
PSD	Particle Size Distribution
RH	Relative Humidity
RSS	Sum of the Squares of the Residuals
SCC	Self-compacting Concrete
SCLC	Self-compacting Cement-based Lightweight Composite
SEM	Scanning Electron Microscope
SGLC	Self-compacting Gypsum-based Lightweight Composite
SBS	Sick Building Syndrome
SP	Superplasticizer
SSA	Specific Surface Area
TGA	Thermal Gravimetric Analysis
UDF	User Defined Function
VCLC	Vibrated Cement-based Lightweight Composite
VIS	Visible Light
VOC	Volatile Organic Compounds
VP	Volumetric Proportion
XRF	X-ray Fluorescence
XRD	X-ray Diffraction

Symbols

Roman

a	Specific surface area, mass based	[cm^{2} g^{-1}]
A	Area	[mm^{2}]
a_0	Parameter	
a_v	The active surface area per unit of reactor volume	[dm^{-1}]
b_0	Parameter	
C	Concentration	[mg m^{-3}]
c	Mass of the cement	[g]
c_0	Initial mass of the cement	[g]
$C_{T,p}$	Temperature related specific heat capacity	[J (kg °C)$^{-1}$]
C_{TiO_2}	Superficial concentration in valance band	[mol dm^{-2}]
$C_{TiO_2'}$	Superficial concentration in conduction band	[mol dm^{-2}]
D	Particle size	[µm]
D_h	Hydraulic diameter	[dm]
d	Diameter	[mm]
d_0	The base diameter of the Hägermann cone	[mm]
D_{TiO_2}	Dosage of the photocatalyst	[g g^{-1}]
$D_{i,m}$	Diffusion coefficient of species i in mixture m	
e^-	Electron	
E	Irradiance on the surface of photocatalyst	[W m^{-2}]
E	The deformation coefficient	
f	Empirical constant	
F_{rupt}	Breaking load	[N]
F_c	Maximum load at fracture	[N]
$\vec{F}$	External body force	
$\vec{g}$	Gravity body force	
H	Height	[mm]
h	Mass of the hemihydrate	[g]
h_0	Initial mass of the unreacted hemihydrate	[g]
h^+	Electron hole	
i_{heat}	Heat transfer indicator	
J_i	Diffusion flux of species i	
k^*	A group of parameters of k and C_{TiO_2}	[min^{-1}]
k'	A group of parameters of k and K	[dm^{5} mol^{-2} min^{-1}]
k	Reaction rate constant	[mg m^{-3}s^{-1}]
K	Adsorption constant	[m^{3} mg^{-1}]
L	Length of the reactor	[mm]
L_0	The distance between the supports of the bending machine	[mm]
m	Mass	[g]
M_i	Molecular weight of species i	
m_s	Surface dried mass of water-saturated sample in air	[g]

m_w	Mass of water-saturated sample in water	[g]
m_d	Mass of oven dried sample	[g]
n	Hydration degree	
p	Pressure	
q	Distribution modulus	
Q_h	Internal heat generation rate	[W m^{-3}]
Q	Volumetric flow rate	[L min^{-1}]
R	Water demand determined by the sprinkling method	
r	Reaction rate	[mg m^{-3} s^{-1}]
Re	Reynolds number	
RH	Relative humidity	
s	Saturation rate pore volume water	
$\vec{s}$	Stress tensor	
S_g	Specific surface area	[dm^2 g^{-1}]
S_m	Mass source term	
t	Time	[min]
th	Thickness of the photocatalyst layer	[dm]
u_o	Initial linear velocity	
$u_{i,fine}$	Velocity at point i in fine grid	
$u_{i,coarse}$	Velocity at point i in coarse grid	
v_{air}	Linear velocity	[m s^{-1}]
$\vec{v}$	Velocity vector	
V	Volume	
W	Width	[mm]
w	Mass of the water	[g]
w_0	Initial mass of the water	[g]
x	Mass fraction	
Y_i	Mass fraction of species I	
Z	Grid convergence index equation constant	

Greek

α	Activities of the free ions	
α_0	Degree of carbonation of monosulfate phase	
α	Parameter, irradiance related	[mol W^{-1} min^{-1}]
β	A group of parameters of γ and sites	[mol dm^2 min^{-1}]
β_{hh}	The water/hemihydrate percentage (vol. %) for $\Gamma_h = 0$	
Γ_{hh}	The relative slump of the gypsum slurry	
κ	Radiation absorption coefficient of the photocatalyst	[cm^{-1}]
γ	A group of parameters of k_{h+}, k^*_{e-}, and k_{dea}	[min^{-1}]
λ	Thermal conductivity	[W (m K)$^{-1}$]
λ	Wavelength of the applied light source	[nm]
λ	Second viscosity	[m^2 s^{-1}]
ρ	Density	[g cm^{-3}]
γ	The super saturation of gypsum	
φ	Volume fraction	

Φ	Primary quantum yield	[mol W^{-1} min^{-1}]
μ	Kinematic viscosity	[N s m^{-2}]
σ	Strength	[N mm^{-2}]
δ	Water layer thickness	[cm]
ξ	Shape factor	
ε_{RMS}	Root mean square error	
$\varepsilon_{i,u}$	Error at point i measuring variable u	
ω	Specific molar volume	[cm^3 mol^{-1}]
ν	Specific volume	[cm^3 g^{-1}]

Subscript

act	Activation
ads	Adsorption
air	Air
ah	Anhydrite
Blaine	Measured according to Blaine method
c	Compressive
CLC	CLC
C_3S	C_3S
C_2S	C_2S
C_3A	C_3A
C_4AF	C_4AF
CS	CS
con	Conversion
d	Compressed water
dea	Deactivation
dh	Dihydrate
e	Effective
e^-	Electron
exp	Experimental
fluid	Fluid, can be water or air
f	Flexural
GAS	Gas
hh	Hemihydrate
h^+	Electron hole
H_2O	Water
HNO_2	HNO_2
i	Fraction size
in	initial concentration
lwa	Lightweight aggregates
λ	Wavelength of the applied light source
max	Maximum
min	Minim
model	Model
n	Nonevaporable

NO	Nitric oxide
NO_2	Nitrogen dioxide
NO_x	Nitric oxide and Nitrogen dioxide
OH·	Hydroxyl radicals
out	Outlet concentration
paste	Cement paste
reactor	Reactor
s	Shrinkage
s	Solid
SGLC	SGLC
solid	Solid
sphere	Sphere
w	Capillary water
v	Void fraction

Appendix A

Measurement of the free moisture content in the used LWA

Sample	**Test1**				**Test2**				
	Sample holder (g)	**Sample holder & sample* (g)**	**Sample holder & sample **(g)**	**Mass loss (%)**	**Sample holder (g)**	**Sample holder & sample * (g)**	**Sample holder & sample ** (g)**	**Mass loss (%)**	**Mean mass loss (%)**
LWA0.1-0.3	105.900	169.50	169.45	0.08	176.50	233.20	233.12	0.14	0.11
LWA0.25-0.5	105.96	149.48	149.40	0.19	119.15	199.29	199.16	0.16	0.18
LWA0.5-1.0	118.86	181.52	181.47	0.08	118.22	185.90	185.85	0.08	0.08
LWA1.0-2.0	120.57	160.58	160.54	0.09	176.56	202.87	202.84	0.10	0.10
LWA2.0-4.0	115.70	151.76	151.72	0.12	121.56	162.21	162.16	0.12	0.12

*** before drying, ** after drying.**

Appendix B

Rheology measurement methods

The sprinkling method (EN 13279-2: 2004)

The sprinkling method is developed to determine the water demand of gypsum binders (EN 13279-2, 2004). The principle of this test is to measure the mass of a powder which can be saturated when it is sprinkled into water with a fixed amount. Puntke (2002) developed a similar test method to determine the water demand for self-compacting concrete using also the saturation theory, applying a different procedure which will be briefly discussed below.

To perform the sprinkling test, a cylindrical glass container with 66 mm internal diameter and 66 mm height and with markings at a height of 16 mm and 32 mm above the inner surface of the base is needed, together with a chronometer and a balance with an accuracy of ± 0.1g. A fixed amount of water (here 100 g) is poured into the glass container, while taking care not to wet the upper part of the cylindrical wall, and the mass (m_0) is measured to ± 0.5g.

The total time for the following procedure is 120 ± 5 s. First, the powder is evenly sprinkled over the surface of the water in such a way that after 30 s the paste has reached the first marking and has reached the second marking after 60 s. The sprinkling procedure is continued until the paste has reached approximately 2 mm below the surface of the water after (90 ± 10) s. During the following 20 s to 40 s, sufficient binder is sprinkled onto the surface of the water and the rim of the glass container that the water surface disappears. Any small dry islands of binder, which appear during the operation, should be saturated at the end of 3 s to 15 s. In the case of binder which tends to settle slowly, the level marks may not be reached within the required time. In this case, the binder shall be sprinkled so that it falls only onto those areas of the water, which are free from binder and not onto binder which has already been sprinkled. The sprinkling time is to be stated. Remove the surplus powder from the rim of the glass container before weighing and measure the mass (m_1) to ± 0.5 g.

The water demand then is calculated based on the water/powder ratio by mass:

$$R = \frac{100}{m_1 - m_0} \tag{AB.1}$$

where m_0 is the mass addition of the glass container and water (g), and m_1 is the mass addition of the glass container, water and powder (g).

The Puntke test is carried out differently from the way described above. The difference is in that the cylindrical container is firstly filled with investigated powder (also with a fixed amount), and then water is sprinkled onto the powder until saturation is reached, while in the meantime mixing the materials. More detailed information is presented in Hunger (2010).

The penetration method

The setting time of concrete, mortar, or paste can also be used as an indication of workability (Ferraris, 1999). Among different available methods, the Vicat cone method is commonly used for testing cement paste, as well as gypsum paste (ASTM C191, EN 196-3, and EN 13279-2); and knife method is widely used for gypsum binders (EN 13279-2, 2004).

The principle of the Vicat cone method is to determine the depth of penetration of the conical penetrator into a plaster paste as its setting progresses, while the knife method is suitable to monitor the time after which the edges of a cut made with a knife through the plaster paste cease to flow together. This is also dependent on the stiffness of the prepared paste, which is related to the initial water content.

A Vicat apparatus (including conical penetrator, glass plate, Vicat ring and straight edge) is used. A mixed plaster is transferred to the Vicat ring, which is placed on the glass plate with the larger opening in contact with it. The mixing procedure is given in next section. The time at which the powder contacts water is set as the zero time. The excess material is removed using a ruler. The guide bar is opened for testing using the release mechanism. The time between the penetration measurements should not be greater than 1/20 of the initial setting time. The cone shall be cleaned and dried between each penetration and there should be at least 12 mm between each penetration mark. The time at which the depth of penetration achieves (22 ± 2) mm above the glass plate is the initial setting time.

For the knife method, the prepared gypsum paste should be poured on to a glass plate, with constant stirring, to form 3 pates about 100 mm to 120 mm in diameter and about 5 mm thick. Then the initial setting time can be determined by making cuts in the pat. The knife shall be cleaned and dried after each cut. Cuts should be made at intervals not greater than 1/20 of expected setting time. The initial setting time is then the time when the cut cease to flow together.

The mini-slump flow test / flow table method

The mini-slump flow test, originally developed by Kantro (1980), is widely used to measure the consistency of cement paste. It is also recommended as a standard method for the determination of the powder water demand for the self-compacting concrete design (EFNARC, 2002). The mini-slump flow test is also referred to the flow table method (EN 13279-2, 2004), which is specified to determine water content.

The spread flow tests are carried out first by filling the test sample into a cone (a Hägermann cone is used in the present study), whereas the cone is placed in the center of a dry, clean, horizontal and non sucking working surface (a glass plate is used here). After filling, the hopper is removed and surplus paste is wiped off to ensure an equal volume of material every time. After 10 s to 15s the cone is lifted vertically to allow a free flow of the sample on the surface of the glass plate (EN 13279-2, 2004). Then the diameters of the resulting pat shall be measured to 1 mm in two directions at right angles to each other.

Appendix C

Specifications of the standards regarding air quality assessment

ISO 22197-1: 2007

This standard sets NO as the model pollutant, specifies the test apparatus, the specification of the test conditions as listed in Table 7.3, the test procedure, as well as the results calculation

$$n_{NO} = (f/22.4)\int(\phi_{NO,in} - \phi_{NO,out})dt \qquad \text{(AC.1)}$$

$$n_{NO_2} = (f/22.4)\int\phi_{NO_2,out}dt \qquad \text{(AC.2)}$$

where n_{NO} is the amount of NO removed by the test sample (μmol); n_{NO2} is the amount of NO formed by the test sample (μmol); f is th air flow rate converted into that at the standard state (0 °C, 101.3 kPa, and dry gas basis) (L min^{-1}); $\varphi_{NO,in}$, $\varphi_{NO,out}$, $\varphi_{NO2,out}$ are the inlet NO volume fraction (μL L^{-1}), the outlet NO volume fraction (μL L^{-1}), and outlet NO_2 volume fraction (μL L^{-1}), respectively. The integrations are taken over the time (min) for which the sample is illuminated.

UNI 11247: 2007

This standard sets a combination of NO and NO_2 as target pollutants. As well it specifies the test apparatus, and the test conditions as also given in Table 7.3. The test results are computed according to

$$A_F = \frac{(C_B - C_L)}{C_B} \times \frac{F}{S} \times I \qquad \text{(AC.3)}$$

where C_B and C_L are the NO_x (NO and NO_2) concentrations at the outlet of the reactor under dark and under photo-irradiation conditions, respectively (μg m^{-3}); F is the gas flow (m^3 h^{-1}); S is the geometrical surface area of the test sample under investigation (m^2); I is the non-dimensional intensity of the luminous flux obtained by comparing the measured intensity I'(W m^{-2}) and 1000 (W m^{-2}) (I = 1000/I'), which corresponds to about 100000 Lux, i.e. the average value that the solar light reaches at noon on an average July day.

ISO 22197-2: 2011

This standard sets acetaldehyde as model pollutant. The test apparatus as well the sample preparation for the test is the same as ISO 22197-1: 2007. The test conditions specification is listed in Table 7.3. The results are calculated from

$$R_A = \frac{(\phi_{A,in} - \phi_{A,out})}{\phi_{A,in}} \times 100 \tag{AC.4}$$

where $\phi_{A,in}$ and $\phi_{A,out}$ are the inlet and out let volume fraction of acetaldehyde (μL L^{-1}), respectively.

$$R_{CO_2} = \frac{\phi_{CO_2} \times 100}{2 \times \phi_{A,in}} \tag{AC.5}$$

where R_{CO2} is the conversion from acetaldehyde to CO_2 (%), ϕ_{CO2} is the CO_2 volume fraction generated during the PCO process (μL L^{-1}).

ISO 22197-3: 2011

This standard sets toluene as model pollutant. The test apparatus as well as the sample preparation for the test is the same as ISO 22197-1: 2007. The test conditions specification is listed in Table 8.3. The results are calculated from

$$R_T = \frac{(\phi_{T,in} - \phi_{T,out})}{\phi_{T,in}} \times 100 \tag{AC.6}$$

where $\phi_{T,in}$ and $\phi_{T,out}$ are the inlet and outlet volume fraction of toluene (μL L^{-1}), respectively.

Appendix D

User-Defined Source of the Rate of Source of Chemical Species

```
/*********************************************************************
Total species source/sink
*********************************************************************/

#include "udf.h"

#define MWNO 0.030 /* all molecular weights in (kg mol-1)*/
#define MWNO2 0.046
#define MWH2O 0.018

#define kNO 5.35e-13  /* all k's in (m2 mol-1 s-1)*/
#define kNO2 1.98e-11
#define KNO 2.09e1    /* all K's in (m3 mol-1)*/
#define KNO2 5.38
#define KH2O 2.39e-3
#define ALPHA 7.20e-4/* constant (mol W-1 s-1)*/
#define BETA 1.03e-7 /* constant (mol m-2 s-1)*/

#define E 10 /*irradiance W m-2*/
#define DTiO2 0.5 /*Photocatalyst content (g g-1) 0.5 standard*/
#define H 0.003 /*height of the reactor is 0.003 m*/

DEFINE_SOURCE(rtotal, c, t, dS, eqn)
{
 real source;
 real term1;
 real term2;
 real term3;
 real term4;
 real termi;
 real termii;
 real termiii;
 real termiv;
 real av;

 real no  = C_YI(c,t,0);   /* mass fraction of NO at the wall */
 real no2 = C_YI(c,t,1);
 real h2o = C_YI(c,t,2);  /* mass fraction of H2O at the wall */
```

```
 real rho = C_R(c,t);

 no  *= rho/MWNO;  /* converting to molar concentrations (mol m-3) */
 no2 *= rho/MWNO2;
 h2o *= rho/MWH2O;

 term1 = -kNO*BETA*KNO*no*KH2O*h2o;
 term2 = sqrt(1 + 4*ALPHA*E*(1 + KNO*no + KNO2*no2 +
KH2O*h2o)/(BETA*KH2O*h2o)) - 1;
 term3 = 4*kNO*KNO*no + 2*kNO2*KNO2*no2;
 term4 = 1 + KNO*no + KNO2*no2 + KH2O*h2o;
 av = DTiO2/H;

 termi = (kNO*KNO*no - kNO2*KNO2*no2)*KH2O*h2o*BETA;
 termii = sqrt(1 + 4*ALPHA*E*(1 + KNO*no + KNO2*no2 +
KH2O*h2o)/(BETA*KH2O*h2o)) - 1;
 termiii = 4*kNO*KNO*no + 2*kNO2*KNO2*no2;
 termiv = 1 + KNO*no + KNO2*no2 + KH2O*h2o;

 source = av*MWNO2*(termi*termii)/(termiii*termiv) +
av*MWNO*(term1*term2)/(term3*term4);
 dS[eqn]=0;

 return source;
}

DEFINE_SOURCE(rNO, c, t, dS, eqn)
{
 real source;
 real term1;
 real term2;
 real term3;
 real term4;
 real av;

 real no  = C_YI(c,t,0);   /* mass fraction of NO at the wall */
 real no2 = C_YI(c,t,1);
 real h2o = C_YI(c,t,2);  /* mass fraction of H2O at the wall */

 real rho = C_R(c,t);

 no  *= rho/MWNO;  /* converting to molar concentrations (mol m-3) */
 no2 *= rho/MWNO2;
 h2o *= rho/MWH2O;

 term1 = -kNO*BETA*KNO*no*KH2O*h2o;
```

```
 term2 = sqrt(1 + 4*ALPHA*E*(1 + KNO*no + KNO2*no2 +
KH2O*h2o)/(BETA*KH2O*h2o)) - 1;
 term3 = 4*kNO*KNO*no + 2*kNO2*KNO2*no2;
 term4 = 1 + KNO*no + KNO2*no2 + KH2O*h2o;
 av = DTiO2/H;

 source = av*MWNO*(term1*term2)/(term3*term4);
 dS[eqn]=0;

 return source;
}

DEFINE_SOURCE(rNO2, c, t, dS, eqn)
{
 real source;
 real term1;
 real term2;
 real term3;
 real term4;
 real av;

 real no  = C_YI(c,t,0);   /* mass fraction of NO at the wall */
 real no2 = C_YI(c,t,1);
 real h2o = C_YI(c,t,2);  /* mass fraction of H2O at the wall */

 real rho = C_R(c,t);

 no  *= rho/MWNO;  /* converting to molar concentrations (mol m-3) */
 no2 *= rho/MWNO2;
 h2o *= rho/MWH2O;

 term1 = (kNO*KNO*no - kNO2*KNO2*no2)*KH2O*h2o*BETA;
 term2 = sqrt(1 + 4*ALPHA*E*(1 + KNO*no + KNO2*no2 +
KH2O*h2o)/(BETA*KH2O*h2o)) - 1;
 term3 = 4*kNO*KNO*no + 2*kNO2*KNO2*no2;
 term4 = 1 + KNO*no + KNO2*no2 + KH2O*h2o;
 av = DTiO2/H;

 source = av*MWNO2*(term1*term2)/(term3*term4);
 dS[eqn]=0;

 return source;
}
```

Summary

Design of environmentally friendly calcium sulfate-based building materials - Towards an improved indoor air quality

This thesis addresses the performance based design and development of an environmentally friendly calcium sulfate-based indoor building product towards an improved indoor air quality. Here “environmental friendly” is referred to the environment related subjects including: (1) the selection of raw materials to decrease the environmental impact caused by their production process; (2) an enhanced thermal comfort resulted from the newly developed composite; (3) the removal function of air pollutants resulted from the newly developed product.

Fundamental research on the used materials (calcium sulfate system) is carried out before applying them into the new development in order to gain a deeper understanding of their properties. The water demand of the used $CaSO_4{\cdot}0.5H_2O$ is determined by the mini-slump flow test. The hydration process of the $CaSO_4{\cdot}H_2O$ system is studied by the ultrasonic wave velocity method. The thermo physical properties of the $CaSO_4{\cdot}H_2O$ system are investigated by both experiments and modeling in different conditions (for instance at room temperature and elevated temperatures).

Based on the gained knowledge about the materials, a novel calcium sulfate-based lightweight composite is designed applying a mix design concept which was originally developed for concrete design. Lightweight aggregates are used in the mix in order to obtain low density and low thermal conductivity. Multiple experiments are performed to investigate the newly developed composite, including: fresh state behavior, mechanical properties, physical properties, thermal properties and fire behavior. Is it wise to use calcium sulfate as binder? This thesis tries to answer this question by not only investigating the developed calcium sulfate-based composites, but also through a thorough comparative study with cement-based composites developed in the present study. Indoor thermal comfort is related to the indoor temperature which is strongly affected by the heat transfer between indoor and outdoor environment. This is addressed by the low thermal conductivity achieved from the newly developed composite.

Indoor air pollutants are one of the most influential factors affecting the indoor air quality. This is addressed in the development of the new product by applying heterogeneous photocatalytic oxidation technology to remove indoor air pollutants. A modified TiO_2 is applied here as the photocatalyst for the indoor photocatalytic oxidation (PCO). Experimental results proved the positive effect on the indoor air quality by PCO. A kinetic reaction rate model is built to further understand the PCO working principle and computational fluid dynamics is employed to model the used PCO reactor, enabling the application of this technology to other geometries and flow conditions.

List of publications

Publications based on this PhD project are listed below:

Journals

1. Yu, Q.L., Cubillos Sanabria, H.A., and Brouwers. H.J.H. (2012). NO and NO_2 degradation applying a novel photocatalytic wall covering under indoor air conditions - part 1: an experimental investigation. To be submitted to *Building and Environment.*
2. Yu, Q.L., Cubillos Sanabria, H.A., Loomans, M.G.L.C., and Brouwers. H.J.H. (2012). NO and NO_2 degradation applying a novel photocatalytic wall covering under indoor air conditions - part 2: a CFD modeling approach. To be submitted to *Building and Environment.*
3. Yu, Q.L., Spiesz, P., and Brouwers, H.J.H. (2012). Development of cement-based lightweight composites - Part 1: Mix design methodology and hardened properties. Submitted to *Cement & Concrete Composites*.
4. Spiesz, P., Yu, Q.L., and Brouwers, H.J.H. (2012). Development of cement-based lightweight composites - Part 2: Durability related properties. Submitted to *Cement & Concrete Composites*.
5. Yu, Q.L., and Brouwers, H.J.H. (2011). The development of self-compacting gypsum based lightweight composite: A theoretical and experimental investigation. Submitted to *Cement & concrete composites*.
6. Yu, Q.L., and Brouwers, H.J.H. (2011). Thermal properties and microstructure of gypsum board and its dehydration products: a theoretical and experimental investigation. *Fire and Materials*, in press, DOI: 10.1002/fam.1117.
7. Yu, Q.L., Ballari, M.M., Brouwers H.J.H. Heterogeneous Photocatalysis Applied to Indoor Building Material: Towards an Improved Indoor Air Quality. *Advanced Materials Research* 255-260: 2836-2840.
8. Yu, Q.L., and Brouwers, H.J.H. Microstructure and mechanical properties of β-hemihydrate produced gypsum: An insight from its hydration process. *Construction and Building Materials* 25(7): 3149-3157.
9. Ballari, M.M., Yu, Q.L., and Brouwers, H.J.H. (2011). Experimental study of the NO and NO_2 degradation by photocatalytically active concrete. *Catalysis Today* 161: 175-180.
10. Yu, Q.L., Ballari, M.M., and Brouwers H.J.H. (2010). Indoor air purification using heterogeneous photocatalytic oxidation, Part 2: Kinetic study. *Applied Catalysis B: Environmental* 99: 58-65.
11. Yu, Q.L., and Brouwers, H.J.H. (2009). Indoor air purification using heterogeneous photocatalytic oxidation, Part 1: Experimental study. *Applied Catalysis B: Environmental* 92: 454-461.

Professional publications

12. Yu, Q.L., and Brouwers, H.J.H. (2012). Recent research developments in calcium sulfate based building materials, part 1. *International Analytical Review "Alitinfoum"* 1(23): 94-105.
13. Yu, Q.L., and Brouwers, H.J.H. (2012). Recent research developments in calcium sulfate based building materials, part 2. *International Analytical Review "Alitinfoum"* 2(24): 1-12.

Conference proceedings

14. Yu, Q.L., Spiesz, P., and Brouwers, H.J.H. (2012). Development of a lightweight cement based composite: an experimental investigation on its strength and thermal properties. Accepted by *18th Ibausil International Conference on Building Materials*, September 2012, Weimar, Germany.
15. Yu, Q.L., Cubillos Sanabria, H.A., Loomans, M.G.L.C., and Brouwers. H.J.H. (2012). Indoor air quality improvement applying photocatalytic oxidation: a computational fluid dynamics modeling approach, accepted by *7th European Meeting on Solar Chemistry and Photocatalysis: Environmental Applications (SPEA7)*, June 2012, Porto, Portugal.
16. Lorenčik, Š., Yu, Q.L., and Brouwers. H.J.H. (2012). Indoor air quality improvement by novel wall covering applying photocatalysis. Accepted by *7th European Meeting on Solar Chemistry and Photocatalysis: Environmental Applications (SPEA7)*, June 2012, Porto, Portugal.
17. Ballari, M.M., Carballada, J., Yu, Q.L., Brouwers, H.J.H., Alfano, O.M., and Cassano, A.E. (2012). Visible light TiO_2 photocatalysts assessment for the indoor air decontamination. Accepted by *7th European Meeting on Solar Chemistry and Photocatalysis: Environmental Applications (SPEA7)*, June 2012, Porto, Portugal.
18. Lorencik, S., Yu, Q.L., and Brouwers, H.J.H. (2012). Indoor air purification using functional wall covering. Accepted by *18th Ibausil International Conference on Building Materials*, September 2012, Weimar, Germany.
19. Cubillos Sanabria, H.A., Yu, Q.L., and Brouwers, H.J.H. (2012). Photocatalytic oxidation of NO_x under indoor conditions using a functional wall covering. Accepted by *18th Ibausil International Conference on Building Materials*, September 2012, Weimar, Germany.
20. Yu, Q.L., Ballari, M.M., and Brouwers, H.J.H. (2011). Heterogeneous photocatalysis applied to indoor building material: towards an improved indoor air quality. *2011 International Conference on Civil Engineering and Building Materials (2011 CEBM)*, Kunming, China, 2011.
21. Yu, Q.L., and Brouwers, H.J.H. (2011). Self-compacting gypsum based light weight composite: theoretical and experimental study. *Proceedings of Weimar Gypsum International Conference*, Weimar, Germany, 2011.
22. Yu, Q.L., and Brouwers, H.J.H. (2011). Gypsum: an investigation of microstructure and mechanical properties, *Proceedings 8th fib International PhD Symposium in Civil Engineering*, 20-23 June 2010, Lyngby, 341-346, Eds. G. Fischer, M. Geiker, O. Hededal, L. Ottoson and H. Stang, DTU Byg, Lyngby, Denmark, 2010.

23. Yu, Q.L., Ballari, M.M., and Brouwers, H.J.H. (2010). Kinetic study of indoor air purification using heterogeneous photocatalytic oxidation. In J Krysa (Ed.), *Proceedings of the 6th European Meeting on Solar Chemistry & Photocatalysis: Environmental Applications*. Prague, Czech Republic, 2010. 245-246.
24. Yu, Q.L., Brouwers, H.J.H., and Korte, A.C.J. de (2009). Gypsum hydration: a theoretical and experimental study, *Proceedings 17th Ibausil, International Conference on Building Materials (internationale Baustofftagung)*, Weimar, 1-0783-1-0418, Eds. H.B. Fischer and K.A. Bode, F.A. Finger-Institut für Baustoffkunde, Weimar, Germany, 2009.
25. Yu, Q.L., Brouwers, H.J.H., and Ballari, M.M. (2009). Experimental study and modeling of the photocatalytic oxidation of NO in indoor conditions, *Proceedings of Nanotechnology in Construction 3 (NICOM3)*, 389-394, Eds. Z. Bittnar, P.J.M. Bartos, J. Nemecek, V. Šmilauer and J. Zeman, Springer, Berlin-Heidelberg, Germany, Prague, Czech Republic, 2009.

Curriculum Vitae

Qingliang Yu was born on 23rd May, 1980 in Henan, China. After finishing high school education in 1999 at Henan Huaiyang High school in Henan, China, he started to study at Wuhan University of Technology (WHUT) in Wuhan, China. In June 2003 he graduated and received his bachelor degree in Civil Engineering with the title of "Best Graduate". He continued his graduate study at WHUT and received his Master of Science degree in Structural Engineering in June 2006, and his research topic was prestressed high performance concrete structures. Afterwards, he worked at the same university as a researcher and his research interest was structural analysis & computation, and high-rise or long-span structure health monitoring. From January 2008 he started a PhD project under the supervision of prof.dr.ir. H.J.H. Brouwers. He firstly worked at University of Twente in Enschede, the Netherlands, and in September 2009 he moved with his supervisor to Eindhoven University of Technology in Eindhoven, the Netherlands, of which the results are presented in this dissertation. In 2010, he was awarded the title "Excellent PhD students working abroad" by the Chinese government for his PhD research achievements. His research interests include the development of sustainable building materials with advanced functionality, such as air purification property, thermal and fire properties etc. In addition, he has great interest in computational fluid dynamics.

During his spare time, he likes doing many kinds of sports such as squash, tennis and football. He also enjoys travelling together with his family and friends.

BOUWSTENEN is een publikatiereeks van de Faculteit Bouwkunde, Technische Universiteit Eindhoven. Zij presenteert resultaten van onderzoek en andere aktiviteiten op het vakgebied der Bouwkunde, uitgevoerd in het kader van deze Faculteit.

BOUWSTENEN zijn telefonisch te bestellen op nummer
040 - 2472383

Kernredaktie
MTOZ

Reeds verschenen in de serie
BOUWSTENEN

nr 1
Elan, a computermodel for building energy design, theory and validation
M.H. de Wit
H.H. Driessen
R.M.M. van der Velden

nr 2
Kwaliteit, keuzevrijheid en kosten
Evaluatie van experiment Klarendal, Arnhem
drs J. Smeets
C. le Nobel, arch. HBO
M. Broos, J. Frenken, A. v.d. Sanden

nr 3
Crooswijk
van 'bijzonder' naar 'gewoon'
drs V. Smit
ir K. Noort

nr 4
Staal in de woningbouw
ir E.J.F. Delsing

nr 5
Mathematical theory of stressed skin action in profiled sheeting with various edge conditions
ir A.W.A.M.J. v.d. Bogaard

nr 6
Hoe berekenbaar en betrouwbaar is de coëfficiënt k in $\underline{x}$ - ko en $\underline{x}$ - ks?
ir K.B. Lub
drs A.J. Bosch

nr 7
Het typologisch gereedschap
Een verkennende studie omtrent typologie en omtrent de aanpak typologisch onderzoek
J.H. Luiten arch. HBO

nr 8
Informatievoorziening en beheerprocessen
ir A. Nauta / drs J. Smeets (red.)
Prof. H. Fassbinder (projectleider)
ir A. Proveniers,
drs J.v.d. Moosdijk

nr.9
Strukturering en verwerking van tijdgegevens voor de uitvoering van bouwwerken
ir W.F. Schaefer
ir P.A. Erkelens

nr 10
Stedebouw en de vorming van een speciale wetenschap
K. Doevendans

nr 11
Informatica en ondersteuning
van ruimtelijke besluitvorming
dr G.G. van der Meulen

nr 12
Staal in de woningbouw,
korrosie-bescherming van de begane grondvloer
ir E.J.F. Delsing

nr 13
Een thermisch model voor de berekening van staalplaatbeton-vloeren onder brandomstandigheden
ir A.F. Hamerlinck

nr 14
De wijkgedachte in Nederland
Gemeenschapsstreven in een stedebouwkundige context
dr ir K. Doevendans
dr R. Stolzenburg

nr 15
Diaphragm effect of trapezoidally profiled steel sheets.
Experimental research into the influence of force application
ir A.W.A.M.W. v.d. Bogaard

nr 16
Versterken met spuit-ferrocement.
Het mechanische gedrag van met spuit-ferrocement versterkte gewapende betonbalken
ir K.B. Lub
ir M.C.G. van Wanroy

nr 17
De tractaten van Jean Nicolas Louis Durand
ir G. van Zeyl

nr 18
Wonen onder een plat dak.
Drie opstellen over enkele vooronder-stellingen van de stedebouw
dr ir K. Doevendans

nr 19
Supporting decision making processes
A graphical and interactive analysis of multivariate data
drs W. Adams

nr 20
Self-help building productivity
A method for improving house building by low-income groups applied to Kenya 1990-2000
ir P. A. Erkelens

nr 21
De verdeling van woningen:
een kwestie van onderhandelen
drs V. Smit

nr 22
Flexibiliteit en kosten in het ontwerpproces Een besluitvormingondersteunend model
ir M. Prins

nr 23
Spontane nederzettingen begeleid
Voorwaarden en criteria in Sri Lanka
ir P.H. Thung

nr 24
Fundamentals of the design of bamboo structures
O. Arce-Villalobos

nr 25
Concepten van de bouwkunde
Prof. dr ir M.F.Th. Bax (red.)
dr ir H.M.G.J. Trum (red.)

nr 26
Meaning of the site
Xiaodong Li

nr 27
Het woonmilieu op begrip gebracht
Jaap Ketelaar

nr 28
Urban environment in developing countries
editors: dr ir Peter A. Erkelens
dr George G. van der Meulen

nr 29
Stategische plannen voor de stad
Onderzoek en planning in drie steden
Prof. dr H. Fassbinder (red.)
ir H. Rikhof (red.)

nr 30
Stedebouwkunde en stadsbestuur
ir Piet Beekman

nr 31
De architectuur van Djenné
Een onderzoek naar de historische stad
P.C.M. Maas

nr 32
Conjoint experiments and retail planning
Harmen Oppewal

nr 33
Strukturformen Indonesischer Bautechnik Entwicklung methodischer Grundlagen für eine 'konstruktive pattern language' in Indonesien
Heinz Frick

nr 34
Styles of architectural designing
Empirical research on working styles and personality dispositions
Anton P.M. van Bakel

nr 35
Conjoint choice models for urban tourism planning and marketing
Benedict Dellaert

nr 36
Stedelijke Planvorming als co-produktie
Prof. dr H. Fassbinder (red.)

nr 37
Design Research in the Netherlands
editors: Prof. dr R.M.Oxman,
Prof. dr ir. M.F.Th. Bax,
Ir H.H. Achten

nr 38
Communication in the Building Industry
Bauke de Vries

nr 39
Optimaal dimensioneren van gelaste plaatliggers

nr 40
Huisvesting en overwinning van armoede
dr.ir. P.H. Thung en dr.ir. P. Beekman (red.)

nr 41
Urban Habitat: The environment of tomorrow
George G. van der Meulen,
Peter A. Erkelens

nr 42
A typology of joints
John C.M. Olie

nr 43
Modeling constraints-based choices for leisure mobility planning
Marcus P. Stemerding

nr 44
Activity-based travel demand modeling
D. Ettema

nr 45
Wind-induced pressure fluctuations on building facades
Chris Geurts

nr 46
Generic Representations
Henri Achten

nr 47
Johann Santini Aichel
Dirk De Meyer

nr 48
Concrete behaviour in multiaxial compression
Erik van Geel

nr 49
Modelling site selection
Frank Witlox

nr 50
Ecolemma model
Ferdinand Beetstra

nr 51
Conjoint approaches to developing activity-based models
Donggen Wang

nr 52
On the effectiveness of ventilation
Ad Roos

nr 53
Conjoint modeling approaches for residential group preverences
Eric Molin

nr 54
Modelling architectural design information by features
Jos van Leeuwen

nr 55
A spatial decision support system for the planning of retail and service facilities
Theo Arentze

nr 56
Integrated lighting system assistant
Ellie de Groot

nr 57
Ontwerpend leren, leren ontwerpen
dr.ir. J.T. Boekholt

nr 58
Temporal aspects of theme park choice behavoir
Astrid Kemperman

nr 59
Ontwerp van een geïndustrialiseerde funderingswijze
Faas Moonen

nr 60
Merlin: A decision support system for outdoor leisure planning
Manon van Middelkoop

nr 61
The aura of modernity
Jos Bosman

nr 62
Urban Form and Activity-Travel Patterns
Daniëlle Snellen

nr 63
Design Research in the Netherlands 2000
Henri Achten

nr 64
Computer Aided Dimensional Control in Building Construction
Rui Wu

nr 65
Beyond Sustainable Building
editors: Peter A. Erkelens
Sander de Jonge
August A.M. van Vliet
co-editor: Ruth J.G. Verhagen

nr 66
Das globalrecyclingfähige Haus
Hans Löfflad

nr 67
Cool Schools For Hot Suburbs
René J. Dierkx

nr 68
A Bamboo Building Design Decision Support Tool
Fitri Mardjono

nr 69
Driving rain on building envelopes
Fabien van Mook

nr 70
Heating Monumental Churches
Henk Schellen

nr 71
Van Woningverhuurder naar Aanbieder van Woongenot
Patrick Dogge

nr 72
Moisture transfer properties of coated gypsum
Emile Goossens

nr 73
Plybamboo Wall-panels for Housing
Guillermo E. González-Beltrán

nr 74
The Future Site-Proceedings
Ger Maas
Frans van Gassel

nr 75
Radon transport in Autoclaved Aerated Concrete
Michel van der Pal

nr 76
The Reliability and Validity of Interactive Virtual Reality Computer Experiments
Amy Tan

nr 77
Measuring Housing Preferences Using Virtual Reality And Belief Networks
Maciej A. Orzechowski

nr 78
Computational Representations of Words and Associations in Architectural Design
Nicole Segers

nr 79
Measuring and Predicting Adaptationin Multidimensional Activity-Travel Patterns
Chang-Hyeon Joh

nr 80
Strategic Briefing
Fayez Al Hassan (nog niet gepubliceerd)

nr 81
Well Being in Hospitals
Simona Di Cicco

nr 82
Solares Bauen
Implementierungs- und Umsetzungsaspekte in der Hochschulausbildung in Österreich
Gerhard Schuster

nr 83
Supporting Strategic Design of workplace Environments with Case-Based Reasoning
Shauna Mallory-Hill

nr 84
ACCEL: a Tool for Supporting Concept Generation in the Early Design Phase
Maxim Ivashkov

nr 85
Brick-mortar interaction in masonry under compression
Ad Vermeltfoort

nr 86
Zelfredzaam Wonen
Guus van Vliet

nr 87
Een ensemble met grootstedelijke allure
Jos Bosman/Hans Schippers

nr 88
On the Computation of Well-Structured Graphic Representations in Architectural Design
Henri Achten

nr 89
De Evolutie van een West-Afrikaanse Vernaculaire Architectuur
Wolf Schijns

nr 90
ROMBO tactiek
Christoph Maria Ravesloot

nr 91
External coupling between building energy simulation and computational fluid dynamics
Ery Djunaedy

nr 92
Design Research in the Netherlands 2005
Editors:
Henri Achten
Kees Dorst
Pieter Jan Stappers
Bauke de Vries

nr 93
Ein Modell zur baulichen Transformation
Jalil H.Saber Zaimian

nr 94
Human Lighting Demands Healthy Lighting in an Office Environment
Myriam Aries

nr 95
A Spatial Decision Support System for the Provision and Monitoring of Urban Greenspace
Claudia Pelizaro

nr 96
Leren Creëren
Adri Proveniers

nr 97
Simlandscape
Rob de Waard

nr 98
Design Team Communication
Ad den Otter

nr 99
Humaan-Ecologisch Georiënteerde Woningbouw
Juri Czabanowski

nr 100
Hambase
Martin de Wit

nr 101
Sound Transmission through Pipe Systems and into Building Structures
Susanne Bron - van der Jagt

nr 102
Het Bouwkundig Contrapunt
Jan Francis Boelen

nr 103
A Framework for a Multi-Agent Planning Support System
Dick Saarloos

nr 104
Bracing Steel Frames with Calcium Silicate Element Walls
Bright Mweene Ng'andu

nr 105
Naar een nieuwe houtskeletbouw
F.N.G. De Medts

nr 106
Anatomy of Dwelling
Enno Wiersma
(nog niet gepubliceerd)

nr 107
Healing Architecture
Ewa Mosiniak
(nog niet gepubliceerd)

nr 108
Geborgenheid
drs T.E.L. van Pinxteren

nr 109
Modelling Strategic Behaviour in Anticipation of Congestion
Qi Han

nr 110
Reflecties op het Woondomein
Fred Sanders

nr 111
On Assessment of Wind Comfort by Sand Erosion
Gabor Dezso

nr 112
Bench Heating in Monumental Churches
Dionne Limpens-Neilen

nr 113
RE. Architecture
Ana Pereira Roders

nr 114
Toward Applicable Green Architecture
Usama El Fiky

nr 115
Knowledge Representation Under Inherent Uncertainty in a Multi-Agent System for Land Use Planning
Liying Ma

nr 116
Integrated Heat Air and Moisture Modeling and Simulation
Jos van Schijndel

nr 117
Concrete behaviour in multiaxial compression
J.P.W. Bongers

nr 118
The Image of the Urban Landscape
Ana Moya Pellitero

nr 119
The Self-Organizing City in Vietnam
Stephanie Geertman

nr 120
A Multi-Agent Planning Support System for Assessing Externalities of Urban Form Scenarios
Rachel Katoshevski-Cavari

nr 121
Den Schulbau neu denken, fühlen und wollen
Urs Christian Maurer-Dietrich

nr 122
Peter Eisenman Theories and Practices
Bernhard Kormoss

nr 123
User Simulation of Space Utilisation
Vincent Tabak

nr 124
Moisture Transport in Cavity Brick Wall
A. Aghai
(nog niet gepubliceerd)

nr 125
In Search of a Complex System Model
Oswald Devisch

nr 126
Lighting in Work Environment direct Effects of Lighting Level and Spectrum on Pshychophysiological Variables
Grazyna Goricka
(nog niet gepubliceerd)

nr 127
Flanking Sound Transmission trough Lightweight Framed Double Leaf Walls
Stefan Schoenwald

nr 128
Bounded Rationality and Spatial-Temporal Pedestrian Shopping Behaviour
Wei Zhu

nr 129
Travel information Impact on activity travel pattern
Zhongwei Sun

nr 130
Co-simulation for performence prediction of innovative integrated mechanical energy systems in buildings
Marija Trčka

nr 131
Allemaal Winnen
M.J. Bakker
(nog niet gepubliceerd)

nr 132
Architectural Cue Model in Evacuation Simulation for Underground Space Design
Chengyu Sun

nr 133
Uncertainty and sensitivity analysis in building performance simulation for decision support and design optimization
Christina Hopfe

nr 134
Facilitating distributed collaboration in the AEC/FM sector using Semantic Web Technologies
Jacob Beetz

nr 135
Circumferentially Adhesive Bonded Glass Panes for Bracing Steel Frame in Façades
Edwin Huveners

nr 136
Influence of temperature on concrete beams strengthened in flexure with CFRP
Ernst-Lucas Klamer

nr 137
Sturen op klantwaarde
Jos Smeets

nr 138
Nog niet bekend
Mariette van Stralen
(nog niet gepubliceerd)

nr 139
Lateral behavior of steel frames with discretely connected precast concrete infill panels
Paul Teewen

nr 140
Integral design method in the context of sustainable building design
Perica Savanovic

nr 141
Household Activity-Travel Behavior: Implementatioń of Within-Household Interactions
Renni Anggraini
(nog niet gepubliceerd)

nr 142
Design Research in the Netherlands 2010
Henri Achten
(nog niet gepubliceerd)

nr 143
Modelling life trajectories and transport mode choice using Bayesian Belief Networks
Marloes Verhoeven

nr 144
Assessing Construction Project Performance in Ghana
William Gyadu-Asiedu

nr 145
Empowering Seniors through Domotic Homes
Masi Mohammadi

nr 146
An Integral Design Concept for Ecological Self-Compacting Concrete
Martin Hunger

nr 147
Governing Multi-Actor Decision Processes in Dutch Industrial Area Redevelopment
Erik Blokhuis

nr 148
A Multifunctional Design Approach for Sustainable Concrete
Götz Hüsken

nr 149
Quality monitoring in infrastrutural Design-Build projects
Ruben Favié

nr 150
Assessment Matrix for Conservation of valuable timber structures
Michael Abels

nr 151
Co-simulation of building energy simulation and computational fluid dynamics for whole-building heat, air and moisture engineering
Mohammad Mirsadeghi

nr 152
External coupling of building energy simulation and building element heat, air and moisture simulation
Daniel Cóstola

nr 153
Adaptive Decision Making In Multi-Stakeholder Retail Planning
Ingrid Janssen

nr 154
Landscape Generator
Kymo Slager

nr 155
Constraint specification in architecture
Remco Niemeijer

nr 156
A Need-based Approach to Dynamic Activity Generation
Linda Nijland

nr 157
Modeling Office Firm Dynamics in an Agent-Based Micro Simulation Framework
Gustavo Garcia Manzato

nr 158
Lightweight Floor System for Vibration Confort
Sander Zegers

nr 159
Aanpasbaarheid van de draagstructuur
Roel Gijsbers

nr 160
“Village in the City” in Guangzhou, China
Yanliu Lin

nr 161
Climate risk assessment in museums
Marco Martens

nr 162
Social Activity-Travel Patterns
Pauline van den Berg

nr 163
Sound Concentration caused by curved Surfaces
Martijn Vercammen